Development of novel therapeutic agents designed to enhance insulin secretion through activation of the trace amine-associated receptor 1 (TAAR1)

Rhianna Katie Lenham, MSc

Thesis submitted in partial fulfilment of the requirements of Nottingham Trent University for the degree of Doctor of Philosophy

September 2024

Declaration

The copyright in this work is held by the author. You may copy up to 5% of this work for private study, or personal, non-commercial research. Any re-use of the information contained within this document should be fully referenced, quoting the author, title, university, degree level and pagination. Queries or requests for any other use, or if a more substantial copy is required, should be directed to the author.

Abstract

Produced in the pancreas, insulin is widely considered the most important hormone involved in metabolic homeostasis. Diabetes mellitus (DM) is a chronic metabolic disease affecting 537 million people worldwide which results from a defect in insulin action, secretion, or both. Over time, existing antihyperglycemic treatments designed to control type 2 DM (T2DM) typically become ineffective due to changes in disease progression including weight gain and increased insulin resistance, highlighting the importance for the continued development of new therapeutic agents which exert their effects through diverse/ novel mechanisms.

Trace amine-associated receptor 1 (TAAR1) is a G protein-coupled receptor located in the brain, stomach, intestines and pancreatic β-cells which has roles in mediating neurodegenerative and metabolic disorders. Although most of the existing research into TAAR1 agonists has focused on their role within the central nervous system for application in schizophrenia treatments, studies have identified activation of pancreatic TAAR1 enhances insulin secretion, thus TAAR1 is a promising target for novel antihyperglycemic treatments for T2DM.

This thesis reports the rational design, synthesis and pharmacological evaluation of a series of ligands intended to exhibit a peripherally restricted TAAR1 agonist profile, based on *N*-((1*H*-imidazol-4-yl)methyl)-4-chloro-*N*-isopropylaniline (RO5073012, **59**), as part of a structure activity relationship study. The analogues are computationally predicted to be substrates of the P-glycoprotein transporter and experimentally predicted to have low blood brain barrier permeability through immobilised artificial membrane reversed-phase high performance liquid chromatography, preventing the likelihood of inducing potential undesired on-target effects. The data obtained from high range rat insulin enzyme-linked immunosorbent assays (Mercodia) shows that the novel analogues enhance insulin secretion in control and glucolipotoxicity conditions designed to mimic an environment typically associated with patients with poorly controlled T2DM. We also demonstrate that one compound, *N*-((1*H*-imidazol-2-yl)methyl)-4-

chloro-*N*-isopropylaniline (**76c**), upregulates the secondary messenger cyclic adenosine monophosphate (cAMP) using the cAMP select ELISA (Cayman Chemical). This suggests **76c** mediates its therapeutic effects via TAAR1 thus indicating a potential role for these molecules as novel therapeutic agents in the treatment of T2DM.

Acknowledgements

Firstly, I would like to take the opportunity to thank my PhD supervisors Dr Mark Turner, Dr Shailesh Mistry and Prof. Charles Laughton for all the help and support you have given me during my PhD. Having such a multidisciplinary group of supervisors across different institutions has allowed me to expand and broaden my skillset in ways that I could not have imagined when I first started, all of which has made me a more well-rounded scientist. I am extremely grateful for everything you have taught me over the last four years, for your words of encouragement, for rebuilding my confidence during the challenging times that arose when experiments didn't go as planned and for reminding me about everything I have achieved so far.

Shailesh, thank you for everything - from finally making the batch of sourdough croissants you promised since my MSc year to all your gardening advice and everything in between! I am honoured to have been the 'social secretary' for the Mistry group and I hope the new replacement is just as good at sending you calendar invites to things you most definitely should just remember! Thank you for all the support you have given me, and I look forward to eventually attending the pizza night you have been organising for the last four years or so!

I would like to thank all the members of technical staff in the chemistry labs in BDI at University of Nottingham and in ISTeC at Nottingham Trent University and all the past and present members of the research groups for all your work advice and friendship during my PhD journey, you really have made it an unforgettable experience! A special thank you goes to Dr Mirjana Antonijevic, Dr Mahesh Puthanveedu, Dr Jomo Kigotho, Dr Bianca Casella, Rhys, Luke, George, Matt, Jaffer, Liam, Jess, Beth and Josh.

Mirjana, Mahesh, Jomo and Bianca – thank you for all your truly wonderful postdoc advice (even if it wasn't always the best and most successful way of doing things). A special mention should go to Mirjana's fantastic taste in Netflix programmes and Bianca's desire to have a Just Dance / Sing Star session! Jomo where do I begin? Thank you for truly being one of the kindest people

I have ever met and for becoming one of my closest friends in such a short period of time. Thank you for being a great housemate in the months we lived together and for cooking a delicious dinner on Christmas Day!

My entire PhD experience wouldn't have been the same without Rhys. I am grateful to call you my friend so thank you for everything and for always being there for me.

Jess, you have been a part of the collaborative Nottingham DTP process from the beginning, and I couldn't be more grateful! Thank you for being a firm believer in safety in numbers as we figured out each step of the way – I honestly don't know where I would be without you!

Josh, thank you for the constant supply of confluent cells whenever I would come across to NTU to complete my pharmacology.

Lastly, I would like to thank my family and friends for all the support and encouragement you have given me throughout my time in education.

List of Figures

List of Tables

List of Schemes

List of Equations

Abbreviations

AMPK	AMP-activated protein kinase
ANOVA	Analysis of variance
ATP	Adenosine triphosphate
BBB	Blood brain barrier
BCA	Bicinchoninic acid protein assay
BINAP	(2,2'-bis(diphenylphosphino)-1,1'-binapthyl
BLAST	Basic local alignment search tool
BRET	Bioluminescence resonance energy transfer
Calcein AM	Calcein acetoxymethyl ester
cAMP	Cyclic adenosine monophosphate
CDI	1,1'-Carbonyldiimidazole
CHI$_{IAM}$	Chromatographic hydrophobicity index
CNS	Central nervous system
COMU	1-((1-Cyano-2-ethyoxy-2-oxoethylideneaminooxy)dimethylaminomorpholino) uronium hexafluorophosphate
CPE	Carboxypeptidase E
Cryo-EM	Cryogenic-electron microscopy
DCC	*N,N'*-Dicyclohexylcarbodiimide
DCF	2,7-Dichlorofluroescein
DIPEA	*N,N*-Diisopropylethylamine
DM	Diabetes Mellitus
DMAP	*N,N*-Dimethylaminopyridine
DMF	Dimethylformamide
DNA	Deoxyribonucleic acid
DPP IV	Dipeptidyl-peptidase IV
EC	Extracellular loop
EC$_{50}$	Half maximal effective concentration
EDC HCl	(3-Dimethylamino-propyl)-ethyl-carbodiimide hydrochloride
EDC/HOBt	EDC/Hydroxybenzotriazole

ELISA	Enzyme-linked immunosorbent assay
Epac	Exchange proteins directly affected by cAMP
Ex/Em	Excitation/emission
F	Bioavailability
FAIS	Fatty acid insulin secretion
FDA	US food and drug administration
FRET	Fluorescence resonance energy transfer
Fura-2 AM	Fura-2-acetoxymethyl ester
GD	Gestational diabetes
GDP	Guanosine diphosphate
GIP	Gastric inhibitory peptide
GLP-1	Glucagon-like peptide 1
GLT	Glucolipotoxicity
GLUT-2	Glucose transporter 2 receptors
GPCRs	G protein-coupled receptors
GRKs	GPCR kinases
GSIS	Glucose stimulated insulin secretion
GTP	Guanosine triphosphate
H$_2$DCF	2,7-Dichlorodihydrofluorescein
H$_2$DCF-DA	2,7-Dichlorodluorescin diacetate
HATU	1-[Bis(dimethylamino)methylene]-1*H*-1,2,3-triazolo[4,5-*b*]pyridinium 3-oxide hexafluorophosphate
HEK-293	Human embryonic kidney-293 cells
hTAAR1	Human trace amine-associated receptor 1
HRMS TOF ES	High resolution mass spectrum time of flight electrospray
HTS	High throughput screening
IAM	Immobilised artificial membrane
IBMX	3-Isobutyl-methylxanthine
IBS	Irritable bowel syndrome
IC	Intracellular loop

IDF	International Diabetes Federation
INS-1	Insulinoma cell line
IRS-2	Insulin receptor substrate 2
I-TASSER	Iterative threading assembly refinement
K_i	Binding affinity
K_{IAM}	Immobilised artificial membrane partition co-efficient
k_{IAM}	Retention factor
KREBS	Krebs-Ringer Buffer
LC-MS	Liquid chromatography-mass spectrometry
Log D$_{7.4}$	Distribution co-efficient
Log P	Partition co-efficient
MAO	Monoamine oxidase
MAPK	Mitogen-activated protein kinase
MoA	Mechanism of action
MODY	Mature onset diabetes in the young
mTAAR1	Murine trace amine-associated receptor 1
MW	Molecular weight
nHBA	Number of hydrogen bond acceptors
nHBD	Number of hydrogen bond donors
OCT-1	Organic cation transporter 1
OCT-2	Organic cation transporter 2
PAMPA	Parallel artificial membrane permeability assay
P_{app}	Compound permeability
PBS	Phosphate buffered saline
PC	Proprotein convertases
PDB	Protein data bank
pEC_{50}	Negative logarithm of EC_{50}
PI3K	Phosphoinositide 3-kinase
PKA	Protein kinase A
PKC	Protein kinase C

P_m	BBB membrane permeability
PMA	Phorbol 12-myristate 13-acetate
ppm	Parts per million
PSA	Polar surface area
PyBOP	Benzotriazole-1-yloxytripyrrolidinophosphonium hexafluorophosphate
PyBrOP	Bromo(tri-1-pyrrolidinyl)phosphonium hexafluorophosphate
RAP1	Ras-proximate-1
Rluc	R. reniformis luciferase
RMSD	Root mean square deviation
RP-HPLC	Reversed-phase high-performance liquid chromatography
RPMI-1640	Roswell Park Memorial Institute-1640 media
R_t	Retention time
rTAAR1	Rodent trace amine-associated receptor 1
SAR	Structure-activity relationship
SGLT-2	Sodium-glucose cotransporter 2
SSR	Species-specificity ratio
t_0	Dead time
T1DM	Type 1 diabetes mellitus
T2DM	Type 2 diabetes mellitus
TA	Trace amines
TAAR1	Trace amine-associated receptor 1
TAARs	Trace amine-associated receptors
TLC	Thin layer chromatography
TM	Transmembrane
V_a	Volume of acceptor well
V_d	Volume of donor well
V_m	Volume of mobile phase
VMAT2	Vesicular monoamine transporter 2
V_s	Volume of stationary phase
WHO	World Health Organisation

zTAAR1   Zebrafish trace amine-associated receptor 1

Table of Contents

1. Introduction

Composed of a network of organs, the digestive system (Figure 1.1) facilitates the breakdown of food into essential nutrients (protein, fat, vitamins and carbohydrates) which are absorbed for survival [1].
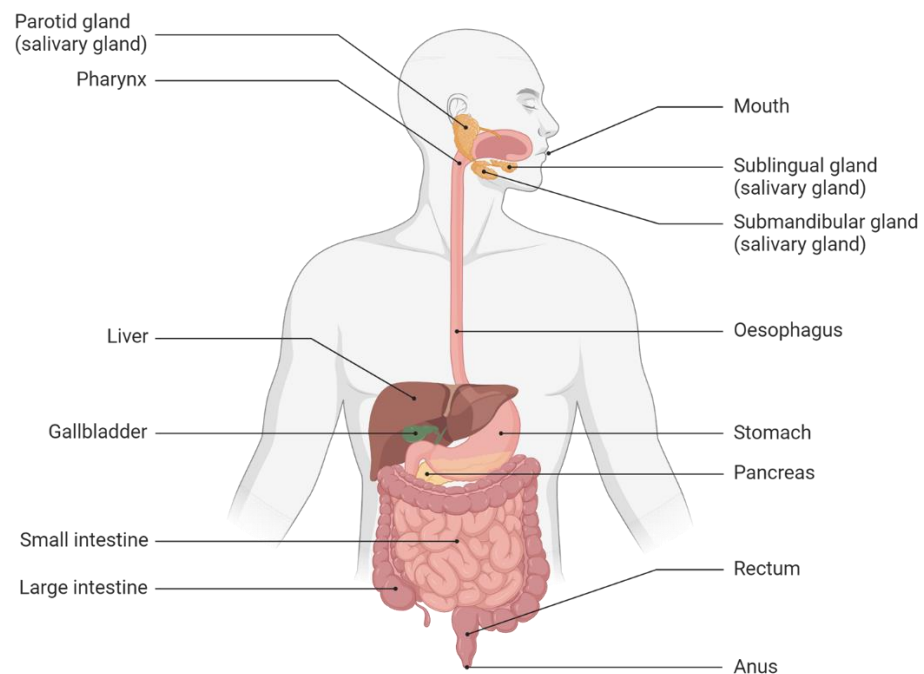
Figure 1.1 The digestive system. Image taken from and created using Biorender.com.

Produced in the pancreas, insulin is a vital hormone involved within the digestive system. The main function of insulin is to ensure correct sugar storage by regulating circulating blood sugar levels [2]. In 2021, a study identified that 40% of adults (aged 18-44) living in America had developed insulin resistance and thus were at an increased risk of developing several chronic metabolic disorders (Figure 1.2) [3, 4].
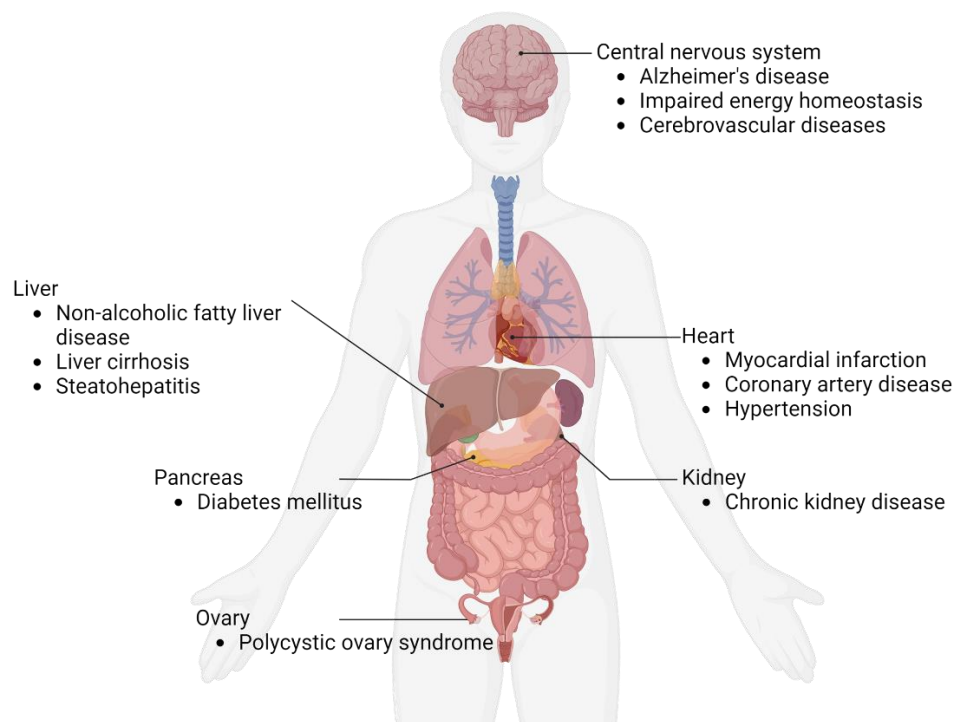
Figure 1.2 *Chronic metabolic disorders which can arise because of insulin resistance. Adapted Zhao et al [3]. Image created using Biorender.com.*

Shown in Figure 1.2, insulin resistance is a risk factor for diabetes mellitus (DM) and in 2021 the International Diabetes Federation (IDF) reported over 537 million adults worldwide are living with diabetes, with the global projection expecting over 783 million adults to have diabetes by 2045 [5]. Approximately, 1.5 million deaths are related to diabetes annually, with the World Health Organisation (WHO) classifying the disorder as a top 10 leading cause of death globally [6, 7]. Although antidiabetic therapeutic agents have been developed to manage diabetes, their effectiveness often declines over time and thus the current challenge is to develop new therapeutic agents to assist with the treatment of DM.

1.1. Diabetes mellitus

Characterised by hyperglycaemia occurring from abnormal glucose homeostasis (fasting blood glucose: ≥ 7 mmol/L), DM is a group of metabolic diseases which result from a defect in insulin action, secretion or both [8-10]. In January 2019, over 400 million people worldwide suffered with DM and this number has continued to soar in recent years [9, 11]. Taken from the IDF Atlas report

in 2021, Figure 1.3 A and B show the estimated age-adjusted prevalence of diagnosed diabetes between ages 20-79 and the proportion of undiagnosed cases for 20–79-year-olds per country respectively, where it is clear diabetes is a global pandemic [5]. Figure 1.4 shows the expected global DM projections [5].

(A) Estimated total number of people worldwide aged between 20–79 suffering with diabetes in 2021.

(B) Predicted number of people worldwide aged between 20–79 with undiagnosed diabetes in 2021.
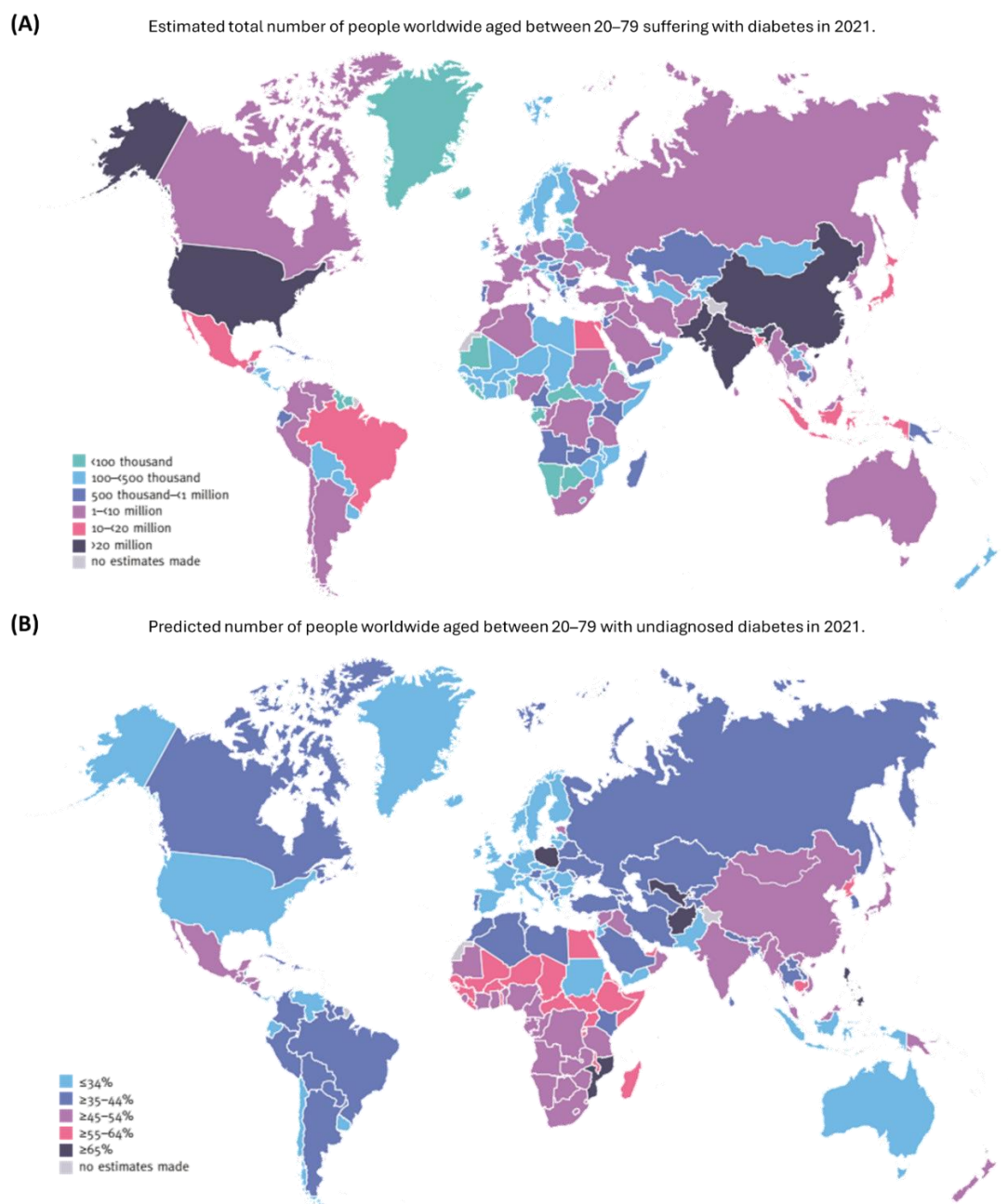
Figure 1.3 (A) World map showing the estimated prevalence of diabetes cases in adults aged 20-79 in 2021. (B) World map indicated the proportion of adults aged 20-79 with undiagnosed diabetes. Taken from International Diabetes Federation Diabetes Atlas 2021, 10th edition [5].

World

2045	783 million
2030	643 million
2021	537 million

↑ 46% increase

North America & Caribbean (NAC)

2045	63 million
2030	57 million
2021	51 million

↑ 24% increase

Europe (EUR)

2045	69 million
2030	67 million
2021	61 million

↑ 13% increase

Western Pacific (WP)

2045	260 million
2030	238 million
2021	206 million

↑ 27% increase

South & Central America (SACA)

2045	49 million
2030	40 million
2021	32 million

↑ 50% increase

Africa (AFR)

2045	55 million
2030	33 million
2021	24 million

↑ 134% increase

Middle East & North Africa (MENA)

2045	136 million
2030	95 million
2021	73 million

↑ 87% increase

South-East Asia (SEA)

2045	152 million
2030	113 million
2021	90 million

↑ 68% increase

Figure 1.4 *World map showing the expected global projections of DM in 2030 and 2045. Taken from International Diabetes Federation Diabetes Atlas 2021, 10th edition [5].*

DM is broadly characterised into two main subdivisions; type 1 and type 2, however other forms are known (mature onset diabetes in the young (MODY), gestational diabetes (GD), latent autoimmune diabetes in adults (LADA), ketosis-prone diabetes, neonatal diabetes and cystic fibrosis diabetes) [12-14]. Resulting from damaged blood vessels due to prolonged excess blood glucose, many long-term complications are associated with DM. Classified into two subdivisions, complications from DM are either macrovascular complications (renal failure, retinopathy and damage to the nervous system) or microvascular (myocardial infarction, damage to the heart and stroke) (Figure 1.2) [10, 15].

These long-term implications highlight the urgency for early diagnosis and the development of new therapeutic agents. In 2011, WHO recommended a new first point-of-call for identifying diabetes – the glycated haemoglobin (HbA1c) test as no prior patient preparation (fasting) is required [16]. Haemoglobin can become glycated with glucose, therefore the HbA1c test analyses the average amount of glycated haemoglobin during a 2–3-month time frame. As increased blood glucose levels afford an increased HbA1c level [17], the American Diabetes Association have recommended HbA1c levels >6.5% indicate a positive diagnosis for DM [18].

1.1.1. Type 1 diabetes mellitus

Type 1 diabetes mellitus (T1DM) is a heritable disease [19]. Often referred to as juvenile diabetes or insulin-dependent diabetes, T1DM is readily diagnosed in children where it is reported offspring of a diabetic father are three times more likely to inherit the condition than children with a diabetic mother [20, 21]. Symptoms of T1DM include weight loss, increased urination, excessive thirst and polyphagia [22].

Accountable for fewer than 10% of all diabetes cases, T1DM is caused by an autoimmune process whereby destruction of pancreatic β-cells results in insulin deficiency, subsequently leading to hyperglycaemia [23, 24]. Markers of the immune destruction of pancreatic β-cells include autoantibodies to glutamic acid and insulin, islet cell autoantibodies and autoantibodies to tyrosine phosphatases IA-2 and IA-2β [10]. Literature suggests the destructive autoimmune process is due to insulitis – a process whereby T cells penetrate the Islets of Langerhans and attack insulin-releasing β-cells. Furthermore, patients of T1DM are likely to develop ketoacidosis [25]. Patients of African or Asian ancestry are prone to developing a subtype of T1DM known as idiopathic diabetes, a condition which lacks the autoimmune component, but results in the individual suffering with episodic ketosis and permanent insulinopenia (low insulin concentration in the bloodstream) [10]. The first-line response for T1DM is insulin-replacement therapy coupled with a healthy and maintained diet. However, this form of therapy has

associated problems including lifelong dependency on regular insulin injections, psychiatric conditions and hypoglycaemia [26].

1.1.2. Type 2 diabetes mellitus

Type 2 diabetes mellitus (T2DM) is the predominant form of diabetes, accounting for 90-95% of cases [27, 28]. Formerly known as non-insulin-dependent diabetes or adult-onset diabetes, T2DM often occurs in later life due to environmental factors and demographic characteristics, with obesity being the largest risk factor [29-32]. Other factors which contribute to the development of T2DM include smoking, drinking alcohol and physical inactivity. Females are more likely to develop the condition and higher incidence rates of T2DM were reported within the Asian and black populations [32, 33]. Despite often occurring in adulthood, the number of T2DM cases reported in children is increasing due to the rise in childhood obesity [34].

T2DM is characterised by insulin insensitivity arising from a decline in insulin production and resistance due to pancreatic β-cell dysfunction and unsuccessful cell signalling of the insulin receptor. In turn, the rate of glucose transportation to vital organs such as skeletal muscle, adipose tissue and the liver is significantly reduced. Consequently, blood glucose and glucagon levels are not reduced and hyperglycaemia occurs [27].

The symptoms of T2DM are very similar to T1DM, however they develop more slowly thus making T2DM difficult to diagnose. Briefly, insulin secretion is reduced due to β-cell dysfunction, subsequently hindering effective cellular uptake of glucose [27]. Unlike T1DM, several pharmacological agents have been developed to manage T2DM (discussed in Section 1.3) with metformin (**1,** shown in Figure 1.5) recognised as the first-line medication. These therapeutic agents coupled with increased physical activity and improved diet have proven to be effective measures to successfully manage T2DM [35]. However, the effectiveness of these therapies often declines over time.
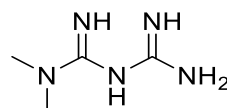
Metformin (1)

Figure 1.5 *Chemical structure of metformin (1).*

1.1.3. Other forms of diabetes

Defined as any degree of glucose intolerance with onset or first recognition during pregnancy, GD is the third most common form of DM [36]. Similar to T2DM, GD occurs due to β-cell dysfunction and is known to affect 1 in 7 pregnancies worldwide [37]. Furthermore, patients affected by GD are seven times more likely to develop T2DM within 10 years [38, 39]. Like T1DM and T2DM risks associated with GD include increased likelihood of C-section delivery, premature birth, pre-eclampsia and obesity [37]. GD can be managed with pharmacological treatment; however, metformin (**1**) is known to cross the placenta affecting metabolic, mitochondrial, proliferative and hepatic signalling pathways. The potential long term effects on the foetus are unknown; thus GD is commonly treated through diet and lifestyle modifications [37].

Like T1DM, MODY is an inherited form of DM with a prevalence of 2% of all diabetes cases [40]. MODY is a cluster of monogenic β-cell disorders and is caused by mutations in key genes (HNF1α, GCK and HNF4α) which regulate glucose homeostasis and results in a decline of β-cell function, subsequently reducing insulin secretion [12, 41]. Symptoms of MODY coincide with those demonstrated by T1DM and T2DM; thus, diagnosis is frequently missed, and inappropriate treatment administered [40].

1.2. Insulin

1.2.1. Pancreas

The pancreas is an endocrine organ composed of both endo- and exocrine tissue which develops from the duodenum [42]. Responsible for the function of the digestive gland, the tubuloacinar

gland makes up the exocrine portion, whilst the endocrine consists of thousands of pancreatic Islets of Langerhans [43] (Figure 1.6).
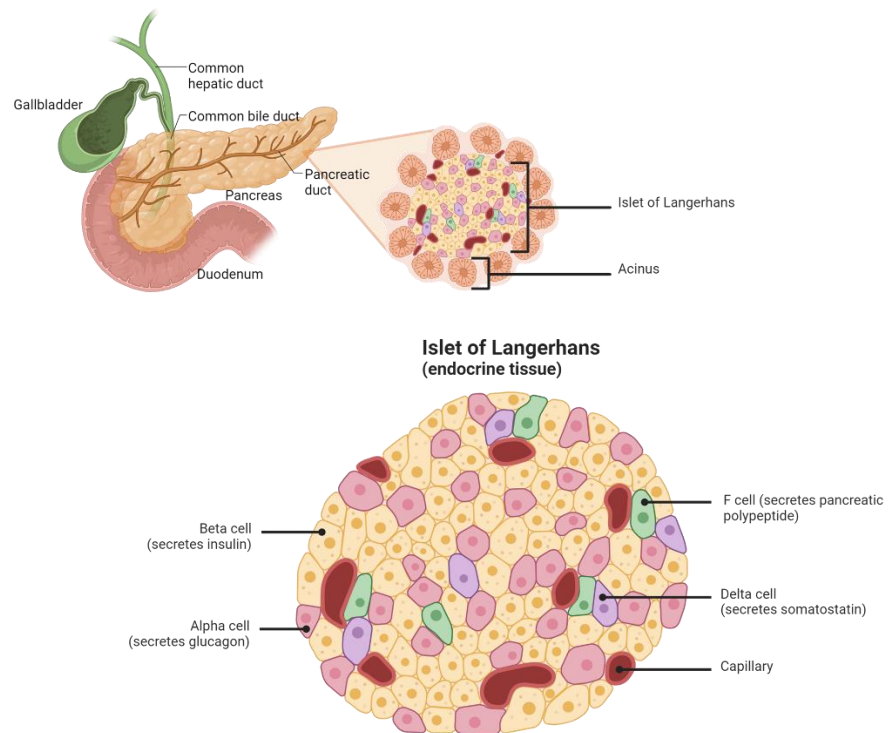
Figure 1.6 *Structure of the pancreas and Islets of Langerhans. Islets of Langerhans are cellular clusters of endocrine tissue responsible for the hormone production involved in glucose homeostasis. Image created using Biorender.com.*

There are four major cell types within the Islets of Langerhans, (Table 1.1) with β-cells making up approximately 70% of the clusters. The remaining 30% is made up of α-cells (20%) and δ-cells and γ-cells accounting for the final 10% of the clusters [44-46].

Table 1.1 *Cell types found in the Islets of Langerhans and their function.*

Cell type	Function
Alpha (α)	Responsible for the secretion of glucagon
Beta (β)	Responsible for insulin production
Delta (δ)	Responsible for the secretion of somatostatin – a growth inhibiting hormone
Gamma (γ) / F cell	Responsible for the secretion of pancreatic polypeptides

Islets of Langerhans have an irregular, oval shape (Figure 1.6) and are found throughout the pancreatic ductal and acinar tissue. Studies have identified the organisation of cell types within the islet clusters; β-cells are sandwiched between two layers of α-cells resulting in a folded trilaminar plate. The purpose of this distribution is to allow blood vessels to circulate along both sides allowing for optimal blood flow and oxygen circulation [47]. Furthermore, this specific arrangement around blood vessels provides the hormones required to carry out the functions stated in Table 1.1 direct access to the circulatory system.

Occuring during metabolic stress, selective destruction of β-cells arises due to the release of cytokines from nearby immune cells; thus a decline in pancreatic function is observed and the pancreas is unable to efficiently secrete the hormones required in Table 1.1 [48]. Typically the deterioration in pancreatic function results from damage caused by numerous conditions including; DM, bloating, weight loss, and autoimmune, chronic and recurrent pancreatitis [48].

1.2.2. Discovery, biosynthesis, structure and storage

Insulin is a vital hormone involved in glucose homeostasis. Successful extraction of insulin was achieved by Banting, Best and MacLeod in the early 20th century [49, 50]. Located on chromosome 11, the insulin gene encodes a 110-amino acid precursor protein known as preproinsulin.

Interaction of the hydrophobic *N*-terminal with the cytosolic ribonucleoprotein signal recognition particles enables translocation to the rough endoplasmic reticulum [51]. After translocation, preproinsulin is cleaved into proinsulin through the removal of a signal peptide located on the *N*-terminus, Figure 1.7 [52, 53]. The proinsulin is folded, leading to the formation of disulfide bonds and is transferred to the Golgi apparatus, where it is transformed into insulin in β-cell secretory granules [54]. During this process, proinsulin is cleaved by either proprotein convertases (PC) 1/3 coupled with carboxypeptidase E (CPE) to yield des-31, 32 proinsulin via the removal of paired arginine residues or via PC2 and CPE leading to the formation of des-64,65 proinsulin due to cleavage occurring at lysine-arginine pairs (Figure 1.8) [55]. Depending on the initial cleavage route taken, a second cleavage occurs at the opposing cleavage site and in turn, the C peptide which connects insulin's A-chain to its B-chain is released; thus proinsulin is converted into insulin (Figure 1.7 and Figure 1.8) [52, 56].
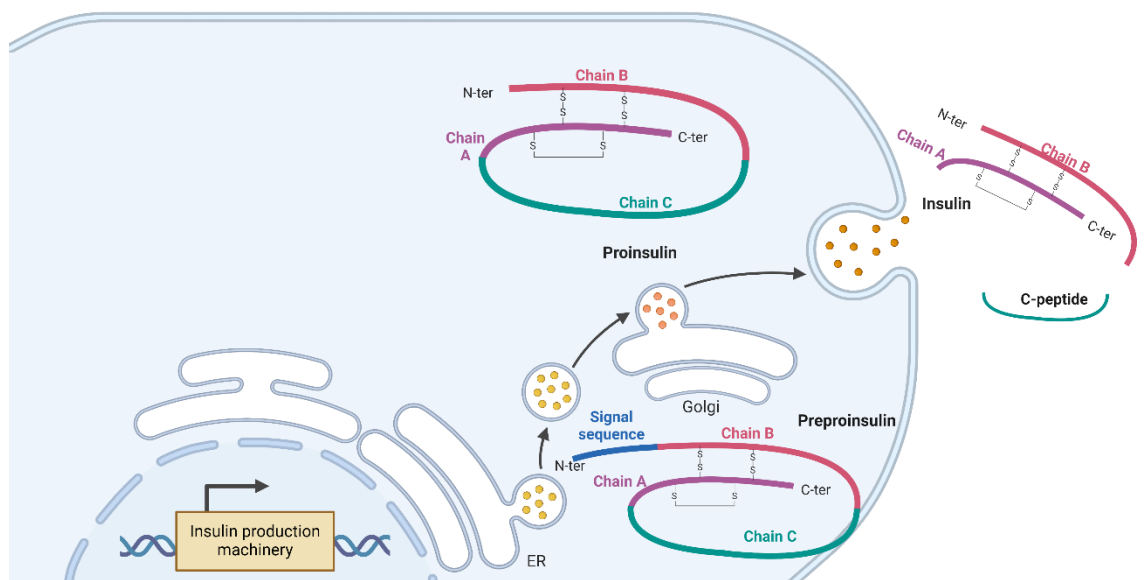
Figure 1.7 *Biosynthesis of insulin and its secretion from pancreatic β-cells. Image created and adapted using Biorender.com.*
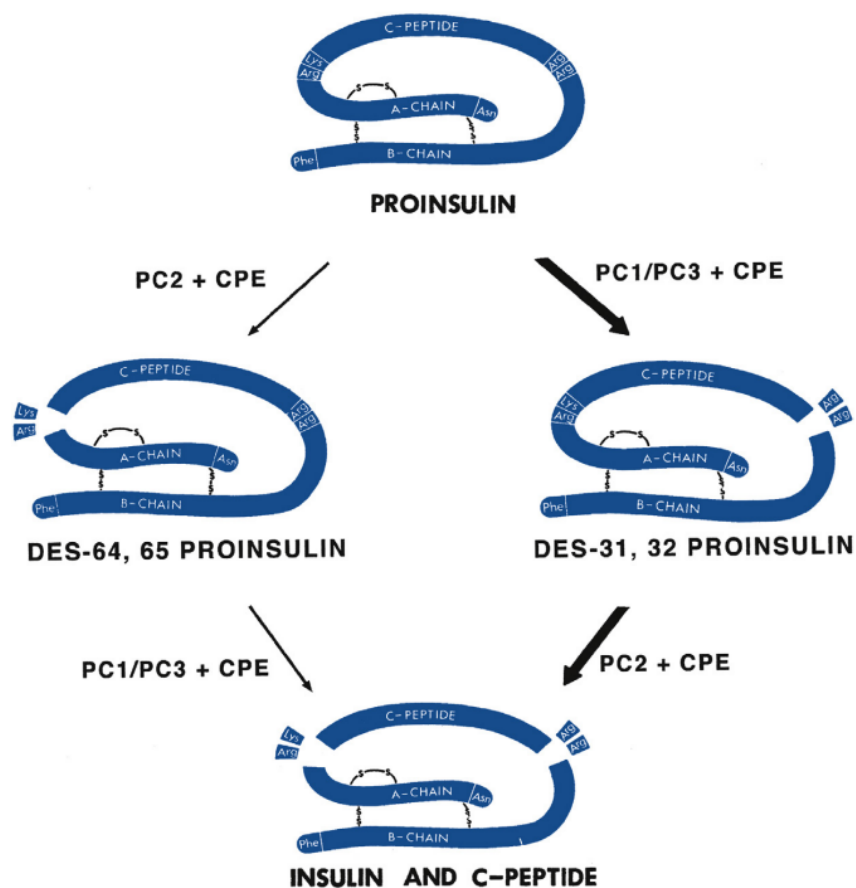
Figure 1.8 Conversion of proinsulin into insulin. (Left) Proinsulin is cleaved at Lys64-Arg65 cleavage site via PC2 and CPE yielding des-64,65 proinsulin. A second cleavage occurs at Arg31-Arg32 to release insulin and the C-peptide. (Right) Proinsulin is cleaved at Arg31-Arg32 cleavage site via PC1/3 and CPE yielding des-31,32 proinsulin. A second cleavage occurs at Lys64-Arg65 to release insulin and the C-peptide. Taken from Steiner et al [55].

Insulin is secreted as a dipeptide hormone composed of two chains, A and B (Figure 1.9). Chain A (composed of 21 amino acids) is linked to chain B (30 amino acids) via two disulfide bridges occurring between residue 7 on both chain A and B as well as residue 20 of chain A and residue 19 of chain B [57]. Hodgkin *et al* determined the structure of insulin by x-ray crystallography in 1969 [58], this work revealed that chain A contains two antiparallel α-helices between residues 1-8 and 12-20 whereas chain B is composed of both an α-helix between residues 9-19 and β-pleated sheets [59]. An intrachain disulfide bridge between residues 6 and 11 of chain A also contributes to the overall structure of insulin [60].
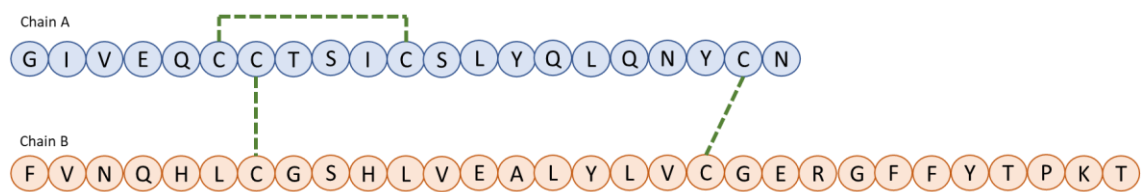
Figure 1.9 Schematic structure of human insulin. Disulfide bridges represented by green dashes.

The structure of insulin is conserved between species with bovine and porcine insulin most closely resembling human insulin. Figure 1.10 contains the protein sequence for human, bovine and porcine insulin and shows the amino acid sequences for bovine and porcine insulin differ from human insulin by 3 and 1 residues, respectively [61].

```
Human chain A        GIVEQCCTSICSLYQLQNYCN

Bovine chain A       GIVEQCCASVCSLYQLQNYCN

Porcine chain A      GIVEQCCTSICSLYQLQNYCN


Human chain B        FVNQHLCGSHLVEALYLVCGERGFFYTPKT

Bovine chain B       FVNQHLCGSHLVEALYLVCGERGFFYTPKA

Porcine chain B      FVNQHLCGSHLVEALYLVCGERGFFYTPKA
```

Figure 1.10 Alignment of amino acid sequence of human insulin, bovine insulin and porcine insulin with differing residues shown in red and underlined.

The metabolic signalling for insulin exocytosis occurs via several pathways resulting in cyclic adenosine monophosphate (cAMP)-dependent signalling cascade activation and the influx of extracellular Ca^{2+} ions [62]. Glucose stimulated insulin secretion (GSIS) is the main mechanism for reducing blood glucose levels. The process of GSIS is shown in Figure 1.11. Glucose enters pancreatic β-cells via the glucose transporter 2 (GLUT-2) receptor and once inside it is metabolised via glycolysis generating pyruvate. Upon entering the mitochondria, pyruvate enters the Krebs cycle, which after a series of biochemical reactions, causes an increase in adenosine triphosphate (ATP) concentration [63, 64]. In turn, cell depolarisation occurs whereby

ATP-sensitive potassium channels close and voltage-gated calcium channels open causing the influx of Ca^{2+} into pancreatic β-cells resulting in the exocytosis of insulin-containing vesicles leading to insulin secretion [63, 65].
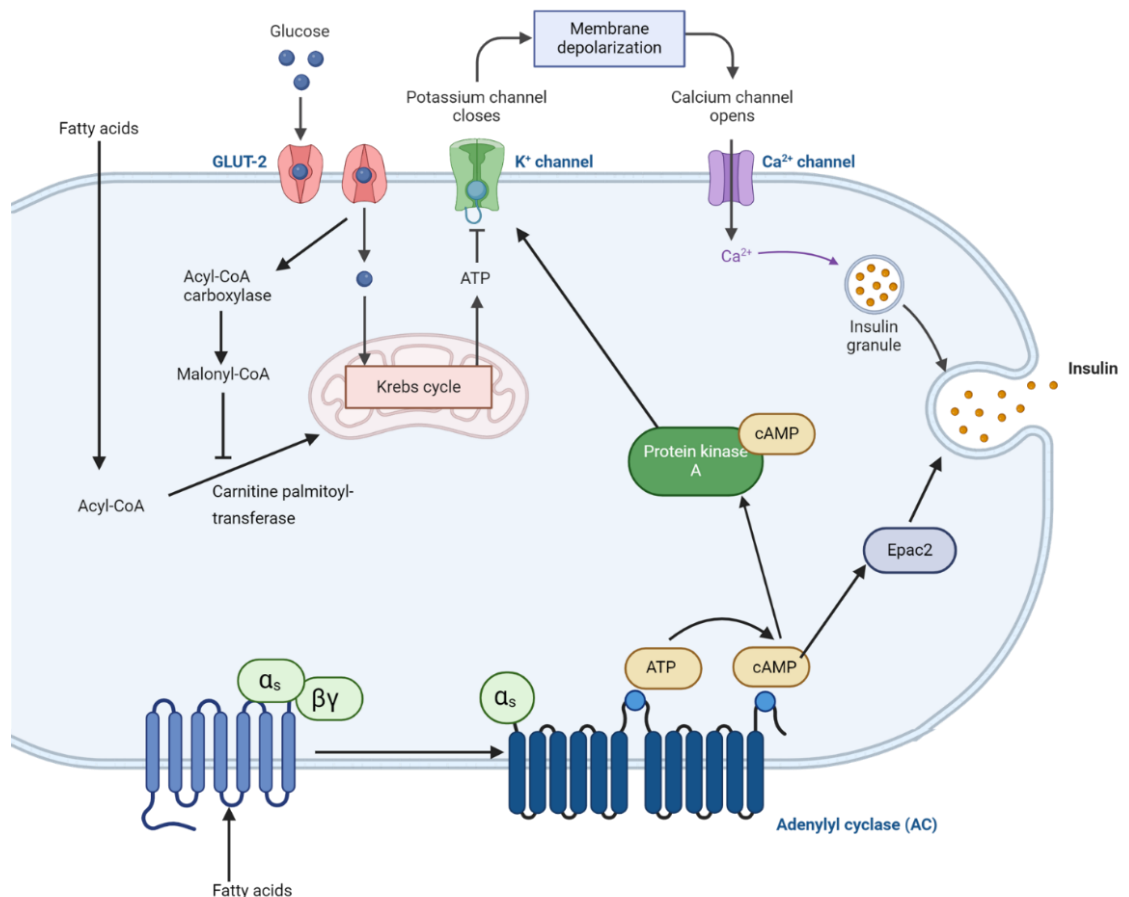
Figure 1.11 *Biological pathways for glucose stimulated insulin secretion (GSIS) and fatty acid stimulated insulin secretion (FAIS). GSIS: glucose enters the cell via GLUT-2 receptors before being metabolised in the mitochondria. A rise in ATP causes cell depolarisation - ATP-sensitive potassium channels to close and voltage-gated calcium channels open, triggering insulin secretion. FAIS: fatty acids enter the cell and are converted to acyl-CoA. Acyl-CoA is metabolised in the mitochondria by transportation via carnitine palmitoyl-transferase. Malonyl-CoA inhibits this process causing an acyl-CoA to levels to accumulate. In turn acyl-CoA increases Ca^{2+} causing insulin exocytosis. Fatty acids can stimulate GPCRs and activate the adenylyl cyclase pathway thus causing upregulation of cAMP, resulting in an increase in insulin secretion. Image adapted by Michael et al, Komatsu et al and Nolan et al and created using Biorender.com [9, 66, 67].*

Furthermore, fatty acids are important to pancreatic β-cell function and are known to increase GSIS via several pathways [68]. Firstly, fatty acids are oxidised into long chain acyl-CoA upon entering the cell, before transportation to the mitochondria by carnitine palmitoyl-transferase. Once inside the mitochondria, the long chain acyl-CoA undergoes β-oxidation forming acetyl-CoA, subsequently controlling baseline insulin secretion levels. Malonyl-CoA causes allosteric inhibition of carnitine palmitoyl-transferase thus preventing long chain acyl-CoA entering the mitochondria. In turn, the accumulation of long chain acyl-CoA causes an influx of cytosolic Ca^{2+} within the cell resulting in an increase in insulin secretion (Figure 1.11) [67, 69]. Lipolysis is another major pathway involved in stimulating insulin secretion via fatty acids [67]. Glucagon-like peptide 1 (GLP-1), is shown to interact with cell-surface receptors and activate the adenylate cyclase pathway where ATP is converted into cAMP (Figure 1.11) [70]. The upregulation of cAMP increases insulin secretion via both protein kinase A (PKA) independent and dependent pathways [71]. The cAMP dependent PKA pathway relies on the influx of Ca^{2+} using the voltage gated calcium channels like insulin secretion via GSIS, whereas insulin secretion via cAMP independent PKA pathway is mediated by exchange proteins directly affected by cAMP (Epac). There are two Epac isoforms (Epac1 and Epac2) expressed in pancreatic β-cells, with Epac2 found to be the isomer responsible for insulin secretion due to its ability to recruit insulin containing granules to the plasma membrane via its activation by ras-proximate-1 (Rap 1) [72]. Furthermore, activated PKA leads to the stimulation of hormone-sensitive lipase, an enzyme involved in regulating the release of free fatty acids into blood circulation; thus providing energy [73].

1.2.3. Roles of insulin

Summarised in Figure 1.12, the roles of insulin include the metabolism of proteins, lipids and carbohydrates, promoting cell division and the uptake of amino acids [74, 75]. As this project's main focus is the development of novel therapeutic agents for the management of DM, this section aims to provide an in-depth discussion of insulin's involvement in regulating metabolic homeostasis.
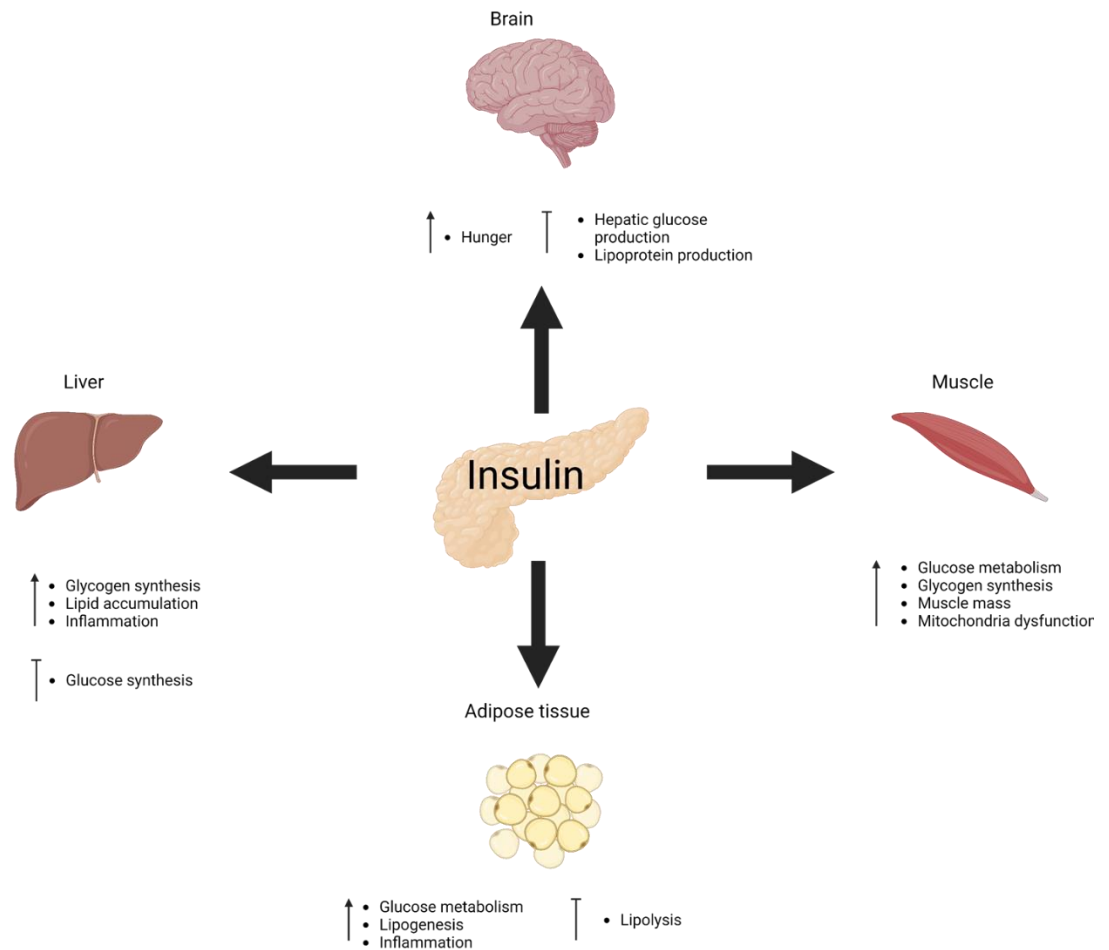
Figure 1.12 *Role of insulin in organ function and metabolism. Adapted from Yee et al [76]. Image created using Biorender.com.*

Insulin is a critical hormone involved in regulating the transportation of intracellular glucose into the liver, muscle and adipose tissue (Figure 1.12) [74]. The mechanism of action (MoA) of insulin is shown in Figure 1.13. Once secreted from pancreatic β-cells, insulin binds to INSR (a receptor tyrosine kinase specific to insulin) located on the target cell's membrane. Upon activation of INSR, the receptor is autophosphorylated following sequential conformational changes [77]. In turn, two downstream signalling pathways, namely the phosphoinositide 3-kinase (PI3K) / protein kinase B pathway and the mitogen-activated protein kinase (MAPK) pathway (Figure 1.13) are activated leading to glucose entering the cell and reduced blood glucose levels [78, 79]. Activation of the above signalling pathways occurs in two distinct ways. For the PI3K pathway,

activation occurs via the binding of PI3K's p85 regulatory subunit to IRS1 whereas for the MAPK

pathway occurs via the binding of Grb2 [80].
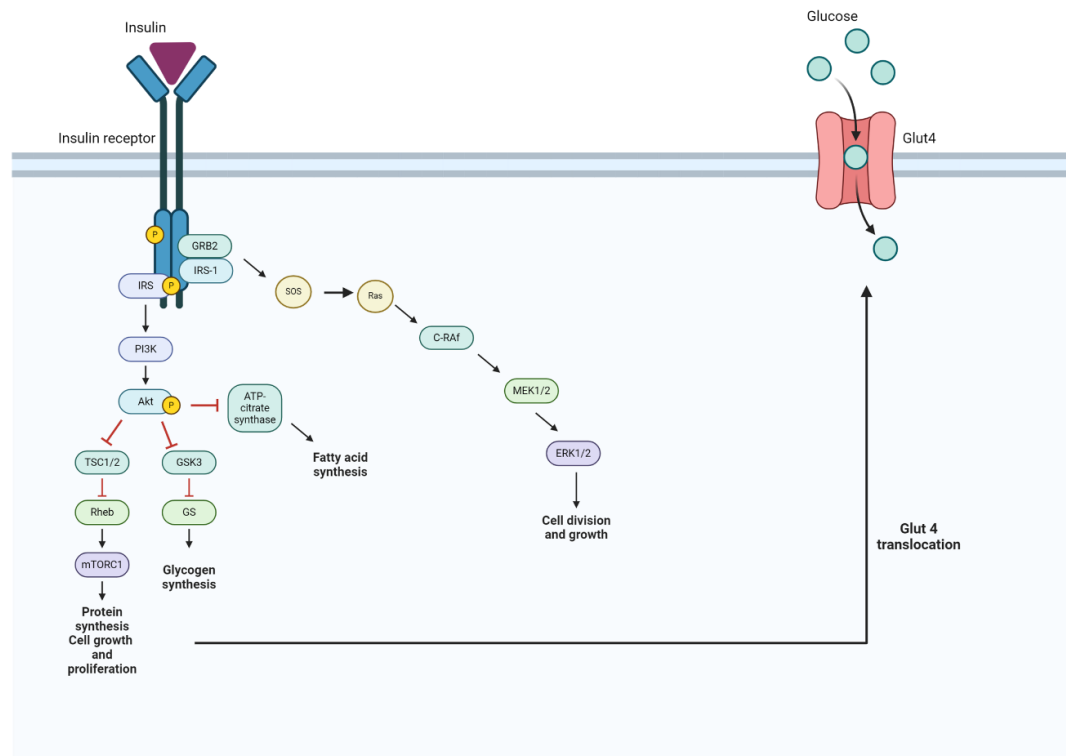
Figure 1.13 *Insulin signalling pathway. Activation of insulin receptor (INSR) leads to phosphorylation of IRS initiating*

PI3K/AKT and mitogen-activated protein kinase signalling cascades. GLUT4 translocation occurs facilitating glucose

uptake. IRS; insulin receptor substrate, PI3K; phosphoinositide 3-kinase, GRB2; growth factor receptor-bound protein

2, GSK; glycogen synthase kinase, GS; glycogen synthase, mTORC1; mammalian target of rapamycin complex 1, ERK;

extracellular signal-regulated kinase. Adapted from Rahman et al, Gabbouj et al and Arneth et al [81-83]. Image created

using Biorender.com.

1.3. History and development of diabetes treatments

T2DM is often managed through lifestyle changes including controlled weight loss, increased

exercise and reduced alcohol intake to maintain glucose homeostasis. In more advanced cases,

where lifestyle changes alone do not lead to glucose homeostasis, antidiabetic therapeutic

agents are administered. The major classes of antidiabetic therapies are biguanides,

sulfonylureas, sodium-glucose cotransporter 2 inhibitors (SGLT-2), dipeptidyl-peptidase IV (DPP

IV) inhibitors, incretin mimetics, α-glucosidase inhibitors and meglitinides (Figure 1.14). They exert their therapeutic effects via three main pathways: inhibition of gluconeogenesis, increased insulin sensitivity or increased insulin secretion. The effectiveness of these therapies often declines over time; therefore, combination therapy can be tailored to the individual patient using agents which follow different therapeutic mechanisms. This highlights the importance of the continued development of new therapeutic agents which exert their therapeutic effects through diverse/novel mechanisms.
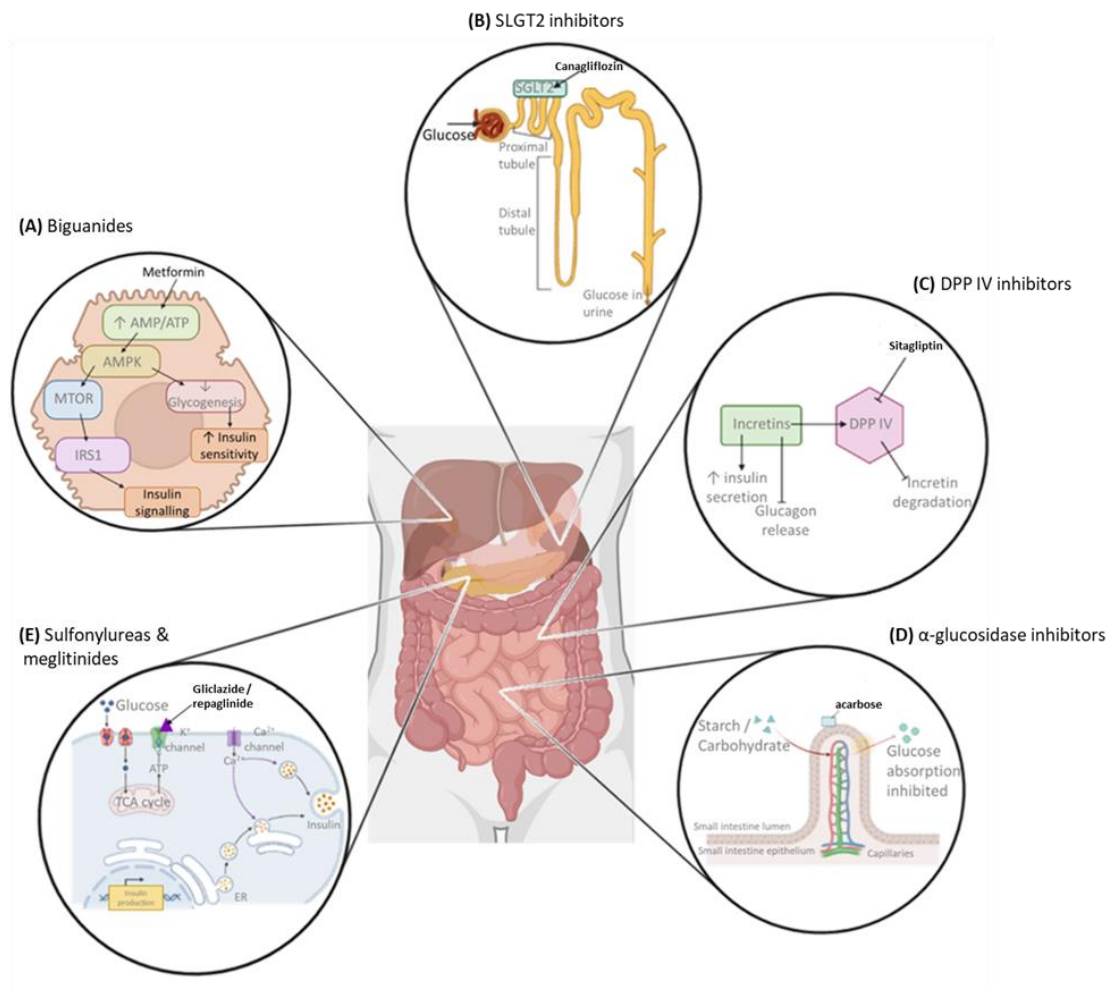
*Figure 1.14 Mechanism of action for current type 2 diabetes mellitus therapeutics. **(A)** Biguanides (e.g. metformin (**1**)) activate the AMPK signalling pathway in liver cells, resulting in upregulating of insulin sensitivity and signalling. **(B)** SGLT2 inhibitors (e.g. canagliflozin, (**2**)) reduce renal glucose reabsorption, thus lowering blood glucose levels. **(C)** Inhibition of DPP IV via DPP IV inhibitors (e.g. sitagliptin, (**8**)). **(D)** α-glucosidase inhibitors (e.g. acarbose, (**9**)) prevent glucose absorption in the small intestine through delaying carbohydrate digestion. **(E)** Sulfonylureas (e.g. gliclazide, (**11**)) and meglitinides (e.g. repaglinide, (**16**)) bind to K^+ channels in pancreatic β-cells causing cell depolarisation. The downstream effects following influx of Ca^{2+} results in enhanced insulin secretion. Image created using Biorender.com.*

1.3.1. Biguanides

Approved in the UK in 1958, metformin (**1**), Figure 1.5, is the only clinical biguanide and the first-line treatment for T2DM [84]. Exerting its therapeutic effects by increasing insulin secretion and sensitivity whilst simultaneously decreasing the synthesis of glucose, Figure 1.14 shows the mechanism of action for **1** [85]. Binding to organic cation transporter 1 (OCT-1) present in hepatic

mitochondria [86], metformin activates the AMP-activated protein kinase (AMPK) signalling cascade, initiating increases in insulin sensitivity. Furthermore, AMPK activation induces fatty acid oxidation and reduces hepatic triglyceride content [87]. Adverse effects of **1** include nausea, vomiting and the induction of lactic acidosis [84]. Because weight gain is not an associated side effect of **1**, it is of particular importance in T2DM cases where the patient is overweight [88, 89]. The primary route of excretion of metformin is via the kidneys [90].

1.3.2. Sodium-glucose cotransporter 2 inhibitors

SGLT2 inhibitors (Figure 1.15) are often the second or third-line treatment for T2DM due to their associated cost. Typically prescribed in combination with **1**, SGLT2 inhibitors increase weight loss whilst reducing glucose reabsorption from the kidneys [91]. In turn, SGLT2 inhibitors trigger glucose to be eliminated via the urine, thus lowering blood glucose levels (Figure 1.14) [92, 93].

Canagliflozin (2)　　　　　　　　**Dapagliflozin (3)**
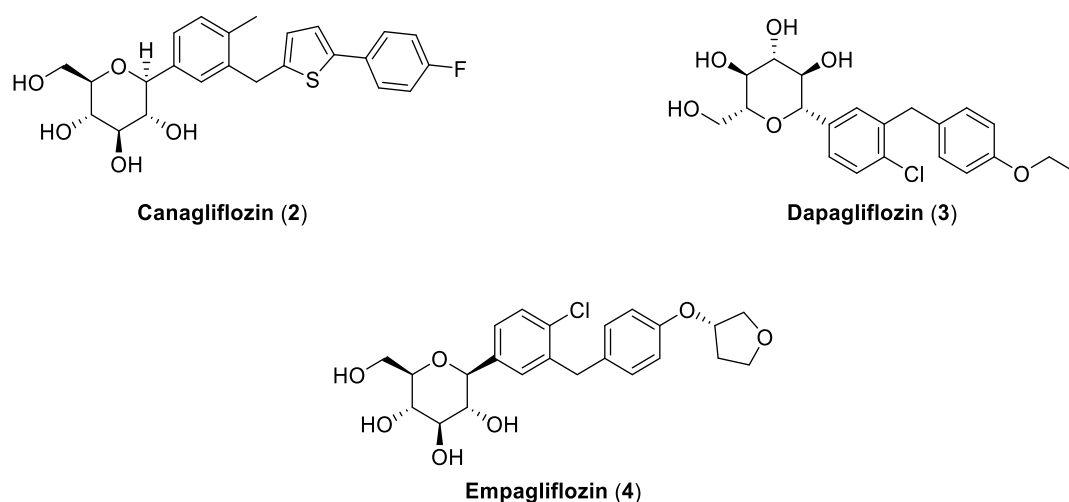
Empagliflozin (4)

Figure 1.15 Chemical structure of SGLT2 inhibitors; canagliflozin (2), dapagliflozin (3) and empagliflozin (4).

Because of their unique MoA, SGLT2 inhibitors are advantageous in mature, well-developed incidences of T2DM whereby insulin resistance has developed due to non-functioning pancreatic β-cells [94]. Despite this, disadvantages are associated with the drug class. Prolonged treatment with SGLT2 inhibitors can lead to adverse effects including increased urination, urinary tract infections and vaginal yeast infections [95].

1.3.3. Dipeptidyl-peptidase inhibitors and incretin mimetics

GLP-1 and gastric inhibitory peptide (GIP) are incretin hormones responsible for regulating postprandial glucose levels. They increase insulin secretion whilst preventing the release of glucagon. DPP IV is an enzyme which rapidly cleaves GLP-1 and GIP. Once bound to the enzyme, DPP IV inhibitors (Figure 1.16) inhibit DPP IV activity, subsequently increasing the levels of GLP-1 and GIP. In turn, insulin secretion is enhanced (Figure 1.14) [96].

Alogliptin (5)   **Linagliptin (6)**

Saxagliptin (7)   **Sitagliptin (8)**
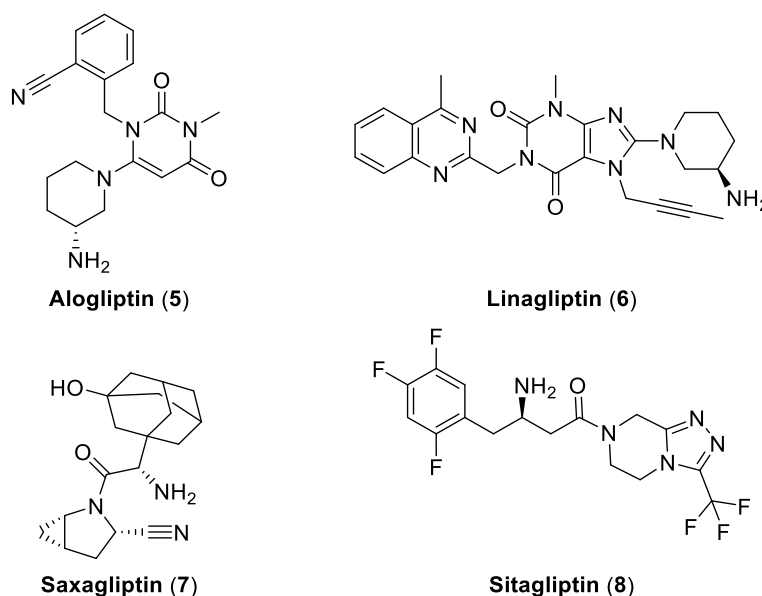
Figure 1.16 Chemical structure of DPP IV inhibitors; alogliptin (5), linagliptin (6), saxagliptin (7) and sitagliptin (8).

Similar to DPP IV inhibitors, insulin mimetics exert their therapeutic effects via mimicking the roles of endogenous incretin hormones (Figure 1.14) [97].

1.3.4. α-Glucosidase inhibitors

The enzyme α-glucosidase hydrolyses carbohydrates to release glucose, thus α-glucosidase inhibitors (Figure 1.17) have proven advantageous in cases where T2DM patients have a carbohydrate-rich diet [98]. Their MoA differs to that of other oral hyperglycaemic compounds as they do not directly alter insulin synthesis and secretion (Figure 1.14). α-Glucosidase inhibitors bind to α-glucosidase located in the brush border of the small intestine. In turn, glucose absorption is inhibited thus preventing a rise in postprandial glucose levels [95].

Acarbose (9)   **Miglitol (10)**
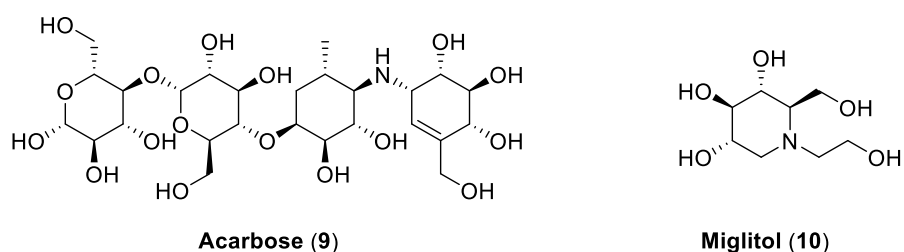
Figure 1.17 *Chemical structure of α-glucosidase inhibitors; acarbose (9) and miglitol (10).*

The use of α-glucosidase inhibitors is limited by their associated adverse effects such as flatulence, bloating and diarrhoea and their rigorous dosing routine [95].

1.3.5. Sulfonylureas

Used to treat T2DM since the 1960s, sulfonylureas (Figure 1.18) stimulate insulin secretion by binding to ATP-sensitive K^+ channels located on the plasma membrane of pancreatic β-cells (Figure 1.14). In turn, sulfonylureas stimulate the process described in Figure 1.7, whereby cell depolarisation occurs due to closure of K^+ channels. Consequently, the rapid influx of Ca^{2+} stimulates insulin secretion, thus reducing the blood glucose concentration [99].

Gliclazide (11)   **Tolbutamide (12)**
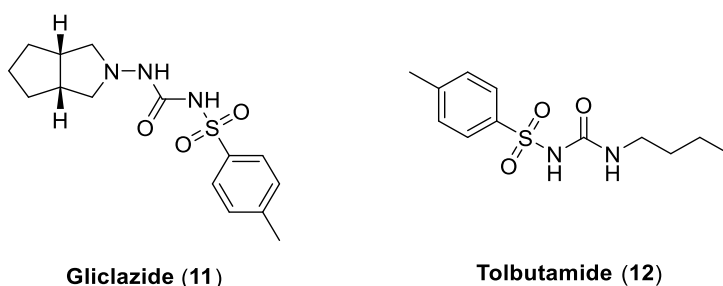
Figure 1.18 *Chemical structure of sulfonylureas; gliclazide (11) and tolbutamide (12).*

Sulfonylureas are characterised into two classes (Table 1.2) where second-generation sulfonylureas are significantly more potent than first-generation. However associated side effects limit their use [95]. Unlike **1**, side effects of sulfonylureas include increased weight gain, hypoglycaemia, arrythmias and myocardial infarction. Also shown in Table 1.2 is the elimination route of various sulfonylureas.

Table 1.2 *Types of sulfonylurea therapeutic agents, their generation and duration of action* [100].

Sulfonylurea	Generation	Elimination route
Gliclazide (**11**)	2	Urine
Tolbutamide (**12**)	1	Urine
Glimepride (**13**)	2	Urine
Glibenclamide (**14**)	2	Bile
Glipizide (**15**)	2	Urine

1.3.6. Meglitinides

Repaglinide (**16**) and nateglinide (**17**) are examples of meglitinides (Figure 1.19). Meglitinides evoke their therapeutic effects via the previously described cell depolarisation mechanism (Figure 1.14) [101]. Like sulfonylureas, the main adverse effects of meglitinides are weight gain and hypoglycaemia, although the frequency of serious hypoglycaemic incidents is much lower. Other side effects of meglitinides include headaches and respiratory tract infections [102]. Despite these associated risks, meglitinides have proven advantageous in patients who also suffer with chronic kidney disease. This is because unlike **1**, the main route of elimination for this drug classification is via hepatic clearance [103].

Repaglinide (16)   **Nateglinide (17)**
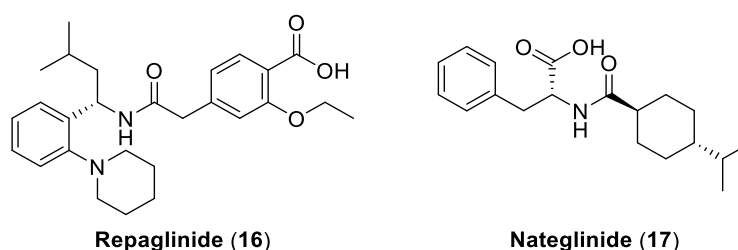
Figure 1.19 *Chemical structure of meglitinides; repaglinide (**16**) and nateglinide (**17**).*

1.4. Trace amine-associated receptor 1

1.4.1. G protein-coupled receptors

Trace amine-associated receptors (TAARs) belong to the G protein-coupled receptor (GPCRs) family. Composed of seven transmembrane (TM) α-helices connected via three intracellular

loops (IC1-3) and three extracellular loops (EC1-3), GPCRs have a wide range of roles including regulating taste, smell and vision as well as responding to hormones and neurotransmitters [104].

Additionally, GPCRs contain an *N*-terminus (extracellular amino terminus) and a *C*-terminus (intracellular carboxyl terminus) sequence of differing lengths (Figure 1.20 A).
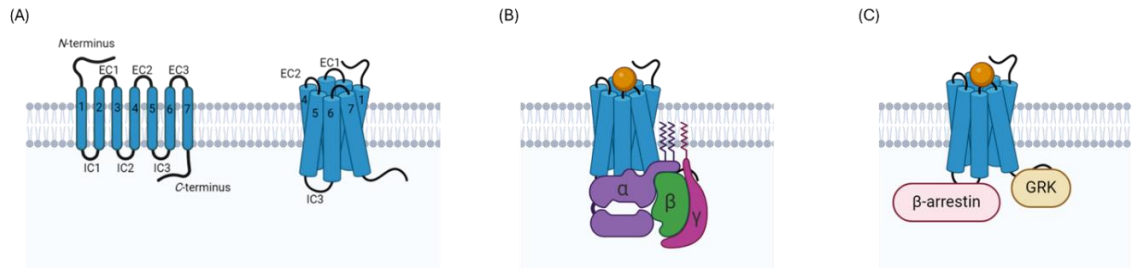
Figure 1.20 (A) Annotated structure of GPCRs showing the 7 transmembrane helices numbered 1-7. EC; extracellular loop, IC; intracellular loop. *(B)* GPCR in complex with heterotrimeric guanine nucleotide-binding G-protein when bound to the C-terminus. *(C)* GPCR in complex with GPCR kinase (GRKs). Once an agonist binds, GRKs phosphorylate the receptor resulting in the binding of β-arrestin. Image created using Biorender.com.

Upon stimulation, GPCRs activate a bound heterotrimeric guanine nucleotide-binding G-protein consisting of an α-subunit and a βγ-complex (Figure 1.20 B). There are several members of the G-protein family including G_s, G_i, G_q, G_t, $G_{12/13}$ G_{14} and small G proteins (Arf, Rab, Ran, Ras and Rho) [105]. Once a ligand binds to the GPCR, a conformational change occurs whereby the G_α subunit dissociates from a $G_{\beta\gamma}$-complex whilst exchanging guanosine diphosphate (GDP) for guanosine triphosphate (GTP). The dissociated G_α and $G_{\beta\gamma}$ subunits modulate various downstream signalling pathways, modulating regulating intracellular secondary messengers and activity. Finally, GTP is hydrolysed to GDP resulting in reformation of the $G_{\alpha\beta\gamma}$ heterotrimeric G protein (Figure 1.21).
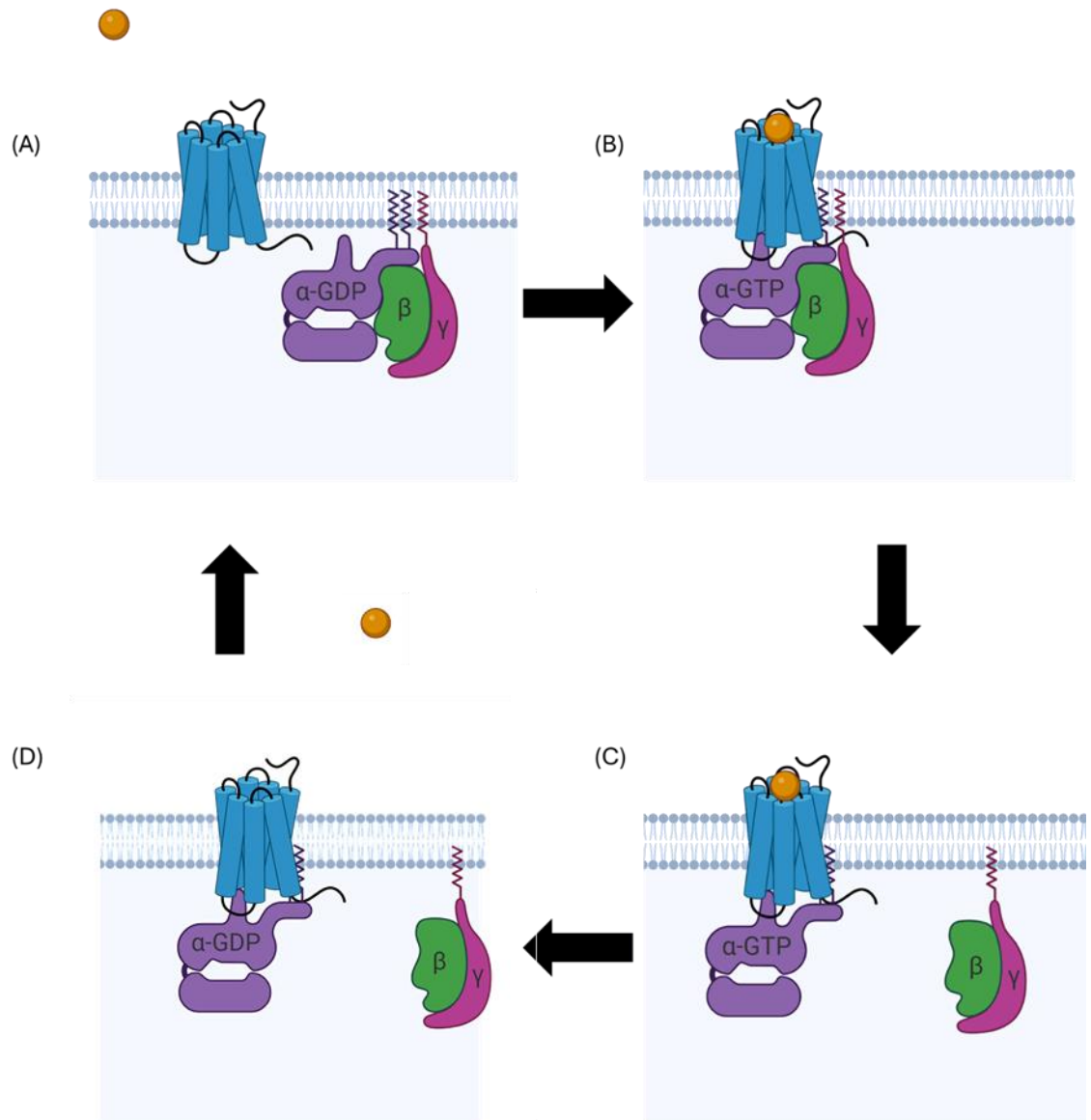
Figure 1.21 *Mechanism of the G-protein cycle.* *(A)* *Agonist interacts with receptor,* *(B)* *agonist binds and exchange of GDP for GTP occurs,* *(C)* *dissociation of Gα and Gβγ subunits inducing agonist's therapeutic effects,* *(D)* *agonist is released and GTP is hydrolysed to GDP.* *Image created using Biorender.com.*

GPCR signal desensitisation occurs via a conserved two-step mechanism; receptor phosphorylation by GPCR kinases (GRKs) followed by β-arrestin binding (Figure 1.20 C) [106]. Once an agonist binds, GRKs phosphorylate the receptor leading to the recruitment of β-arrestin, which sterically inhibits the G-protein coupling to the receptor whilst simultaneously allowing for clathrin-mediated endocytic receptor internalisation [107]. This causes a reduction in receptor signalling and subsequently desensitisation or degradation of the inactive receptor [108].

GPCRs are characterised into six subfamilies (rhodopsin-like, secretin, metabotropic glutamate, frizzled, adhesion and orphan) due to similarities within their structure and sequence [104, 109] and as such GPCRs are recognised as important drug targets. It is estimated over 35% of approved drugs target GPCRs, with the receptor class accounting for 17% of all drug targets (Figure 1.22). GPCRs are reported as the largest family of protein therapeutic targets due to their significant involvement in the central nervous system (CNS) and cardiovascular system [110].
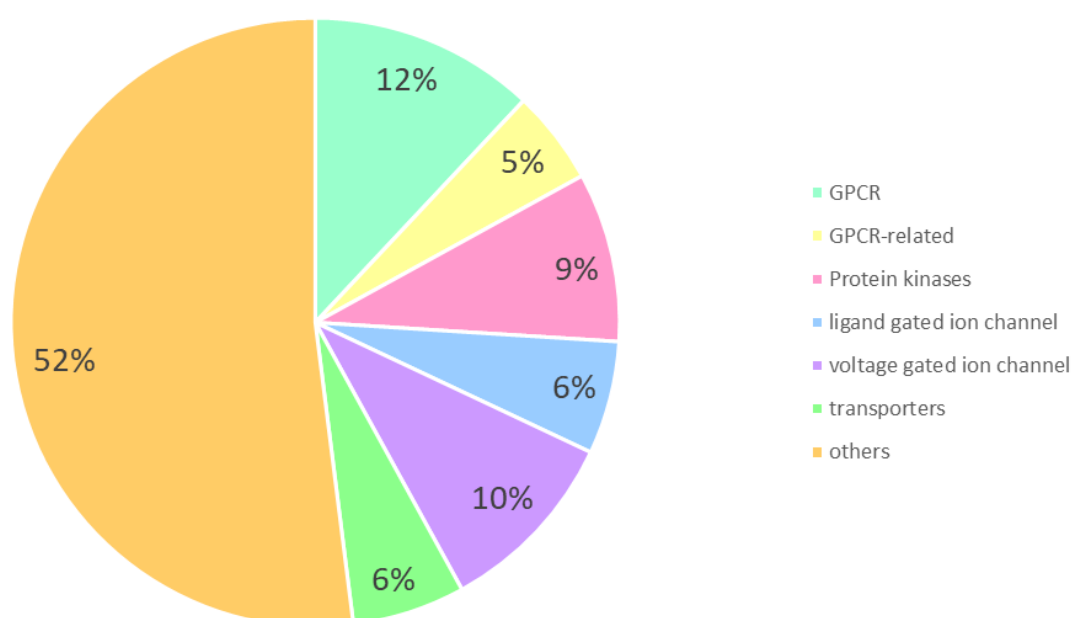
Figure 1.22 *Percentage approximation of different targets for approved drugs. Adapted from Sriram et al [110].*

1.4.2. GPCR activation

GPCR ligands are categorised based on the site they use to bind to the receptor. Ligands can either bind at the orthosteric binding site where they compete with endogenous ligands or at a topographically distinct site known as an allosteric binding site [111]. Orthosteric binding ligands are further classified depending on the nature of their efficacy. Agonists activate the receptor, in turn generating a biological response and can be classified as either full agonists – where the maximum signal response capable within the system is achieved, partial agonists where a lower signal response is detected compared to full agonists due to a reduced maximal efficacy for the

receptor or inverse agonists [112]. The latter have negative intrinsic efficacy and reduce constitutive activity via eliciting a decline in the number of receptors in the active conformation. In turn, inverse agonists exert an opposite effect when compared to the agonist [113]. Once bound, antagonists produce no effect on their own instead blocking the effects of agonists and inverse agonists [112, 114].

The cubic ternary complex model describes interactions between the G-protein, receptor and ligand interactions. In this model the receptor possesses two binding sites: one for the G-protein, G, and the other for the agonist, A and exists in two states, either active (R_a) or inactive (R_i). Activation of G can represent constitutive activity when R_aG is formed or once the receptor is activated via A [115]. Agonist activation can result in the formation of an AR_aG complex and it is assumes that all receptor species (R_a, R_i, AR_a, R_aG and AR_aG) coincide in equilibrium [116]. As shown in Figure 1.23 agonist binding to the inactive receptor state (AR_i) stimulates the formation of AR_a.
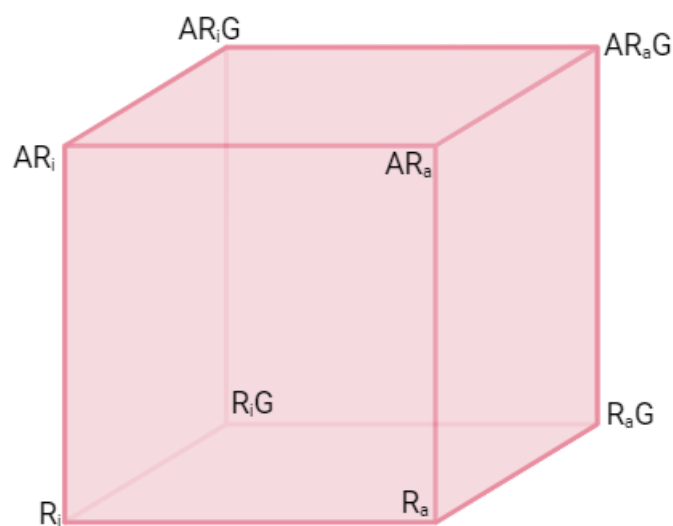
Figure 1.23 *Cubic ternary complex model of GPCRs. GPCR (R) exists in an active (R_a) or inactive (R_i) state and either bound to an agonist (A), the G-protein (G) or both. Adapted Weiss et al [116]. Image created using Biorender.com.*

Despite differences between their structures, all GPCRs evoke their therapeutic effects via cell signalling through an active conformation of the receptor (R_a), which can be further stabilised by a bound ligand (Figure 1.23).

1.4.3. Discovery and structure of TAAR1

Discovered independently by Borowsky *et al* and Bunzow *et al* in the early 2000s, trace amine-associated receptor 1 (TAAR1) is a family A G_s-coupled GPCR belonging to the TAAR family [117-119]. During the discovery, Borowsky's research team was searching for novel serotonin-like receptors by screening genomic deoxyribonucleic acid (DNA) with conserved regions of TMs 6 and 7 of known serotonin receptors. Identifying a new family of GPCRs, Borowsky *et al* realised the receptors exhibit a high affinity for tyramine (**18**, half maximal effective concentration (EC_{50}) at human TAAR1 (hTAAR1): 0.2-1.1 µM [120]) and phenethylamine (**19**, EC_{50} at hTAAR1: 0.3 µM [120]), Figure 1.24, thus coined the term trace amine receptors.

Tyramine (**18**)
EC_{50} (hTAAR1): 0.2-1.1 µM

Phenethylamine (**19**)
EC_{50} (hTAAR1): 0.3 µM
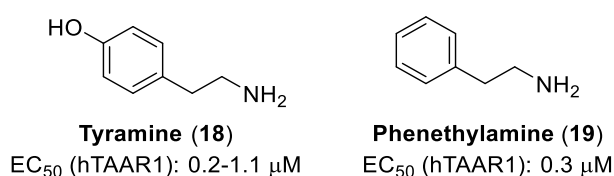
Figure 1.24 Chemical structure of tyramine (18) and phenethylamine (19).

Similarly, Bunzow *et al* researched new catecholamine receptors by screening complimentary DNA extracted from rodent pancreatic tumour cells against conserved regions of TMs 3 and 6 of known catecholamine GPCRs. Identifying a novel GPCR, Bunzow's research team established its pharmacology profile and later named the receptor TAR_1, embedding Borowsky *et al*'s GPCR family discovery. It was later discovered the receptors identified by Zeng *et al* (1998) and Lee *et al* (2000) belonged to Borowsky's newly identified class of GPCRs, thus in 2005 Lindermann *et al* introduced a uniform naming system [121].

Found on chromosome 6q23.2, hTAAR1 is 109 kb long [122]. Recorded research is sparse on the exact structure of hTAAR1, although several homology models have been produced based on its

similarity to Family A GPCRs [123, 124]. Figure 1.25 demonstrates hTAAR1 shares an 83% homology with rodent TAAR1 (rTAAR1) and 82% similarity with murine TAAR1 (mTAAR1) differing by 75 and 85 amino acid residues, respectively [125].
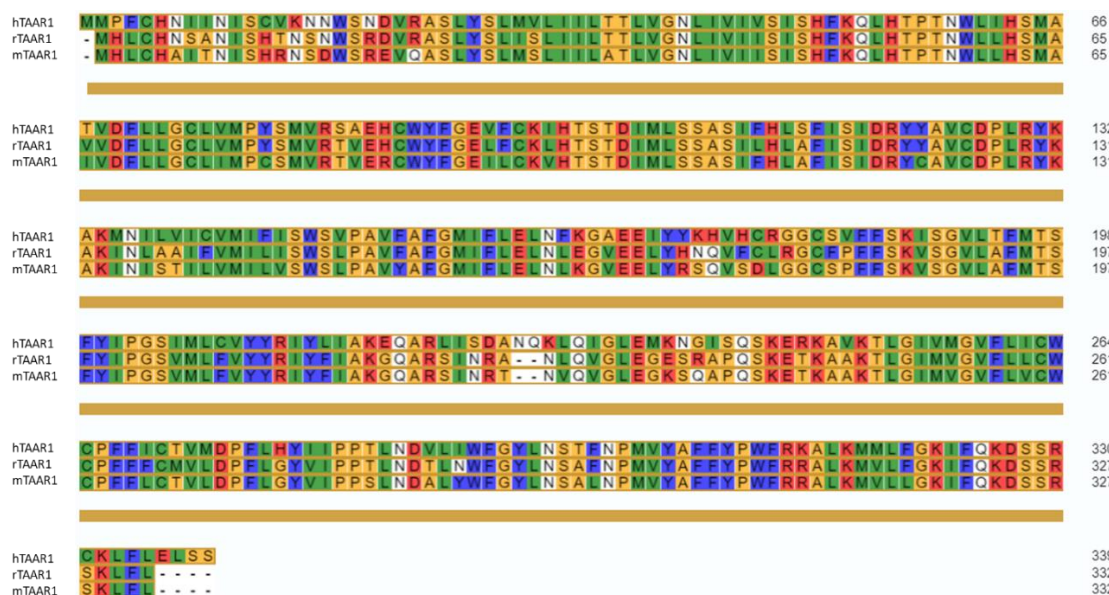
Figure 1.25 *Alignment of amino acid sequence of human TAAR1 (hTAAR1), rodent TAAR1 (rTAAR1) and murine TAAR1 (mTAAR1). Colour denotation: green; non-polar amino acids, yellow; special case amino acids, red; polar amino acids, blue; aromatic amino acids. Data obtained from UniProt [126].*

Despite being suggested to be a promising pharmacological target, the large sequence differences shown in Figure 1.25 hinders TAAR1's potential. Current research into developing TAAR1 drug-like compounds has revealed species-specificity between human, rodent and mouse TAAR1 isoforms to be the main drawback. Within the drug discovery process, promising compounds are subject to *in vitro* and *in vivo* experimentation on rodent and murine models, thus the lack of interspecies sequence homology evidenced in Figure 1.25 is hypothesised to prevent accurate prediction of expected interactions which may occur between ligand and TAAR1 and the likelihood of inducing a therapeutic effect in humans. This hypothesis is confirmed by Wainscott *et al* whereby 3-iodothyronamine (**20**), octopamine (**21**) and dopamine (**22**) displayed greater potency in rTAAR1 compared to hTAAR1 (Figure 1.26) [121]. Furthermore,

TAAR1 species variation also occurs due to pseudogenizations, deletions and duplications within the coding regions of DNA [117].
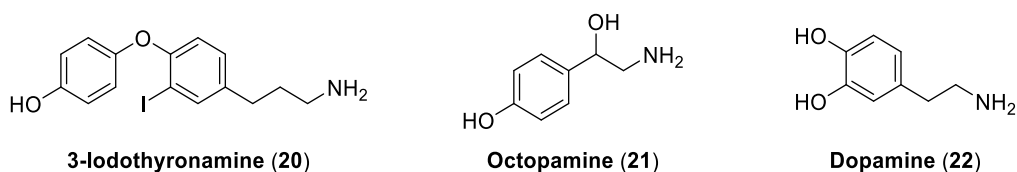
Figure 1.26 *Chemical structure of 3-iodothyronamine (20) and neurotransmitters octopamine (21) and dopamine (22).*

1.4.4. TAAR isoforms

In mammals, there are nine main isoforms of TAAR (1-9) with only TAAR1 being extensively studied. Known to identify primary amines, TAARs 1-4 are evolutionarily recognised as the oldest members of the TAAR family whilst TAARs 5-9 detect tertiary amines [127, 128].

Human TAAR isoforms

Reported by Lindermann *et al*, six TAAR isoforms are functional within humans (TAAR1, TAAR2, TAAR5, TAAR6, TAAR8 and TAAR9) [127]. It is expected the divergence of humans and orangutans caused the pseudogenization of hTAAR3 whereas divergence between humans and gorillas is responsible for the pseudogenization of hTAAR4 [129].

TAAR1 is located throughout the body - Borowsky *et al* and Linderman *et al* report hTAAR1 in the brain and spinal cord whereas Cisneros *et al* indicate hTAAR1 is present in astrocytes [127, 130, 131]. Furthermore, hTAAR1 receptors are also present in the stomach, intestines, and pancreatic β-cells [132, 133]. Unlike other hTAAR isoforms, hTAAR1 is the only isoform not present in the olfactory system.

Literature is sparse concerning the distribution of TAAR2 however tissue distribution of TAAR5, TAAR6, TAAR8 and TAAR9 has been reported. Babusyte *et al* state TAAR5 is expressed in B lymphocytes and leukocytes whereas TAAR6 is expressed in the kidney and several regions of the brain including the hippocampus, frontal cortex, amygdala, and substantia nigra [134, 135]. Like

TAAR6, TAAR8 is also found in the kidneys and amygdala region of the brain, although its expression within leukocytes is unknown [131, 134, 136]. In contrast to TAARs 5, 6 and 8, TAAR9 is predicted to be present in skeletal muscle and spleen [137, 138].

Animal TAAR isoforms

In contrast to humans, studies show many TAAR isoforms are present in animals. It is reported mice have 15 functional TAAR variants whereas rodents have 17 [119]. Zebrafish have a much larger TAAR (zTAAR) family consisting of 112 isoforms. Like mammals, the expected physiological role of zebrafish TAAR is to function as olfactory receptors, however there are no known ligands which activate zTAAR [139].

1.5. Signal transduction in TAAR1

1.5.1. Neurological disorders

Due to hTAAR1s expression in the CNS coupled with its specific position on chromosome 6q23.2, hTAAR1 is expected to contribute to neurological disorders including schizophrenia and Parkinson's disease. Characterised by symptoms including hallucinations, social withdrawal and poor memory, schizophrenia is a mental illness affecting 0.72% of the global population [140]. The pathophysiology of schizophrenia occurs due to dysregulation of dopamine transmission whereby alterations in dopamine receptor stimulation arises [124]. hTAAR1 is proven to be a negative regulator of dopamine transmission via GSK3β signalling – a pathway recognised in schizophrenia [129]. Furthermore, current studies demonstrate mTAAR1 activation inhibited hyperactivity of *N*-methyl-D-aspartate receptors whilst rTAAR1 activation modulated ventral tegmental area activity, both of which are processes associated with causing schizophrenia symptoms [141]. Therefore, agonists of hTAAR1 are proposed to have positive therapeutic effects in the management of the mental disorder [124].

As in the treatment of schizophrenia, hTAAR1 is expected to be a therapeutic target for Parkinson's disease – a neurological disorder characterised by degeneration of dopaminergic

neurons [142] which affects approximately 2000 in 100,000 patients over the age of 80, making it the second most common neurodegenerative disorder. Symptoms of Parkinson's disease include tremor, postural instability, and rigidity [143-145]. Studies suggest inhibition of hTAAR1 by antagonists will enhance dopamine stimulation [146]. Further neurological roles of hTAAR1 include overcoming substance abuse, addiction and depression [147, 148].

1.5.2. Metabolic disorders

As well as the CNS, TAAR1 is also expressed in the periphery (gastrointestinal tract, spleen, pancreas, heart, liver, kidney and immune cells [117, 146]) whereby it is reported to have a role in metabolic disorders including irritable bowel syndrome (IBS), obesity, and T2DM. Dopamine transmission can be a factor of food reward, thus contributes to food addiction and binge-eating disorders [149]. In turn these disorders may result in obesity – a condition caused by an increase in adipocytes hindering immune response [150]. Furthermore, obesity is a risk factor for many diseases including, cancer, cardiovascular disease, and DM thus significantly decreasing a patient's quality of life [150, 151].

Studies suggest TAAR1 is a potential target for the development of a novel class of therapeutic agents designed to overcome obesity and binge-eating disorders. Ferragud *et al* hypothesise activation of hTAAR1 will reduce compulsive overeating. Testing their hypothesis on rodent models, Ferragud *et al* report compulsive eating was inhibited when rodents were administered the TAAR1 agonist RO5256390 (**23**) discovered by Roche (Figure 1.27) and further hypothesised the effects evoked by activated rTAAR1 occurred through modulation of dopaminergic terminals in the medial prefrontal cortex [149]. Similarly, Rutigliano *et al* imply analogues of **20** are promising anti-obesity drugs effective at TAAR1 [152].
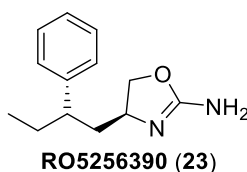
RO5256390 (23)

Figure 1.27 *Chemical structure of Roche agonist, RO5256390 (23).*

Affecting up to 23% of the general population, IBS is a chronic condition with symptoms including recurrent abdominal pain and changes in bowel habits [153]. During the body's response to IBS a rise in leukocyte concentration in the gastrointestinal mucosa occurs thus hTAAR1 is hypothesised to be a suitable therapeutic target for IBS, although literature confirming this hypothesis is limited [117].

1.5.3. hTAAR1 as a therapeutic target for T2DM

hTAAR1 is shown to have roles within T2DM via activation of cAMP dependent signalling cascade demonstrated in Figure 1.28. Upon agonist binding, hTAAR1 activates adenylate cyclase thus initiating the PKA and Epac2 signalling cascades which amplify insulin secretion [63, 65]. Furthermore, as reported in Section 1.2.2, activated PKA inhibits K^+ channel opening leading to membrane depolarization and a rise in insulin secretion occurs [71].
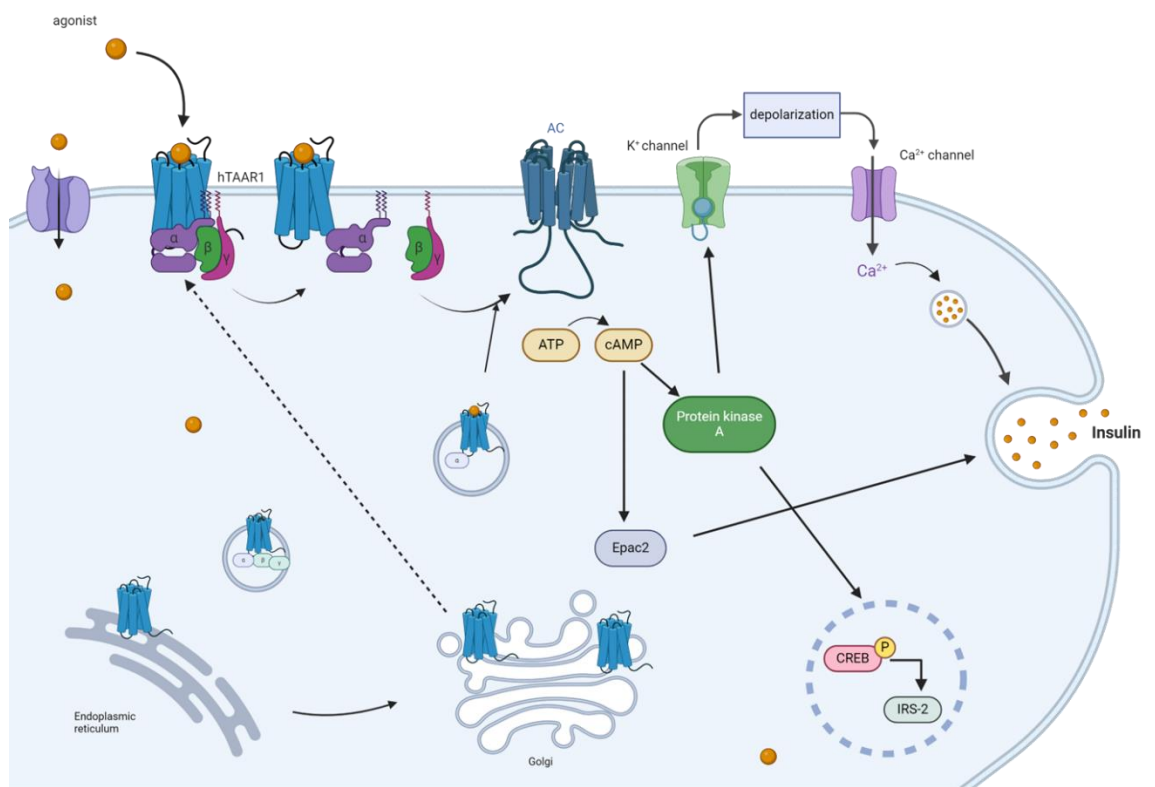
Figure 1.28 *Therapeutic effects of activated pancreatic hTAAR1. Agonists bind to hTAAR1 resulting in dissociation of Gα subunit and leading to activation of adenylate cyclase. cAMP levels increase stimulating the PKA and Epac2 signalling cascades resulting in insulin endocytosis. Activated PKA inhibits K^+ channel opening, increasing intracellular Ca^{2+} levels and enhanced insulin secretion. Catalytic PKA subunits phosphorylate CREB leading to insulin receptor substrate-2 (IRS-2) upregulation. Adapted from Michael et al [9]. Image created using Biorender.com.*

Within pancreatic β-cells, activated hTAAR1 causes upregulation of insulin receptor substrate-2 (IRS-2) – a gene responsible for mediating the effects of insulin [154]. Upon activation PKA evokes phosphorylation of CREB which binds to the cAMP response element located on the IRS promotor thus increasing IRS-2 expression (Figure 1.28) [9, 155-157]. The signalling pathway in Figure 1.28 indicates hTAAR1 is a rational therapeutic target for a new class of therapeutics agents designed to manage T2DM.

1.5.4. Intracellular localisation of TAAR1

Although several roles of TAAR1 have been established (described above), understanding TAAR1's trafficking and subcellular localisation remains challenging due to the weak plasma

membrane expression observed during *in vitro* microscopy studies [158, 159]. As such it is widely recognised the majority of TAAR1 signalling occurs intracellularly due to the absence of *N*-glycosylation sites (Figure 1.29) [148, 158, 160].
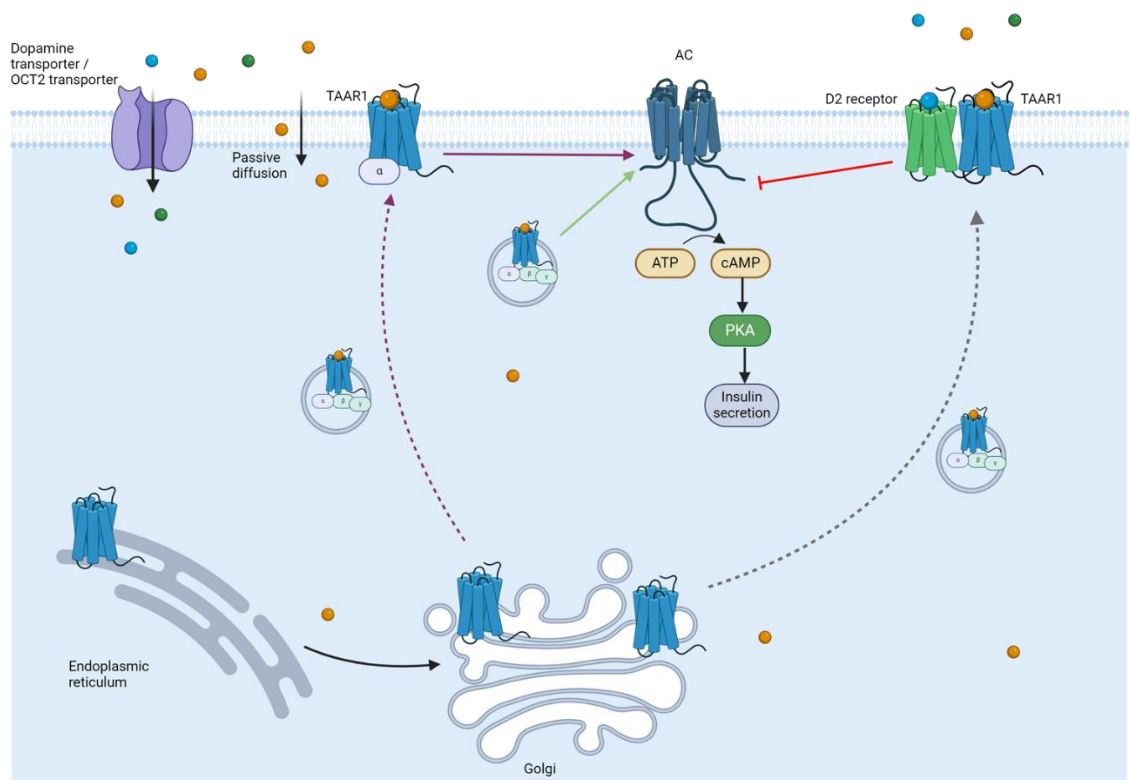
***Figure 1.29** Trafficking of TAAR1 to the cell surface membrane, intracellular localisation and cross-talk between TAAR1 and the dopaminergic system. **Purple pathway:** TAAR1 traffics to the cell membrane and is expressed in poor yields where it is activated by an extracellular agonist activating the adenylate cyclase (AC) signalling pathway. **Green pathway:** Agonist enters the cell through a transporter found at the plasma membrane. Once inside the cell, agonist binds to intracellular TAAR1 receptors that stimulate the AC signalling pathway. **Grey pathway:** TAAR1 forms a heterodimer with D2 receptors inhibiting the AC signalling pathway. Adapted from Rutigliano et al [148] and Underhill et al [161]. Image created using Biorender.com.*

Several efforts have been made to promote cell surface expression of TAAR1 either via modification of intracellular loops or by inserting the first nine residues of human β_2-adrenoceptors into the *N*-terminus of TAAR1 to develop an *N*-glycosylated variant [132, 162, 163]. Additionally, Quato *et al* identified TAAR5 traffics to the plasma membrane more readily than TAAR1. Unlike TAAR5, TAAR1 lacks a F(X)6LL amino acid sequence in the *C*-terminus, thus it is

further suggested this is also responsible for the lack of TAAR1 cell surface expression as the *C*-terminal motif promotes GPCR trafficking [158].
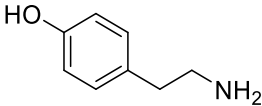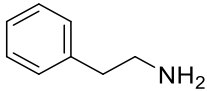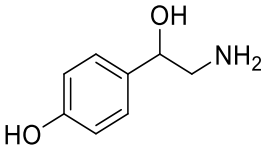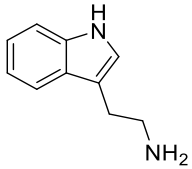
Within brain monoaminergic systems, it has been observed that TAAR1 co-localises with dopamine D2 receptors, thus it is suggested an accessory protein may be required to promote efficient TAAR1 trafficking to the cell membrane (Figure 1.29) [159]. Furthermore, it is suggested that the dopamine transporter acts as a channel for TAAR1 agonists into the cell, increasing the accessibility and binding potential to the intracellular TAAR1 receptors (Figure 1.29) [148, 159]. Given that insulin secreting pancreatic β-cells express D2 receptors, vesicular monoamine transporter 2 (VMAT2) and organic cation transporter 2 (OCT-2) transporters, it is suggested the heterodimerisation observed between TAAR1 and D2 receptors in the CNS and exploiting ligand transportation into the cell via neurotransmitter transporters could occur in the pancreas, subsequently leading to enhanced insulin secretion (Figure 1.29).

1.6. hTAAR1 activation

1.6.1. Endogenous ligands

Borowsky *et al* and Bunzow *et al* identified hTAAR1 is activated by endogenous monoaminergic modulators (trace amines, TA) and classical monoamine neurotransmitters [164]. Synthesised via the decarboxylation of amino acids or metabolism of monoamine precursors, TAs (**18** and **19**, Figure 1.24) are primary amines structurally related to classical monoamine neurotransmitters such as dopamine (**22**, Figure 1.26). The potency of several endogenous TAs for hTAAR1 is shown in Table 1.3.

Table 1.3 *Structure of endogenous ligands that activate hTAAR1. Potency is recorded as pEC$_{50}$ in micromolar concentration (µM)* [162, 165-167].

Compound	Structure	Potency (*p*EC$_{50}$)
Tyramine (**18**)		5.8-6.7
Phenethylamine (**19**)		6.2-7.0
Octopamine (**21**)		4.8-5.8
Tryptamine (**24**)		4.68

TAs are metabolised via the enzyme monoamine oxidase (MAO) (Figure 1.30). The half-life of TAs is very short (~30 seconds), thus they are only present in nanomolar concentrations [168]. The roles of TAs within humans has recently been identified and correlates with the therapeutic effects evoked by hTAAR1 activation [169].
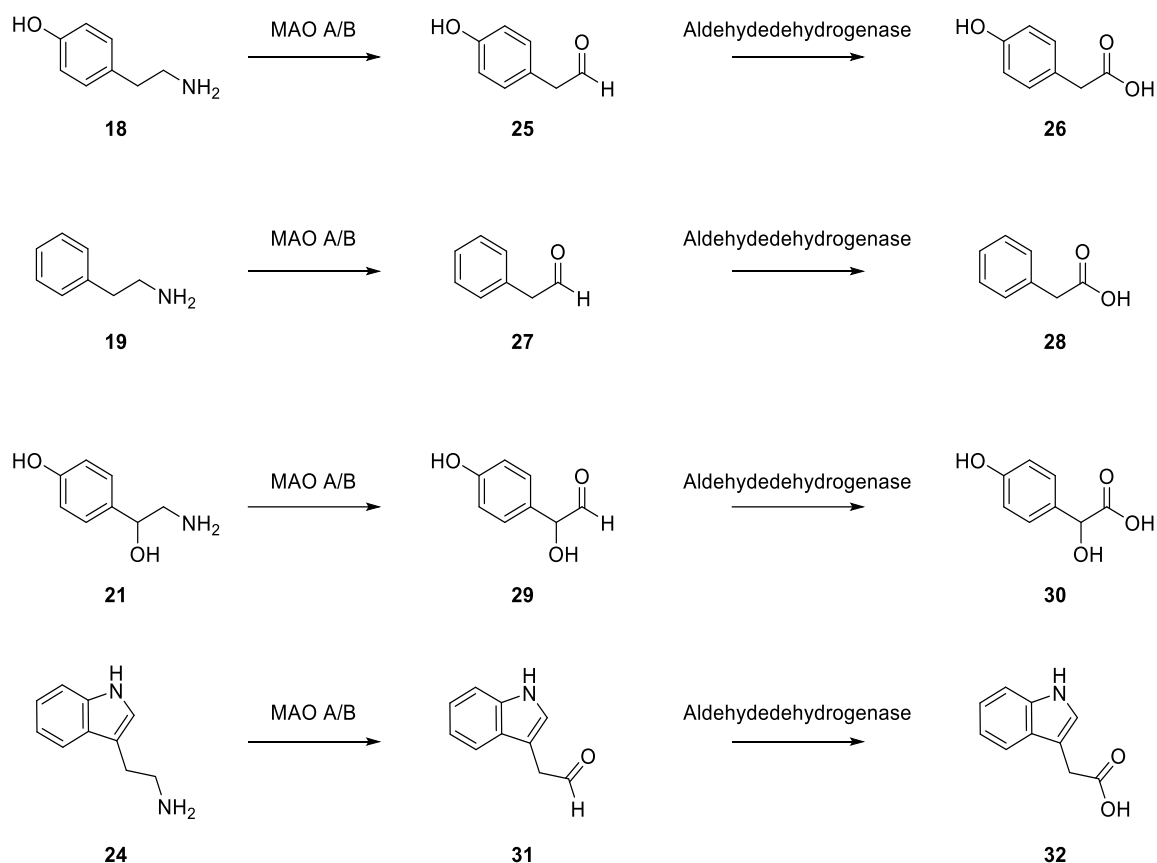
Figure 1.30 *Metabolism of TAs **18, 19, 21** and **24** to yield metabolites **25**-**32**. MAO; monoamine oxidase.*

1.6.2. Known structure-activity relationships studies for TAAR1 agonists

Early work

The development of pharmacological agents aimed to target hTAAR1 is an emerging research area due to increased knowledge of hTAAR1. Initial development of novel TAAR1 targeting compounds began through the exploration of 3-iodothyronamine (**20,** Figure 1.26) derivatives by Chiellini *et al* [170, 171]. Adapted from Guariento *et al*, Table 1.4 shows the chemical structure of these analogues (compounds **33**-**46**). Unfortunately, the Emax values for compounds **33**-**46** was not reported, but the calculated pEC_{50} values at mTAAR1 obtained from bioluminescence resonance energy transfer (BRET) assays is shown in Table 1.4 [132]. Expansion in the development of **20** led to the discovery of Guanabenz (**47,** Figure 1.31) by Lam *et al* [124].
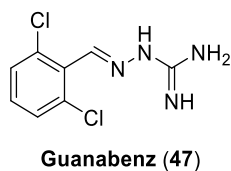
Guanabenz (**47**)

Figure 1.31 *Chemical structure of TAAR1 agonist, Guanabenz (**47**) developed by Lam et al* [124].
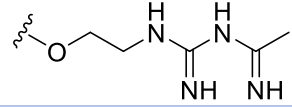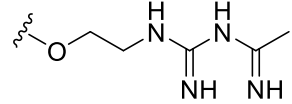
From the structures of compounds **33**-**47**, coupled with their biological activity at mTAAR1, a common basic pharmacophore of TAAR1 drug-like molecules can be identified due to all agonists containing basic amine moieties and substituted aryl rings, suggesting these features are essential for optimal TAAR1 binding.

Table 1.4 Structure-activity relationship (SAR) exploration carried out by Chiellini et al to identify novel TAAR1 agonists. pEC_{50} values reported in molar concentration (M) and in reference to mTAAR1 obtained from cAMP BRET assays [132].

3-iodothyonamine
(20)

33-46
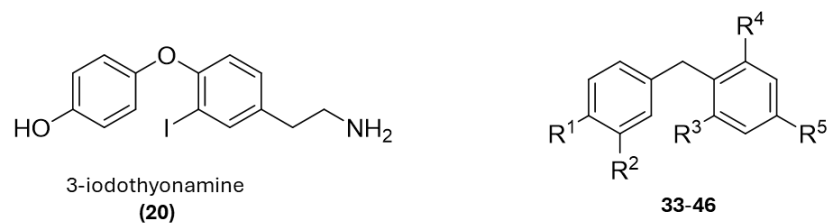
Compound	R^1	R^2	R^3	R^4	R^5	pEC_{50}
20	-	-	-	-	-	6.72
33	NH_2	H	H	H	$(CH_2)_2NH_2$	6.1
34	OH	H	H	H	$O(CH_2)_2NH_2$	5.66
35	NH_2	H	H	H	$O(CH_2)_2NH_2$	5.77
36	NH_2	H	H	CH_3	$O(CH_2)_2NH_2$	6.62
37	NH_2	H	H	CH_3	$(CH_2)_2NH_2$	6.92

Table 1.4 Continued.

Compound	R^1	R^2	R^3	R^4	R^5	pEC_{50}
38	OH	H	H	CH_3	$(CH_2)_2NH_2$	7.01
39	$NHCOCH_3$	H	H	CH_3	$(CH_2)_2NH_2$	5.51
40	NH_2	H	H	CH_3	$(CH_2)_2NH_2$	6.80
41	NH_2	H	H	CH_3	$O(CH_2)_2NH_2$	6.87
42	$NHCH_2CH_3$	$CH(CH_3)_2$	H	CH_3	$(CH_2)_2NH_2$	6.99
43	$N(C_2H_5)COCH_3$	$CH(CH_3)_2$	H	CH_3	$(CH_2)_2NH_2$	6.36
44	$N(C_2H_5)COCH_3$	$CH(CH_3)_2$	H	CH_3	$(CH_2)_2NHCOCH_3$	5.00
45	NH_2	H	H	CH_3		5
46	$NHCOCH_3$	H	H	CH_3		5

Biguanides

Moving away from analogues of **20**, virtual screening strategies were employed to identify additional TAAR1-targeting chemotypes. Previous drug discovery programmes identified biguanide structures demonstrate antimalarial, antiseptic and antidiabetic properties, thus suggesting it is a promising core for novel hTAAR1 therapeutics [132]. Furthermore, the proposed core scaffold could act as the amine moiety identified in the TAAR1 pharmacophore.

Efforts by Guariento *et al* [132] and Tonelli *et al* [133] explored the structure-activity relationship (SAR) of biguanide compounds and their effects at hTAAR1. Whilst compound **54** (Figure 1.32) showed improved selectivity towards hTAAR1 compared to mTAAR1 overcoming species-specificity, it had low potency (EC_{50} at hTAAR1: 11400 nM). To form additional interactions with the receptor and increase potency at hTAAR1, the aromatic moiety was replaced with 2-pyrimidine yielding **55**, Figure 1.32 [132]. Unfortunately, this substitution hindered its biological activity at hTAAR1 and thus **55** was identified as a partial agonist. Removing the rigid piperazine linker and replacing it with the more flexible CH_2 led to the development of compound **51** (EC_{50} at hTAAR1: 1200 nM, Figure 1.32) [133]. Monosubstitution of the chloro group was also investigated and showed para substitution led to greater activity (**50**, EC_{50} at hTAAR1: 1800 nM, Figure 1.32) compared to ortho and meta substitutions. Evaluation of species-specificity of **50** revealed a low species-specificity ratio (SSR) of mTAAR1 vs hTAAR1 (2.31) hinting small lipophilic substituents are required to ensure selectivity and potency at hTAAR1, however it suffered bioavailability (F) concerns in mouse models (F: 19.5%) [133]. Although further investigation is required to develop effective and potent hTAAR1 agonists characterised with a biguanide moiety, **50**, **51** and **55** provide rationale for use as lead compounds in future SAR studies investigating agonism at hTAAR1.

48
EC$_{50}$ (mTAAR1): 410 nM, (hTAAR1): 1000 nM

49-51

52
EC$_{50}$ (mTAAR1): 2380 nM, (hTAAR1): 1380 nM

53-54

55
EC$_{50}$ (mTAAR1): 9000 nM
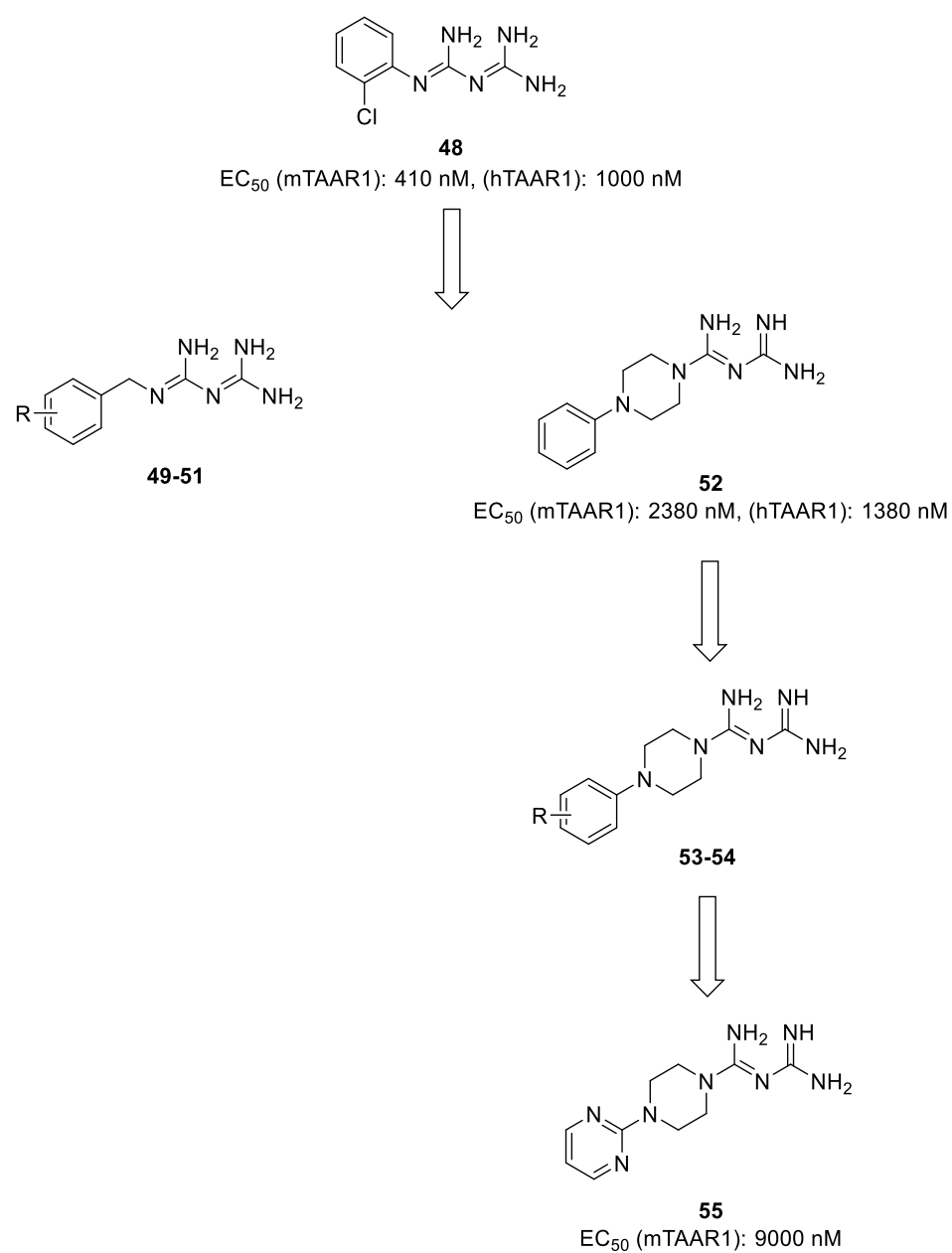
			EC$_{50}$	
			mTAAR1	hTAAR1
R=	**49**	3-Cl	97 nM	7000 nM
	50	4-Cl	780 nM	1800 nM
	51	3,4-Cl	36 nM	1200 nM
	53	2-Cl	2660 nM	-
	54	4-OMe	-	11400 nM

Figure 1.32 *Chemical structures of TAAR1 agonists **48**-**55** containing a biguanide moiety. Adapted from Guariento et al [132] and Tonelli et al [133].*

Roche

Most of the efforts to advance the development of hTAAR1 agonists has been carried out by Roche, with over 30 patents documented in the literature. Roche's early efforts in developing hTAAR1 agonists focused on structural modifications of adrenergic compounds. Derived from S18616 (**56**, Figure 1.33), a partial agonist of α_{2A}-adrenergic receptor identified from a thorough search of literature databases [172], RO5166017 (**57**, Figure 1.33) is a highly potent and selective TAAR1 agonist. Whilst **57** showed high potency and selectivity at mTAAR1 (EC_{50}: 3 nM) and rTAAR1 (EC_{50}: 14 nM), it suffered from high metabolic clearance in rat models thus limiting its development. Identifying **57** underwent *N*-dealkylation due to the presence of C-N bonds, efforts were made to introduce a linker substituent at the benzylic position yielding compound RO5256390 (**58**, Figure 1.33), a highly potent and selective hTAAR1 agonist (EC_{50}: 18 nM) [172].

S18616 (**56**)
EC_{50} (hTAAR1): 15 nM

RO5166017 (**57**)
EC_{50} (mTAAR1): 3 nM, (TAAR1): 14 nM, (hTAAR1): 59 nM

RO5256390 (**58**)
EC_{50} (hTAAR1): 18 nM
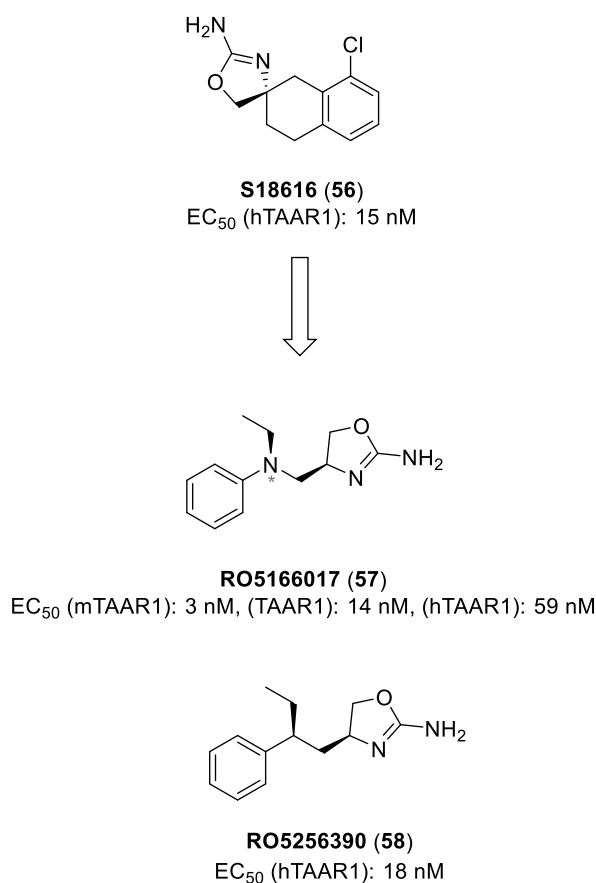
Figure 1.33 *Chemical structure of α_{2A}-adrenergic partial agonist S18616 (**56**), and hTAAR1 agonists RO5166017 (**57**) and RO5256390 (**58**).*

RO5073012 (**59,** Figure 1.34) was the result of a SAR study derived from the Roche compound library [173]. This compound belonging to the imidazole series was first described in a 2008 patent showing preference to an aminomethyl-4-imidazole core. RO5073012 (**59**) is a highly selective hTAAR1 agonist against the α_{2A}-adrenergic receptor, determined by (*S*)-4-(2,4-difluorophenyl-3-tritio)-4,5-dihydro-2-oxazolamine (**60**) binding assays (Figure 1.34) [173]. Additionally, further *in vitro* investigation identified RO5073012 (**59**) as a partial agonist of hTAAR1 with balanced functional activity across species (EC$_{50}$(hTAAR1): 23 nM, (rTAAR1): 25 nM and (mTAAR1): 23 nM) overcoming the species-specificity drawbacks previously identified by Guariento *et al* [132] and Tonelli *et al* [133, 173]. Preclinical *in vivo* studies found RO5073012 (**59**) was active in rat CNS behavioural models [173].

RO5073012 (59)
EC$_{50}$ (mTAAR1): 23 nM, (rTAAR1): 25 nM, (hTAAR1): 23 nM

60
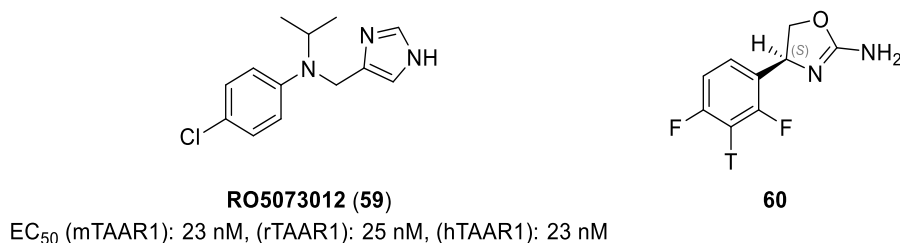
Figure 1.34 *Chemical structure of RO5073012 (59) and (S)-4-(2,4-difluorophenyl-3-tritio)-4,5-dihydro-2-oxazolamine (60).*

Further advances by Roche led to the patent of ralmitaront (**61**, Figure 1.35) in 2017 for the treatment of CNS disorders. The patent states the 5-ethyl-4-methyl-pyrazole-3-carboxamide derivative is observed to have reduced side effects and increased activity and selectivity at hTAAR1 compared to other drug-like molecules described in prior art [174]. As the most advanced Roche agonist, ralmitaront (**61**) was entered into clinical trials [175]. Phase I trials assessed its safety and efficacy in schizophrenia cases, where the drug was well tolerated. Subsequently, **61** advanced to phase II trials, although Roche terminated the studies due to interim analysis showing ralmitaront was not an effective treatment for schizophrenia.
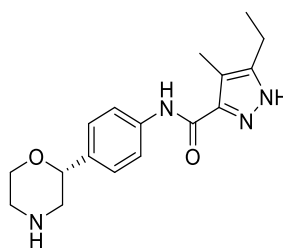
Ralmitaront (61)
EC_{50} (hTAAR1): 0.0585 µM

Figure 1.35 *Chemical structure of ralmitaront (61).*

Ulotaront (Sunovian Pharmaceuticals)

Identified from a targeted agnostic approach, ulotaront (**62,** Figure 1.36) was discovered due to its lack of antagonism at 5-HT$_{2A}$ and dopamine D2 receptors [176]. Ulotaront (**62**) is a hTAAR1 agonist with additional agonism at 5-HT1A receptors and is undergoing clinical trial investigation [176]. Successful results from phase II trials showing reduced side effects and improved efficacy resulted in ulotaront (**62**) being awarded the US Food and Drug Administration (FDA) breakthrough therapy designation for schizophrenia treatment [175]. Subsequently **62** was entered into phase III trials, however two studies have revealed **62** failed to significantly benefit patients with schizophrenia compared to the placebo. Additional phase III trials are still ongoing.
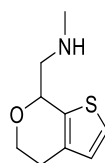
Ulotaront (62)

Figure 1.36 *Chemical structure of ulotaront (62).*

1.7. Project aims

This chapter has provided an in-depth account of hTAAR1, highlighting its roles in various neurological and metabolic disorders and its potential as a therapeutic target in T2DM. Despite the challenges encountered by previous drug-discovery programs including variance in species-specificity hindering development and concerns of efficacy for ralmitaront (**61**) and ulotaront

(**62**) which were experienced within clinical trials, there remains a demand to develop novel treatments for T2DM. RO5073012 (**59**), a compound belonging to a class of aminomethyl-4-imidazole based hTAAR1 agonists, has shown balanced functional activity across species and potency at hTAAR1 overcoming previous drawbacks. In the absence of an x-ray crystal structure of hTAAR1, this project aims to use computational tools (Chapter 2) to develop and evaluate an accurate and representative model of hTAAR1 to aid with the development of structure-based drug design of hTAAR1 agonists.

Next, using RO5073012 (**59**) as a lead compound, this project will rationally design and synthesise a library of imidazole based hTAAR1 agonists. *In silico* methods will be applied to generate a hypothesised binding pose within the hTAAR1 binding site and rationalise the molecular interactions owing to their binding affinity as well as evaluation of their pharmacological profile in our phenotypic assay in pancreatic β-cells looking at insulin secretion. As RO5073012 (**59**) is reported to have good CNS penetration due to its development in schizophrenia treatment, efforts will be made to ensure the novel class of therapeutic agents do not cross the blood brain barrier (BBB), eliminating the likelihood of inducing central effects.

2. Development of hTAAR1 homology models and docking of selective hTAAR1 ligands

Throughout the initial stages of drug discovery, computational tools are used to identify drug-like compounds for their proposed therapeutic target. The process to identify novel potent therapeutic ligands is often hindered by the limited diversity and size of screening libraries available. As such efforts into high-throughput screening (HTS) - an automated process which can screen up to 500,000 compounds in a relatively short timeframe, were developed. Despite its ability to screen such large compound numbers, HTS is only likely to identify a handful of compounds which elicit the desired biological response [177, 178]. Associated costs of HTS can be high due to the extensive optimisation required to improve the potency of the identified hit molecules [179]. Therefore, further efforts into progressing computer-aided drug design were employed [178].

A novel, cheaper approach to HTS is virtual screening, for which molecular docking is the most used technique; a process which predicts binding affinities and physical interaction between a drug and its therapeutic target [180-182]. To ensure reliable data is obtained, the quality of receptor structure is imperative, thus crystal structures with high resolution are the most favoured [183, 184]. Unfortunately, there were no published structures of hTAAR1 available in the Protein Data Bank (PDB) at the time of starting this project, and to date the crystal structure of TAAR1 has not been solved, therefore it was prudent to develop a hTAAR1 homology model to provide insight in supporting the development of a new class of therapeutic agents.

Homology modelling is one of the most accurate computational structure prediction methods [185, 186]. It predicts a 3D structure of a protein from its amino acid sequence, using a protein with a similar amino acid sequence as a template [185]. The process to build a homology model involves four key steps[186]. Firstly, a Basic Local Alignment Search Tool (BLAST) search is completed to identify a suitable template available in the PDB database. To identify an appropriate template,

various factors need to be considered. Namely, a high sequence similarity between the target and template sequence, environmental factors such as solvent type, pH and amino acid protonation state, resolution of the experimental structure, and whether a bound ligand is present in a pocket similar to the binding region of the target site [185, 187, 188]. Once a template has been selected, sequence alignment occurs ensuring any residues conserved between the target receptor and template protein correlate with one another, thus improving the model quality [189]. This is demonstrated by Kopp and Schwede who report deterioration in model quality when the template and target receptor have less than 50% similarity, and with no reliable or accurate data obtained when similarity is below 25% [190]. Next, the model is built using backbone regeneration and side chain remodelling before energy minimization. Finally, the model is validated to eliminate any errors which may have arisen during the building and development stage. Often specialist, freely available programmes (PROCHECK, WHATIF, VERIFY3D and PROSAII) are used to validate homology models by identifying protein stereochemistry and scoring the residues based on their correlation between sequence position and location within the structure [191]. This includes identifying and detecting misfolded amino acids due to the location of polar residues and solvation potentials, identifying sensible geometry and symmetry within the receptor, and using Ramachandran plots [191, 192].

2.1. Development of a hTAAR1 homology model

2.1.1. Initial homology modelling

To determine the most reliable model of hTAAR1 to recapitulate known SAR, three different homology modelling programmes were used to generate <1000 homology models, with an overview of the most promising models shown in Table 2.1. These models were selected based on their ability to preference the *S*-enantiomer of 4-(2,4-difluorophenyl-3-tritio)-4,5-dihydro-2-oxazolamine (**60**) over the *R*-enantiomer, and their free-of-charge availability.

Provided by Prof. Charles Laughton, University of Nottingham, UK, models 1-20 were built using Modeller with either β$_2$-adrenoceptors or dopamine D4 receptors as a template [193-198]. Correlating with the literature, Family A GPCRs were deemed suitable templates for hTAAR1 because β$_2$-adrenoceptors have the best predicted homology over the full protein sequence whereas helix-by-helix comparison reveals dopamine D4 receptors most closely resemble TMs 2 and 3 of hTAAR1 [199, 200]. The corresponding models were screened to identify their ability to differentiate between the two enantiomers of the radioligand 4-(2,4-difluorophenyl-3-tritio)-4,5-dihydro-2-oxazolamine. Any models which showed preference for the *S*-enantiomer were used in this study relating to experiments completed by Galley *et al* [173, 201]. Additionally, the active state of the receptors was chosen for several templates to increase the probability for the discovery of agonists. An additional 10 readily available structures of hTAAR1 were accessed online. Homology models 21-25 were obtained from Iterative Threading ASSEmbly Refinement (I-TASSER), whilst models 26-30 were acquired from Robetta [202-205].

Table 2.1 *hTAAR1 homology model overview. In cases where more than one PDB entry is stated, homology models were built using an average of the stated PDB entries.*

	GPCR template	Active or inactive state	PDB entries	Modelling software
Model 1	β₂-adrenoceptor	Inactive, antagonist-bound	5JQH	Modeller
Model 2	β₂-adrenoceptor	Inactive, antagonist-bound	4BVN	Modeller
Model 3	β₂-adrenoceptor	Active, agonist-bound	3PDS, 3P0G, 7DHR, 7DHI	Modeller
Model 4	β₂-adrenoceptor	Active, agonist-bound	3PDS, 3P0G, 7DHI	Modeller
Model 5	Dopamine D4 receptor	Inactive, antagonist-bound	6IQL	Modeller
Model 6	β₂-adrenoceptor	Active, agonist-bound	3PDS, 3P0G, 7DHI	Modeller
Model 7	β₂-adrenoceptor	Active, agonist-bound	3PDS, 3P0G, 7DHI	Modeller
Model 8	β₂-adrenoceptor	Active, agonist-bound	3PDS, 3P0G, 7DHI	Modeller
Model 9	β₂-adrenoceptor	Active, agonist-bound	3PDS, 3P0G, 7DHI	Modeller
Model 10	β₂-adrenoceptor	Active, agonist-bound	3PDS, 3P0G, 7DHI	Modeller
Model 11	β₂-adrenoceptor	Active, agonist-bound	3PDS, 3P0G, 7DHI	Modeller
Model 12	β₂-adrenoceptor	Active, agonist-bound	3PDS, 3P0G, 7DHI	Modeller
Model 13	β₂-adrenoceptor	Active, agonist-bound	3PDS, 3P0G, 7DHI	Modeller
Model 14	β₂-adrenoceptor	Active, agonist-bound	3PDS, 3P0G, 7DHI	Modeller
Model 15	β₂-adrenoceptor	Active, agonist-bound	3PDS, 3P0G, 7DHI	Modeller
Model 16	β₂-adrenoceptor	Active, agonist-bound	3PDS, 3P0G, 7DHI	Modeller
Model 17	β₂-adrenoceptor	Active, agonist-bound	3PDS, 3P0G, 7DHI	Modeller
Model 18	β₂-adrenoceptor	Active, agonist-bound	3PDS, 3P0G, 7DHI	Modeller
Model 19	β₂-adrenoceptor	Active, agonist-bound	3PDS, 3P0G, 7DHI	Modeller
Model 20	β₂-adrenoceptor	Active, agonist-bound	3PDS, 3P0G, 7DHI	Modeller
Model 21	-	-	-	I-TASSER

Table 2.1 (Continued)

	GPCR template	Active or inactive state	PDB entries	Modelling software
Model 22	-	-	-	I-TASSER
Model 23	-	-	-	I-TASSER
Model 24	-	-	-	I-TASSER
Model 25	-	-	-	I-TASSER
Model 26	-	-	-	Robetta
Model 27	-	-	-	Robetta
Model 28	-	-	-	Robetta
Model 29	-	-	-	Robetta
Model 30	-	-	-	Robetta

2.1.2. Software validation

To examine whether the PDB entries reported in Table 2.1 were appropriate for use as hTAAR1 homology model templates and to determine the suitability of the proposed software, the co-crystalised ligands (**63-68**) were docked back into the original receptor. Successful redocking of co-crystalised ligands was achieved, Figure 2.1. The bound and re-docked ligands in structures PDB: 5JQH, 4BVN, 3PDS, 3P0G, 7DHR and 7DHI overlay well, with the crystal structure binding pose obtained by the top docking score thus providing confidence Schrödinger Glide 12.6 and the applied docking protocol will accurately predict agonistic binding within hTAAR1.

The main differences observed across all β_2-adrenoceptors is the downward left shift of docked isoprenaline (**67**), the right-shift of the aromatic moiety of docked salbutamol (**68**) and the slightly distorted conformation of the secondary amine present on cyanopindolol (**65**), Figure 2.1. These differences are expected due to variation within crystallisation conditions and protein conformation during the time of crystallisation. Unlike the β_2-adrenoceptors, bound and top-scoring redocked pose of L745870 (**69**) present in PDB: 6IQL were not well aligned, Figure 2.2. Analysis of lower ranked docking scores did not reveal a more favourable docking pose.
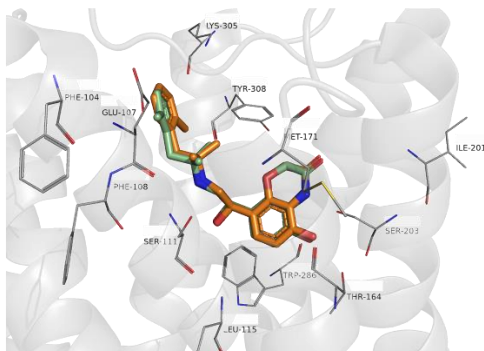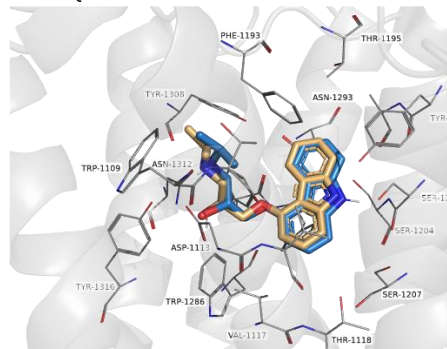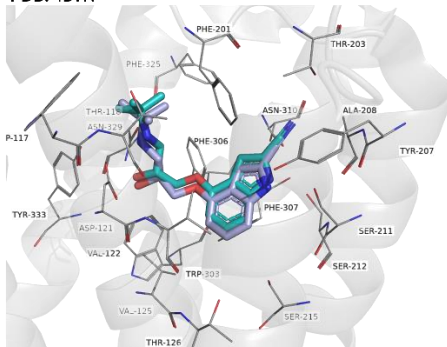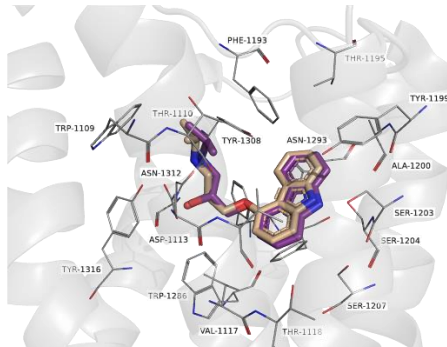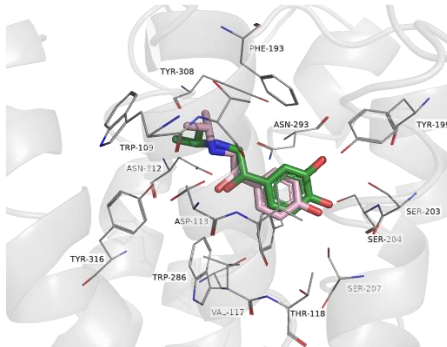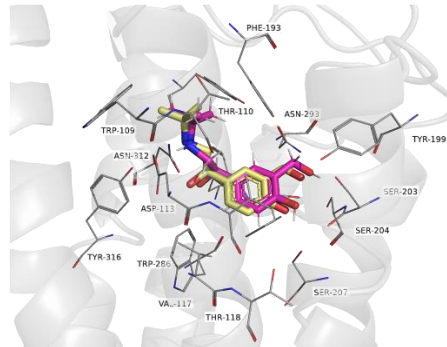
Figure 2.1 *Overlay of crystal structure agonists and antagonists present in six Protein Data Bank (PDB) entries with top ranking docking pose generated. Docking performed using Schrödinger's Maestro and Glide 12.6 packages and images created using PyMOL 4.6.0. From left to right: PDB: 3P0G – green; co-crystalised P0G (**63**), orange; docked pose. PDB: 5JQH – light orange; co-crystalised carazolol (**64**), skyblue; docked pose. PDB: 4BVN – lilac; co-crystalised cyanopindolol (**65**), turquoise; docked pose. PDB: 3PDS – wheat; co-crystalised 8-hydroxy-5-{1R}-1-hydroxy-2-((2-[3-sulfanylpropoxyl)phenyl]ethyl)amino)ethyl]quinoline-2(1H)-one (**66**), deep purple; docked pose. PDB: 7DHR – light pink; co-crystalised isoprenaline (**67**), forest green; docked pose and PDB: 7DHI – pale yellow; co-crystalised salbutamol (**68**), magenta; docked pose.*

PDB: 6IQL
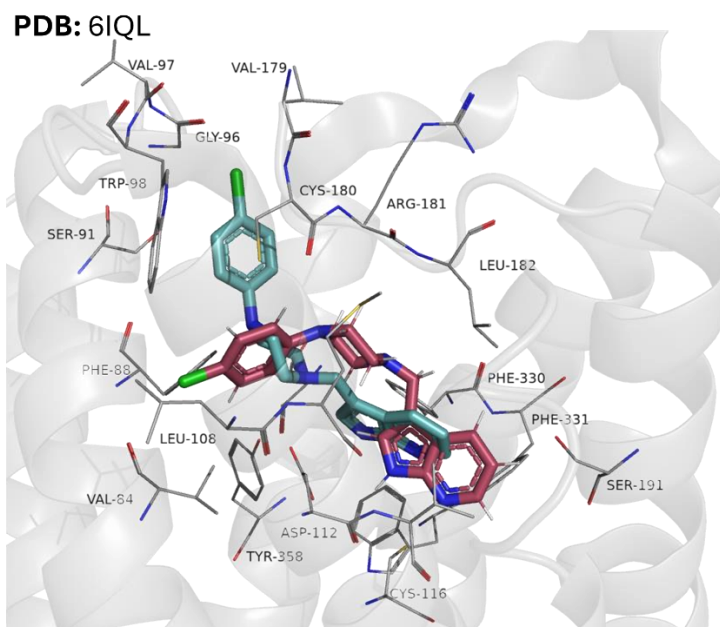
*Figure 2.2 Overlay of crystal structure antagonist L745870 (**69**) (deep teal) present in PDB entry 6IQL with top ranking docked pose generated (raspberry). Docking performed using Schrödinger's Maestro and Glide 12.6 packages and images created using PyMOL 4.6.0.*

Molecular docking predicts both a docked pose (composed of ligand orientation and conformation) along with a corresponding docking score for compounds to identify those with high-affinity binding and potentially biologically active molecules [179, 206]. In some software, namely AutoDock Vina, the predicted binding affinity (K_i) a ligand has for the target site may be calculated from the docking score using various algorithms [207].

Schrödinger Glide Score is an empirical scoring function that scores docked poses according to ligand geometry, solvent exposure, lipophilic interactions and potential effects from the Coulomb and van der Waals integration energies [207]. The docking score generated in the Schrödinger suite is the recommended function to rank the docking of ligands. It generates a score identical to the Glide Score but takes into account any Epik state penalties which may arise from predicting pKa values and protonation state distributions between the ligand and receptor, making it a more accurate scoring system [208].

Shown in Table 2.2 three of the docked co-crystalised ligands (**63-65**) generated 'good' docking scores (PDB: 3P0G, 5JQH and 4BVN) [209]. For the remaining β_2-adrenoceptor ligands, it is likely many of the interactions formed between ligand and protein were hydrophobic in nature, evidenced by the lack of interactions displayed in Figure 2.1. The poor alignment of **69** shown in Figure 2.2 is further confirmed by the high docking score obtained, Table 2.2. Because the docked poses still closely resemble the co-crystalised bound ligands for most of the receptors it is assumed Schrödinger Maestro and Glide 12.6 are acceptable software for use in this study.

Table 2.2 *Docking score corresponding to the overlaid poses shown in Figure 2.1 and Figure 2.2.*

PDB entry	Docking score (kcal/mol)
3P0G	-10.860
5JQH	-9.378
4BVN	-10.184
3PDS	-7.380
7DHR	-6.417
7DHI	-7.695
6IQL	-5.627

2.1.3. Binding site detection

Understanding the chemical and physical properties of the binding site is paramount to account for strong and favourable interactions between ligand and protein [210]. The SiteMap program within Schrödinger Maestro allows areas of the protein to be scored based upon set criteria, assessing their suitability as potential active sites [211]. Because limited information is known about the hTAAR1 receptor, potential binding sites for models 1-4, 6-30 were identified using SiteMap. As Asp103$^{3.32}$ (superscript represents Ballesteros-Weinstein nomenclature) is a

conserved residue amongst aminergic GPCRs and to correlate with the literature, it was critical potential binding sites contain this residue [123, 131, 133, 212, 213].

The druggability of the homology models was predicted using structure-based techniques. For models 1-4, 6-27 and 29-30 the predicted binding sites were expected to interact with drugs with high affinity (druggability scores ranging between 0.914 – 1.122). Model 28 failed to generate a potential binding site containing Asp103$^{3.32}$ so was deemed unsuitable as an accurate representation of hTAAR1, thus its use in this study was discontinued. As model 5 is co-crystalised with L745870 (**69**), it was assumed this binding site would be appropriate for hTAAR1, thus the sitemap program was not applied. Across models 1-27, 29-30 the orthosteric binding site was similar to other available structures for aminergic GPCRs, with several residues within the core binding site being identical to other readily available TAAR1 homology models, suggesting the models generated are accurate representations of hTAAR1 [123, 124, 133].

2.1.4. Visual observations

Examination of the binding site, containing key residues identified in the literature resulted in differences between the binding sites of each homology model and the corresponding software to be observed [124, 176]. Although many residues are well aligned, it is clear the ring structures of Trp89^{ECL1}, His99$^{3.28}$ and Phe195$^{5.43}$ occupy different chemical space over the range of homology models analysed. Minimal differences were observed between the binding sites of models 1-25 (Figure 2.3) suggesting the active state of models 3, 4 and 6-20 does not affect potential binding between the ligand and target site despite undergoing a conformational change.
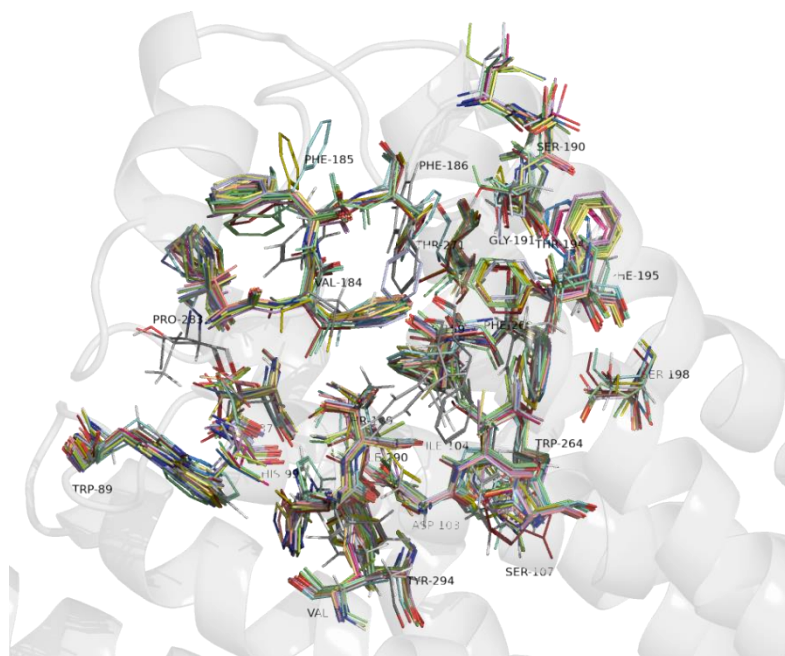
Figure 2.3 *Alignment of key residues in hTAAR1 binding site of homology models 1-4, 6-25. Images created using PyMOL 4.6.0.*

Using a different Family A GPCR template, as demonstrated in model 5 shows variation at Trp89[ECL1], His99[3.28], Pro283[7.32] and Tyr294[7.43] (Figure 2.4).
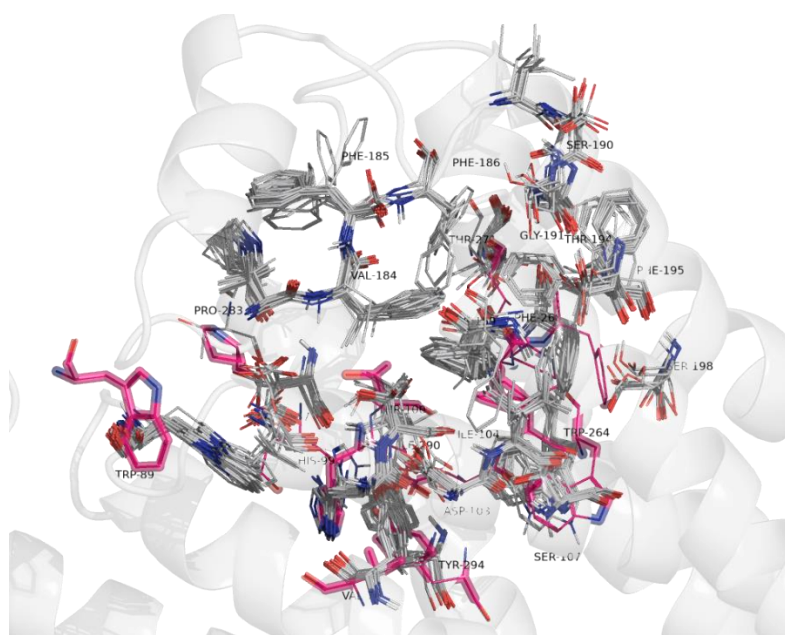
Figure 2.4 *Differences observed in hTAAR1 binding sites when the template receptor is varied. Grey; β$_2$-adrenoceptor homology models, magenta; dopamine D4 receptor homology model. Images created using PyMOL 4.6.0.*

Contrasting to the models generated using Modeller and I-TASSER software, models 26-30 demonstrate vast levels of variation (Figure 2.5). It is hypothesised the differences in conformation of aromatic rings present in sidechains of Trp89[ECL1] and Phe185[ECL2] could block ligand entry into the binding pocket, therefore reducing the predicted ligand binding affinity.
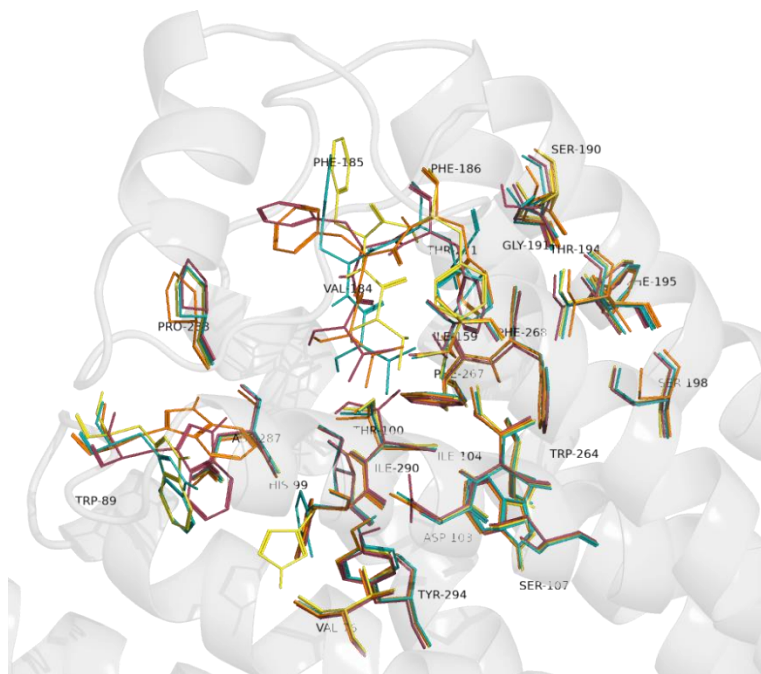
Figure 2.5 Alignment of key residues in hTAAR1 binding site of homology models 26-30. Images created using PyMOL 4.6.0.

2.1.5. Statistical evaluation of hTAAR1 homology models

Quantitative comparison of three-dimensional structures is essential in structural biology. The most used technique to determine the similarity between two superimposed coordinates is root mean squared deviation (RMSD) [214, 215]. RMSD analysis was used to assess the differences between homology models 1-27 and 29-30 and was achieved using an in-house python script utilizing mdtraj (Appendix 9.1). The script generated graphs (Figure 2.6 and Figure 2.7) where the models are positioned according to their similarity: the lower the RMSD the more similar the models are. The visual differences observed in Figure 2.3-Figure 2.5 correlate with the results

obtained from RMSD analysis. Figure 2.6 shows model 5 is significantly different to the other homology models due to the use of a dopamine D4 receptor as the starting template.
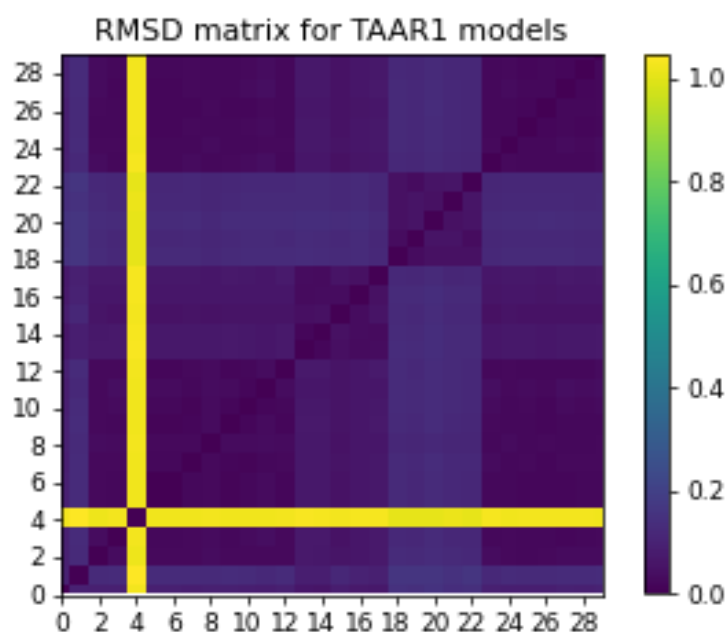
Figure 2.6 *Root mean square deviation for the binding site of hTAAR1 homology models designed using β₂-adrenoceptors and dopamine D4 receptors.*

Removing model 5 from analysis, Figure 2.7 shows minimal variation within each set of models generated using individual software and the similarities between the Modeller and I-TASSER software.
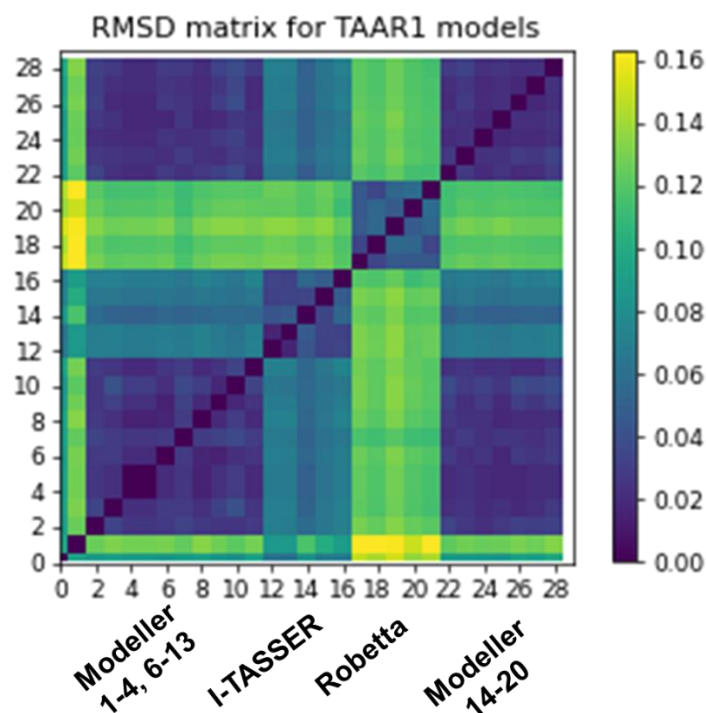
Figure 2.7 *Root mean square deviation for the binding site of hTAAR1 homology models designed using β₂-adrenoceptors.*

To compliment the RMSD data, cluster analysis was performed on each of the homology models. This statistical process classified the models into specific groups or 'clusters' based on the similarities within characteristics and properties between the other homology models present in this study [216, 217]. An algorithm is applied whereby the objects in a specific dataset are separated based on their similarities therefore, the homology models belonging to the same cluster will have a greater similarity than two homology models found in two different clusters. This analysis allowed us to understand the effects of using different PDB templates and modelling software identifying the similarities and differences between the hTAAR1 homology models generated. Based on the clustering patterns, Figure 2.8 shows the binding sites of the Robetta homology models are different to those produced using Modeller and I-TASSER. Additionally, the inactive models (models 1 and 2) occupy a different chemical space to the activated models.
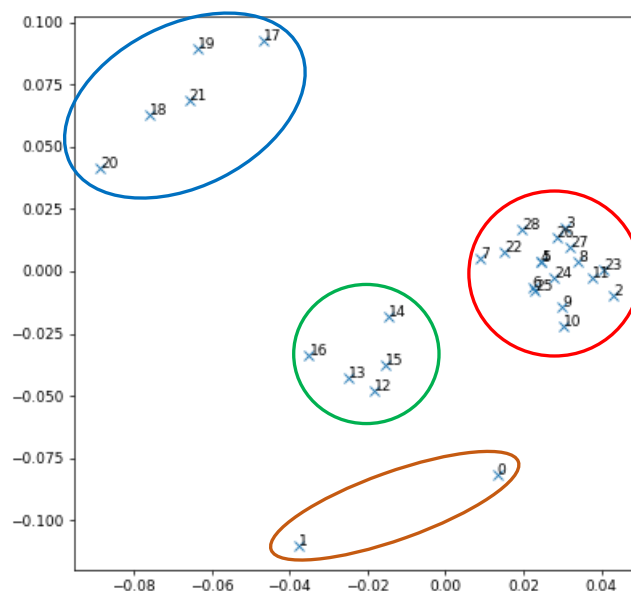
Figure 2.8 *Cluster analysis plot for the binding site of hTAAR1 homology models. X-axis: embedding dimension 1. Y-axis: embedding dimension 2. All models are built using active PDB entries except for plots 0 and 1 which were built using inactive PDB structures. Models are identified with a number and the distance between the models represents the RMSD. Blue; Robetta, Green; I-TASSER, Red; Modeller (active forms), Orange; Modeller (inactive forms).*

The clustering analysis was calculated using the aforementioned python script (Appendix 9.1). The analysis was based on the measure of the RMSD and the superposition of α-carbons of selected amino acid residues found within the active site [124]. The amino acid residues used in the cluster analysis were considered crucial for the binding of TAAR1 ligands and identified in literature hTAAR1 homology models [124].

The data shown in Figure 2.8 suggests that some models are nearly duplicates of one another due to the closeness between data points. From this information, it is possible to select a representative model from each cluster to signify all homology models in that group, however as little is known regarding hTAAR1, it was concluded all models will be employed for the subsequent docking steps to gain the most accurate representation of hTAAR1.

2.2. Molecular docking of literature compounds into hTAAR1 homology models

Final validation of the hTAAR1 homology models resulted from docking a series of known hTAAR1 agonists, an antagonist and decoy compounds into the models using Maestro from the Schrödinger suite. The grid used comprised of all the residues involved in hTAAR1 binding according to the literature [124]. All ligands were docked into the binding site with a hydrogen bond constraint with Asp103$^{3.32}$ applied [123, 133, 212]. The binding poses of compounds docked into the homology models were evaluated considering several factors. Firstly, the number of hydrogen bonds that the compounds were making with crucial residues in the active site, as well as further stabilisation through other interactions and the binding score generated. Although it is suggested an accurate binding representation is achieved with a docking score of -10, it is imperative to self-assess the generated poses to determine reasonable results. For example, targets with shallow active sites will generate accurate binding poses via achieving a docking score of -8, whilst metalloproteins generate a docking score of -15 [218]. As the cut-off for a 'good' docking score is a sliding scale, for this project, good docking scores were determined as the lowest value recorded providing the observed pose met the previously stated requirements, correlated with the literature values and the positioning of compounds within the binding pocket was determined sensible.

2.2.1. Endogenous agonists

Trace amines are a class of endogenous compounds which are distributed throughout the mammalian brain. They are metabolically and structurally related to classical monoamine neurotransmitters and under physiological conditions, are found at extremely low concentrations [219, 220].

Endogenous agonists of hTAAR1 include the trace amines tryptamine (K_i: 1084 nM) and tyramine (K_i: 34 nM). Tryptamine (**24**) and tyramine (**18**) were docked into each homology model with the data reported in Table 2.3.

Upon docking of **24**, 8 homology models (1, 4, 5, 7, 10, 13, 17, 24, 25) generated 'good' docking scores whereas tyramine (**18**) obtained top scores from only 4 models (4, 14, 17, 25). As homology models 4, 14, 17 and 25 produced consistent high scores for both endogenous agonists, the interactions predicted and docked poses produced where analysed in depth.

Table 2.3 *Docking score for the top scoring docked pose for endogenous agonists tryptamine (**24**) and tyramine (**18**) into hTAAR1 homology models.*

	Docking score (kcal/mol)	
	Tryptamine (24)	**Tyramine (18)**
Model 1	-6.709	-6.084
Model 2	-7.111	-5.209
Model 3	-5.650	-4.978
Model 4	-6.694	-7.574
Model 5	-6.839	-5.626
Model 6	-6.755	-5.578
Model 7	-6.496	-5.531
Model 8	-6.141	-5.341
Model 9	-6.556	-5.127
Model 10	-7.191	-6.085
Model 11	-6.698	-6.381
Model 12	-6.658	-6.286
Model 13	-7.029	-6.405
Model 14	-7.408	-7.314
Model 15	-6.275	-5.390
Model 16	-6.229	-5.396
Model 17	-6.805	-6.968
Model 18	-5.603	-4.260
Model 19	-6.256	-5.109
Model 20	-6.521	-4.314
Model 21	-6.991	-5.390
Model 22	-6.235	-6.362
Model 23	-6.762	-5.242
Model 24	-6.756	-5.584

Table 2.3 Continued

	Docking score (kcal/mol)	
	Tryptamine (24)	**Tyramine (18)**
Model 25	-7.087	-6.904
Model 26	-6.707	-5.473
Model 27	-	-5.460
Model 28	-	-5.548
Model 29	-	-4.026
Model 30	-	-4.026

The results showed homology models 4, 14, 17 and 25 exhibited several of the features crucial for hTAAR1 binding. The top predicted binding poses for tryptamine and tyramine in homology models 4, 14, 17 and 25 are shown in Figure 2.9 and Figure 2.10. The aromatic rings are deeply inserted into the binding pocket whilst the primary amine moieties formed strong interactions with $Asp103^{3.32}$. The salt bridge and hydrogen bond length predicted between the endogenous agonists and $Asp103^{3.32}$ were deemed optimal for homology models 4, 17 and 25 varying between 1.75 – 3.04 Å, whilst slightly elongated bond lengths (2.86 – 3.94 Å) were predicted for model 14 [221]. Furthermore, for each of the selected homology models, **18** and **24** were further stabilised via π-π or π-cation interactions with $Phe185^{ECL2}$, $Phe267^{6.51}$ and $Phe268^{6.52}$. Additionally, the site where both compounds bind is lined with residues reported in other hTAAR1 molecular docking studies including $Phe195^{5.43}$, $Val184^{ECL2}$, $Ile290^{7.39}$, $Ile104^{3.33}$, $Trp264^{6.48}$, $Tyr294^{7.43}$, $Thr100^{3.29}$ [124, 176, 222]. These residues help form the hydrophobic pocket present in the binding site and contribute to ligand binding and stabilisation through van der Waals interactions [213].
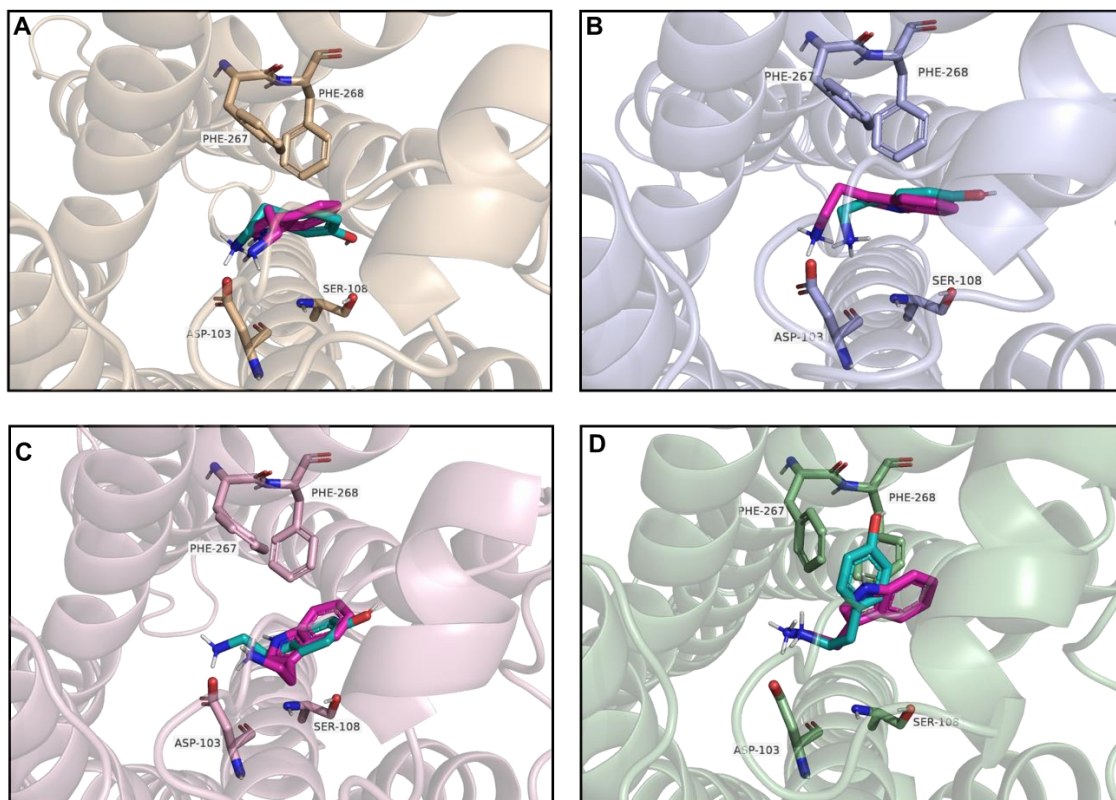
Figure 2.9 (A) *Docked pose of tyramine (**18**) (cyan) and tryptamine (**24**) (magenta) in homology model 4. **(B)** Docked pose of **18** (cyan) and **24** (magenta) into homology model 14. **(C)** Docked pose of **18** (cyan) and **24** (magenta) into homology model 17. **(D)** Docked pose of **18** (cyan) and **24** (magenta) into homology model 25. All Images visualised down transmembrane 3. Crucial receptor residues lining the pocket are shown as sticks. Docking performed using Schrödinger's Maestro and Glide 12.6 packages and images created using PyMOL 4.6.0.*
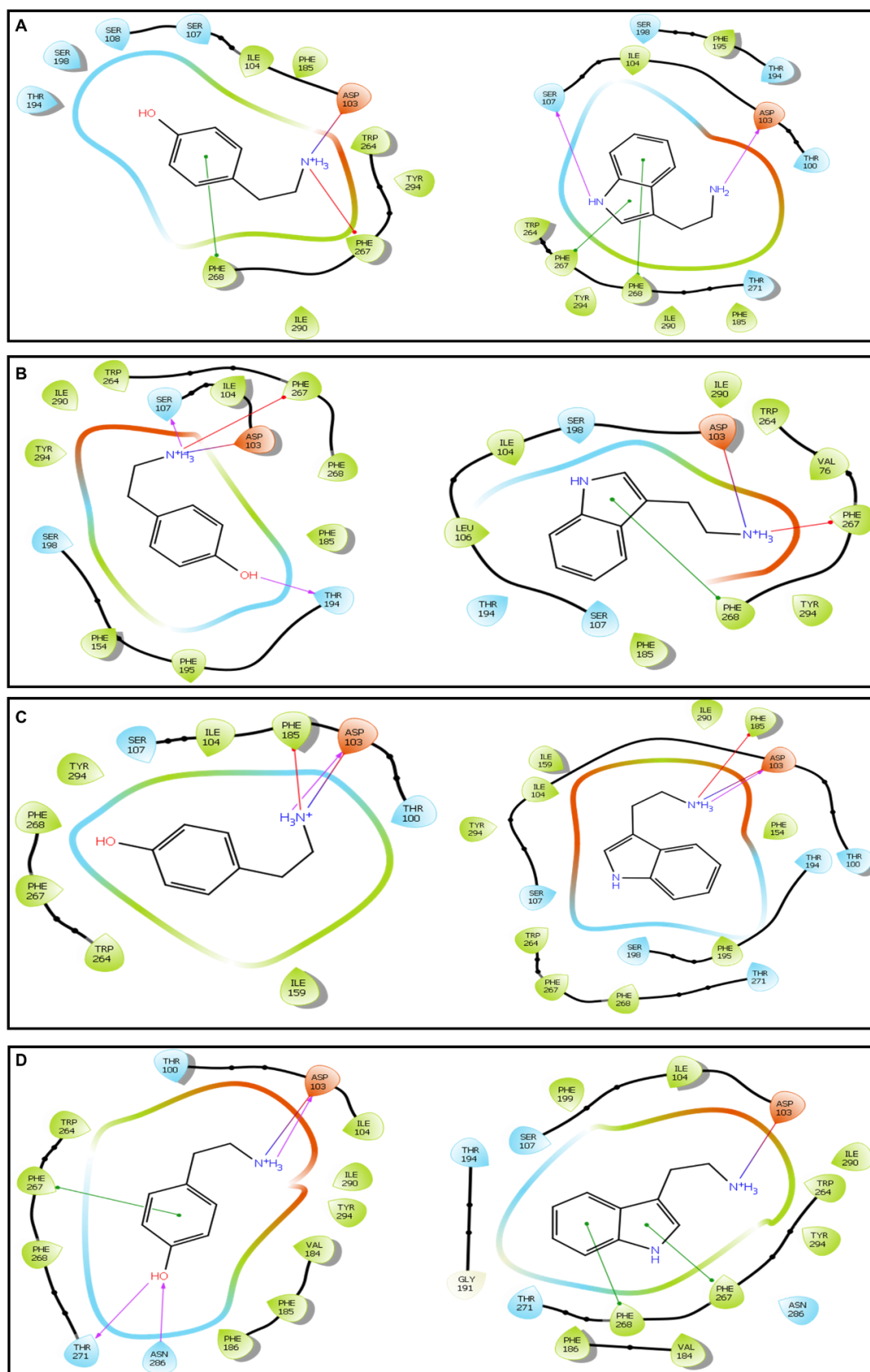
Figure 2.10 *Tyramine (**18**, left) and tryptamine (**24**, right) interactions with hTAAR1 homology models. (**A**) Homology model 4. (**B**) homology model 14. (**C**) Homology model 17. (**D**) Homology model 25. Images generated with Maestro from the Schrödinger suite.*

For both docked compounds, models 8 and 18 generated low docking scores. The binding poses of **18** and **24** in homology models 8 and 18 were compared to those of models 4, 14, 17 and 25 (Figure 2.11). Despite optimal hydrogen bond lengths being predicted between ligand and Asp103$^{3.32}$, it is clear compound positioning within the binding site is the cause for the poor docking scores. Unlike the poses generated for models 4, 14 and 17, both the aliphatic and aromatic moieties of tryptamine and tyramine are not well aligned. Additionally, the aromatic rings of tryptamine and tyramine are not positioned deep into the binding sites, therefore the use of these two homology models were discontinued.
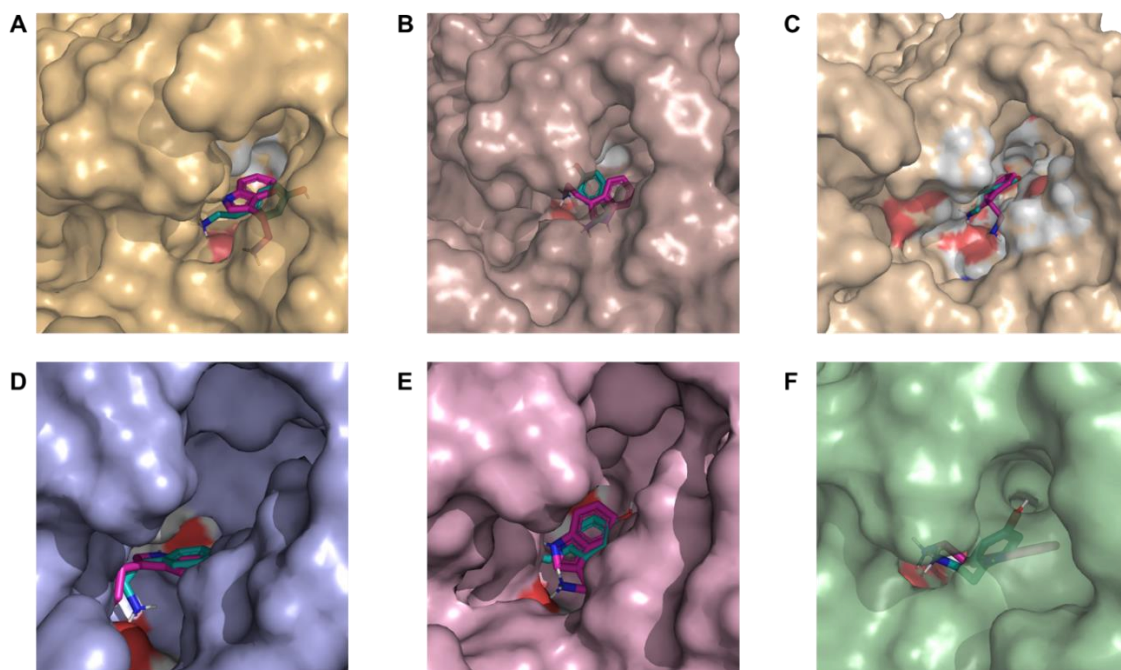
Figure 2.11 *Surface representation of hTAAR1 homology models and the docked pose of tyramine (**18**, cyan) and tryptamine (**24**, magenta). (**A**) Homology model 8. (**B**) Homology model 18. (**C**) Homology model 4. (**D**) Homology model 14. (**E**) Homology model 17. (**F**) Homology model 25. Docking performed using Schrödinger's Maestro and Glide 12.6 packages and images created using PyMOL 4.6.0.*

Correlating with the hypothesis stated in section 2.1.4, whereby variation between side chain orientation could prohibit ligand entry into the active site, no docking data was obtained for tryptamine (**24**) in models 27-30. As these models failed to generate data for an endogenous agonist of hTAAR1, their use in this study was also terminated.

2.2.2. Synthetic agonists

Galley *et al* identified a selective hTAAR1 agonist, RO5073012 (**59**, Figure 1.34) after exploring and developing a subset from the Roche compound library [173]. Preliminary *in vitro* data indicates RO5073012 (**59**, Figure 1.34) has a strong binding affinity for hTAAR1 (12 nM). To further evaluate the hTAAR1 homology models, **59** along with the radioligand (**60**) used to determine its binding affinity were docked into the remaining hTAAR1 homology models.

Most of the homology models gave 'good' docking scores upon the docking of (*S*)-4-(2,4-difluorophenyl-3-tritio)-4,5-dihydro-2-oxazolamine (**60**). This was expected due to the initial preference the Modeller models displayed for **60**, during the model design stage of this project, and the results obtained from the cluster analysis showing a likeness between the Modeller and I-TASSER models. Therefore, to get an accurate representation of the models, those that produced 'good' docking scores for RO5073012 (**59**) (11, 17, 21 and 25, Table 2.4) where studied in greater detail.

Table 2.4 *Docking score the top scoring docked pose for synthetic agonists RO5073012 (**59**) and (S)-4-(2,4-difluorophenyl-3-tritio)-4,5-dihydro-2-oxazolamine (**60**) into hTAAR1 homology models.*

	Docking score (kcal/mol)	
	RO5073012 (59)	**(S)-4-(2,4-difluorophenyl-3-tritio)-4,5-dihydro-2-oxazolamine (60)**
Model 1	-6.296	-6.058
Model 2	-6.241	-6.965
Model 4	-5.506	-6.863
Model 5	-5.627	-6.533
Model 6	-5.226	-5.811
Model 7	-4.816	-7.063
Model 9	-5.378	-6.269
Model 10	-5.012	-5.890
Model 11	-6.498	-6.480
Model 12	-5.844	-6.356
Model 13	-4.595	-6.376
Model 14	-5.485	-8.182
Model 15	-5.957	-5.931
Model 16	-4.794	-5.571
Model 17	-6.046	-6.359
Model 19	-5.603	-5.393
Model 20	-6.055	-5.849
Model 21	-6.839	-6.506
Model 22	-5.241	-5.924
Model 23	-6.338	-5.843
Model 24	-5.485	-5.470
Model 25	-5.827	-7.027
Model 26	-5.614	-5.493

The data presented in Figure 2.12 and Figure 2.13 shows the 6-membered aryl rings of both **59** and **60** are deeply inserted into the binding pocket correlating with the poses generated by tryptamine (**70**) and tyramine (**18**). Similarly, the amines present in the aromatic heterocycles formed strong interactions with Asp103[3.32]. Optimal hydrogen bond lengths were predicted between RO5073012 (**59**) and the hTAAR1 homology models (1.64 – 1.84 Å) whilst slightly longer salt bridges are expected (2.74 – 4.80 Å). Similar bond lengths (1.67 – 4.22 Å) are reported for compound **60**.
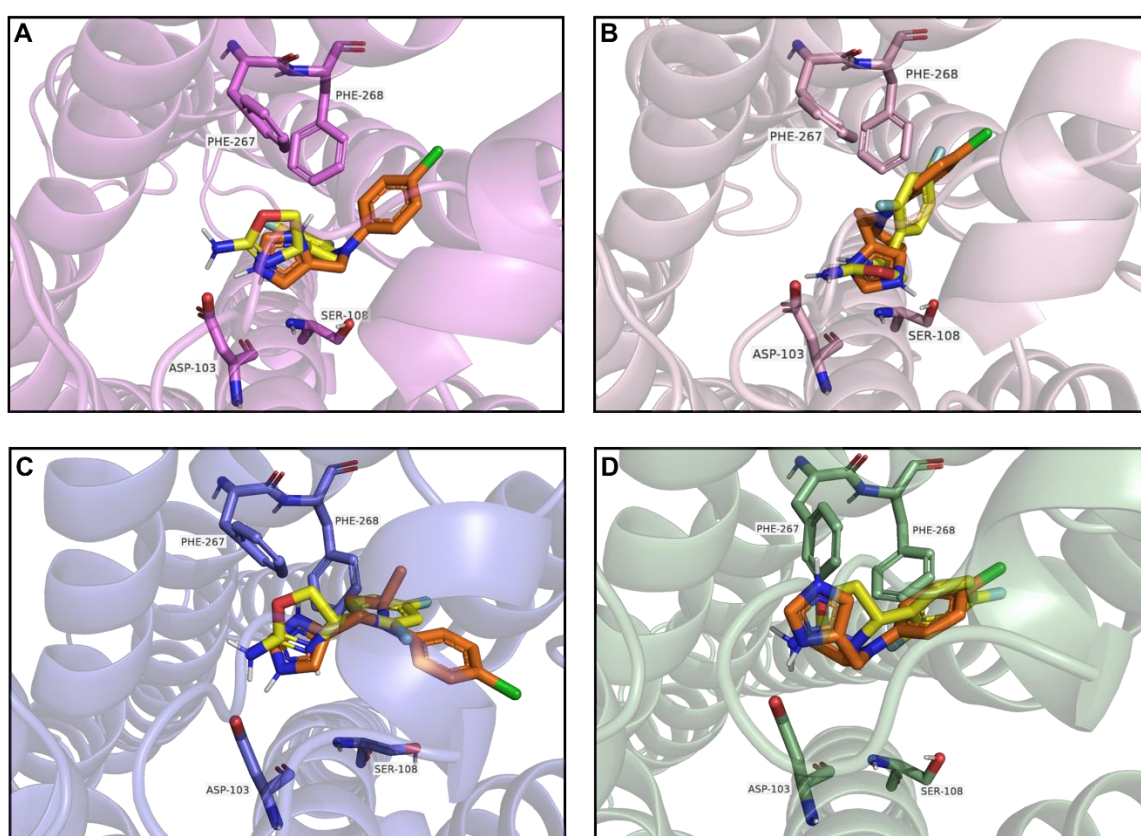
Figure 2.12 (A) *Docked pose of RO5073012 (**59**, orange) and (S)-4-(2,4-difluorophenyl-3-tritio)-4,5-dihydro-2-oxazolamine (**60**, yellow) into homology model 11. **(B)** Docked pose of **59** (orange) and **60** (yellow) into homology model 17. **(C)** Docked pose of **59** (orange) and **60** (yellow) into homology model 21. **(D)** Docked pose of **59** (orange) and **60** (yellow) into homology model 25. All Images visualised down transmembrane 3. Docking performed using Schrödinger's Maestro and Glide 12.6 packages and images created using PyMOL 4.6.0.*

Like the data generated for tyramine and tryptamine, RO5073012 (**59**) and (*S*)-4-(2,4-difluorophenyl-3-tritio)-4,5-dihydro-2-oxazolamine (**60**) were further stabilised via π-π or π-

cation interactions with Phe185^{ECL2} and Phe267$^{6.51}$, with **59** undergoing halogen-bonding with Met158$^{4.60}$ in model 21. Additionally, the binding site is composed with the same residues as those stated in 2.1.3, forming a hydrophobic pocket and subsequently further stabilisation via van der Waals interactions [124, 176].
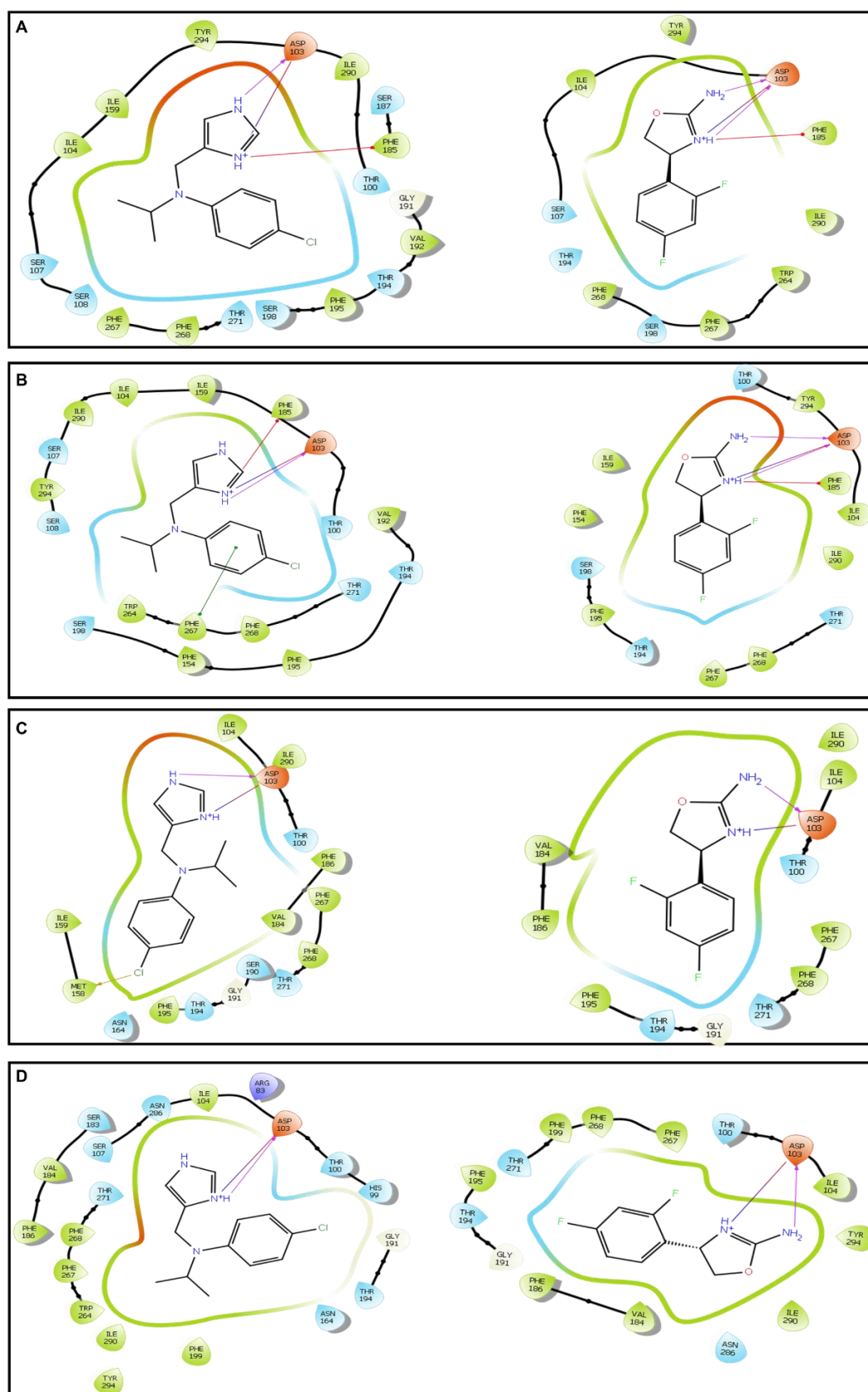
Figure 2.13 *RO5073012* (**59**, *left*) *and* (*S*)-4-(2,4-difluorophenyl-3-tritio)-4,5-dihydro-2-oxazolamine (**60**, *right*) *interactions with hTAAR1 homology models.* (**A**) *Homology model 11.* (**B**) *Homology model 17.* (**C**) *Homology model 21.* (**D**) *Homology model 25.*

Comparable to the data generated in the docking of endogenous agonists **18** and **24**, some models generated low docking scores for both RO5073012 (**59**) and (*S*)-4-(2,4-difluorophenyl-3-tritio)-4,5-dihydro-2-oxazolamine (**60**). As the models were designed to yield good docking data for **60**, the binding poses of models 6, 10 and 16 were studied and compared with models 11, 17 and 25 to provide rationale for the low scores, Figure 2.14.

For model 16, it is clear the conditions set to identify a suitable homology model were not met due to the positioning of compounds **59** and **60** within the binding pocket, Figure 2.14. Both agonists failed to occupy the full space available within the binding site and subsequently docked to the left of the binding site, with the aromatic moieties being poorly aligned with one another. Although the docked poses generated for **59** and **60** are much deeper in the binding pocket for homology model 6 and 10, the aromatic moieties were ill-aligned. Furthermore, in models 6, 10 and 16, **60** yielded a twisted confirmation, subsequently resulting in poor alignment of the aromatic heterocyclic rings present in both **59** and **60**. As the top predicted binding poses of compounds **59** and **60** in models 6, 10 and 16 were misaligned and failed to optimise the chemical space available within the binding site, the use of models 6, 10 and 16 to determine an accurate and reliable homology models for hTAAR1 in this study was terminated.
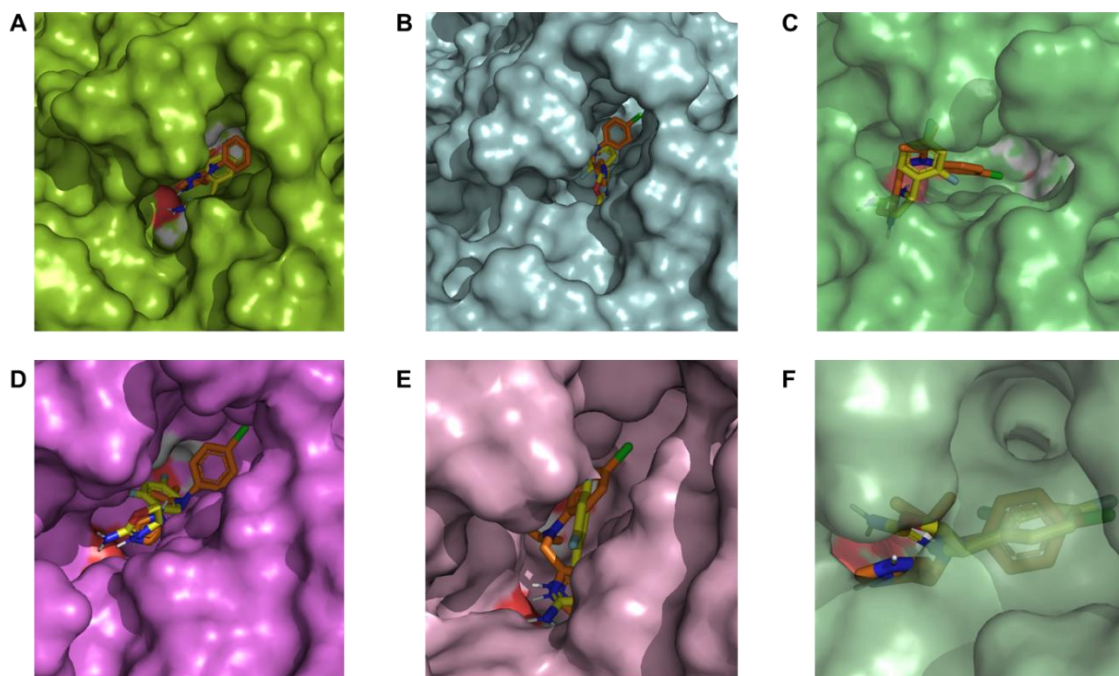
Figure 2.14 *Surface representation of hTAAR1 homology models and the docked pose of RO5073012 (**59**, orange) and (S)-4-(2,4-difluorophenyl-3-tritio)-4,5-dihydro-2-oxazolamine (**60**, yellow). **(A)** Homology model 6. **(B)** Homology model 10. **(C)** Homology model 16. **(D)** Homology model 11. **(E)** Homology model 17. **(F)** Homology model 25. Docking performed using Schrödinger's Maestro and Glide 12.6 packages and images created using PyMOL 4.6.0.*

2.2.3. EPPTB

Stalder *et al* discovered EPPTB (**70,** Figure 2.15), a selective mouse TAAR1 antagonist ($K_i = 0.0009$ µM), during a SAR study following high throughput screening of the Roche compound library [223]. Dependent on the experimental model used, literature suggests **70** exhibits the behaviour of both inverse agonism and weak antagonism in hTAAR1; however, to the best of my knowledge it is the only selective antagonist of TAAR1 [123]. Therefore, it was prudent to predict the binding pose of EPPTB (**70**) in our homology models to assess the interactions predicted and whether the docking scores correlate with that of the literature K_i value.
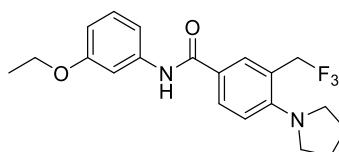
Figure 2.15 *Chemical structure of EPPTB (**70**).*

The docking scores generated for EPPTB (**70**) in homology models 1-5, 7, 9, 11-15, 17, 19-26 are shown in Table 2.5. All models generated 'poor' docking scores upon the docking of **70**. The reason for this is unknown however it is plausible the scores generated reflect EPPTB (**70**) is a weak antagonist of hTAAR1 and as such has failed to generate strong interactions and optimal positioning within the binding pocket.

Table 2.5 *Docking score for the top scoring docked pose for antagonist EPPTB (**70**) and hTAAR1 homology models.*

	Docking score (kcal/mol)
Model 1	-4.980
Model 2	-5.552
Model 4	-6.187
Model 5	-3.549
Model 7	-5.572
Model 9	-5.325
Model 11	-4.353
Model 12	-5.447
Model 13	-5.111
Model 14	-6.343
Model 15	-3.568
Model 17	-4.764
Model 19	-4.462
Model 20	-2.571
Model 21	-4.227
Model 22	-
Model 23	-3.618
Model 24	-4.712
Model 25	-3.824
Model 26	-1.881

Considering all the above parameters, the model that most accurately reproduced known hTAAR1 ligand structure-activity relationships was model 17, a model built using a β_2-adrenoceptor (PDB: 3PDS, 3P0G and 7DHI) as a template. Therefore, EPPTB (**70**) was docked into this model with the data shown in Figure 2.16, Figure 2.17 and Figure 2.18.

The ethoxy-substituted aniline moiety is deeply inserted into the binding pocket whilst the pyrrolidinyl-phenyl is extending out of the binding site. A hydrogen bond with Asp103[3.32] occurs via the aniline nitrogen, with the compound being further stabilised through π-π interactions with Phe267[6.51]. Contrasting to the docking poses generated for **18**, **59**, **60** and **24** the binding pose of EPPTB (**70**) in homology model 17 does not correlate with literature reports. Cichero *et al* report the pyrrolidine nitrogen to participate in hydrogen bonding with Asp103[3.32], with further hydrogen bonding occurring between the ethoxy substituent and Trp291[7.40] whilst Liao *et al* suggest the pyrrolidinyl-phenyl is positioned in a hydrophobic pocket consisting of residues Ile104[3.33], Phe195[5.43], Trp264[6.48] and Phe267[6.51] [123, 224].

The reason for the variation in binding pose in each homology model is unknown. The hypothesis previously stated whereby EPPTB (**70**) is a weak antagonist of hTAAR1 and has failed to generate accurate and reliable interactions with the binding pocket is still valid and is supported by the variation in species-specificity between the human and mouse TAAR1 binding sites [117, 121]. To prove this hypothesis, EPPTB was docked into two mTAAR1 cryogenic electron microscopy (cryo-EM) structures (PDB: 8WC3 and 8WCC), however the results were of limited use. Both structures had relatively low resolutions thus could not accurately detect all receptor-ligand interactions. Furthermore, the cryo-EM structures (PDB: 8WC3 and 8WCC) were determined in their active states due to the presence of bound agonists. Therefore, using molecular docking to gain an accurate representation and understanding of antagonist binding would be challenging due to the conformational change in the receptor. This was demonstrated

as the docking protocol failed to generate any EPPTB (**70**) docked poses when a hydrogen bond constraint was applied, thus making the data incomparable with the homology model.

Another explanation for the wide variation in EPPTB (**70**) binding pose could be due to the template used to generate the homology models. Liao *et al* built their homology model using a dopamine D2 receptor (PDB: 6CM4) and as evidenced in section 2.1.4 using different PDB templates can cause variation in amino acid residues orientation, thus altering the chemical space available within the binding pocket [224].
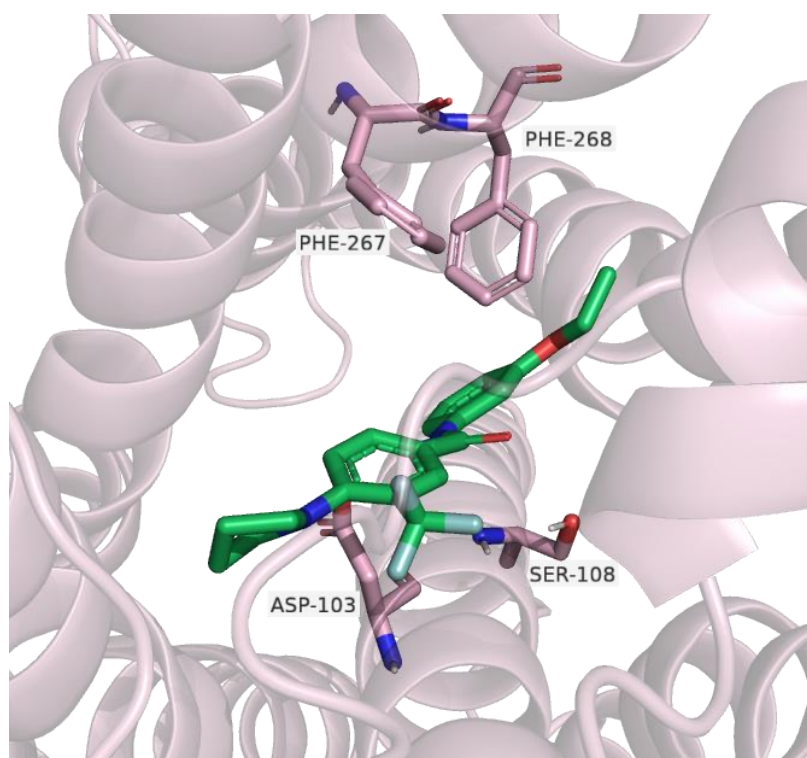
Figure 2.16 *Docked pose of EPPTB (**70**, green) into homology model 17. Image visualised down transmembrane 3.*

Docking performed using Schrödinger's Maestro and Glide 12.6 packages and image created using PyMOL 4.6.0.
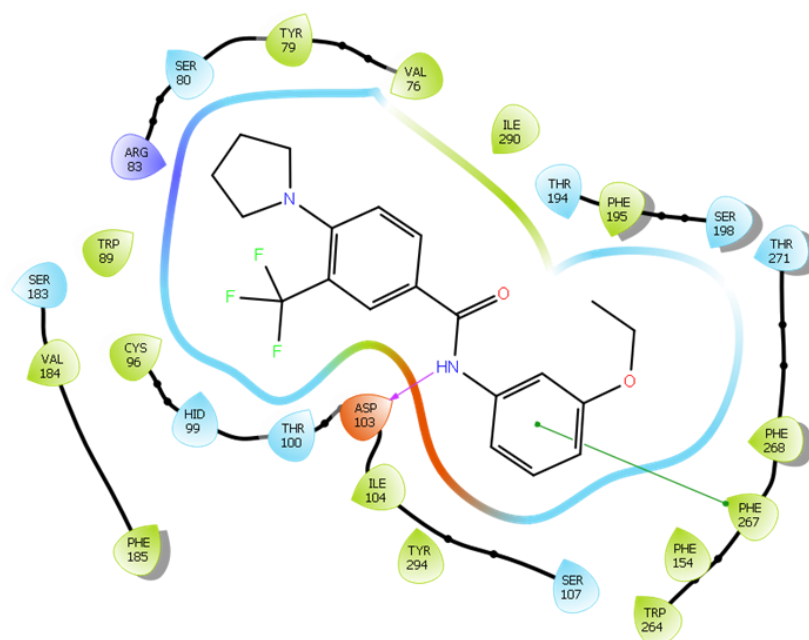
Figure 2.17 *EPPTB (**70**) interactions with hTAAR1 homology model 17.*
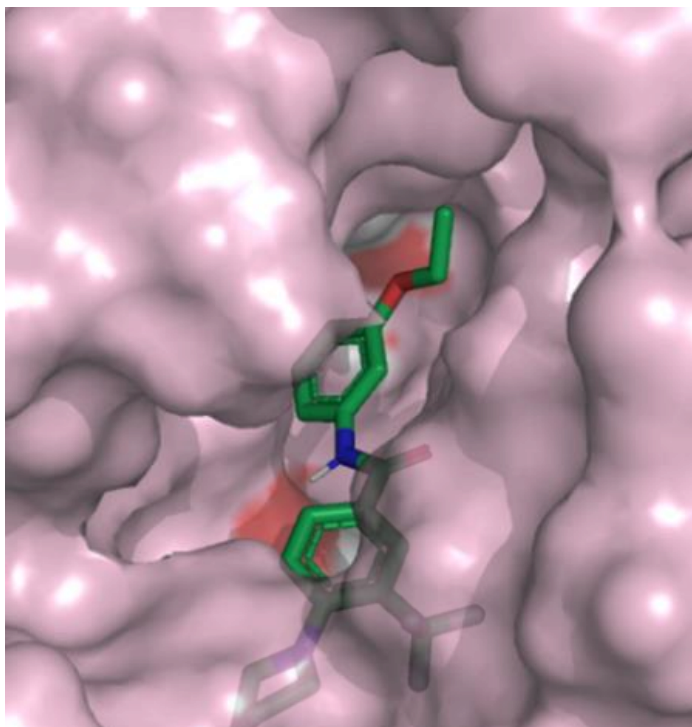
Figure 2.18 *Surface representation of hTAAR1 homology model 17 and the docked pose of EPPTB (**70**, green). Docking*

performed using Schrödinger's Maestro and Glide 12.6 packages and images created using PyMOL 4.6.0.

2.2.4. Decoy compounds

Decoy drug compounds are molecules which have similar chemical and physical properties (namely molecular weight, charge and hydrophobicity) of active compounds but are not expected to elicit a response at the target of interest [225]. Using the data published by Galley *et al*, four poorly active hTAAR1 agonists were identified as decoy compounds [173]. They were subsequently docked into the homology model, with the data shown in Table 2.6. The purpose of this virtual screen was to demonstrate the accuracy of the proposed hTAAR1 homology model in recognising and generating low binding energy poses.

Three of the decoy compounds gave docking scores lower than those generated for the endogenous and synthetic agonists previously reported (**71-73**), correlating with their reported poor activity. Unfortunately, the homology model could not differentiate between RO5073012 (**59**), (*S*)-4-(2,4-difluorophenyl-3-tritio)-4,5-dihydro-2-oxazolamine (**60**) and compound **74**, generating very similar docking scores for the three compounds, Table 2.6.

***Table 2.6** Docking score for the top scoring docked pose for decoy compounds (**71**-**74**) in homology model 17.*

	Docking score (kcal/mol)
71	-5.263
72	-5.941
73	-5.725
74	-6.421

The top predicted binding pose for decoy compounds **71**-**74** are shown in Figure 2.19, with the predicted interactions reported in Figure 2.20. Although the compounds bind in a similar area of chemical space, the increased linker length present in RO5073012 (**59**) is vital for maximising the binding site occupancy and ensuring the aryl ring is positioned deep within the hydrophobic binding pocket, Figure 2.19. All compounds form interactions with Asp103$^{3.32}$ via hydrogen

bonding due to the constraint applied in the docking protocol. Decoy compounds **71** and **72** were further stabilised through π-π interactions with Phe268[6.52] with **72** undergoing halogen-bonding with Thr271[6.55]. Contrasting to the predicted interactions for RO5073012 (**59**), (*S*)-4-(2,4-difluorophenyl-3-tritio)-4,5-dihydro-2-oxazolamine (**60**), compound **74** does not undergo any further stabilisation through π-π or π-cation interactions. This suggests the developed homology model can differentiate between active and decoy compounds thus is a suitable, accurate and reliable depiction of hTAAR1.
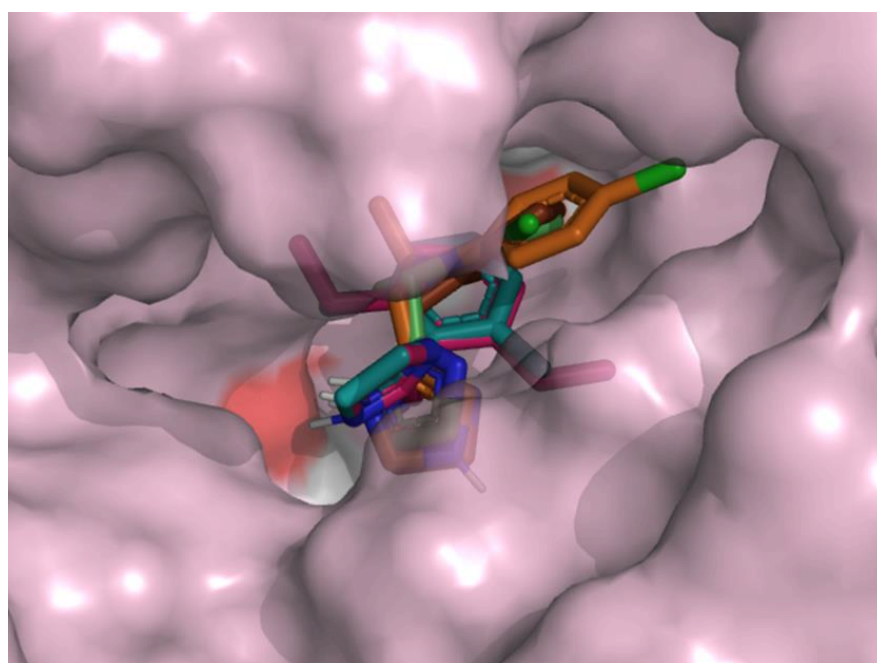
Figure 2.19 *Surface representation of hTAAR1 homology model 17 and the top predicted docked pose of decoy compounds **71**-**74**. RO5073012 (**59**) is shown in orange to identify key differences in binding poses. Docking performed using Schrödinger's Maestro and Glide 12.6 packages and image created using PyMOL 4.6.0.*
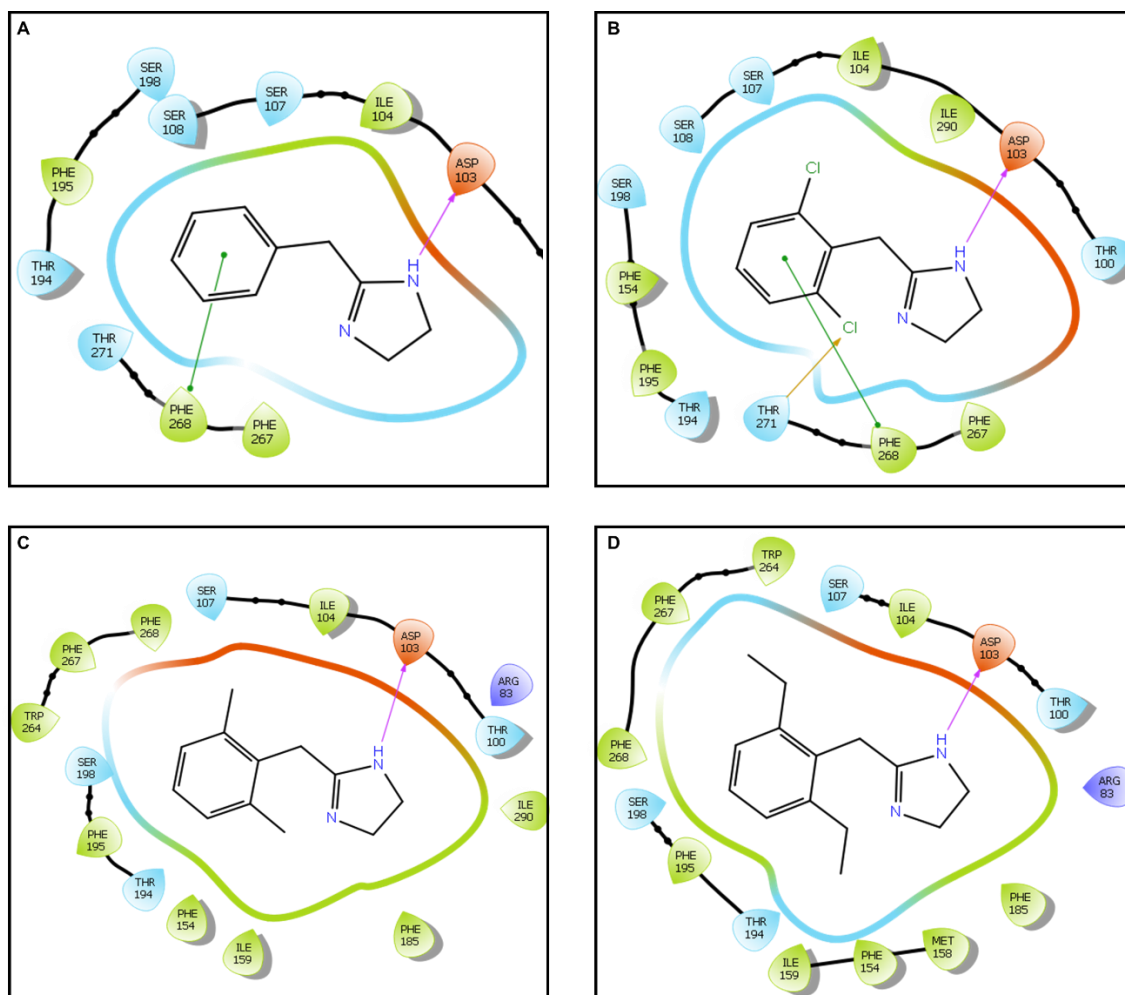
Figure 2.20 *Decoy TAAR1 compounds and their predicted interactions with a hTAAR1 homology model **(A)** Compound 71, **(B)** Compound 72, **(C)** Compound 73 and **(D)** Compound 74.*

2.3. Comparison between molecular docking into hTAAR1 cryo-EM structure (PDB: 8W88) and hTAAR1 homology model

In 2023, several cryo-EM structures of hTAAR1 were published. Particularly a structure with agonist SEP363856 (ulotaront, **62**) bound was of interest due to its high resolution (2.6 Å). This allowed us to compare the generated docking of tyramine, tryptamine, RO5073012, (*S*)-4-(2,4-difluorophenyl-3-tritio)-4,5-dihydro-2-oxazolamine and EPPTB (**18, 24, 59, 60, 70**) in the homology model of hTAAR1 with the cryo-EM structure (PDB: 8W88) of the receptor.

The superimposition of the selected homology model of hTAAR1 and cryo-EM structure (PDB: 8W88) was completed to assess the similarities and differences between the structures

including side chain orientation and ligand positioning within the binding pocket. Shown in Figure 2.21, minimal differences were observed between the homology model and the cryo-EM structure (PDB: 8W88, RMSD: 0.867). It is expected the variations observed in the side chains will cause differences in the predicted ligand binding affinity and compound positioning within the binding pocket.
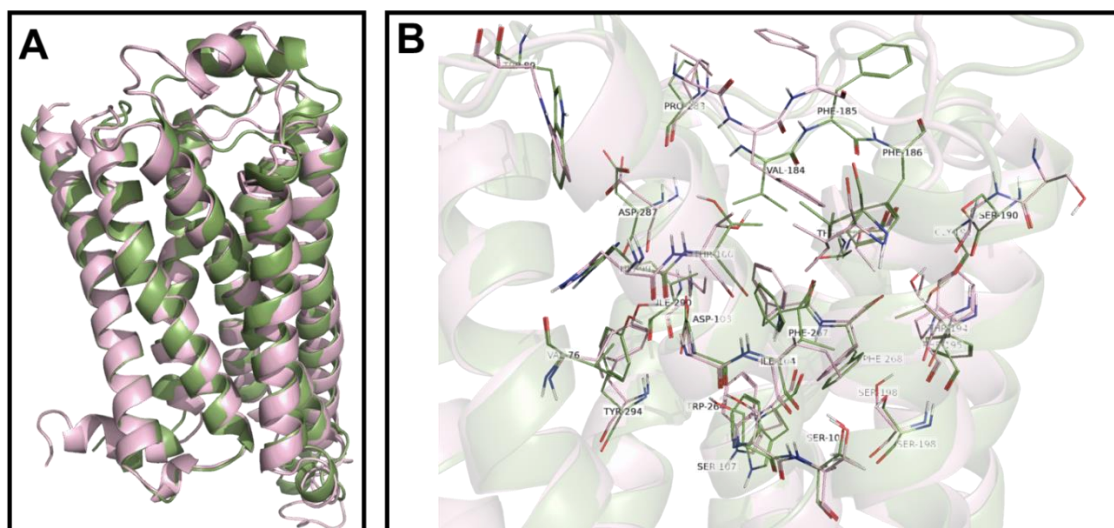
Figure 2.21 (A) Side view of the superimposition of hTAAR1 homology model 17 (pink) and cryo-EM structure (PDB: 8W88, green). *(B)* View from the top of the superimposition of hTAAR1 homology model 17 (pink) and cryo-EM structure (PDB: 8W88, green). Key receptor residues are shown as sticks. Docking performed using Schrödinger's Maestro and Glide 12.6 packages and images created using PyMOL 4.6.0.

To validate the docking method previously employed, ulotaront (**62**) was redocked with a hydrogen bond constraint with Asp103$^{3.32}$ applied into the original cryo-EM (PDB: 8W88) using Schrödinger Maestro in almost the exact same binding pose, Figure 2.22. The grid used was generated using the centroid of bound ulotaront (**62**).
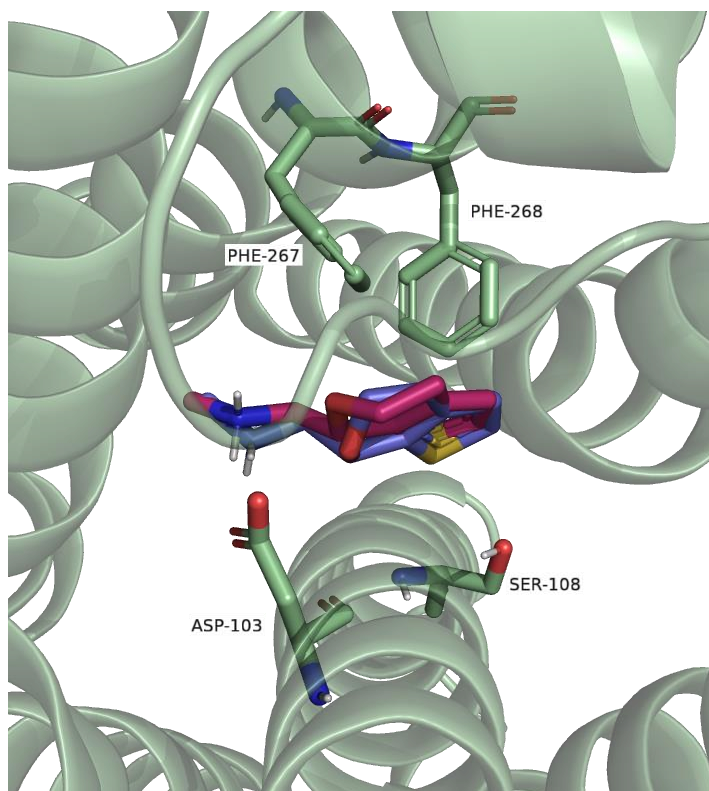
Figure 2.22 *hTAAR1 receptor with bound ulotaront (**62**, pink) and redocked pose (purple) in the cryo-EM structure of hTAAR1 (PDB: 8W88). Image visualised down transmembrane 3. Docking performed using Schrödinger's Maestro and Glide 12.6 packages and Images created using PyMOL 4.6.0.*

This validated method was then used to dock tyramine (**18**), tryptamine (**24**), RO5073012 (**59**), (*S*)-4-(2,4-difluorophenyl-3-tritio)-4,5-dihydro-2-oxazolamine (**60**) and EPPTB (**70**) in hTAAR1 cryo-EM structure (PDB: 8W88) to determine the accuracy of the binding poses obtained. From Figure 2.23, it is clear the binding poses of the TAAR1 ligands occupy a similar area of chemical space within the pocket, however differences in ligand orientation can be observed. For RO5073012 (**59**), the superimposed binding poses differ in the positioning of the aniline ring, with the pose in the cryo-EM model twisting at the tertiary aniline nitrogen. Similarly, the phenyl ring present in (*S*)-4-(2,4-difluorophenyl-3-tritio)-4,5-dihydro-2-oxazolamine (**60**) is positioned down and deep into the pocket in the cryo-EM structure, whilst in the homology model it has opted for a more upwards orientation. It is thought this is due to the slight differences which have occurred in side chain positioning of Phe267[6.51] and Phe268[6.52] within the protein

structures, allowing the compounds to adopt a conformation which favours entry into the hydrophobic pocket and stabilisation via π-π interactions with the named residues.

These variations correlate to the docking scores reported, Table 2.7. The results indicate that the differences between the aromatic moieties of RO5073012 (**59**) and (*S*)-4-(2,4-difluorophenyl-3-tritio)-4,5-dihydro-2-oxazolamine (**60**) does not alter the ligand's binding affinity for the receptor due to the relatively small increases in docking score observed in the cryo-EM structure compared to the homology model. In contrast, the downward orientation of tryptamine (**24**) present in the cryo-EM docked pose increased the docking score from -6.8 to -7.6 kcal/mol, potentially improving the binding affinity the ligand has for the receptor.
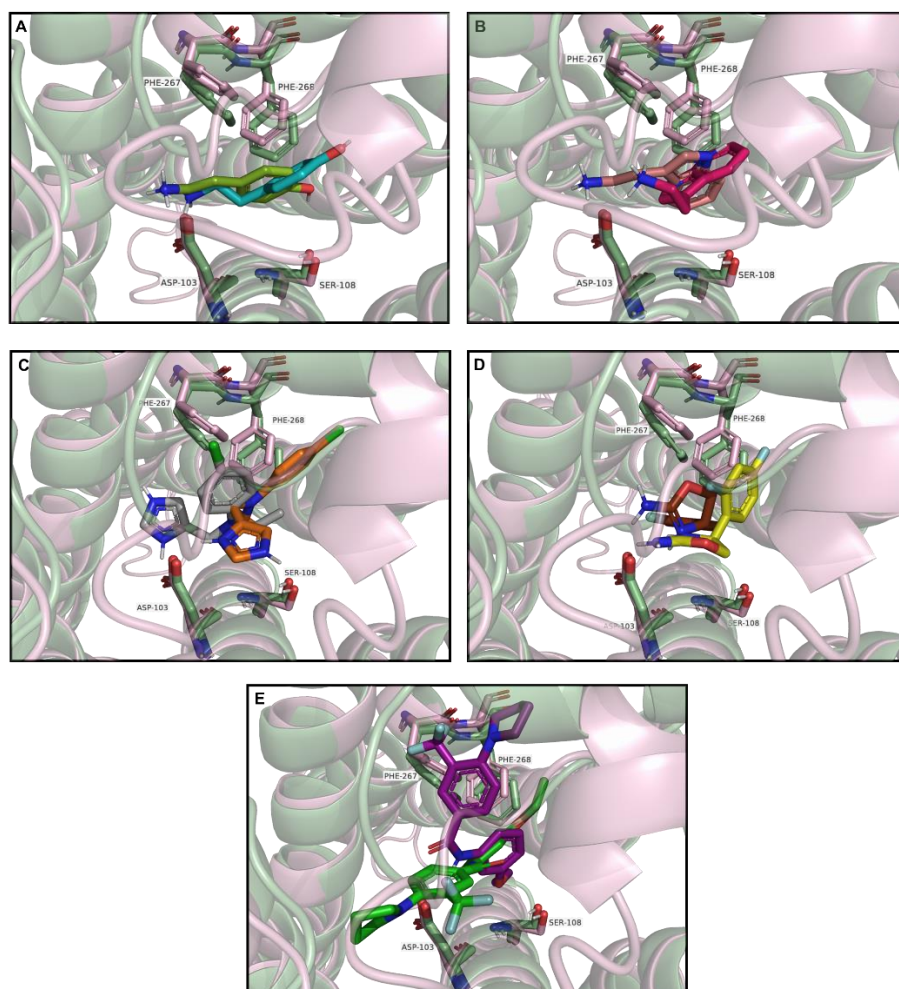
Figure 2.23 (A) *Superimposition of hTAAR1 homology model 17 (pink ribbon) with docked endogenous agonist tyramine (**18**, cyan) and cryo-EM structure (PDB:8W88, green ribbons) with docked endogenous agonist tyramine (**18**, lemon). **(B)** Superimposition of hTAAR1 homology model 17 (pink ribbon) with docked endogenous agonist tryptamine (**24**, magenta) and cryo-EM structure (PDB:8W88, green ribbons) with docked endogenous agonist tryptamine (**24**, salmon). **(C)** Superimposition of hTAAR1 homology model 17 (pink ribbon) with docked agonist RO5073012 (**59**, orange) and cryo-EM structure (PDB:8W88, green ribbons) with docked agonist RO5073012 (**59**, grey). **(D)** Superimposition of hTAAR1 homology model 17 (pink ribbon) with docked agonist (S)-4-(2,4-difluorophenyl-3-tritio)-4,5-dihydro-2-oxazolamine (**60**, yellow) and cryo-EM structure (PDB:8W88, green ribbons) with docked agonist (S)-4-(2,4-difluorophenyl-3-tritio)-4,5-dihydro-2-oxazolamine (**60**, brown). **(E)** Superimposition of hTAAR1 homology model 17 (pink ribbon) with docked antagonist EPPTB (**70**, green) and cryo-EM structure (PDB:8W88, green ribbons) with docked antagonist EPPTB (**70**, purple). All Images visualised down transmembrane 3. Docking performed using Schrödinger's Maestro and Glide 12.6 packages and images created using PyMOL 4.6.0.*

Table 2.7 *Docking score for the top scoring docked pose for TAAR1 agonists (**18, 24, 59, 60, 62**) and antagonist EPPTB (**70**) into hTAAR1 cryo-EM structure (PDB: 8W88).*

Ligand	Docking score (kcal/mol)
Ulotaront (**62**)	-7.674
Tryptamine (**24**)	-7.642
Tyramine (**18**)	-6.950
RO5073012 (**59**)	-6.526
(**S**)-4-(2,4-difluorophenyl-3-tritio)-4,5-dihydro-2-oxazolamine (**60**)	-6.796
EPPTB (**70**)	-3.308

The data presented in Figure 2.24 shows the predicted interactions between ligand and hTAAR1 cryo-EM structure (PDB: 8W88). For **18**, **24** and **60** the 6-membered aryl rings are deeply inserted in the binding pocket, with **18** and **24** undergoing further stabilisation via π-π interactions corresponding to the data reported when using the hTAAR1 homology model. Contrastingly, the twisted confirmation yielded in the docked pose of RO5073012 (**59**), has led to additional interactions to be reported. Like in 2.2.2, the compound undergoes π-π stacking with Phe267[6.51], however further π-interactions have occurred between the imidazole ring and the side chains of Trp264[6.48] and Tyr294[7.43]. Furthermore, RO5073012 (**59**) participates in halogen bonding with Val184[ECL2], increasing the stability of the binding pose generated. Despite little overlap occurring between the two docked poses of EPPTB (**70**), the cryo-EM model also

failed to mimic the interactions and positioning reported by Cichero *et al* and Liao *et al* [123, 224].

Again, it is expected this is due to the poor selectivity EPPTB (**70**) has for human TAAR1.
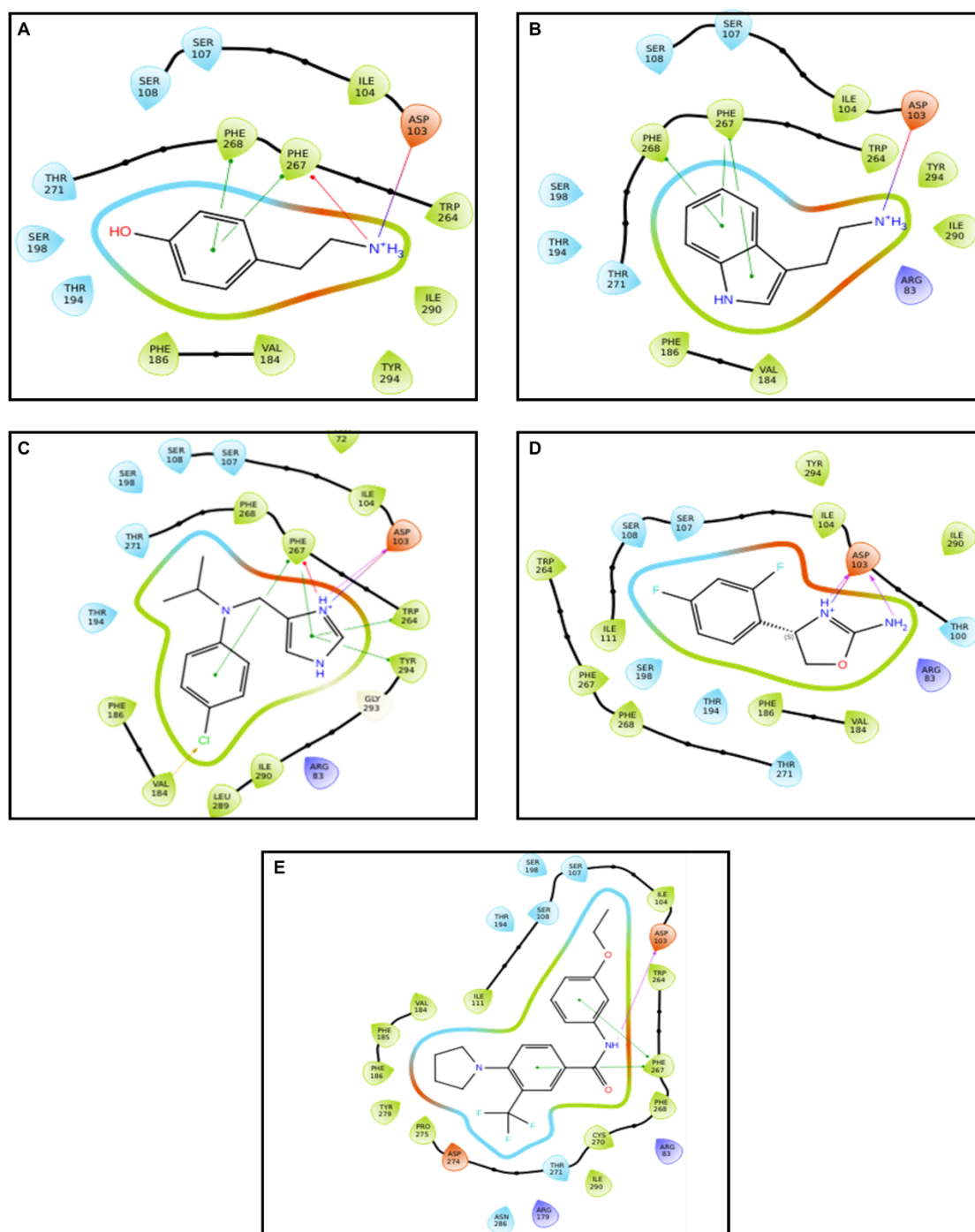
Figure 2.24 *Potential interactions between hTAAR1 cryo-EM structure (PDB: 8W88) and agonists **18 (A), 24 (B), 59 (C), 60 (D)** and antagonist **70 (E)***.

2.4. Conclusion

This chapter has detailed the efforts to generate a high quality hTAAR1 model, with data presented on the development and evaluation of a hTAAR1 homology model, the comparison with a recently published cryo-EM structure (PDB: 8W88) and the molecular docking of TAAR1 agonists (**18**, **24**, **59**, **60**, **62**) and an antagonist (**70**) into both structures.

The docking protocol applied could accurately reproduce the binding pose of ulotaront (**62**) bound to hTAAR1 cryo-EM structure (PDB: 8W88) suggesting that the docking modes generated in the homology model were accurate and reliable. The described homology model (model 17), based on active β_2-adrenoceptors (PDB: 3PDS, 3P0G and 7DHI) as a template, could accurately differentiate between active and decoy compounds described in the literature. In accordance with previous studies, our homology model resulted in an orthosteric binding site similar to other agonist based binding models and adapted an appropriate conformational change. This was proven when antagonist EPPTB (**70**) was docked into the model. To overcome this limitation and prove that our homology model adopted an active conformation, EPPTB (**70**) was docked into mTAAR1 cryo-EM structures (PDB: 8WCC and 8WC3). The purpose was to show the generation of a high docking score, indicating strong interactions with mTAAR1. Unfortunately, the results of this experiment were unclear, and the hypothesis not met. Using an inactive mTAAR1 structure bound to an antagonist would provide clarity on the true binding pose of antagonist EPPTB (**70**), however no such structure is available.

It is unclear with the current limited evidence whether the binding poses described in the cryo-EM structure are more accurate than our homology model. However, given the similarity between the binding regions of the two receptors, evidenced by the RMSD of 0.867, it is easy to visualize that the binding poses are not significantly different. In comparing the two receptors, the main contributor to the differential binding of tyramine (**18**), tryptamine (**24**), RO5073012 (**59**) and (*S*)-4-(2,4-difluorophenyl-3-tritio)-4,5-dihydro-2-oxazolamine (**60**) is through side chain

variations of Ser190$^{5.39}$, Phe185^{ECL2}, Phe186^{ECL2}, Thr194$^{5.42}$, Phe267$^{6.51}$ and Phe267$^{6.52}$. Although the binding mode of TAAR1 ligands slightly differed between the homology model and cryo-EM structure, the results suggest that this had minimal effect due to the small variations within the docking scores obtained. Investigation into the accuracy of binding pose generated by the hTAAR1 homology model and cryo-EM structure (PDB: 8W88) warrants further investigation which will follow in Chapters 3, 4 and 5.

3. Synthesis of RO5073012 (59) and related compounds

The well-documented synthesis of RO5073012 (**59**) along with its high affinity for hTAAR1 and favourable pharmacokinetic profile was used as the rationale for its selection as a lead compound [173]. Using the published synthetic route for RO5073012 (**59**) and similar compounds, it was prudent to synthesise the analogues and evaluate their pharmacological profile in our phenotypic pancreatic β-cells. This generated a benchmark pharmacological profile for lead compounds using our own pharmacological techniques and also allowed evaluation of the general synthetic route.

3.1. Molecular docking

3.1.1. Molecular docking into hTAAR1 homology model 17

As a result of the findings in Chapter 2, RO5073012 (**59**) and its literature analogues (**75a-b** and **76a-c**) [173] were docked into the high quality hTAAR1 homology model, model 17 , as the extensive validation carried out in Chapter 2, showed this model was able to accurately differentiate between active and decoy compounds. The analogues were observed to make a similar pattern of residue interactions as those reported by Borowsky *et al*, with minimal variation displayed between compound positioning within the hTAAR1 binding site (Figure 3.1) [131].
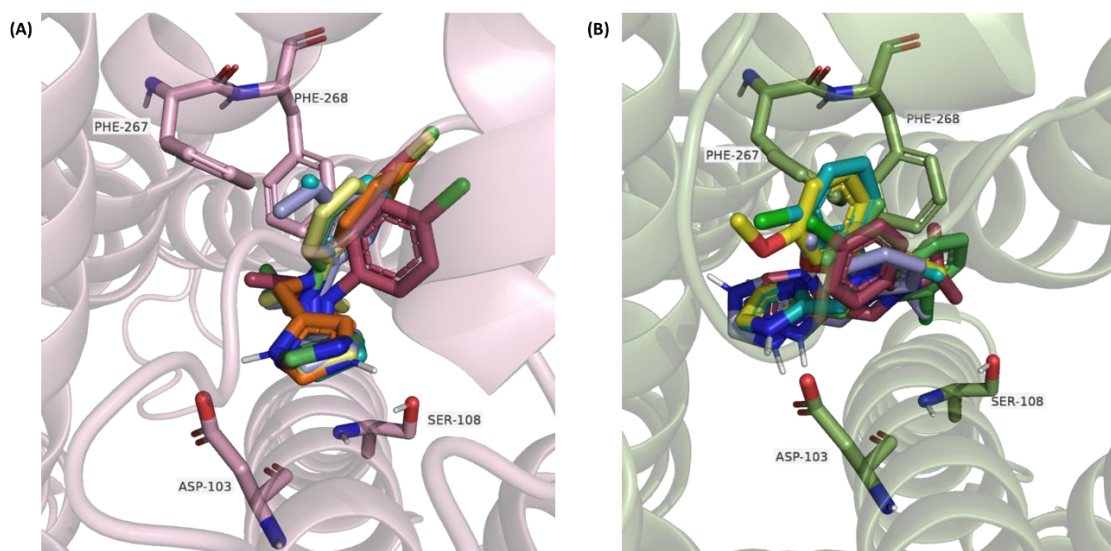
Figure 3.1 Docked poses of RO5073012 (59) and its literature analogues (75a: blue, 75b: green, 76a: yellow, 76b: cyan, 76c: raspberry and 59: orange) into hTAAR1 homology model 17 (A) and cryo-EM structure (PDB: 8W88) (B). Image visualised down transmembrane (TM) 3. Docking performed using Schrödinger's Maestro and Glide 12.6 packages and images created using PyMOL 4.6.0.

Shown in Figure 3.1 A, the docked pose of **76b** possesses a twisted phenyl ring, differing from compounds **59**, **75a-b**, **76a** and **76c**. Ligand interactions with TAAR1 homology model 17 are shown in Figure 3.2, where slight differences between compound positioning and predicted interactions are observed. For all compounds, the imidazole moiety is expected to be in the protonated form with predicted hydrogen bond lengths between compound **75b** and **76b** and Asp103[3.32] varying between 1.76-2.81 Å, slightly shorter than the optimal range (2.7–3.3 Å), Figure 3.2 [221]. As both compounds are further stabilised by π-π and π-cation interactions with Phe185[ECL2] and Phe267[6.51], it is hypothesised the differences in docking score must be due to the amino acids surrounding the chloro-substituent. The twisted pose obtained by **76b**, facilitates the substituted phenyl entering a hydrophobic pocket, suggesting **76b** has a higher affinity for hTAAR1 compared to **75b** due to the more favourable interactions made and the higher docking score obtained, Table 3.1. As for **75b**, a slightly lower docking score is reported for **76c** (-5.754 kcal/mol). This is due to the imidazole ring being angled away from Asp103[3.32] resulting in the formation of an elongated salt bridge.
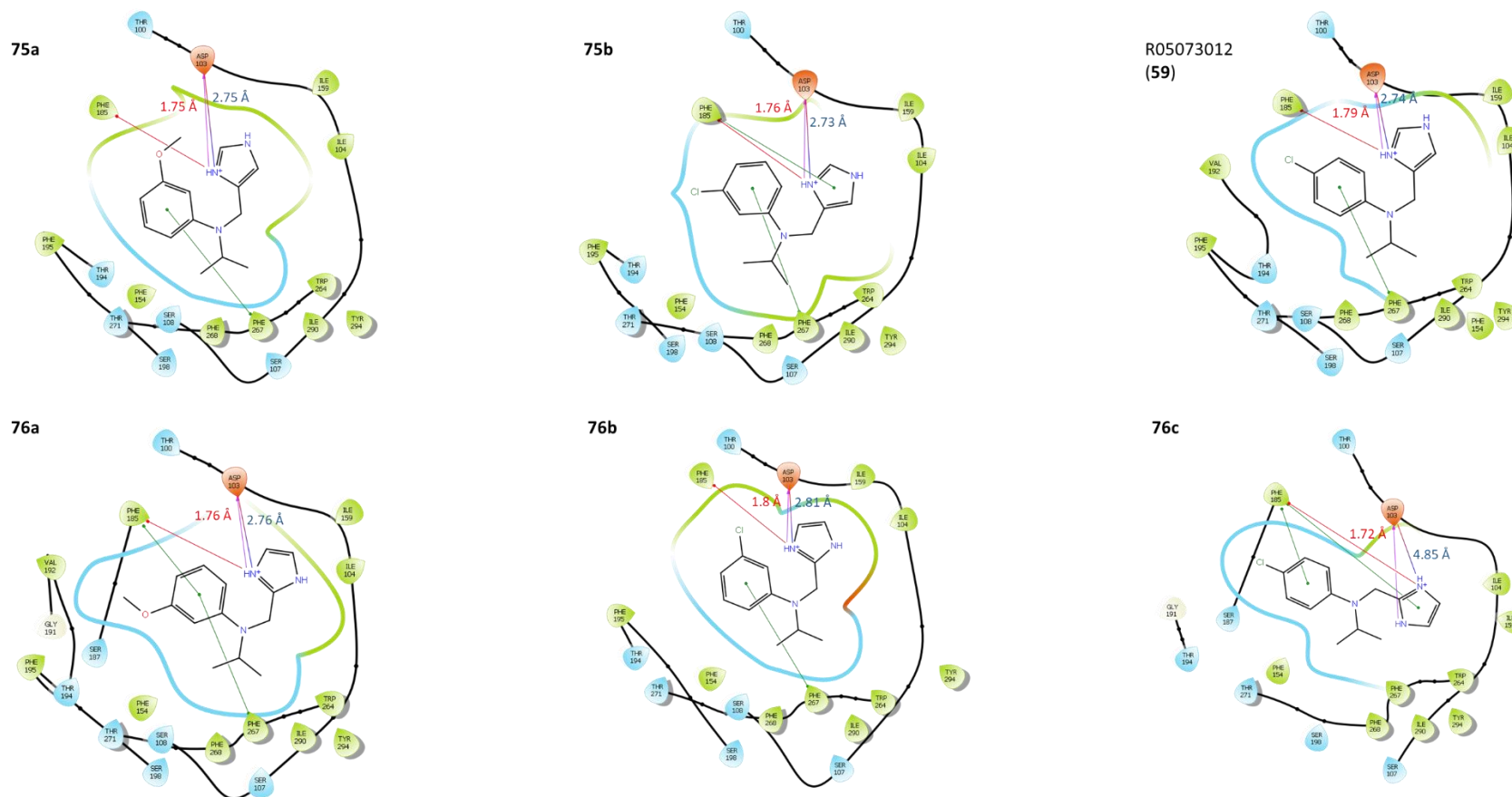
Figure 3.2 *Predicted interactions between hTAAR1 homology model 17 with RO5073012 (**59**) and other closely related SAR compounds (**75a-b** and **76a-c**). Hydrogen bond length measurements shown in red. Expected length of salt bridges shown in blue. Amino acid description: Green; hydrophobic and cyan; polar.*

Table 3.1 *Docking scores for RO5073012 (**59**) and closely related compounds (**75a-b** and **76a-c**) in complex with hTAAR1 homology model 17 and hTAAR1 cryo-EM structure (PDB: 8W88).*
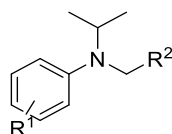
Compound	R^1	R^2	Docking score (kcal/mol)	
			hTAAR1 homology model 17	hTAAR1 Cryo-EM structure (PDB: 8W88)
RO5073012 (**59**)	*p*-Cl	4-imidazolyl	-6.046	-6.526
75a	*m*-OMe	4-imidazolyl	-6.614	-5.146
75b	*m*-Cl	4-imidazolyl	-5.602	-7.202
76a	*m*-OMe	2-imidazolyl	-6.414	-6.316
76b	*m*-Cl	2-imidazolyl	-6.299	-5.971
76c	*p*-Cl	2-imidazolyl	-5.754	-6.892

3.1.2. Comparison between molecular docking into hTAAR1 homology model 17 and the hTAAR1 cryo-EM structure (PDB: 8W88)

To confirm the docked poses generated using the validated homology model, the compound library was docked into the cryo-EM structure (PDB: 8W88) [222]. As for the homology model, all 6 compounds (**59**, **75a-b** and **76a-c**) adopted a similar binding pose within the pocket, however variation between compound alignment was displayed (Figure 3.1 B). Ligand interactions with the hTAAR1 cryo-EM structure (PDB: 8W88) are shown in Figure 3.3 and on comparison with the docked poses obtained in model 17 (Figure 3.1), differences between the positioning of the substituted aniline can be observed. This is due to the aniline moiety being oriented towards TM6 in the cryo-EM structure (PDB: 8W88). The predicted hydrogen bond lengths between all

compounds and Asp103$^{3.32}$ varied between 1.67 − 2.09 Å, with slightly longer salt bridges expected, Figure 3.3.

Additional stabilisation of compounds within the cryo-EM structure's binding site is reported via π-π and π-cation interactions with Trp264$^{6.48}$, Phe267$^{6.51}$, Phe268$^{6.52}$ and Tyr294$^{7.43}$, with RO5073012 (**59**) undergoing further stabilisation via halogen bonding with Val184^{ECL2}, whilst **76a** forms an additional hydrogen bond with Ile290$^{7.39}$. Although more interactions are predicted between the cryo-EM structure and the literature analogues compared with the homology model, generally the interactions are similar. Furthermore, minimal variation is observed between the docking scores reported for the cryo-EM structure and that of the homology model (Table 3.1). This data, combined with the ligand interactions reported, suggests the homology model generated is an accurate representation of hTAAR1 in its active state, correlating with the findings reported in Chapter 2.
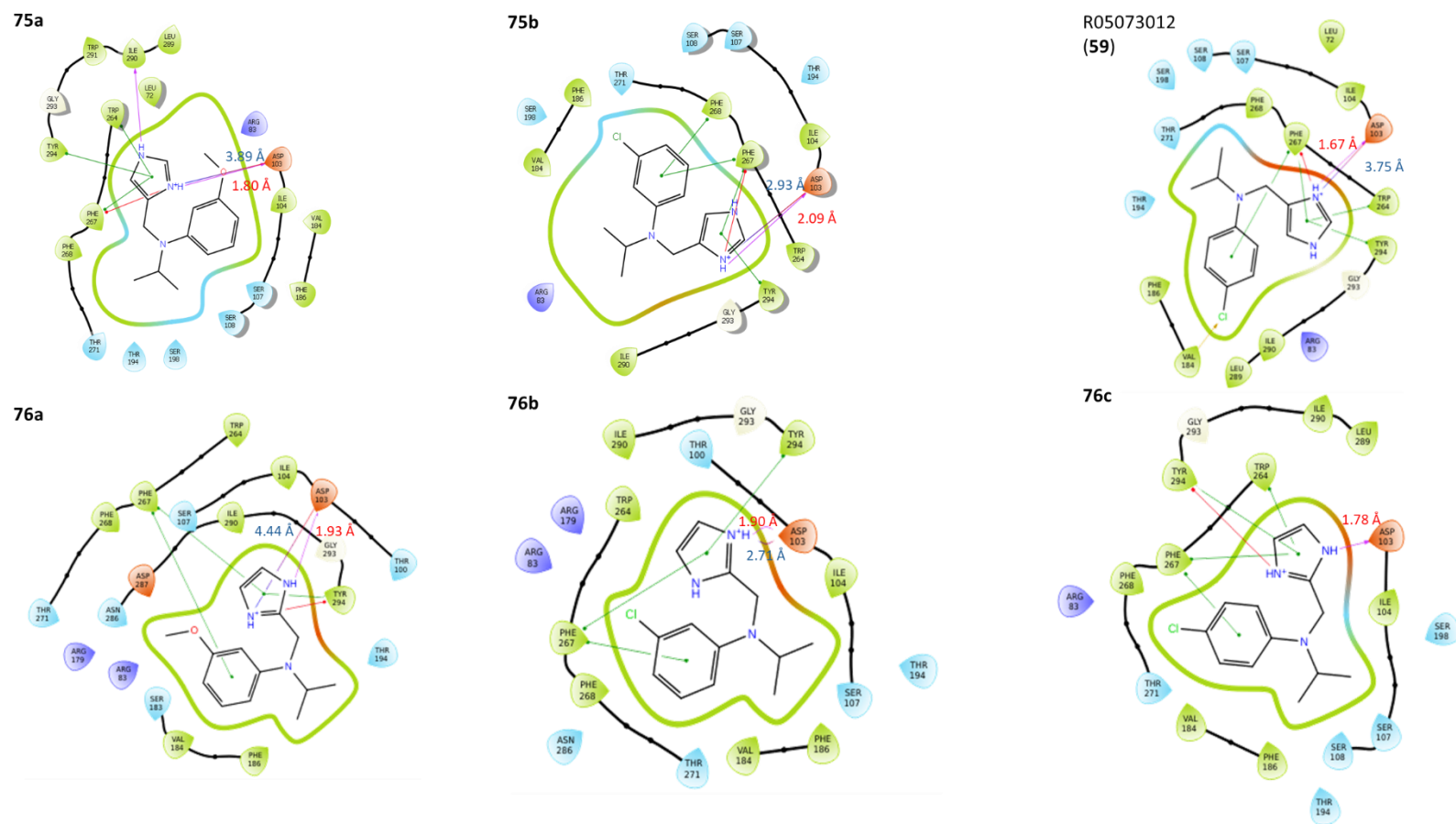
Figure 3.3 *Predicted interactions between hTAAR1 cryo-EM structure (PDB: 8W88) with RO5073012 (59) and other closely related SAR compounds (75a, 75b and 76a-c). Hydrogen bond length measurements shown in red. Expected length of salt bridges shown in blue. Amino acid description: Green; hydrophobic and cyan; polar.*

3.2. Synthetic route employed

Compounds **77a-c** were obtained according to the approach described in Scheme 3.1. Reductive amination using 4-imidazolecarboxaldehyde (**78**) resulted in greater yields, with **77c** displaying a 100 % yield increase compared to the 2-imidazolyl analogue. Although the low yield obtained for **79c** (Table 3.2) correlates with that reported by Yi *et al*, it differs from other sources which report negligible differences between the positional isomers [173, 226-228].

Scheme 3.1 Synthesis of RO5073012 (**59**) and closely related compounds **75a-b, 76a-c** by reductive amination.
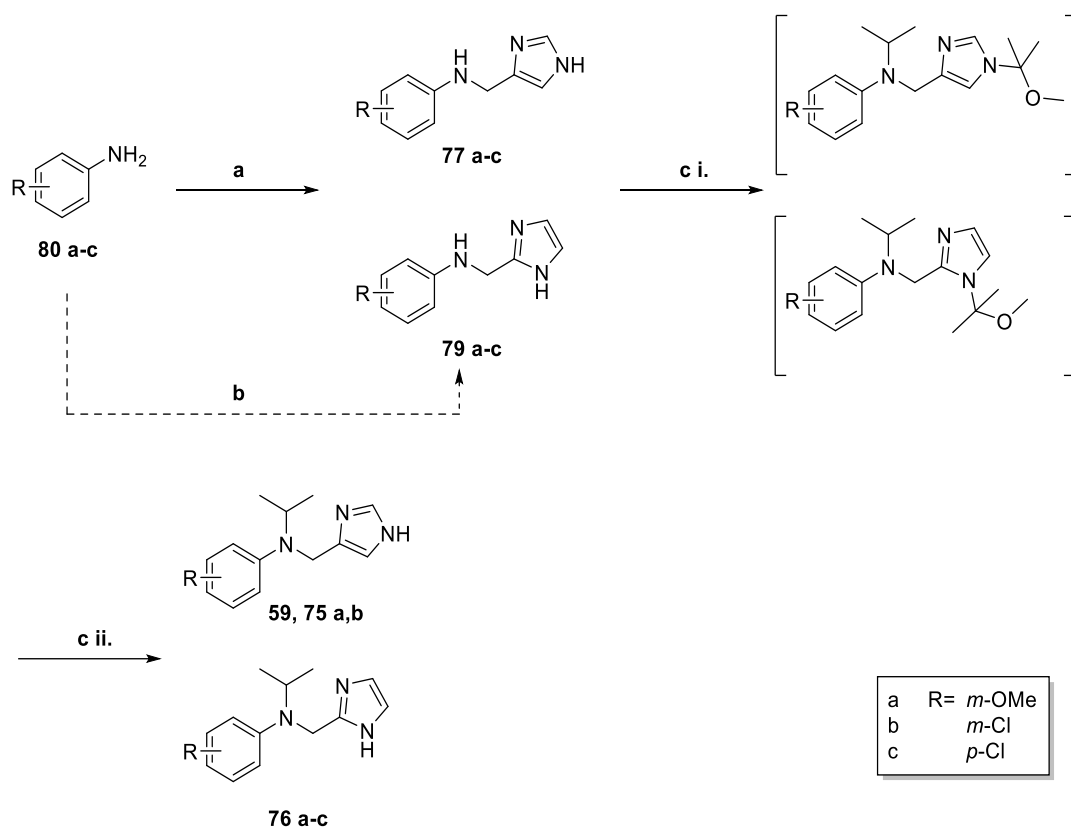
Reagents and conditions: (a) i. 78 or **81**, CeCl₃.7H₂O, EtOH, rt, 0.3-1 hr. **ii.** NaBH₄, rt, 2-18 hr (32-70%). **(b) i.** MeOH, 60°C, 18 hr. **ii.** NaBH₄, rt, 1.5 hr (30-41%). **(c) i.** 2-methoxypropene, trifluoroacetic acid (TFA), NaBH(OAc)₃, 1,2-dichloroethane (1,2-DCE), 60°C, 18 hr. **ii.** 1M HCl, 60°C, 1 hr (2-45%).

Initial reductive amination of 3-chloroaniline (**80b**) or 4-chloroaniline (**80c**) with 2-imidazolecarboxaldehyde (**81**) was found not to process to completion, with unreacted starting material observed by liquid chromatography-mass spectrometry (LC-MS) analysis (Scheme 3.1).

Zhu *et al* found that the addition of a Lewis acid catalyst increased the rate of imine formation whilst investigating reductive amination of aryl aldehydes with substituted anilines using sodium borohydride [229]. Unfortunately, using the method indicated by Zhu *et al*, the yields obtained for **79b-c** did not greatly improve, Table 3.2 [229]. Despite the minimal changes in yield obtained, the optimised method by Zhu *et al*, resulted in fewer impurities, thus a more simplistic purification was required. During purification via flash column chromatography, changing the mobile phase from containing MeOH to a solution of 1M NH_3 in MeOH further improved the yields; the presence of ammonia decreased the silica's acidity, thus leading to better sensitivity and separation as the affinity for the stationary phase decreased [230, 231].

Table 3.2 Effects of Lewis acid catalysts $CeCl_3.7H_2O$.

	Solvent	Yield (%)	
		Absence of $CeCl_3.7H_2O$	Presence of $CeCl_3.7H_2O$
79b	Methanol	38	-
	Ethanol	-	45
79c	Methanol	30	-
	Ethanol	-	32

Unlike the chloro-substituents of **79b-c**, **79a** contains a methoxy-substituent. The presence of the methoxy group, gives compound **79a** electron donating properties by the mesomeric effect, thus making 3-methoxyaniline (**80a**) a better nucleophile when compared to **80b-c**. Therefore, a moderate yield (41%) was achieved without the need of a Lewis acid catalyst [232].

Reaction of 2-methoxypropene with **77a-c** or **79a-c** afforded the tertiary amines **59**, **75a-b** and **76a-c**. Initially, the reaction mixture was neutralised with 1M $NaOH_{(aq)}$ before extraction with

EtOAc, however it was found at pH 7, the compounds remained in their ionised form. Increasing to pH 14, resulted in the uncharged form of the molecule thus leading to a higher crude obtained of the reactions (Scheme 3.1).

Selective deprotection of the 2-methoxypropan-2-yl moiety with 1M HCl was achieved utilising the resonance forms of the imidazole ring. Once the reaction had gone to completion, it was quenched with 1M NaOH$_{(aq)}$. Like the prior step, increasing to pH 14 led to higher yields obtained due to the lack of charge present on the molecule.

3.3. Pharmacological evaluation of compounds (59, 75a-b and 76a-c) in pancreatic rat insulinoma cell line, INS-1.

The Islets of Langerhans located within the pancreas are comprised of glucagon-releasing α-cells, insulin-releasing β-cells, somatostatin-releasing δ-cells and F / γ-cells[44-46]. Derived from a rat insulinoma induced by X-ray irradiation, Asfari *et al* produced the insulinoma cell line (INS-1) [233]. Despite the requirement of β-mercaptoethanol within the culture media to maintain their functional characteristics and proliferation, key features of INS-1 cells include their responsiveness to glucose within physiological range and high insulin content, thus making them a suitable cell line for this study [233-235].

Pancreatic β-cell dysfunction is often caused by prolonged exposure to excess glucose (hyperglycaemia) or fatty acids (hyperlipidaemia), resulting in impaired β-cell function including gene expression and ultimately glucose-induced insulin secretion [236, 237]. Several attempts have been made to identify the mechanisms underpinning this phenomenon known as glucolipotoxicity (GLT), however they remain partially understood. Sako and Grill and Elks [238-240] show high concentrations of free fatty acids damage β-cell function, whilst Roche *et al* show INS-1 cells exposed to glucose exhibit sustained synthesis of essential intermediates such as citrate and malate required in the Krebs cycle [241]. Additionally, further sources show hyperglycaemia-induced oxidative stress hindering β-cell survival [242-244].

To mimic the mechanisms of chronic exposure to high glucose and fatty acids in altering the function of various cell types, the Turner group, Nottingham Trent University, UK, developed an experimental media (GLT media) containing 28 mM glucose, 200 μM palmitic acid, 200 μM oleic acid and 2% bovine serum albumin (BSA) [245]. The use of specific fatty acids palmitic acid and oleic acid were selected as these are identified as the most abundant free fatty acids in humans [246].

The toxicity of **59, 75a-b** and **76a-c** was determined using calcein acetoxymethyl ester (calcein AM) cell viability dye using the INS-1 cell line. Calcein AM is a non-fluorescent dye which identifies living cells due to its ability to permeate the cell membrane. After cell penetration, calcein AM is converted to calcein, a strong fluorescing compound via acetoxymethyl ester hydrolysis (Figure 3.4). As all live and intact cells contain the esterase required to undergo the hydrolysis reaction, the use of calcein AM to determine cell viability / number is an accepted model [247, 248].
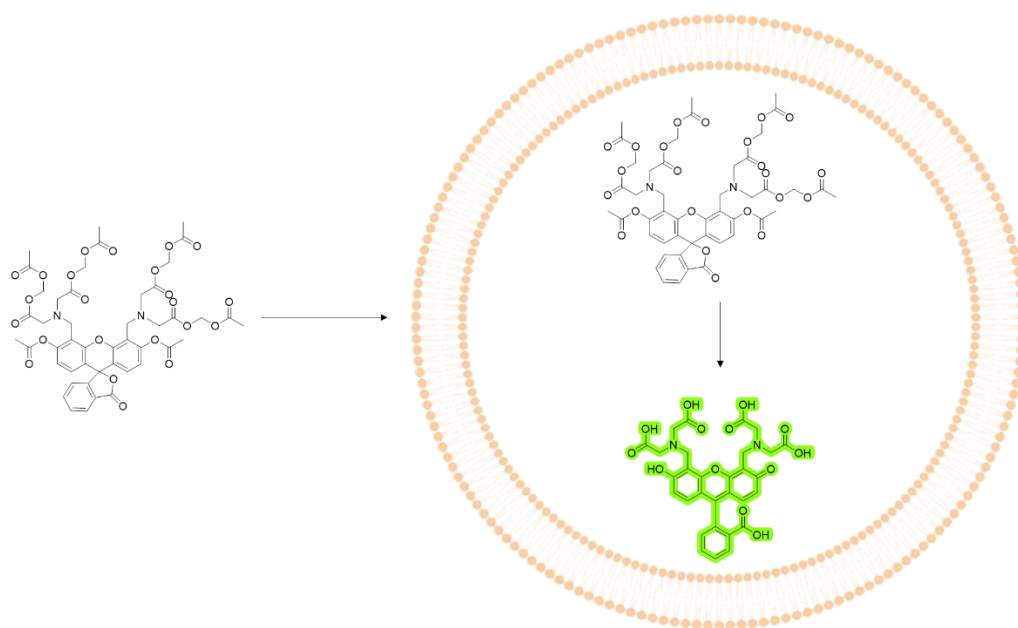
Figure 3.4 *Principle of calcein AM cell viability assays. Upon entering the cell, calcein AM is hydrolysed into calcein, a highly fluorescent compound.*

Initially the assay was completed following a modified protocol published by Abcam [247]. Cells were cultured in standard or GLT media in either the presence or absence of test compound (**59**, **75a-b** and **76a-c**) for 5 days. After cell treatment and preparation, cells were incubated at 37°C in freshly prepared calcein AM solution (1 calcein AM : 500 dilution buffer) for 30 minutes. Following incubation, spent calcein AM solution was removed and replaced with cell lysis buffer. Lysates were prepared and stored on ice before being transferred into a 96-well plate and fluorescence measured at excitation / emission (Ex/Em) = 485/530 nm (Figure 3.5).

(A) Prepare cells

⇩

Prepare Calcein AM solution
(1 Calcein AM : 500 dilution buffer)

⇩

Add prepared Calcein AM solution
to each well

⇩

Incubate at 37°C for 30 minutes

⇩

Prepare cell lysates, transfer to 96
well plate

⇩

Read fluorescence
(Ex/Em = 485/530 nm)

(B) Prepare cells

⇩

Prepare Calcein AM solution
(1 Calcein AM : 500 dilution buffer)

⇩

Add prepared Calcein AM solution
to each well

⇩

Incubate at 37°C for 60 minutes

⇩

Wash cells with Krebs-ringer buffer
and prepare cell lysates, transfer to
96 well plate

⇩

Read fluorescence
(Ex/Em = 490/520 nm)

*Figure 3.5 Calcein AM assay protocol flow charts. **(A)** Adapted from Abcam [247], **(B)** adapted from Cripps et al [249].*

The protocol published by Abcam (Figure 3.5 A) failed to generate reliable and consistent data. This is due to the cells treated with GLT media control showing significant differences with respect to the non-GLT control, thus differing from the literature. Therefore, the method published by Cripps *et al* was adapted and used instead following the 5-day treatment period, Figure 3.5 B [249]. Correlating with Cripps *et al*, INS-1 cells treated with GLT media for 5 days

showed a small and non-statistically significant increase in viability, demonstrating the assay conditions were viable (Figure 3.6).

Cellular toxicity of compounds was determined at both 0.1 µM and 1 µM concentrations (Figure 3.6). Across both concentrations, compounds **59**, **76a**, **77a** and **77c** were found to be non-toxic to the treated INS-1 cells in both control and GLT conditions, evidenced by the lack of statistically significant difference obtained from one-way analysis of variance (ANOVA) analysis. At 0.1 µM, statistical differences were reported for **75b** (p = 0.003) in GLT conditions, however these differences do not indicate cytotoxicity due to the rise in cell viability. It is hypothesised the reported significant difference observed in Figure 3.6 is in response to an increase in cell proliferation. To confirm this hypothesis, further experimentation is required; the cell viability assays need to be repeated and normalised to total cellular protein content, obtained from completing a Pierce bicinchoninic acid (BCA) protein assay [250, 251]. Unfortunately, time constraints and limited funding prevented completion of these experiments, thus the hypothesis was not confirmed. As these findings were not seen at the higher concentration, **75b** underwent further analysis. **76b** was shown to be cytotoxic due to the statistically significance reported at both concentrations (0.1 µM p = 0.0045 and 1 µM p = 0.022), thus was excluded from further analysis.
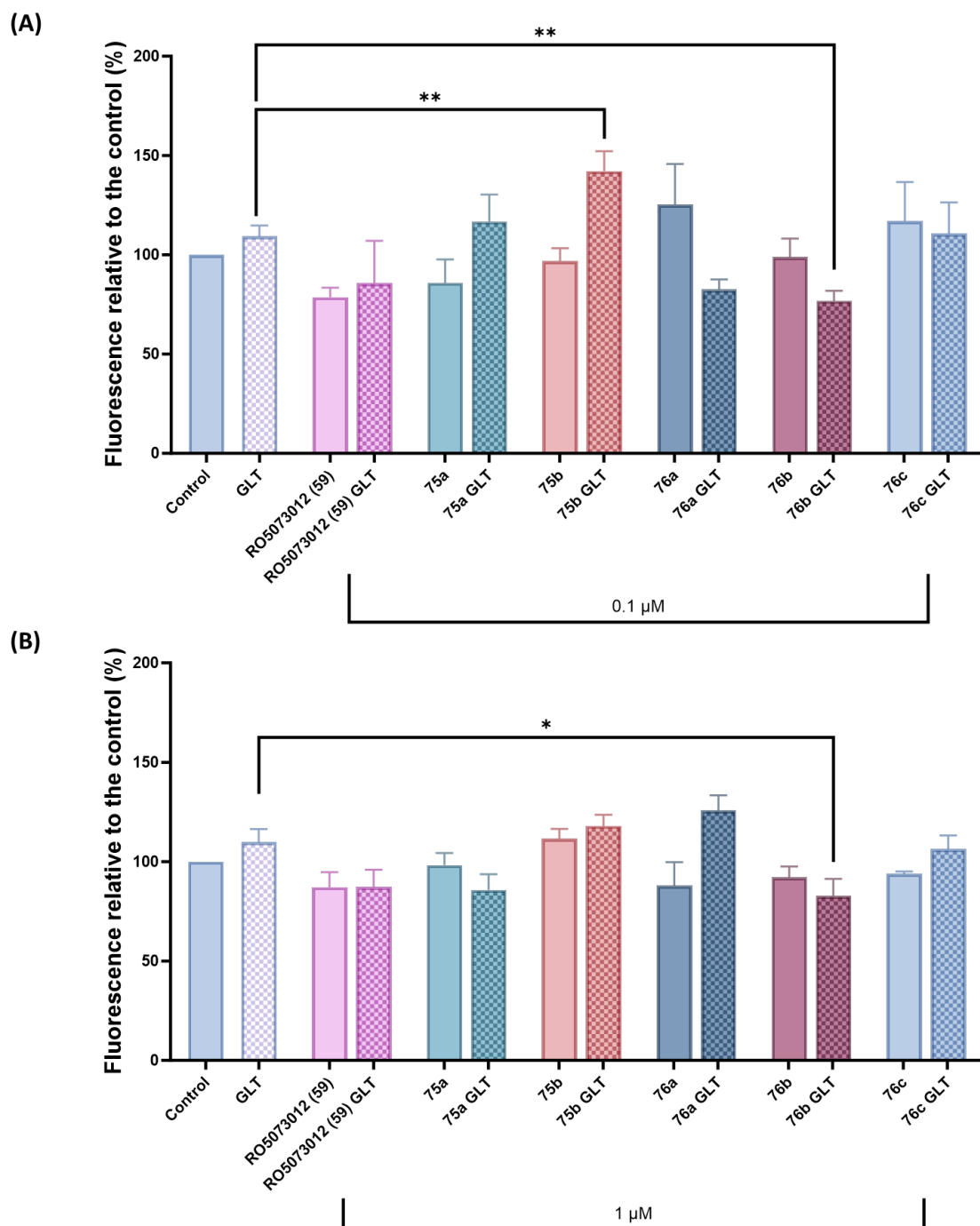
Figure 3.6 *Cell toxicity of RO5073012 (**59**) and literature analogues (**75a**, **75b** and **76a-c**). Cell viability detected via fluorescence with Ex/Em 490/520 nm and expressed as % change compared to control from 4 or more independent experiments ± SEM. Checked fill represents GLT conditions. Toxicity was determined for each compound at (**A**) 0.1μM (p(**75b**) = 0.003, p(**76b**) = 0.0045) and (**B**) 1 μM (p(**76b**) = 0.022). Asterisk denotation: * p<0.05, ** p<0.01, *** p<0.001.*

To investigate whether compounds **59**, **75a**, **75b**, **76a** and **76c** can enhance insulin secretion, insulin secretion was quantified between control and GLT conditions using a high range rat insulin enzyme-linked immunosorbent assay (ELISA) (Mercodia) and normalised to protein content following the methods reported by Cripps *et al* and the manufacturer's protocol [249, 252].

Many substances including amino acids, fatty acids and glucose are known to stimulate pancreatic β-cells to secrete insulin; phorbol 12-myristate 13-acetate (PMA) activates protein kinase C (PKC) to induce a glucose independent increase in insulin secretion (Figure 3.7 A), whilst 3-isobutyl-1-methylxanthine (IBMX), a phosphodiesterase inhibitor, increases cAMP levels thus leading to a rise in insulin release (Figure 3.7 B) [253-256]. Additionally, glucose-induced insulin secretion is controlled by amino acids (Figure 3.7 C) [257-259]. Therefore, to ensure the ELISA was an appropriate assay to determine insulin secretion, a secretagogue cocktail composed of these substances was used to validate the assay [260].
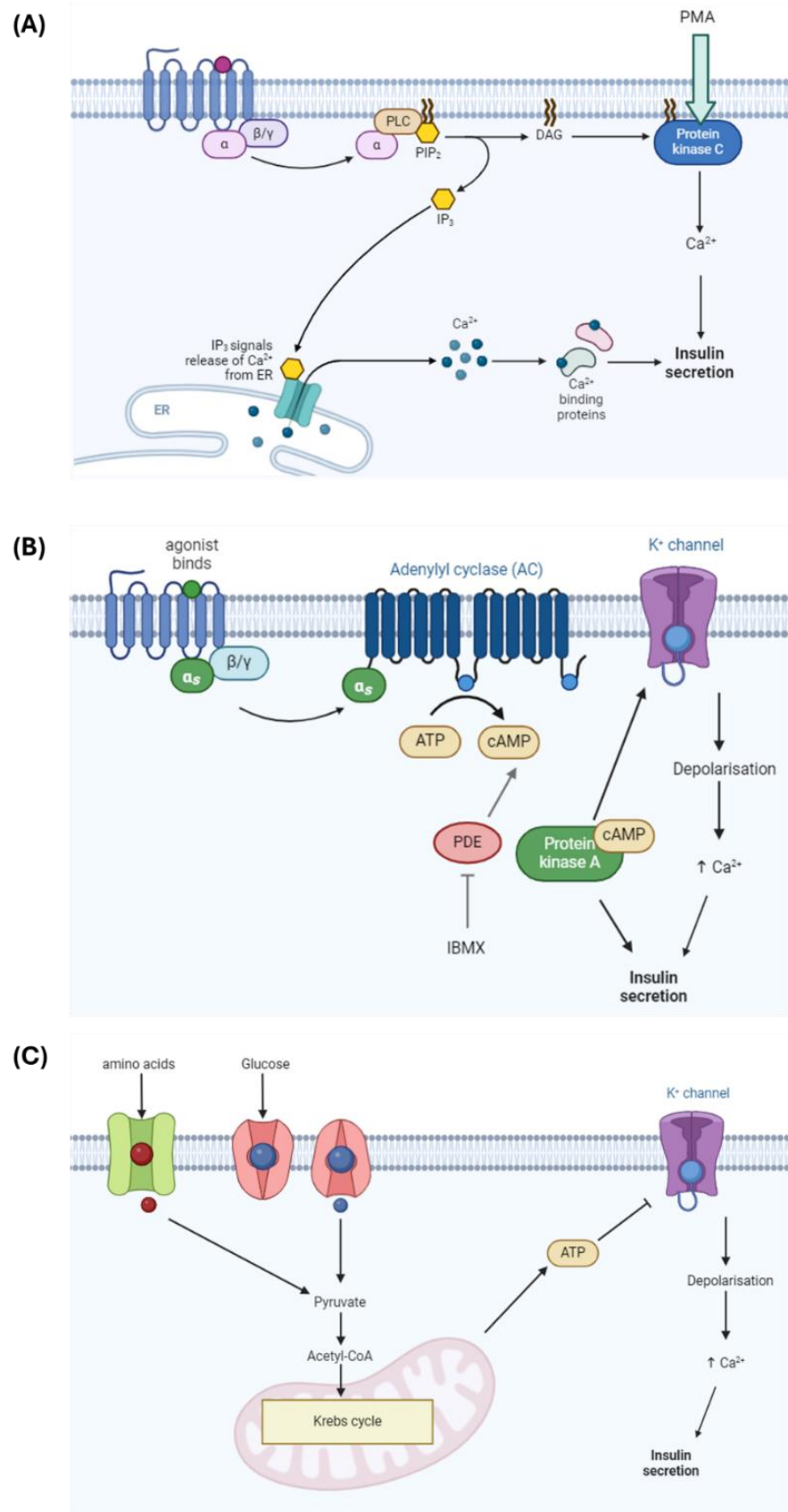
Figure 3.7 *Signalling pathway of **(A)** phorbol 12-myristate 13-acetate (PMA), **(B)** 3-isobutyl-1-methylxanthine (IBMX)*

*and **(C)** amino acids leading to insulin secretion in pancreatic β-cells. Image adapted and created using Biorender.com.*

Further confirmation of the results obtained was achieved through the testing of endogenous agonist tyramine (**18**) and antagonist EPPTB (**70**). Consistent with Cripps *et al*, tyramine significantly enhanced insulin secretion whilst EPPTB significantly suppressed insulin secretion (Figure 3.8), indicating the assay protocol provided a window to accurately determine the effects of **59**, **75a**, **75b**, **76a** and **76c**. As shown in Figure 3.8 A, a positive trend was observed for compounds **76a** and **76c**, suggesting they enhance insulin secretion in non-GLT conditions, but further experimental repeats are required to confirm this trend. This positive trend is further confirmed in GLT conditions as both compounds show statistically significant differences towards enhancing insulin secretion (Figure 3.8 B). Compound **59** also statistically enhances insulin secretion in GLT conditions. Statistically significant differences were reported for **76a** in both non-GLT and GLT conditions. Despite exhibiting enhanced insulin secretion in GLT conditions, **75a** supressed insulin secretion in non-GLT conditions. To prevent potential hypoglycaemia in the absence of metabolic stress occurring in a clinical environment, **75a** did not undergo any further analysis.
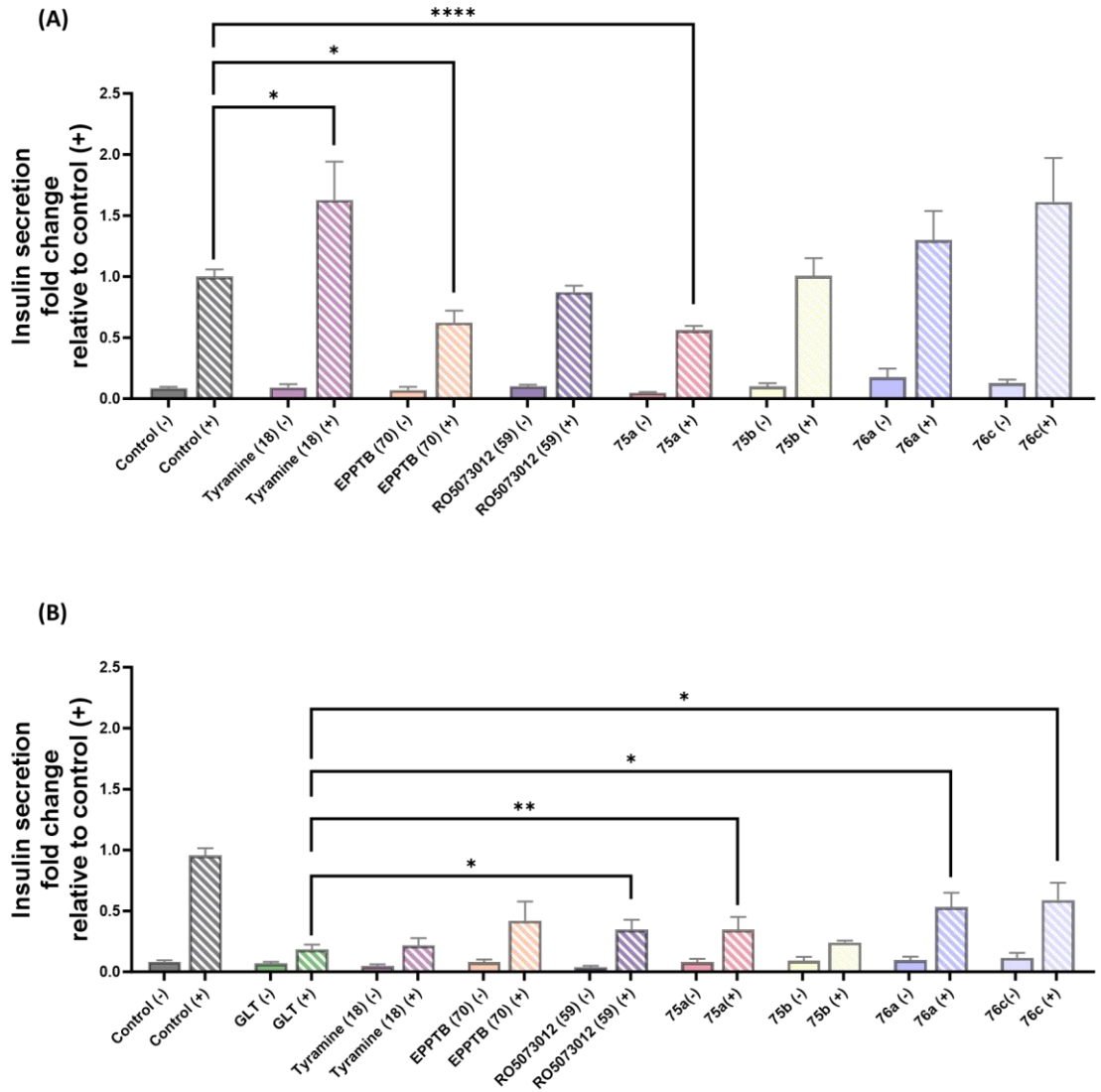
Figure 3.8 *Changes in insulin secretion resulting from 5-day treatment with tyramine (**18**), RO5073012 (**59**), **75a**, **75b**, **76a** and **76c** at a final concentration of 1μM or the inverse agonist EPPTB (**70**) at a concentration of 10 nM. Insulin secretion was determined by ELISA following incubation ± secretagogue cocktail (13.5 mM glucose, 1μM phorbol 12-myristate 13-acetate, 1mM isobutyl-methylxanthine, 1 mM tolbutamide, 10 mM leucine, 10 mM glutamine) for 2 hrs and detected via absorbance at 450 nm and normalised to cellular protein content relative to secretagogue-stimulated control from 3 or more independent experiments. Dashed fill represents secretagogue-stimulated conditions. Comparisons between compounds and the controls used unpaired t-tests. **(A)** control (p(tyramine (**18**)) = 0.0119, p(EPPTB (**70**)) = 0.0473, p(**75a**) <0.0001), **(B)** GLT (p(**59**) = 0.0149, p(**75a**) = 0.0053, p(**76a**) = 0.0493, p(**76c**) = 0.0242. Asterisk denotation: * p<0.05, ** p<0.01, **** p<0.0001.*

3.4. Investigation of blood brain barrier permeability

Given that the development of previously reported hTAAR1 agonists were aimed at treating schizophrenia and thus have been shown to exert effects in the CNS, it is critical to investigate pharmacokinetic parameters. This is to ensure the compounds designed in this project avoid on-target central effects such as hallucinations. Formed of endothelial cells, capillary basement membranes, astrocyte end-feet and pericytes, the BBB is a selective semi-permeable membrane, Figure 3.9. Its purpose is to regulate ion and small molecule movement between the periphery and the CNS in order to protect the brain [261, 262].
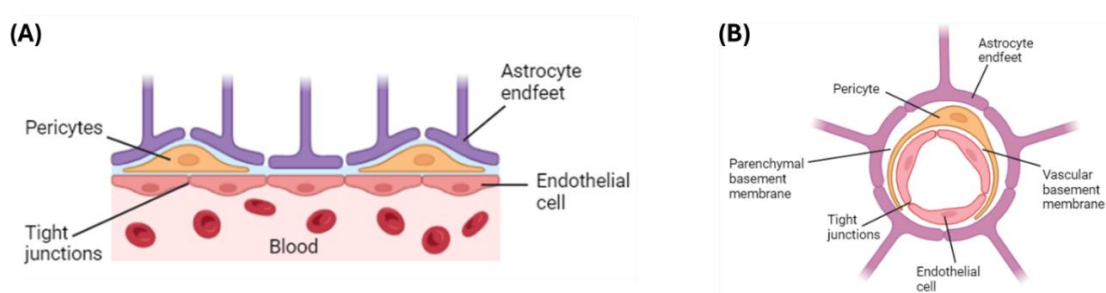
Figure 3.9 (A) *Anatomical structure of the blood brain barrier including its components. (B) Cross section of the blood brain barrier. Image adapted and created using Biorender.com.*

The BBB score is a computational prediction, developed by Gupta *et al*, to determine the likelihood of compounds penetrating the BBB [263]. The test assesses physico-chemical properties of the compounds including number of hydrogen bond acceptor / donors, polar surface area (PSA), pKa, number of aromatic rings and number of heavy atoms present. The scoring classification shows compounds with a score <4 are unlikely to penetrate the BBB whilst those between 4-6 penetrate the barrier and subsequently can be classified as CNS drugs [263]. Additionally, Egan *et al* developed a set of rules which utilise the compound's partition co-efficient (log P), PSA, polarity and lipophilicity of a molecule to characterise its absorption. Upon validation of this computerised model, the model coined the name 'BOILED-Egg' due to the shape of the region most populated by well absorbed molecules [264]. Using the model, it is

suggested compounds which lie within the 'yolk' are likely to be brain-penetrant drugs whereas those that remain in the 'white' are expected to have high gastrointestinal absorption [264].

Other methods of predicting BBB penetration use the log P and the distribution co-efficient (log $D_{7.4}$). Compounds with a log $D_{7.4}$ 0-3 and a log P between 1.5-2.7 are predicted to have good BBB permeation [265]. Although log P and log $D_{7.4}$ are widely recognised methods for determining the lipophilicity of a drug molecule, several limitations are associated with them. Experimental log P and log $D_{7.4}$ are calculated through the addition of a drug-like molecule into a mixture of octan-1-ol in water, shaking the solution until equilibrium is reached and measuring the concentration of the drug in both phases [266]. Unfortunately, octan-1-ol and water are not fully immiscible with one another, and often small octanol droplets remain suspended in the aqueous layer [267]. In turn, this leads to an overestimation of the drug concentration within the aqueous layer and subsequently results in a reduced log P or log $D_{7.4}$ value to be obtained. Furthermore, using octan-1-ol to represent the lipophilic phase does not account for any interactions which may form between a polar compound and the cell membrane [267].

Due to these limitations, indirect methods have been developed to estimate the lipophilicity of drug-like compounds. Reversed-phase high-performance liquid chromatography (RP-HPLC) is recognised as a method used to determine lipophilicity parameters of a drug-like molecule [268]. Often the stationary phase used is a commercially available C8 or C18 silica column (Figure 3.10), thus is not representative of the cell membrane.

C8   **C18**
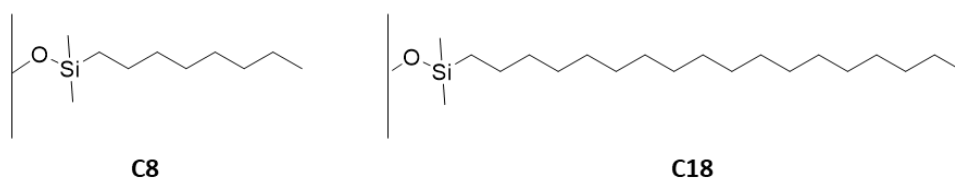
Figure 3.10 *C8 (octyl) and C18 (octadecyl) silica-based stationary phases.*

Developed and patented by Pidgeon and Venkataran, immobilised artificial membrane (IAM) columns are designed to mimic biological systems. Manufactured by Regis Technologies Inc, IAM columns contain phosphatidylcholine head groups which are covalently bonded via the aliphatic moiety to silica particles located on the column surface (Figure 3.11), whilst the polar choline group is angled towards the mobile phase, thus providing a system which replicates the lipid environment of a fluid cell membrane [269]. To further mimic physiological cell conditions, the mobile phase is adjusted to pH 7.4.
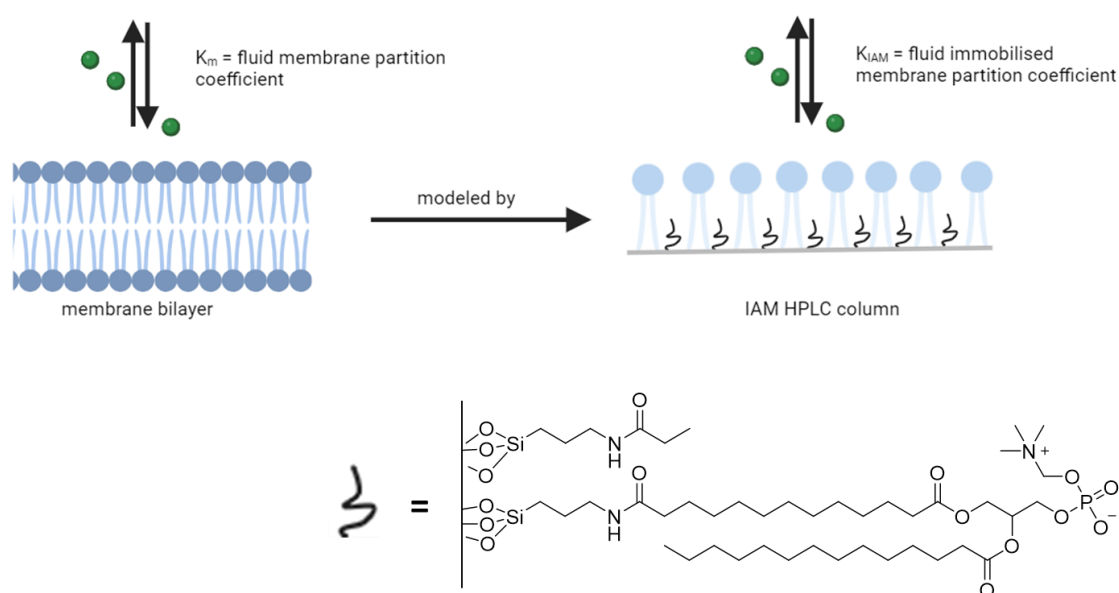
Figure 3.11 *Pictorial representation of IAM HPLC column. Image created using Biorender.com.*

Although designed to mimic a biological environment, current IAM columns are not true representative models of the cell membrane as they do not contain all essential key features such as carbohydrates, glycoproteins, transporters and cholesterol which are often present within eukaryotic membranes. Efforts into developing IAM columns containing cholesterol are underway but further work is required to produce IAM columns which contain all the key features stated above [270].

Using IAM columns, the partition parameters of a drug-like compound, including BBB permeability, can be determined experimentally [270]. The affinity a compound has for the phospholipids (partition co-efficient, K_{IAM}), is directly proportional to the retention factor (k_{IAM}) obtained on the IAM stationary phase. It is determined from the retention time (R_t) using Equation 1 and Equation 2 [271].

Equation 1 *Partition coefficient (K_{IAM}) is proportional to the retention factor (k_{IAM}).*

$$log k_{IAM} = log K_{IAM} + log\left(\frac{Vs}{Vm}\right)$$

Where Vs/Vm is the volume ratio of the stationary and mobile phases respectively and k_{IAM} is retention factor obtained from R_t and the dead time (t_0) according to Equation 2.

Equation 2 *Calculation to determine k_{IAM} from retention time and dead time.*

$$k_{IAM} = \frac{(R_t - t_0)}{t_0}$$

The Chromatographic Hydrophobicity Index (CHI_{IAM}) is a hydrophobicity parameter proposed by Valkó *et al* and is the acetonitrile concentration (expressed as %) showing equal distribution of the compound in the mobile and stationary phase when k_{IAM} = 1. Chromatographic determination of phospholipid-binding is based on measuring gradient retention times and can be calibrated using CHI_{IAM} values [272].

Galley *et al* designed RO5073012 (**59**) as a hTAAR1 agonist to treat schizophrenia and reported good CNS penetration via brain/plasma ratios, therefore it is expected the literature analogues will also penetrate the BBB. This hypothesis was confirmed via the BOILED-Egg model using Swiss-ADME as well as the data shown in Table 3.3 [273].

The CHI_{IAM} values for compounds **59**, **75b**, **76a** and **76c** are shown in Table 3.3. As a higher concentration of acetonitrile is required to elute **59**, **75b**, **76a** and **76c** from the IAM stationary phase, it suggests these compounds are likely to cross the BBB correlating with Galley *et al* and the data shown in Table 3.3 [274].

*Table 3.3 Drug likeliness of RO5073012 (**59**) and its literature analogues (**75b**, **76a**, **76c**). Values in green indicate compliance with Lipinski's rule of 5 and Veber rules [275, 276]. MW; molecular weight (g mol^{-1}), nHBA; number of hydrogen bond acceptors, nHBD; number of hydrogen bond donors, Log P; partition co-efficient, Log $D_{7.4}$; distribution co-efficient, BBB score; blood brain barrier score, R_t; average retention time. All predicted data (ϕ) obtained from SwissADME [273].*

Compound	MW	nHBA$^\phi$	nHBD$^\phi$	Log P$^\phi$	Log $D_{7.4}{}^\phi$	BBB score$^\phi$	CHI$_{IAM}$	R_t (min)
RO5073012 (**59**)	249.74	1	1	2.99	2.94	5.35	43.40	3.10
75b	249.74	1	1	2.99	2.94	5.35	42.80	3.06
76a	245.32	2	1	2.53	2.35	5.16	35.05	2.56
76c	249.74	1	1	3.22	3.11	5.35	41.20	2.96

The likelihood of compounds **59**, **75b**, **76a** and **76c** penetrating the BBB was further investigated following the calculation developed by Yoon *et al* whereby BBB membrane permeability, P_m, of a drug via passive diffusion is expressed based on correction to molecular size, Equation 3 [277].

Equation 3 Membrane permeability (P_m) obtained from k_{IAM} correction with molecular weight (MW).

$$P_m = \left(\frac{k_{IAM}}{MW^4}\right) x 10^{10}$$

Yoon *et al* and Karasova *et al* validated this method using twenty-one structurally diverse reference drugs with known penetration across the BBB, Table 3.4 [277, 278]. The reference compounds were selected and classified based on the following criteria: the rate the drug enters the brain, the drug's pharmacological activity linked to BBB permeation, the blood-brain distribution under steady state and parallel artificial membrane permeability assay (PAMPA) data reported in the literature [277]. The results showed drugs with low passive penetration through the BBB had P_m values < 9.48, whereas the drugs with high passive penetration through the BBB had scores > 17.6. Karasova *et al* concluded these values as a window to accurately

predict the likelihood of drug-like molecules remaining in the periphery with any compounds having P_m scores between 9.48-17.6 likely to require active transport systems to be delivered into the brain indicated by *in vivo* experimentation [278].

Due to the likelihood that CNS activity increases with decreasing PSA, further validation of the model was completed through establishing the correlation between PSA and P_m. In both studies, good correlations were observed (r^2 = 0.741-0.930) with the CNS active drugs identified as those with PSA < 60. Good correlation was also observed between log P and P_m (r^2 = 0.706-0.786), suggesting this model is an acceptable method for *in vitro* prediction of BBB permeation [277, 278].

Using this scoring window, it is clear compounds **59**, **75b**, **76a** and **76c** are predicted to cross the BBB via passive diffusion (Table 3.4) and thus future work will investigate the development of compounds with reduced P_m scores.

Table 3.4 *Calculated membrane permeability (P_m) scores for blood brain barrier permeable (✓), impermeable drugs (✗) and compounds RO5073012 (**59**), **75b**, **76a**, **76c**.*

Compound	CNS permeability	P_m	Compound	CNS permeability	P_m
Atenolol	✗	11.19	**Loperamide**	✗/✓	94.95
β-Estradiol	✓	218.23	**Nadolol**	✗	11.78
Caffeine	✓	12.85	**Piroxicame**	✗	1.31
Cefuroxime	✗	0.38	**Progesterone**	✓	86.10
Chlorpromazine	✓	863.00	**Promazine**	✓	689.96
Cimetidine	✗	6.57	**Propranolol**	✓	301.41
Corticosterone	✗	8.23	**p-Toluidine**	✓	352.56
Desipramine	✓	656.61	**Testosterone**	✓	50.87
Enalapril	✗	0.71	**RO5073012 (59)**	-	18.97
Hydrocortisone	✗	4.13	**75b**	-	18.74
Ibuprofene	✓	15.83	**76a**	-	16.56
Imipramine	✓	511.62	**76c**	-	18.07
Lomefloxacine	✗	2.11			

3.5. Pharmacophore development

Composed of key electronic and steric features that are essential for interaction between target and drug, pharmacophores are the molecular framework used to understand the relationship between activity and structure for a set of compounds [279, 280].

The identified substrate binding region of hTAAR1 has numerous subsites which vary in size, physicochemical properties, solvent exposure, and amino acid composition. Using the subsite

properties, docking data and the pharmacological data obtained, a 3-point pharmacophore suitable for ligand development was proposed (Figure 3.12). Essential key features of the proposed pharmacophore are the presence of two hydrophobic moieties as well as a hydrogen bond acceptor / donor region to interact with Asp103[3.32]. It is expected compounds will be further stabilised through π-π interactions with Phe267[6.51] and Phe268[6.52] residues[133]. The pharmacophore identified in Figure 3.12 will be used in the design of future SAR studies to investigate modification of the substituents on the phenyl ring (Chapter 4) and linker modifications through the addition of an amide bond (Chapter 5), to prevent BBB permeation as well as further pharmacophore development.
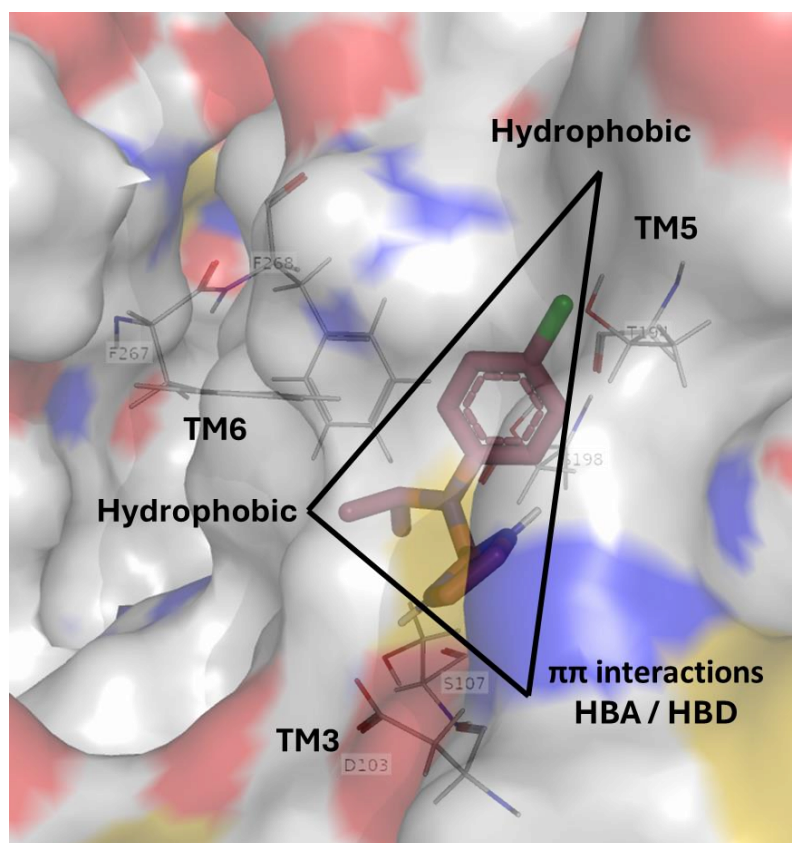
Figure 3.12 Proposed 3-point pharmacophore for hTAAR1 overlayed onto compound 76c.

3.6. Conclusions

RO5073012 (**59**) and literature analogues have been reported to have high affinity and selectivity for hTAAR1 compared to adrenergic α2 receptors as well as favourable

physicochemical properties including low MW, providing rationale for the selection as a lead compound. Docking of RO5073012 (**59**), **75a-b** and **76a-c** into a validated hTAAR1 homology model resulted in the expected interactions within the active site to be obtained, albeit the hydrogen-bond lengths were predicted to lie outside the optimal length (2.7–3.3 Å) [221].

Synthesising RO5073012 (**59**) and other analogues through standard reductive amination methods resulted in low yields, therefore a method containing the Lewis acid catalyst, $CeCl_3.7H_2O$ was developed to produce intermediate compounds (Scheme 3.1), however yields were not vastly improved. Methoxy-substituted compounds did not require the Lewis acid catalyst to deliver high yields.

Most of the literature compounds did not exhibit cytotoxicity towards INS-1 cells, and four compounds (**59**, **75a**, **76a**, **76c**) enhanced insulin secretion relative to the GLT control. 4-Chloro-substitution led to statistically significant increases for insulin secretion to be achieved for both the 2-substituted imidazole (**76c**) and 4-substituted imidazole (**59**) compounds, suggesting this is the optimal position for substitution around the phenyl ring to occur. Methoxy-substituted compounds did enhance insulin secretion in GLT conditions, however compound **75a** significantly decreased insulin secretion in non-GLT conditions. In a clinical environment, this could potentially lead to hypoglycaemia in conditions where there is no ongoing metabolic stress, thus the use of **75a** in this study was discontinued. Coupled with the data obtained for **76b** whereby cellular toxicity was induced, it can be concluded that substitutions on the phenyl ring in the *meta*-position are unfavourable for hTAAR1 efficacy.

Further work will explore substitution modifications in the *para-* position to further improve the activity and pharmacokinetic profile of these promising molecules to prevent penetration of the BBB and to reduce side effects in the CNS from occurring. Additionally, reducing BBB penetration could better inform the pharmacophore profiling of pancreatic hTAAR1 agonists to assist in future drug design. To ensure the enhanced insulin secretion is due to interactions with

hTAAR1, further experimentation is required. This could include completing additional high range rat insulin ELISA assays to determine competition with selective antagonist EPPTB as well as quantifying cAMP accumulation. This will allow us to indirectly infer whether the effects observed are through $G_{\alpha s}$ signalling pathways and potentially hTAAR1.

4. Modifications to the substituted aniline via the introduction of heterocyclic amines

There are several patents published by Roche pharmaceutical company that investigate substituted aryl and heteroaryl moieties for the use as hTAAR1 agonists for schizophrenia treatments [281, 282], thus implying their therapeutic effects occur within the CNS, and that they can cross the BBB. For our purposes (the development of therapeutics for T2DM) this is an unnecessary and probably an unfavourable characteristic.

Taking advantage of the data obtained in Chapter 3 along with known SAR, a series of analogues were designed and developed to reduce the propensity to cross the BBB. Analogues were designed to have increased polarity to avoid the potential of inducing on-target central effects such as hallucinations and synthesised using the central scaffold of lead compounds RO5073012 (**59**) and **76c**. The chloro-substituents were replaced with either piperazine-derived ring structures or morpholine substitution of the aniline (Figure 4.1) and their pharmacological profile evaluated in our phenotypic pancreatic β-cells. Although the substitutions made were selected based on the likelihood of reducing the propensity to cross the BBB, it is worth noting that these compounds contain a 1,4-masked aniline and as such are highly susceptible to metabolism [283]. Metabolites which form during oxidation of the aniline nitrogen can cause oxidative stress within cells and covalently bind to DNA, thus anilines in drug-like compounds have the potential to be harmful to human health [284]. Although for the purpose of this study, the presence of a masked aniline is deemed acceptable, should any promising compounds be identified, future work should look at using an aniline bioisostere to improve the safety profile of the molecules.

82a
pK_a: **13.8**

82b
pK_a: **13.8**

82c
pK_a: **13.8**

82d
pK_a: **13.8**

83a
pK_a: **13.6**

83b
pK_a: **13.6**

83c
pK_a: **13.6**

83d
pK_a: **13.6**
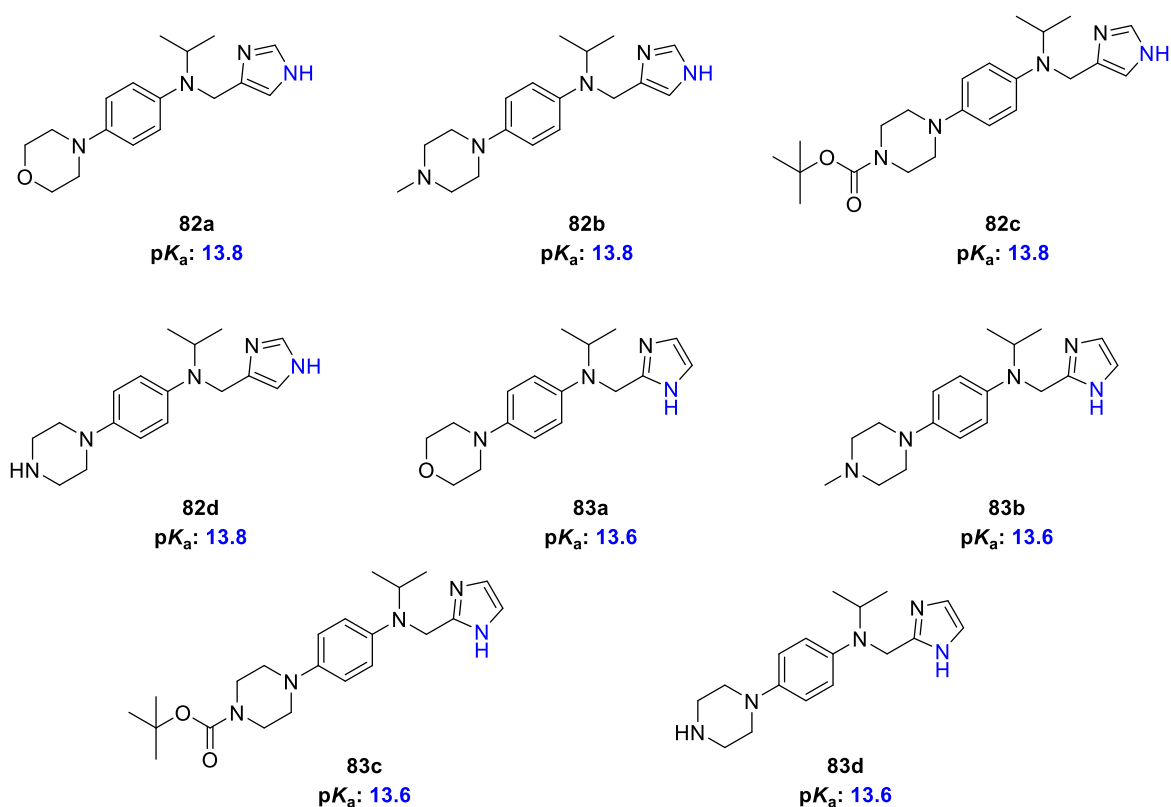
*Figure 4.1 Proposed ligands to investigate aniline substitutions of RO5073012 (**59**).*

4.1. Molecular docking

4.1.1. Molecular docking into hTAAR1 homology modelling

Using the data obtained in Chapter 3, ligands were designed with the intention of increasing polarity. As both **59** and **76c** were found to significantly increase insulin secretion, it was hypothesised para-substituted anilines were required to induce the therapeutic effect, therefore all modifications in this compound series occurred at carbon 4 of the aniline ring. The chloro-substituents of **59** and **76c** were replaced with either morpholine or piperazine rings, in which it was envisaged the replacement of the lipophilic Cl substituent with polar groups may prevent BBB penetration thus reducing the potential of inducing undesired side effects. Both substituents introduced steric bulk to the compounds whilst extending the aniline moiety allowing for maximum occupancy of the binding site, as well as the potential for hydrogen bonding with the receptor via the heteroatoms present.

Utilising the validated docking protocol outlined in Chapter 2, **82a-d** and **83a-d** were docked into model 17 and cryo-EM structure (PDB: 8W88). As for **59**, **75a-b** and **76a-c**, the analogues (**82a-d** and **83a-d**) made a similar pattern of residue interactions as those reported by Borowsky *et al*, however variation at the aniline moiety was observed, Figure 4.2[131].
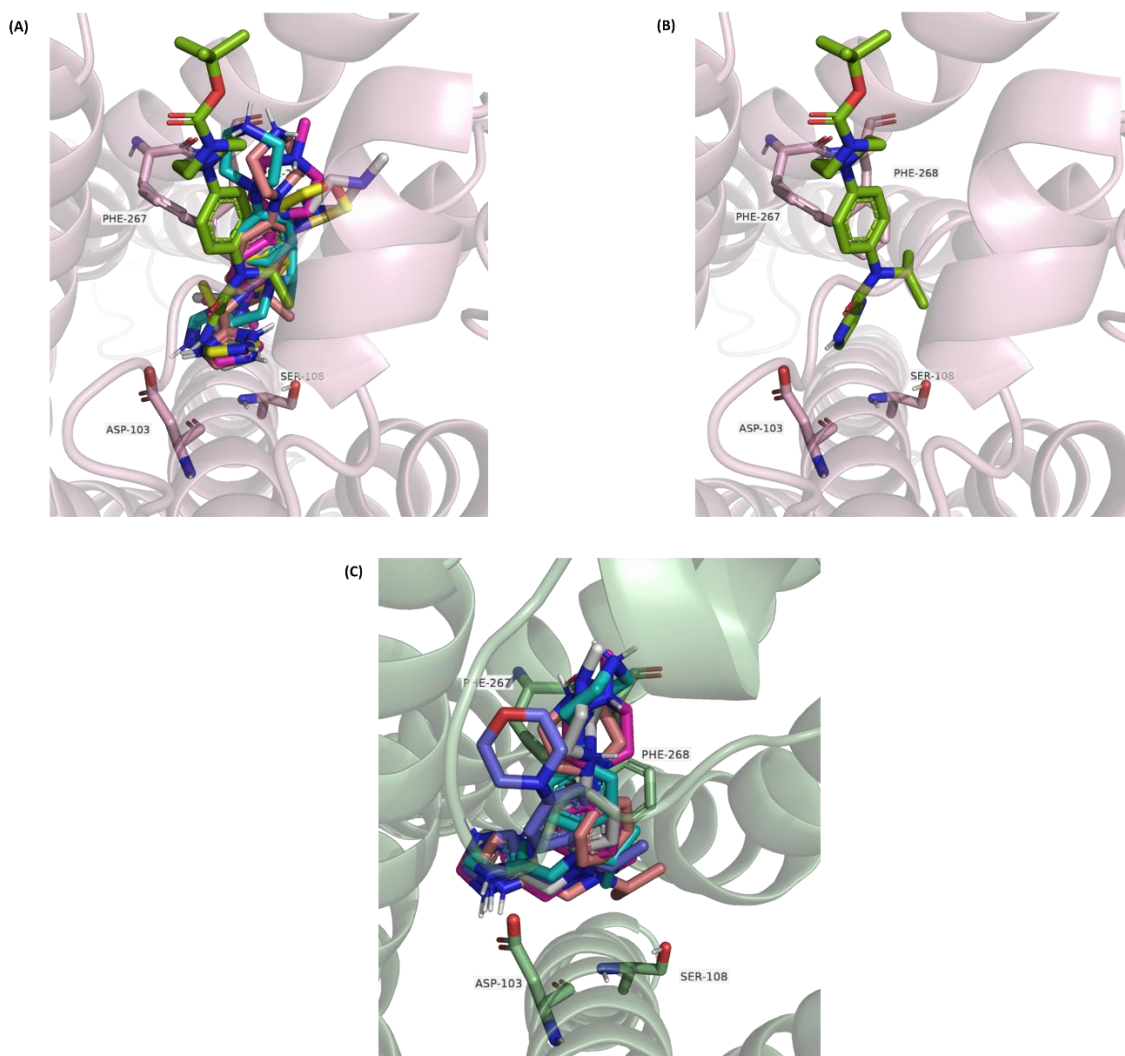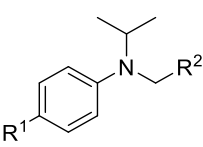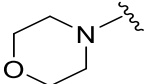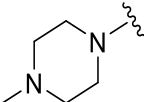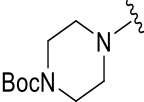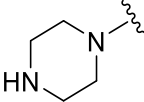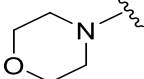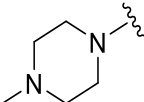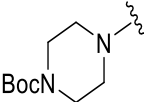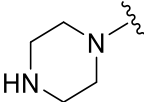
Figure 4.2 (A) *Docked pose of **82a-d** and **83a-d** (**82a**: yellow, **82b**: magenta, **82c**: sand, **82d**: cyan, **83a**: slate, **83b**: grey, **83c**: smudge, **83d**: salmon) into hTAAR1 homology model 17.* ***(B)*** *Explicit pose of **83c** in homology model 17.* ***(C)*** *Cryo-EM structure (PDB: 8W88). Image visualised down transmembrane (TM) 3. Docking performed using Schrödinger's Maestro and Glide 12.6 packages and images created using PyMOL 4.6.0.*

The docked pose of **83c** (Figure 4.2 B) showed the most variation in the position of the piperazine ring and *t*Bu group of Boc whilst retaining expected position of the imidazole moiety, Figure 4.2. This variation occurred due to the aniline and imidazole rings adopting a conformation whereby

they are out of plane with one another. The twisted conformation observed facilitates the *tert*-butyl carbamate moiety to be directed towards the entrance of the binding pocket. The low docking score obtained (-3.173 kcal/mol), Table 4.1, suggests **83c** has a weaker affinity for hTAAR1 compared to the 4-imidazolyl analogue (**83c**, -4.87 kcal/mol). As for the remaining compounds, minimal variation was observed between the 2-imidazolyl and 4-imidazolyl analogues.

Table 4.1 *Docking scores for* *82a-d* *and* *83a-d* *in complex with hTAAR1 homology model 17 and hTAAR1 cryo-EM*

structure (PDB: 8W88).

Compound	R^1	R^2	Docking score (kcal/mol)	
			hTAAR1 homology model 17	hTAAR1 Cryo-EM structure (PDB: 8W88)
82a	(morpholinyl)	4-imidazolyl	-5.519	-6.404
82b	(4-methylpiperazinyl)	4-imidazolyl	-6.139	-6.684
82c	(4-Boc-piperazinyl)	4-imidazolyl	-4.876	n/a
82d	(piperazinyl)	4-imidazolyl	-6.723	-7.140
83a	(morpholinyl)	2-imidazolyl	-6.362	-6.404
83b	(4-methylpiperazinyl)	2-imidazolyl	-6.722	-6.640
83c	(4-Boc-piperazinyl)	2-imidazolyl	-3.173	-0.271
83d	(piperazinyl)	2-imidazolyl	-7.014	-7.607

Ligand interactions with hTAAR1 homology model 17 are shown in Figure 4.3 where slight

differences between compound positioning and predicted interactions are observed. For all

compounds, the predicted hydrogen bond lengths varied between 1.70-2.03 Å, slightly shorter

than the optimal range (2.7–3.3 Å) [221]. Compound **83a** is the only analogue to not undergo further stabilisation via π-π and π-cation interactions with Phe185^{ECL2} and Phe267$^{6.51}$, however this does not seem to affect its binding affinity for hTAAR1 due to the high docking score obtained (-6.362 kcal/mol).
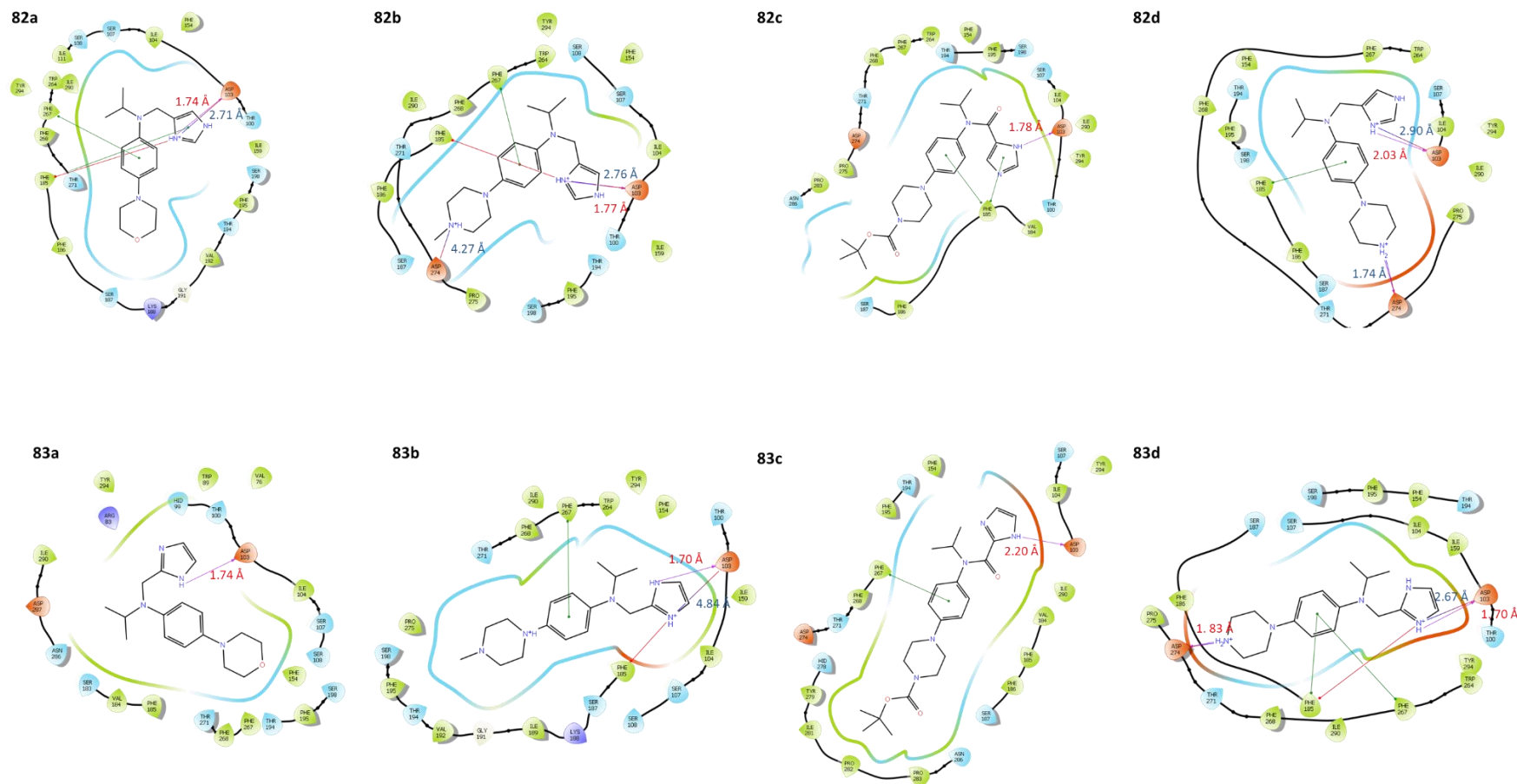
Figure 4.3 *Predicted interactions between hTAAR1 homology model with compounds* **82a-d** *and* **83a-d**. *Hydrogen bond length measurements shown in red. Expected length of salt bridges shown in*

blue. Amino acid description: Green; hydrophobic and cyan; polar.

4.1.2. Comparison between molecular docking into hTAAR1 homology modelling and hTAAR1 cryo-EM (PDB: 8W88)

The proposed ligands were also docked into the cryo-EM structure (PDB: 8W88) in which compounds **82a-d** and **83a-d** exhibited top-scoring binding poses consistent with the poses adopted in hTAAR1 homology model 17. As for the low docking scores obtained within the homology model, **82c** failed to produce an adequate predicted binding pose.

Ligand interactions with the hTAAR1 cryo-EM structure (PDB: 8W88) are shown in Figure 4.4, again showing slight differences between compound positioning and predicted interactions. The predicted hydrogen bond lengths between compounds **82a**, **82b**, **82d**, **83a**, **83b** and **83d** and Asp103$^{3.32}$ varied between 1.47-2.07 Å.

Additional stabilisation of compounds within the cryo-EM structure's binding site is reported via π-π and π-cation interactions with Trp264$^{6.48}$, Phe267$^{6.51}$ and Tyr294$^{7.43}$, for **82a**, **82b**, **82d**, **83a**, **83b** and **83d**. As hypothesised during the design process of this SAR study, the heteroatoms present in the ring structures of compounds **82a**, **82b**, **83a**, **83b** allowed for additional hydrogen bond interactions to be observed between ligand and hTAAR1, Figure 4.4. This further stabilisation was present in corresponding poses for hTAAR1 homology model 17 for **82b** and **82d** (Figure 4.4).
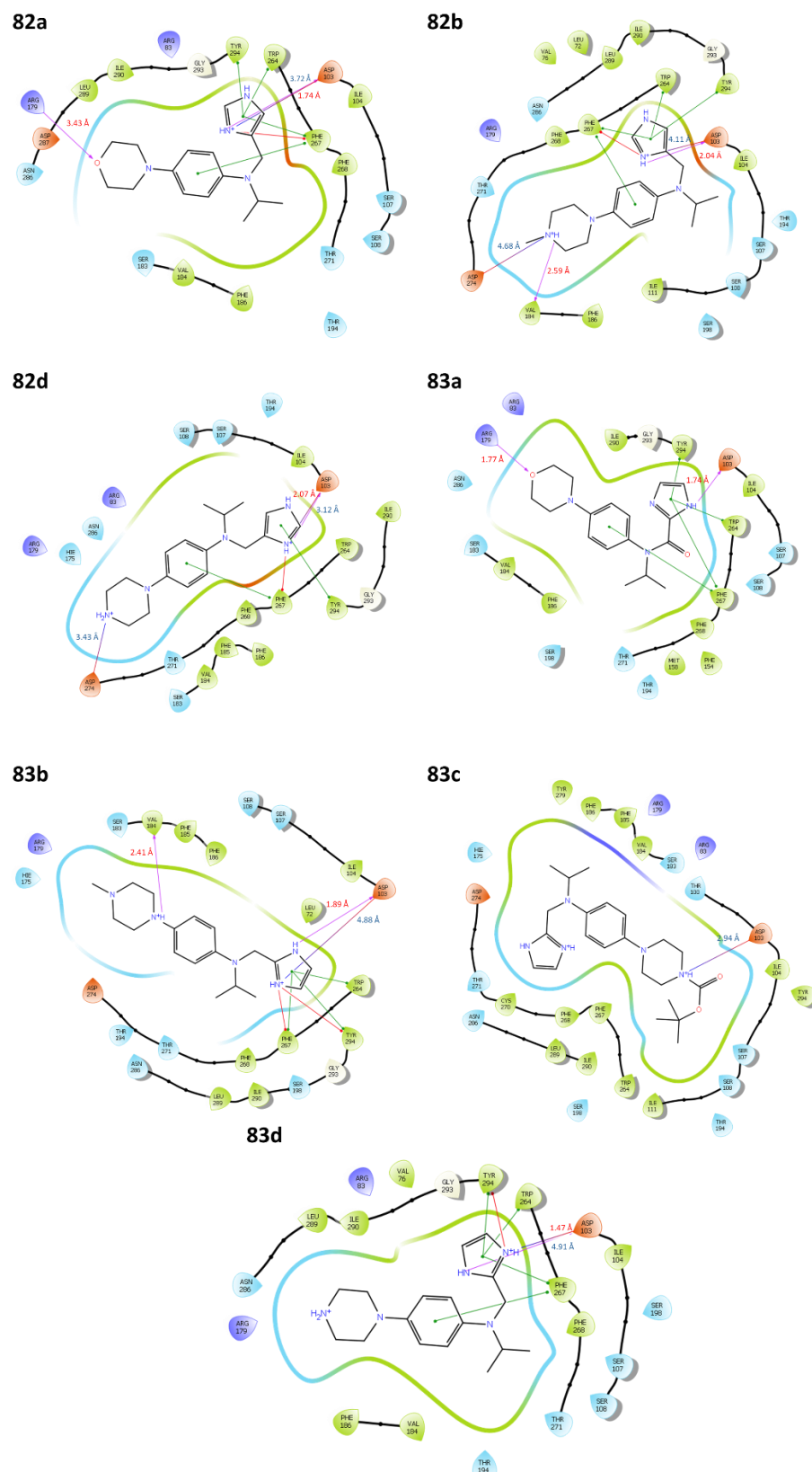
Figure 4.4 *Predicted interactions between hTAAR1 cryo-EM structure (PDB: 8W88) with compounds **82a, 82b, 82d, 83a-d**. Hydrogen bond length measurements shown in red. Expected length of salt bridges shown in blue. Amino acid description: Green; hydrophobic and cyan; polar.*

4.2. Synthetic route employed

Often accountable for their therapeutic effects, many synthetic and natural drug-like molecules contain an amine moiety [285]. Numerous chemical routes have been developed for the manipulation of amines, including alkylation and reductive amination [285]. Introduced in Chapter 3, reductive amination involves the initial condensation of an amine with an aldehyde/ketone to form an imine. In the presence of a reducing agent, the imine is reduced to form a more substituted amine [286]. Unlike alkylation, reductive amination selectively controls the formation of carbon-nitrogen bonds, which coupled with its simplicity, it is often the first point of call for amine synthesis within the pharmaceutical and chemical industries [285].

Various reducing agents have been developed, each with a different selectivity for the imine compared to the starting carbonyl compound. Typically based around borane, reducing agents often contain a BH_3-amine complex or a borohydride group, however hydrogenation using gaseous H_2 and a metal catalyst is known [287]. Table 4.2 contains an overview of commonly employed reducing agents highlighting their advantages and disadvantages.

Table 4.2 *Overview of reducing agents used in reductive amination.*

Reducing agent	Notes
Sodium borohydride	**Advantages:** $NaBH_4$ is a cheap and selective reducing agent. Additionally, it can attack sterically hindered compounds. **Disadvantages:** Cannot reduce aromatic nitro compounds without a catalyst present [288, 289]. Undesirable reduction of ketones can occur.
Sodium triacetoxyborohydride	**Advantages:** $NaBH(OAc)_3$ is a cheap, mild reducing agent which can selectively reduce aldehydes over ketones. **Disadvantages:** Cannot react in protic solvents due to its rapid decomposition. A high excess of $NaBH(OAc)_3$ is required due to only one hydrogen atom available [290, 291].
Sodium cyanoborohydride	**Advantages:** $NaBH_3CN$ is a highly selective reducing agent which demonstrates different selectivity for functional groups in a range of different pH conditions. It is highly soluble in a range of solvents unlike $NaBH(OAc)_3$. **Disadvantages:** Expensive, highly toxic, can contaminate product with cyanide [291, 292].
2-Picoline borane	**Advantages:** 2-picoline borane is a non-toxic, cheap, and selective reducing agent. It is stable at high temperatures and works in a range of solvent systems [292, 293].
Pyridine-borane	**Advantages:** Cheap, selective by charge [294]. **Disadvantages:** Pyridine-borane is less stable than the aforementioned 2-picoline borane and can cause fire upon decomposition [292].
Catalytic hydrogenation	**Advantages:** Catalytic hydrogenation is an economical and effective method to generate the hydrogen required in reductive amination. **Disadvantages:** Low yields can occur due to its poor selectivity, leading to a mixture of products forming.

Several multistep reactions were carried out for the synthesis of **82a-d** and **83a-d** many of which being reductive amination.

4-morpholinoaniline (**84a**) and 4-(4-methylpiperidin-1-yl)aniline (**84b**) were converted to the corresponding secondary amine (**85a-b** and **86a-b**) via reductive amination. This was achieved by using the modified one-pot reductive amination using 2-imidazolecarboxaldehyde (**81**) or 4-imidazolecarboxaldehyde (**78**) in the presence of Lewis acid catalyst $CeCl_3.7H_2O$, previously outlined in Chapter 3 [229]. The amine moiety of compounds **85a-b** and **86a-b** were reacted with 2-methoxypropene via reductive amination, using $NaBH(OAc)_3$ as the reducing agent to afford the final compounds (**82a-b** and **83a-b**), Scheme 4.1.

*Scheme 4.1 Synthesis of compounds **82a-b** and **83a-b**.*
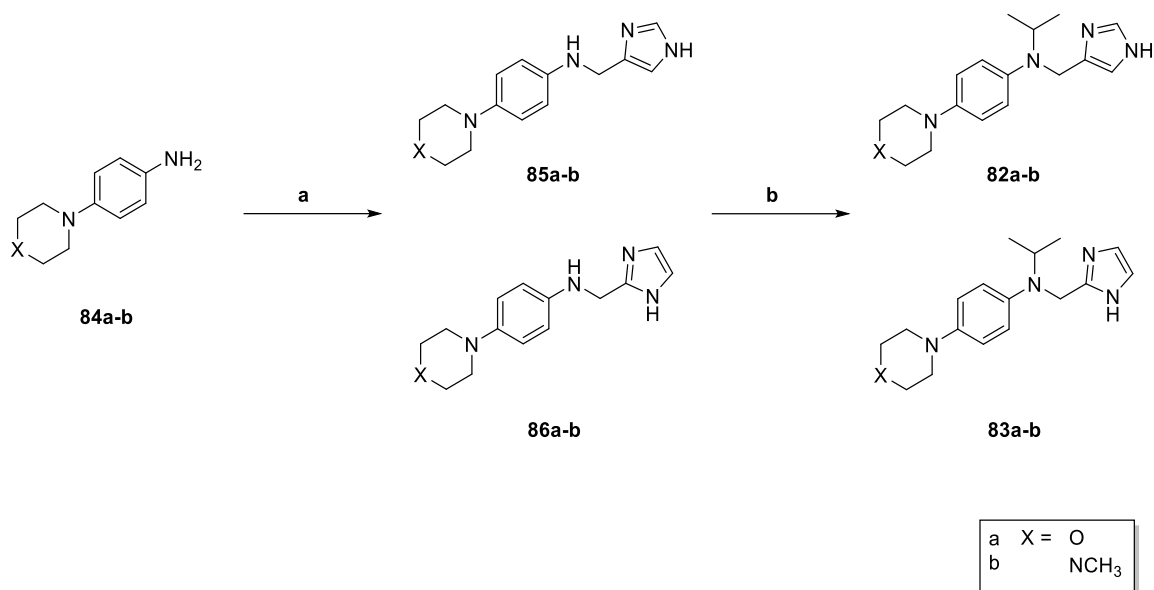
Reagents and conditions: (a) i. 78 / 81, $CeCl_3.7H_2O$, EtOH, rt, 0.3-1 hr. **ii.** $NaBH_4$, rt, 2-18 hr (27-51%). **(b) i.** 2-methoxypropene, TFA, $NaBH(OAc)_3$, 1,2-DCE, 60°C, 18 hr. **ii.** 1M HCl, 60°C, 1 hr (2-31%).

The synthesis of **82c** and **83c** was attempted following several procedures. At first, Buchwald-Hartwig cross coupling proposed by Dholkawala *et al* was tried, Scheme 4.2 [295].

Scheme 4.2 Attempted synthesis of *82c* and *83c*.

| a, **82** = 4-imidazolyl |
| b, **83** = 2-imidazolyl |
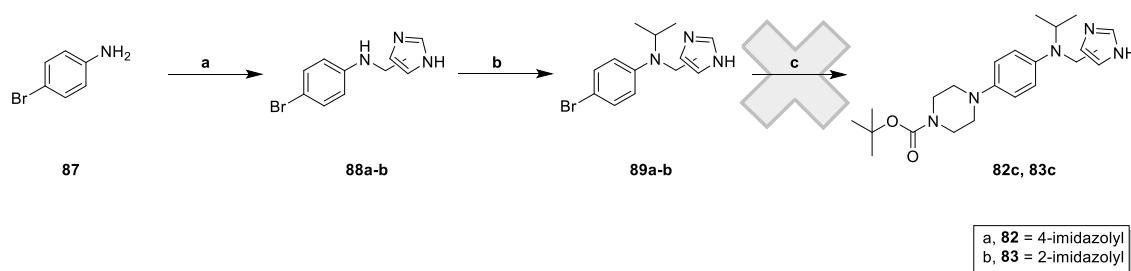
Reagents and conditions: (a) i. 78 / 81, CeCl$_3$.7H$_2$O, EtOH, rt, 1 hr. **ii.** NaBH$_4$, rt, 2-18 hr (29-39%). **(b) i.** 2-methoxypropene, TFA, NaBH(OAc)$_3$, 1,2-dichloroethane (1,2-DCE), 60°C, 18 hr. **ii.** 1M HCl, 60°C, 1 hr (33-42%). **(c)** *tert*-butyl 4-(4-aminophenyl)piperazine-1-carboxylate (**90**), Cs$_2$CO$_3$, Pd(OAC)$_2$, (2,2'-bis(diphenylphosphino)-1,1'-binapthyl (BINAP), toluene, 110°C, 12 hr.

This approach employed the synthesis of **89a-b** by the 2-step reductive amination reaction of 4-bromoaniline (**87**) with **78** or **81** to yield intermediates (**88a-b**) [229]. Secondary amines **88a-b** underwent further reductive amination with 2-methoxypropene [173]. The resulting tertiary amines (**89a-b**) and *tert*-butyl 4-(4-aminophenyl)piperazine-1-carboxylate (**90**) were reacted in the presence of palladium (II) acetate, (2,2'-bis(diphenylphosphino)-1,1'-binapthyl (BINAP) and Cs$_2$CO$_3$ in toluene. Unfortunately, this synthetic route was not successful and upon reaction monitoring no change occurred. Therefore, it was decided to attempt the reaction again, changing the palladium catalyst and phosphine-derived ligand systems, Table 4.3. However, like the method described above, the new systems were also unsuccessful at yielding the desired products.

Table 4.3 Buchwald-Hartwig reaction conditions attempted for the synthesis of *82c* and *83c*.

	Catalyst	Ligand	Solvent system
Condition 2	Pd$_2$(dba)$_3$	Xanphos™	1,4-dioxane
Condition 3	Pd$_2$(dba)$_3$	Xphos™	toluene

Next, the order of reaction was modified whereby the isopropyl moiety of the compound was added prior to the imidazole ring. This was achieved via alkylation, Scheme 4.3. Reagent **90** was reacted with 2-iodopropane in 1,4-dioxane, affording **91** following a modified procedure by Guest *et al* [296]. Due to the absence of an acidic environment, this synthetic route was selected over the previously employed reductive amination to eliminate potential undesired deprotection of the Boc group present on the piperazine moiety from occurring.

Scheme 4.3 Synthesis of compounds **82c-d** and **83c-d**.

82	= 4-imidazolyl
83	= 2-imidazolyl
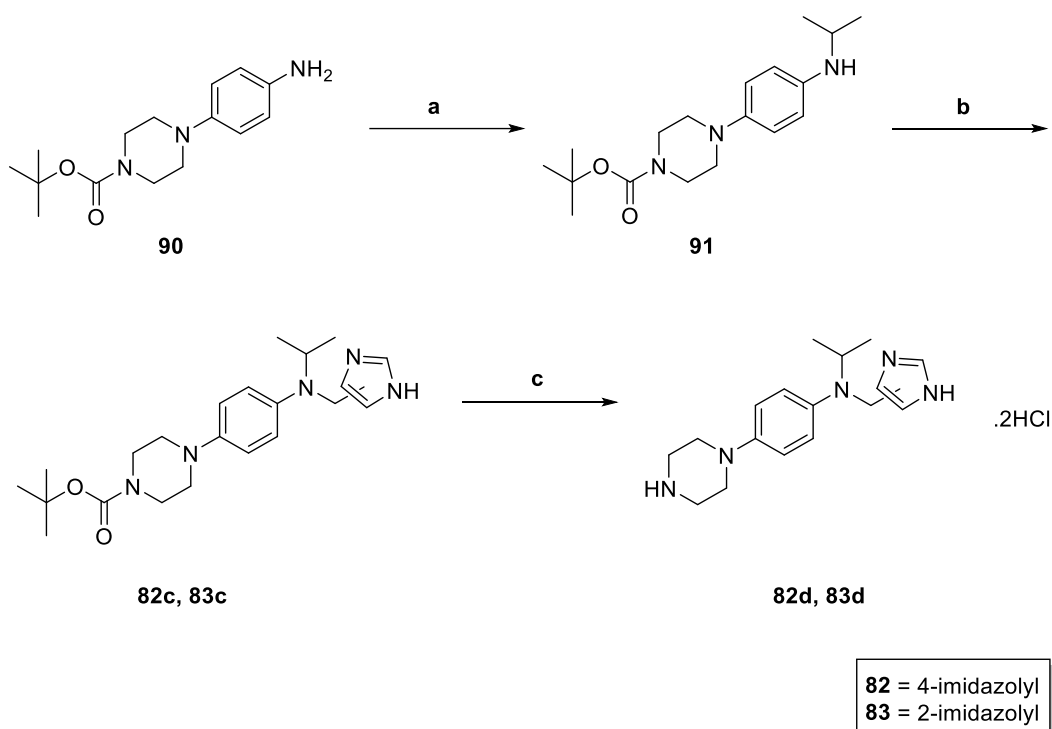
Reagents and conditions: (a) potassium carbonate, 2-iodopropane, 1,4-dioxane, microwave, 150°C, 1 hr (55%). **(b)** picoline borane, MeOH: AcOH (10:1), rt, 18 hr (17-31%). **(c)** 4M HCl in 1,4-dioxane, MeOH, rt, 30 min (73-80%).

Reductive amination of **91** with **78** or **81** also took several attempts. Initially, the reaction was attempted using NaBH$_4$ in the presence of CeCl$_3$.7H$_2$O as previously used, however this synthetic route was not successful, and the final product was not made. A literature search identified other potential reaction conditions, varying the reducing agent, equivalents used and the presence of a catalyst. The conditions shown in Table 4.4 were attempted and successful

synthesis and isolation of **82c** and **83c** was obtained using condition 5. The high crude yields

obtained for conditions 2-4 are due to the presence of unreactive starting material, evidenced

via LC-MS. A final treatment with hydrochloric acid in 1,4-dioxane gave **82d** and **83d** as products,

Scheme 4.3.

Table 4.4 *Reductive amination reaction conditions attempted for the synthesis of **82c** and **83c***.

	Reducing agent	Equivalents used (aldehyde: reducing agent: 112)	Catalyst present	Yield (%)	Success	Reference
Condition 2	NaBH(OAc)$_3$	1: 1.2: 1.1	-	115 (crude)	✗	297
Condition 3	NaBH(OAc)$_3$	1: 1.1: 1	-	108 (crude)	✗	298
Condition 4	NaBH(OAc)$_3$	1: 3: 1.1	Acetic acid	86 (crude)	✗	299
Condition 5	Pic-BH$_3$	1: 1: 1	-	92	✓	290

4.3. Pharmacological evaluation of compounds 82a-d and 83a-d in pancreatic rat insulinoma cell line, INS-1.

The toxicity of analogues **82a-d** and **83a-d** was determined using calcein AM cell viability dye

following the optimised protocol by Cripps *et al* (Chapter 3) [249]. Like for compounds **59**, **75a-b**

and **76a-c**, the toxicity of **82a-d** and **83a-d** was determined at both 0.1 µM and 1 µM

concentrations (Figure 4.5).

Only one compound, **82d**, was found to be cytotoxic (Figure 4.5) to the treated INS-1 cells in

control conditions due to the statistical decrease reported (p = 0.0029), thus was excluded from

further analysis. The remaining ligands, **82a-c** and **83a-d** were found to be non-toxic to the

treated INS-1 cells in both control and GLT conditions, evidenced by the lack of statistically

significant differences obtained from one-way ANOVA analysis. Therefore, the ability to enhance insulin secretion was determined for ligands **82a-c** and **83a-d**.

(A)

(B)
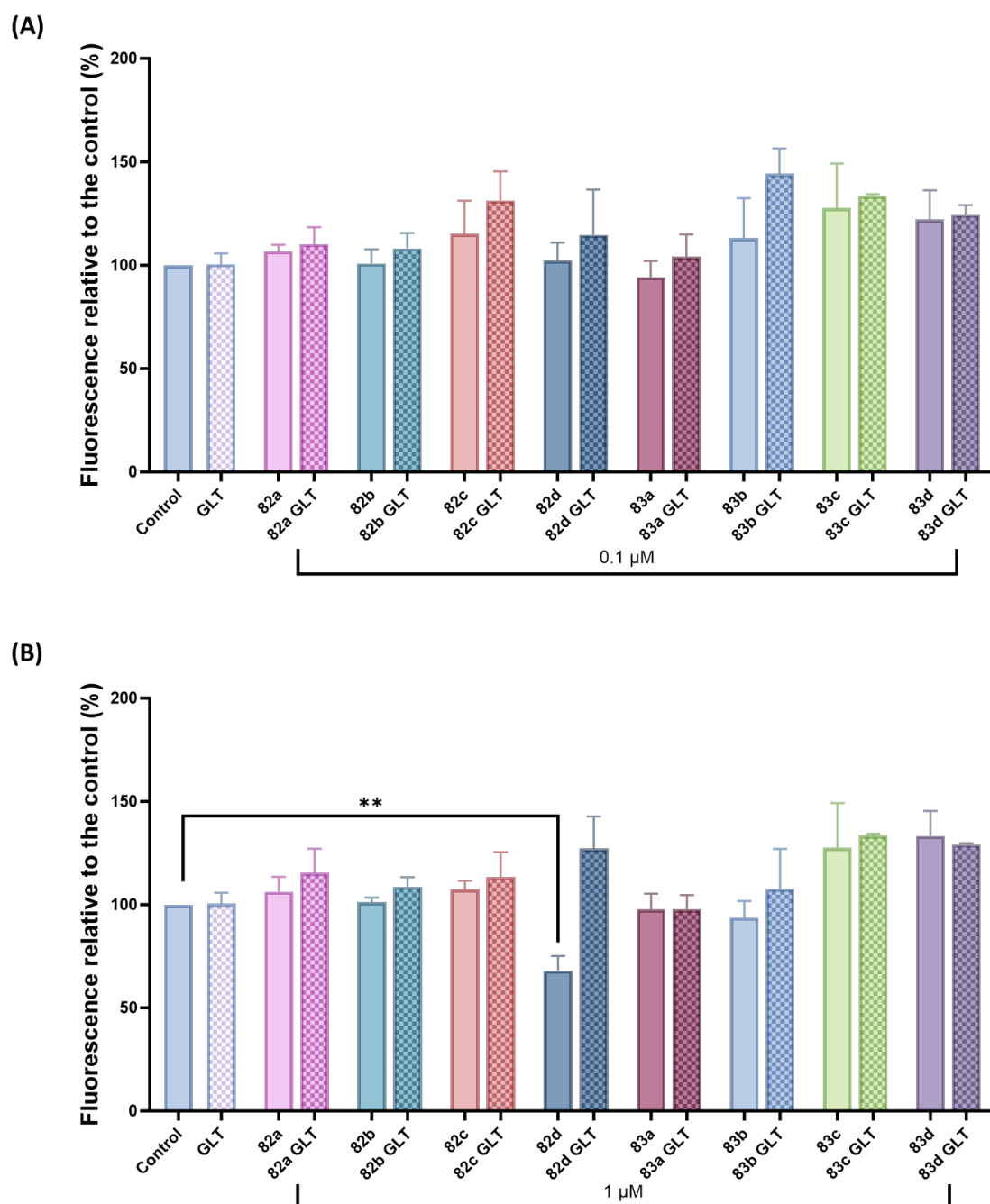
Figure 4.5 *Cell toxicity of hTAAR1 analogues **82a-d** and **83a-d**. Cell viability detected via fluorescence with Ex/Em 490/520 nm and expressed as % change compared to control from 3 or more independent experiments ± SEM. Toxicity was determined for each compound at (**A**) 0.1 μM and (**B**) 1 μM (p(**82d**) = 0.0029). Asterisk denotation: ** p<0.01.*

The ability of compounds **82a-c** and **83a-d** to enhance secretagogue stimulated insulin secretion in the pancreatic INS-1 cell line was determined using the high range rat insulin ELISA (Mercodia) in a similar manner to that described in Section 3.3. The data shown in Figure 4.6 displays the amount of insulin secreted and normalised to cellular protein content before being further normalised to the stimulated control. Tyramine (**18** (p = 0.017)), **82b** (p = 0.0491) and **83a** (p = 0.0004) all statistically increased insulin secretion in non-GLT conditions, whilst a statistical decrease was obtained for EPPTB (**70** (p = 0.0001)) and **83b** (p = 0.0307), Figure 4.6 A. Shown in Figure 4.6 B, compound **83a** also enhanced insulin secretion in the GLT conditions with statistical significance (p = 0.0155), whereas **83b** and **83d** were shown to statistically suppress insulin secretion (p = 0.0368 and 0.035, respectively). As for the data reported for **75a** (Section 3.3), **83b** and **83d** did not undergo any further analysis due to their undesirable pharmacological profile. Despite **82b** enhancing insulin secretion in non-GLT conditions, no changes in secretion were observed in the GLT conditions (p = 0.7261), thus did not meet the aims of this project.
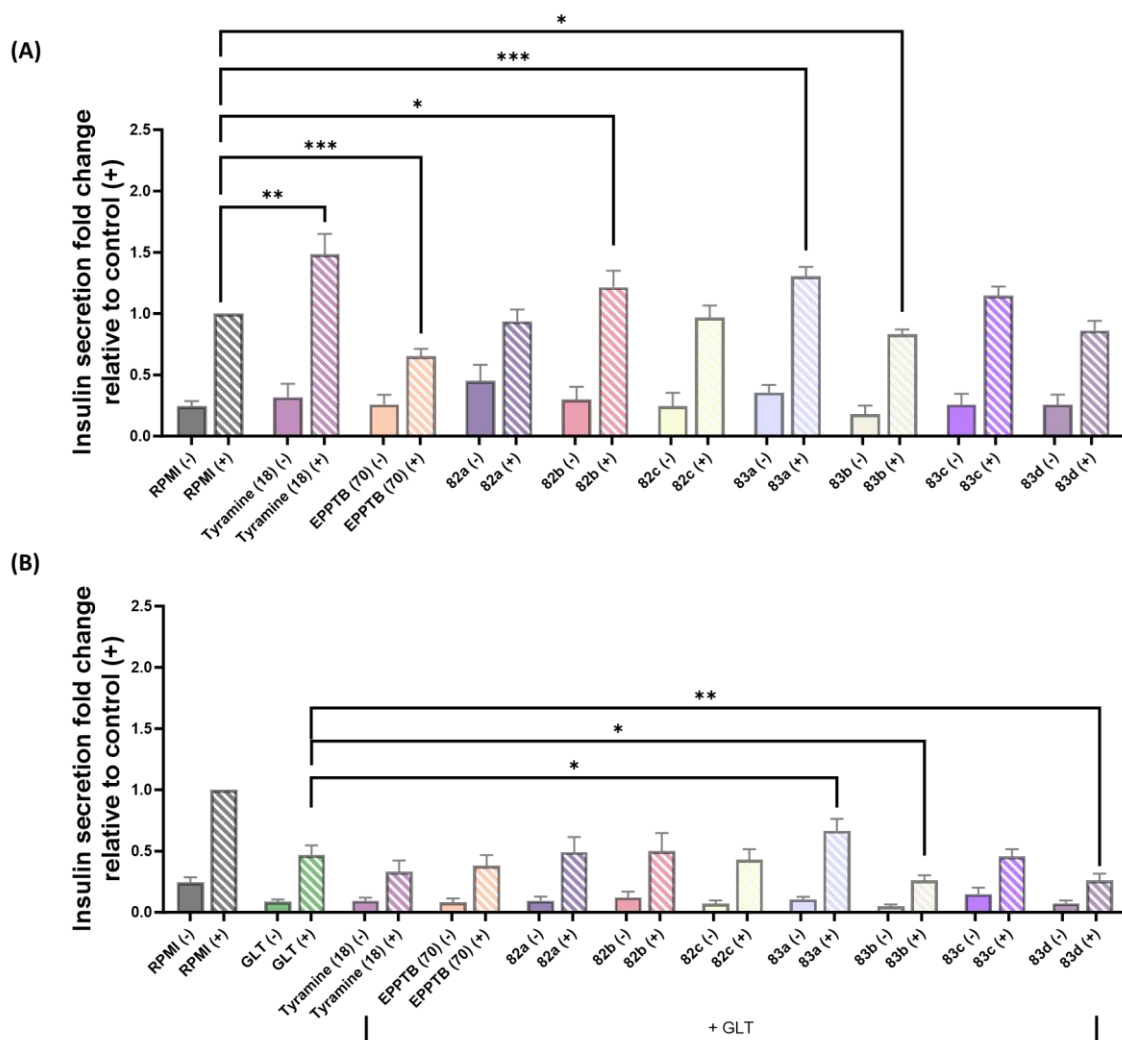
Figure 4.6 Changes in insulin secretion resulting from 5-day treatment with tyramine (**18**) and **82a-c** and **83a-d** at a final concentration of 1 µM or the inverse agonist EPPTB (**70**) at a concentration of 10 nM. Insulin secretion was determined by ELISA following incubation ± secretagogue cocktail (13.5 mM glucose, 1µM phorbol 12-myristate 13-acetate, 1mM isobutyl-methylxanthine, 1 mM tolbutamide, 10 mM leucine, 10 mM glutamine) for 2 hrs and detected via absorbance at 450 nm and normalised to cellular protein content relative to secretagogue-stimulated control from 3 or more independent experiments. Comparisons between compounds and the controls used unpaired t-tests. **(A)** control p(tyramine (**18**)) = 0.0017, p(EPPTB (**70**)) = 0.0001, p(**82b**) 0.0491, p(**83a**) 0.0004, p(**83b**) 0.0307), **(B)** GLT (p(**83a**) = 0.0155, p(**83b**) = 0.0368, p(**83d**) = 0.0035). Asterisk denotation: * p<0.05, ** p<0.01, **** p<0.0001.

As the hTAAR1 signalling pathway shown in Figure 1.28 demonstrates activation of adenylyl cyclase via downstream signalling of $G_{\alpha s}$ proteins, it was prudent to investigate the effects of cAMP production in INS-1 cells when stimulated with compounds (**59**, **76a**, **76c**, **82b**, **83a**)

previously found to enhance insulin secretion. Intracellular cAMP production was quantified between control and experimental GLT conditions using a cyclic AMP select ELISA kit obtained from Cayman Chemical and normalised to the control following the methods reported by Cripps *et al* and the manufacture's protocol [249, 300].

To ensure the ELISA was an appropriate assay to determine cAMP production in the presence or absence of compounds **59**, **76a**, **76c**, **82b**, **83a**, IBMX, an adenosine A1 receptor antagonist was added to inhibit cAMP hydrolysis via cyclic nucleotide phosphodiesterases [301]. Additionally, the effects on cAMP accumulation of compounds **18** and **70** were tested to further confirm the results obtained. Shown in Figure 4.7, it can be suggested that the assay protocol was appropriate to provide a window to accurately determine the effects of due to the positive control of **18** significantly enhancing cAMP levels in control conditions ($p = 0.0069$) compared to the control. For consistency between assays performed in this thesis, cAMP accumulation stimulated by compound **18** was determined at a final concentration of 1 µM whilst Cripps *et al* tested the effects using a final concentration of 10 µM [249]. Despite the differences in concentration used, minimal changes were observed as both concentrations tested were proven to significantly enhance cAMP accumulation in control conditions.

Differing from the literature, the data shown in Figure 4.7 suggests **70** is an antagonist due to the lack of intrinsic efficacy displayed [159, 165, 249]. Constitutive receptor signalling theory states that when cellular receptor expression is high, a more measurable signal can be obtained due to the greater number of active receptors available [302]. This theory could be used to explain the differences in intrinsic efficacy for EPPTB in response to cAMP accumulation when determined using Cayman Chemical's cyclic AMP select ELISA kit. Within the manufacture's protocol [300], there are two methods to prepare and extract cell culture samples; freeze the plate at -80°C for two hours followed by adding 1ml cold ELISA buffer for every 35 cm^2 of surface area, or to incubate for 20 minutes in 1ml 0.1 M HCl for every 35 cm^2 surface area. Following the latter

method, it was clear that the volume of HCl used to lyse the cells was not large enough as visual examination revealed many cells remained on the surface of the well, resulting in potential discrepancy within cell number that the assay was performed on. It is hypothesised this resulted in a lower receptor expression within the samples and a smaller signal to be obtained. Therefore, to overcome potential constitutive receptor signalling, the optimal volume of HCl required to lyse all cells needs to be determined and the assay repeated.
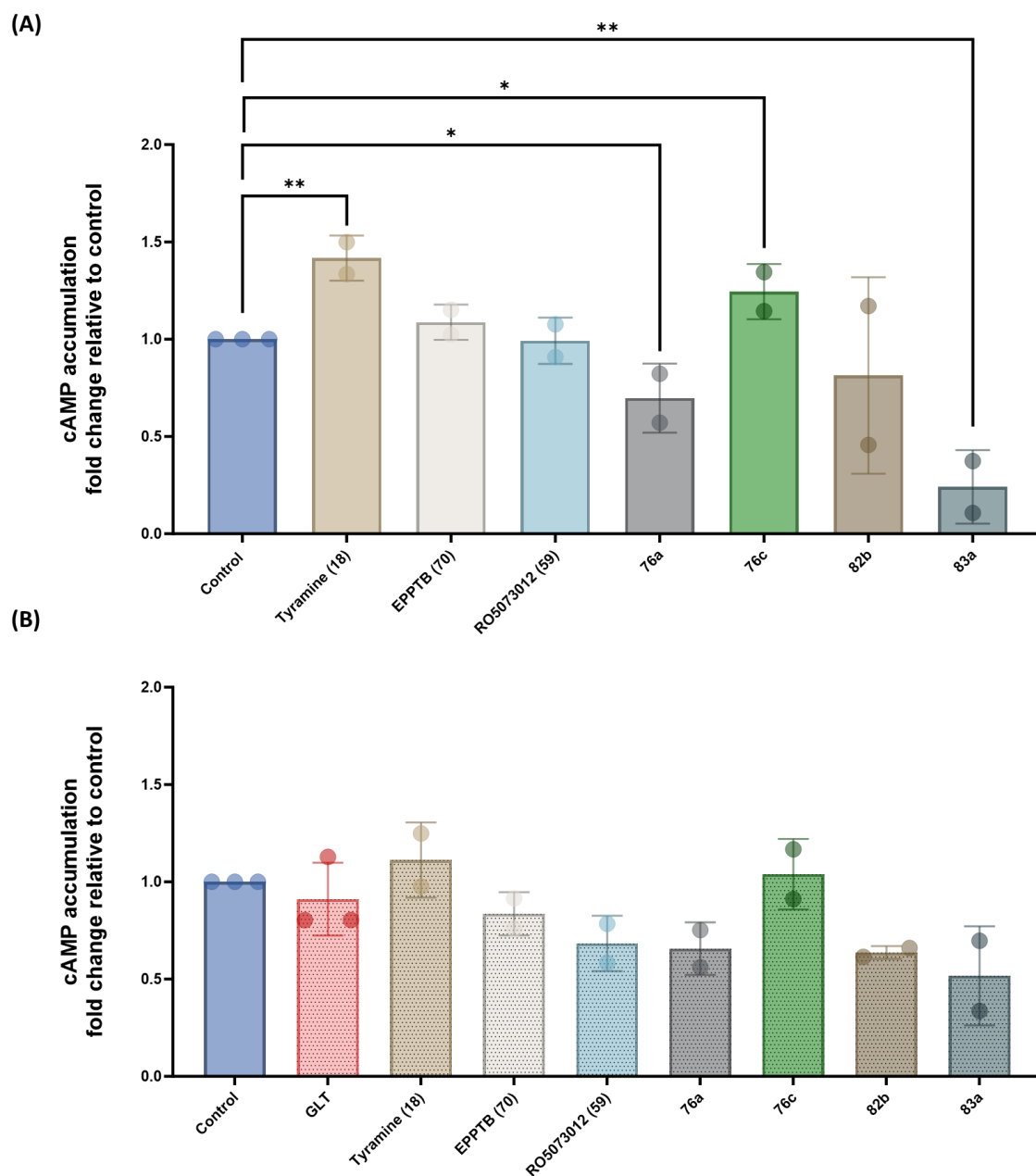
Figure 4.7 *Changes in cAMP accumulation following a 30-minute treatment with 0.5 mM IBMX in Krebs-ringer buffer,*

*tyramine (**18**) and compounds **59, 76a, 76c, 82b** and **83a** at a final concentration of 1 µM or the antagonist EPPTB*

*(**70**) at a concentration of 10 nM in either control **(A)** or experimental GLT **(B)** conditions. Cyclic AMP levels were*

determined via cAMP select ELISA and detected via absorbance at 415 nm and normalised to the relative to control

*from 2 or more independent experiments. **(A)** control (p(tyramine (**18**)) = 0.0069, p(**76a**) 0.00466, p(**76c**) = 0.0481,*

*p(**83a**) 0.0047, **(B)** GLT. Asterisk denotation: * p<0.05, ** p<0.01, **** p<0.0001.*

Shown in Figure 4.7, compound **76c** significantly increased cAMP accumulation fold change (p = 0.0481), whilst **76a** and **83a** significantly decreased cAMP accumulation (p = 0.00466 and 0.0047, respectively), suggesting the mode of action for compounds **76a** and **83a** is not through the proposed signalling pathway described in Figure 1.28. Time constraints associated with this project prevented further investigation into identification of the mode of action of these drug-like molecules.

No significant changes were detected in experimental conditions. It is theorised that lower levels of cAMP are secreted in the GLT phenotype and therefore harder to generate significant responses. A small margin of error was calculated for most compounds however for **82b** and **83a** much larger error in data points was obtained. It is believed repeating the experiment to obtain data from 3 or more independent experiments, will reduce the reported error thus increasing the accuracy and reliability of the data. The high assay cost coupled with the budget for this PhD project prevented further experimental replicates from being carried out.

4.4. Investigation of blood brain barrier permeability
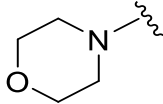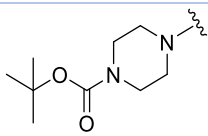
Shown in Chapter 3, analogues RO5073012 (**59**), **75a-b** and **76a-c** are expected to cross the BBB due to the lipophilic properties of the substituents attached. Reports show drugs which elicit their therapeutic effects within the CNS have a MW < 400 Da and have a low ability to form hydrogen bonds due to their high lipid solubility [303], therefore, the chloro-substituents of **59** and **76c** were replaced with either morpholine or piperazine rings. The purpose of introducing polar groups was to prevent BBB penetration via increased hydrogen bond formation, thus reducing the potential of inducing undesired side effects. Using the computational methods described in Chapter 3.4, along with obtaining experimental IAM chromatography data, it is predicted analogues **82a-c**, **83a** and **83c** have reduced BBB penetration due to the polarity introduced Table 4.5.

Table 4.5 *Drug likeliness of compounds **82a-c**, **83a** and **83c**. All compounds comply with Lipinski's rule of 5 and Veber rules [275, 276]. MW; molecular weight (g mol-1), nHBA; number of hydrogen bond acceptors, nHBD; number of hydrogen bond donors, Log P; partition co-efficient, Log D$_{7.4}$; distribution co-efficient, BBB score; blood brain barrier score R$_t$; average retention time. All predicted data (ϕ) obtained from SwisADME [273].*
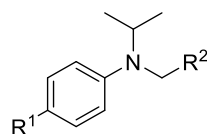
Compound	R^1	R^2	MW	nHBA$^\phi$	nHBD$^\phi$	Log P$^\phi$	Log D$_{7.4}^\phi$	BBB score$^\phi$	CHI$_{IAM}$	R$_t$ (min)	P$_m$
82a		4-imidazolyl	300.40	2	1	2.32	2.22	5.00	26.16	2.07	5.62
82b		4-imidazolyl	313.44	2	1	2.47	0.88	5.27	30.94	2.36	5.53
82c		4-imidazolyl	399.53	3	1	3.2	3.19	4.65	37.50	2.75	2.51

Table 4.5 Continued.

Compound	R^1	R^2	MW	nHBA$^\Phi$	nHBD$^\Phi$	Log P$^\Phi$	Log D$_{7.4}$$^\Phi$	BBB score$^\Phi$	CHI$_{IAM}$	R_t (min)	P$_m$
83a		2-imidazolyl	300.40	2	1	2.54	2.40	5.00	24.64	1.97	5.32
83c		2-imidazolyl	399.53	3	1	3.43	3.36	4.65	35.56	2.49	2.39

Shown in Table 4.5 are computationally predicted log P and log $D_{7.4}$ data for compounds **82a-c**, **83a** and **83c** suggesting these compounds are likely to cross the BBB despite the polar substituents present. Contrastingly, the log P and log $D_{7.4}$ values predicted for **83c** lie outside of the BBB permeation range (1.5-2.7 and 0-3 respectively), thus suggesting **83c** will remain in the periphery and the likelihood of inducing undesired side effects prevented. For all compounds the BBB score developed by Gupta *et al* expects all 5 analogues to cross the BBB [263], however on further evaluation using the BOILED-Egg model **82a-c**, **83a** and **83c** are predicted to be P-glycoprotein substates and thus will be actively effluxed back into the periphery [264, 273].

Experimental CHI_{IAM} values for compounds **82a-c**, **83a** and **83c** are shown in Table 4.5. Compared to the data obtained for compounds **59**, **75b** and **76c** (Table 3.3) lower acetonitrile concentrations are required to elute analogues **82a**, **82b** and **83a** from the IAM phase, indicating these compounds are less likely to cross the BBB. The CHI_{IAM} score for compounds **82c** (CHI_{IAM}: 37.50) and **83c** (CHI_{IAM}: 35.56) are comparable with that of **76a** (CHI_{IAM}: 35.05) hinting that these compounds are likely to permeate the BBB due to presence of the *N*-Boc protecting group.

The BBB membrane permeability, P_m, of compounds **82a-c**, **83a** and **83c** (Table 4.5) was calculated using the method previously described (Equation 3, Chapter 3.4). For compounds **82a-c**, **83a** and **83c**, the experimentally calculated P_m are comparable with the literature classified low BBB permeable drugs [278], suggesting the compounds are likely to remain in the periphery. Despite the computationally calculated log P, log $D_{7.4}$ and BBB scores obtained for compounds **82a**-**c**, **83a** and **83c** suggesting the compounds are likely to permeate the BBB, investigation using the BOILED-egg model indicates these compounds are likely to be P-glycoprotein substrates, thus should **82a-c**, **83a** and **83c** permeate the BBB, they should be effluxed back into the periphery before they have had chance to exert any therapeutic effects. Although this analysis coupled with the experimentally obtained P_m data strongly suggests compounds **82a-c**, **83a** and **83c** are likely to remain in the periphery and thus should not induce

any undesired on-target central effects, the algorithms applied do not consider BBB damage. Studies show that T2DM alters the structure and function of the BBB as well as decreasing the integrity of the BBB [304, 305]. Subsequently T2DM often results in the BBB having increased permeability, thus potentially allowing unwanted compounds to enter and interact with the CNS [304, 305]. As the aim of this project is to develop therapeutic agents which remain in the periphery, further experimentation is required to solidify the data shown in Table 4.5. This could be achieved via the completion of *in vivo* studies whereby changes in BBB permeability in both diabetic and healthy individuals would be identified.

4.5. Pharmacophore development

The data expressed in this chapter provides further insight into the development of the pharmacophore for peripheral hTAAR1 agonists. The originally proposed pharmacophore shown in Figure 3.12 states essential key features include the presence of two hydrophobic moieties for interactions with residues on TM 5 and TM 6, however **82a** was the only compound shown to significantly enhance insulin secretion in both control and experimental conditions.

Whilst it could be suggested the hydrophilic nature of the morpholine substituent is responsible for pharmacological interaction with hTAAR1 at TM 6 as further evidenced by the ether substituent present in compounds **75a** and **76a**, compounds **59** and **76c** also enhanced insulin secretion. As **59** and **76c** (Figure 4.8) do not contain the hydrophilic properties associated with the ether present in **75a**, **76a** and **83a** (Figure 4.8) it could be suggested the polar carbon bond contributes to inducing the desired biological effect due to the associated properties of the substituents attached, although further investigation is required.

59, 76c	R^1 =	4-Cl
75a, 76a		3-OMe
83a		

| 59, 75a | R^2 = | 4-imidazolyl |
| 76a, 76c, 83a | | 2-imidazolyl |
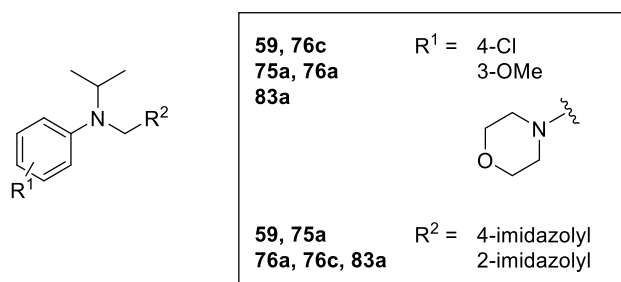
Figure 4.8 *Structural overview for compounds 59, 75a, 76a, 76c and 83a.*

All substituents (chloro, methoxy and morpholino) contain electronegative atoms thus can donate electrons into the aromatic system via the mesomeric effect, whilst also possessing an electron withdrawing inductive effect. As such, it is likely the electron density surrounding the substituent contributes to inducing the desired biological response. To test this hypothesis, an electron density map for analogues **59**, **75a**, **76a, 76c** and **83a** should be determined in which it is envisaged all substituents around the aniline will have a similar electron distribution.

Additionally, the findings in this chapter support the inclusion of a heteroaromatic ring to induce interactions with the essential residue Asp103$^{3.32}$ on TM 3 along with hydrophobic interactions with TM 6. A revised 3-point pharmacophore suitable for hTAAR1 ligand development is shown in Figure 4.9, however due to the absence of binding data obtained in this project, further analysis is required to confirm its accuracy.
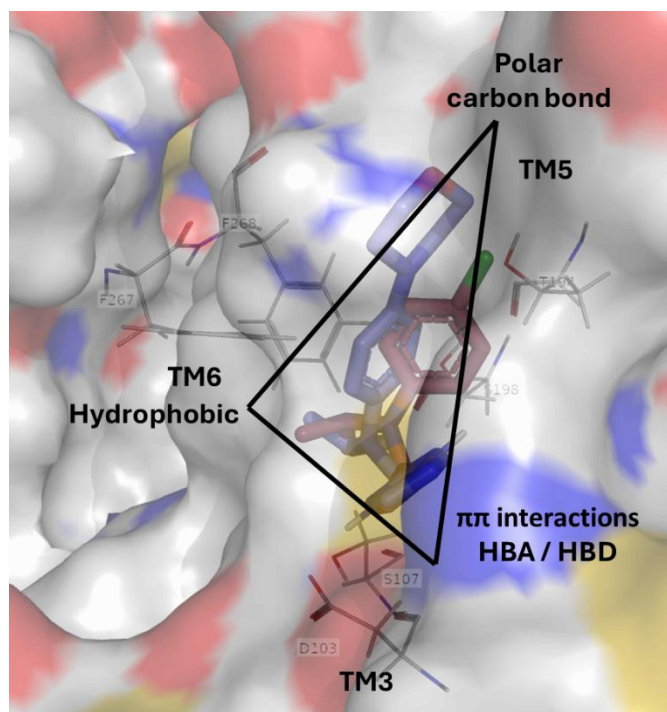
Figure 4.9 *Revised 3-point pharmacophore for peripheral hTAAR1 agonists.*

4.6. Conclusions

Expanding on the data shown in Chapter 3, a set of potential hTAAR1 agonists (compounds **82a-d** and **83a-d**) were designed with increased polarity compared to that of RO5073012 (**59**) and literature analogues (**75a**, **76a** and **76c**) to prevent BBB penetration. Docking of **82a-d** and **83a-d** into a validated hTAAR1 homology model resulted in the expected interactions within the active site to be obtained; however the predicted hydrogen bonds were slightly shorter than the optimal length [221]. Similar findings were shown when docking of **82a-d** and **82a-d** was carried out in cryo-EM structure (PDB: 8W88).

Synthesis of **82a-b** and **83a-b** was completed using the optimised reductive amination method developed in Chapter 3, whereby the Lewis acid catalyst $CeCl_3.7H_2O$ was present to increase the rate of imine formation. Successful synthesis of **82c** and **83c** took several attempts. Initially Buchwald-Hartwig cross coupling was attempted using compounds **89a-b** as the starting material and reacting them in the presence of *N*-Boc-piperazine, $Pd(OAC)_2$ and BINAP, though challenges arose during this process including the reaction not occurring. Substituting BINAP for

Xanthphos™ or Xphos™ did not aid with reaction progression. Therefore, to overcome this challenge, the order of reaction was modified with efforts made to limit the potential of undesirably removing the *N*-Boc protecting group. Firstly, an alkylation reaction was completed to add the isopropyl moiety to the substituted aniline, followed by reductive amination using picoline borane for the imidazolyl-moiety attachment. The treatment of **82c** and **83c** in 1M HCl for 30 minutes yielded compounds **82d** and **83d**.

Compounds **82a-c** and **83a-d** were non-toxic towards INS-1 cells, with one compound (**83a**) enhancing insulin secretion relative to the GLT control. Compounds **83b** and **83d** significantly decreased insulin secretion in GLT conditions (p = 0.0368 and 0.035, respectively), with **83b** also showing a significant reduction in the control conditions (p = 0.0307). As for **75a**, the use of **83b** and **83d** in this study was discontinued to prevent potential hyperglycaemia occurring. To identify whether these observed effects where through interaction with a $G_{\alpha s}$PCR, cAMP accumulation was determined for **18**, **59**, **70**, **76a**, **76c**, **82b** and **83a**. Whilst endogenous agonist tyramine (**18**) significantly enhanced cAMP accumulation (p = 0.0069) correlating with the literature, EPPTB (**70**) did not and as such acted as an antagonist in this study. One compound, **76c** significantly enhanced cAMP in INS-1 cells (p = 0.0481), indicating its mode of action is through agonism of $G_{\alpha s}$PCR. Given the signalling pathway shown in Figure 1.28, it is believed the effects of **76c** occur via agonism of TAAR1; however further investigation is required to confirm this hypothesis. Despite shown to enhance insulin secretion, the predicted peripherally active TAAR1 agonist **83a** significantly decreased cAMP levels (p = 0.0047) in the tested INS-1 cell line; thus, further efforts are required to identify its mode of action. Although **76a** was also found to enhance insulin secretion whilst decreasing cAMP levels (p = 0.0046), it is predicted to permeate the BBB; therefore, no further investigation is required to identify its mode of action due to the potential of inducing on-target CNS psychotic effects.

The rationale behind the design of compounds **82a-d** and **83a-d** was proven to be effective as BBB membrane permeability analysis indicates analogues **82a-c**, **83a** and **83c** are likely to remain in the periphery. This is due to the BOILED-Egg model indicating these compounds are likely to be P-glycoprotein substrates, their decreased lipid solubility and the experimentally calculated P_m being within the literature classification for compounds with low passive BBB permeability (P_m: <9.48), however, to confirm this hypothesis, compounds **82a-c**, **83a** and **83c** should be tested on a BBB cell model. Introduction of polar substituents to reduce BBB penetration advanced the pharmacophore profiling of pancreatic hTAAR1 agonists.

5. Modifications to the CH₂ linker

Galley *et al* show RO5073012 (**59**) has TAAR1 agonistic activity in human embryonic kidney-293 (HEK-293) cell lines expressing hTAAR1, rTAAR1 and mTAAR1 as well as in *in vivo* rodent models [173], which coupled with the functional pharmacological evaluation presented in Chapter 3, suggests **59** could enhance insulin secretion through a TAAR1-mediated mechanism. Its ability to behave as an agonist against different species receptor variants along with its potency and selectivity for hTAAR1 over adrenergic α2 receptors were properties which made **59** an attractive lead compound for further SAR investigation. The molecular modelling studies previously discussed in this thesis allow for prediction of agonist binding to the intracellular binding pocket of hTAAR1 resulting in identification of regions which could be modified to allow for maximal interaction with the receptor. The docking of **59** showed the aminomethylene linker did not participate in any critical interactions with amino acid residues present within the hTAAR1 binding site. The other functional groups present on **59** such as the phenyl and imidazole moieties were significant for stabilisation of the molecule through hydrogen bonding and π-π interactions. We therefore decided to modify the linker region by developing a series of compounds containing an amide bond to allow for further interactions with hTAAR1 to occur such as hydrogen bond interactions with Arg83[ECL1].

Classical routes to synthesise amides rely on the use of coupling reagents or prior conversion of the carboxylic acid into an activated form (e.g. acyl halide or activated ester) or using a catalyst [306, 307]. On this basis, the strategy employed investigated the use of eight conditions involving coupling reagents as well as using an acyl chloride.

5.1. Molecular docking

5.1.1. Molecular docking into hTAAR1 homology models

Incorporating an amide moiety in the linker region, opens the possibility for additional hydrogen bond interactions to occur between the ligand and hTAAR1, whilst maintaining the previously

predicted interactions. Subsequently, this could increase the analogue's binding affinity for hTAAR1 as well as potentially improving the compound's overall efficacy, biochemical and physicochemical properties. Moreover, this strategy could allow for further functionalisation of promising compounds through introducing amide bioisosteres such as sulfonamides, esters or amidines [308].

Using the substitutions explored in compounds **82a-d** and **83a-d** along with **59** and **76c**, a series of eight analogues containing an amide bond (**92a-d** and **93a-d,** Figure 5.1) were docked into the intracellular binding site of hTAAR1 homology model 17, Figure 5.2. Upon analysis it was observed that a slightly lower docking score was generated for these molecules (Table 5.1) compared to compounds **82a-d** and **83a-d** (Chapter 4).

92a
pK_a: **10.9**

92b
pK_a: **10.9**

92c
pK_a: **10.8**

92d
pK_a: **10.9**

93a
pK_a: **11.4**

94b
pK_a: **11.4**

93c
pK_a: **11.3**

93d
pK_a: **11.4**
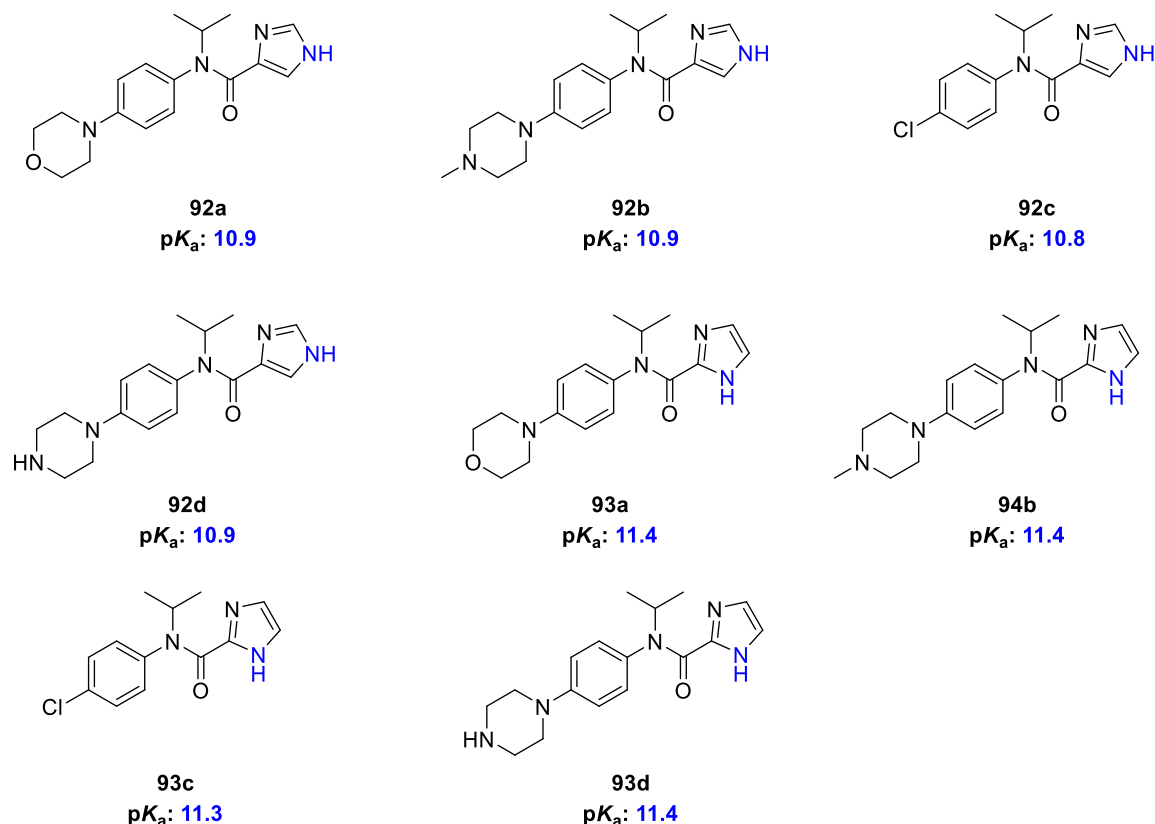
Figure 5.1 Proposed ligands to investigate linker modifications of 59 and 92a-d and 93a-d.
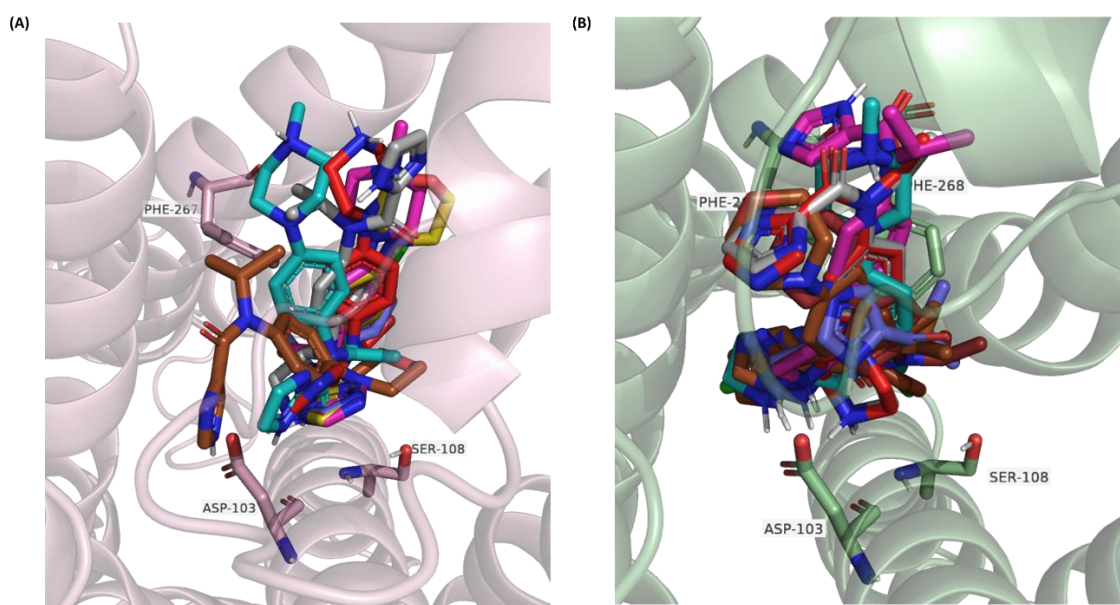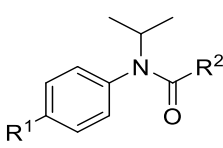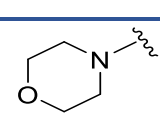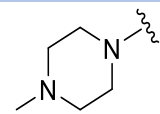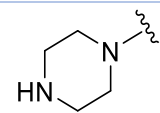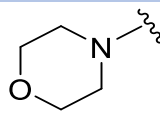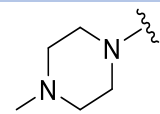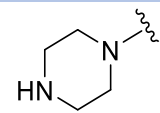
Figure 5.2 *Docked pose of **92a-d** and **93a-d** (**92a**: brown, **92b**: magenta, **92c**: blue, **92d**: red, **93a**: yellow, **93b**: cyan, **93c**: chocolate and **93d**: grey) into hTAAR1 homology model 17 **(A)** and cryo-EM structure (PDB: 8W88) **(B)**. Image visualised down transmembrane (TM) 3. Docking performed using Schrödinger's Maestro and Glide 12.6 packages and images created using PyMOL 4.6.0.*

The docked poses of **92a** and **93d** show the most variation in binding pose as the imidazole moiety is oriented towards the entrance of the binding site between TMs 5 and 6 for compound **93d**, whilst for compound **92a**, it has shifted towards TM 7 (Figure 5.3). As such **93d** failed to form a hydrogen bond with conserved residue Asp103$^{3.32}$ via the pyrrolic NH in the imidazole moiety. Instead, the crucial residue interaction was formed via the piperazine moiety (Figure 5.4) differing from compounds **92a-d** and **93a-c** and notably RO5073012 (**59**). Upon further analysis, this change in ligand/receptor interaction is expected due to a reduction in pK_a being predicted for the pyrrolic NH when an amide is present (Figure 5.1). Surprisingly, the conformation of the docked pose generated for compound **93d** gave a comparable docking score (-5.437 kcal/mol) compared to the other analogues in this series (Table 5.1), however it was slightly lower than that of RO5073012 (**59**) (-6.045 kcal/mol). This suggests that although more favourable, the critical interaction with residue Asp103$^{3.32}$ does not need to involve the imidazole moiety, allowing for further modifications of this moiety to be explored.

Table 5.1 *Docking scores for compounds **92a-d** and **93a-d** in complex with hTAAR1 homology model 17 and hTAAR1 cryo-EM structure (PDB: 8W88).*

Compound	R^1	R^2	Docking score (kcal/mol)	
			hTAAR1 homology model 17	hTAAR1 Cryo-EM structure (PDB: 8W88)
92a	(morpholinyl)	4-imidazolyl	-5.071	-5.313
92b	(4-methylpiperazinyl)	4-imidazolyl	-5.641	-3.533
92c	Cl	4-imidazolyl	-4.941	-5.148
92d	(piperazinyl)	4-imidazolyl	-5.153	-4.442
93a	(morpholinyl)	2-imidazolyl	-6.288	-5.956
93b	(4-methylpiperazinyl)	2-imidazolyl	-4.928	-2.357
93c	Cl	2-imidazolyl	-5.889	-4.602
93d	(piperazinyl)	2-imidazolyl	-5.437	-4.923
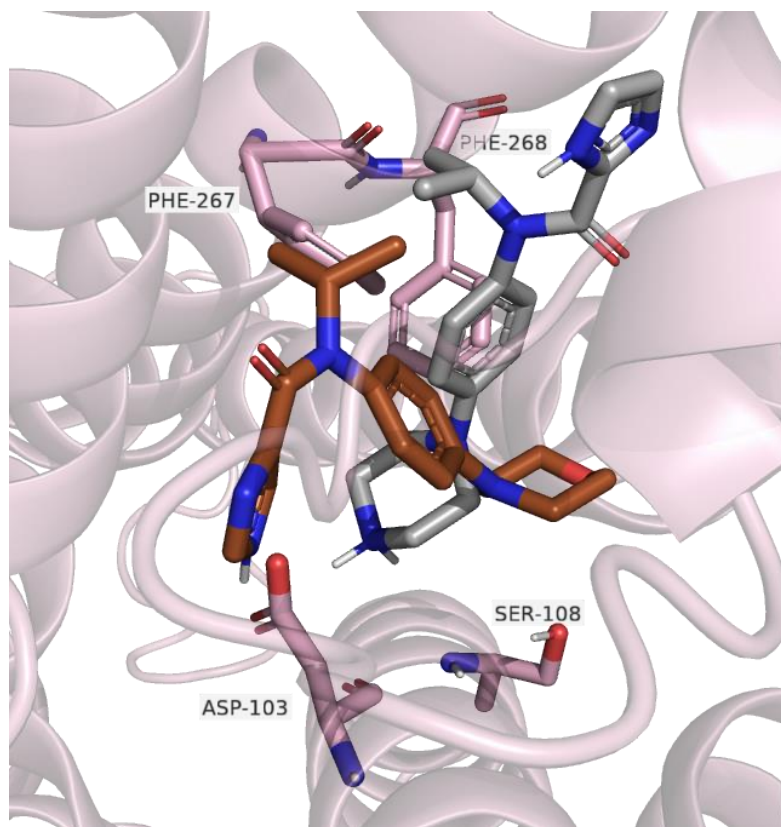
*Figure 5.3 Docked pose of compounds **92a** (brown) and **93d** (grey), into hTAAR1 homology model 17 showing variation in imidazole orientation. Docking performed using Schrödinger's Maestro and Glide 12.6 packages and images created using PyMOL 4.6.0.*

The positioning of the imidazole moiety is consistent for analogues **92a**, **92c-d** and **93a-c** which allowed for hydrogen bond interactions with Asp103[3.32] to occur differing from the data shown in Chapter 3 whereby the protonated form of the imidazolium ring meant ionic interactions were predicted with Asp103[3.32]. The predicted hydrogen bond lengths between compounds **92a-c** and **93a-d** and Asp103[3.32] varied between 1.78 – 1.92 Å. A slightly longer salt bridge (3.19 Å) was predicted between Asp103[3.32] and analogue **93d**. Despite a shift in position within the binding site, **93c** also formed a hydrogen bond with Asp103[3.32] via the pyrrole-like NH in the imidazole moiety, albeit slightly shorter than the optimal length [221].

The binding poses obtained for compounds **92a**, **92c-d** and **93a-c** facilitated the substituted aniline moiety to be directed towards the top of TM 6 owing to further stabilisation by π-π interactions with Phe185[ECL2] and Phe267[6.51], halogen bonding with Thr271[6.55] and additional

hydrogen bonds with Asp274$^{6.58}$, Figure 5.4. Despite variation within their binding pose, compounds **92b** and **93d** also undergo additional stabilisation via interactions with Phe185^{ECL2} and Arg83$^{2.64}$, thus leading to the moderate-high docking score obtained (Table 5.1).
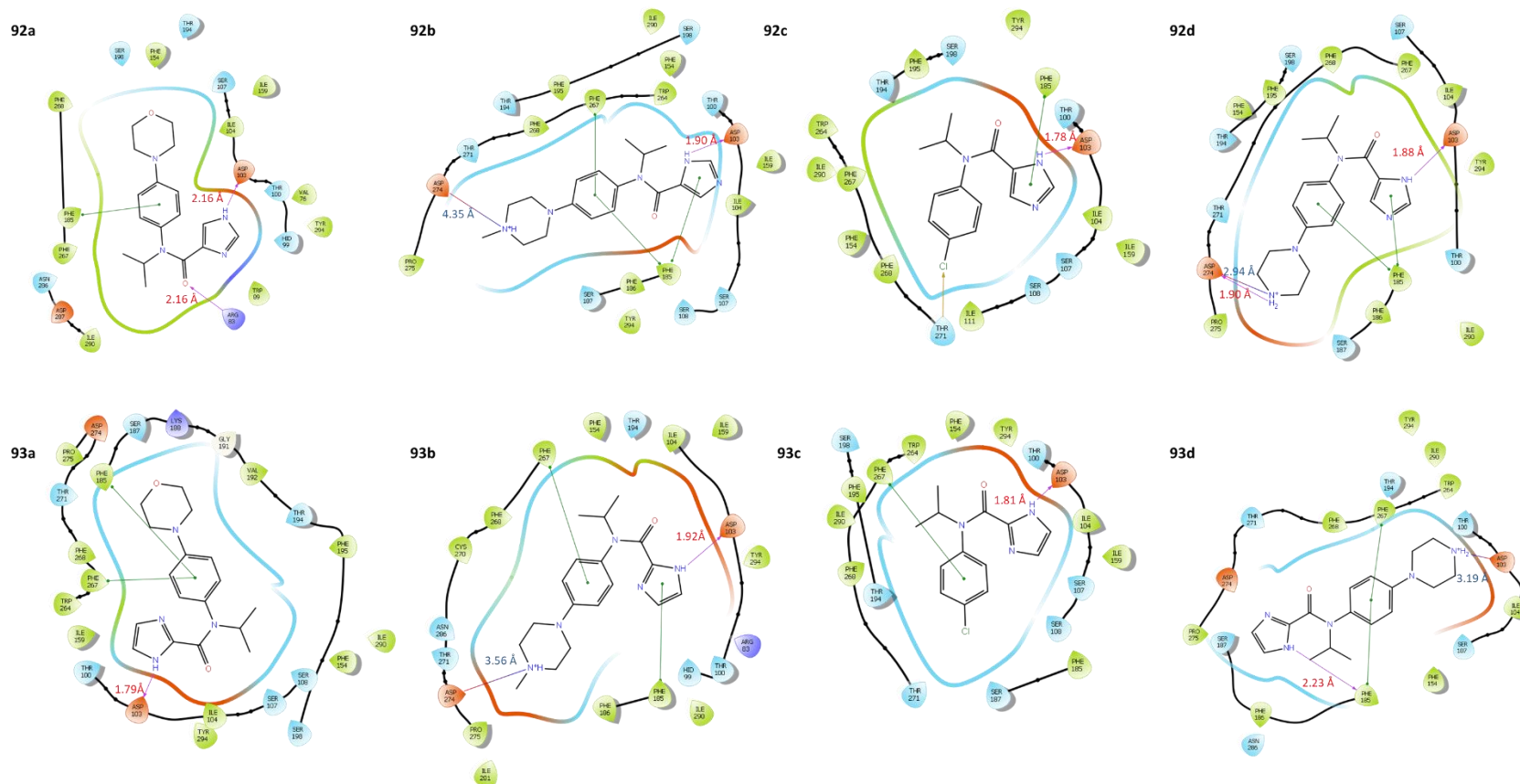
Figure 5.4 *Predicted interactions between hTAAR1 homology model with compounds **92a-d** and **93a-d**. π-interactions and hydrogen bond length measurements shown in red. Expected length of salt bridges shown in blue. Amino acid description: Green; hydrophobic, blue; positively charged, cyan; polar.*

Comparison of **92a-d** and **93a-d** with their corresponding aniline ligand (**59**, **76c**, **82a-b**, **82d**, **83a-b**, **83d**) is shown in Figure 5.5, where no clear trend within changes to binding pose is observed. The docked poses of ligands **92c** and **93c** overlay well with literature analogues **59** and **76c** respectively, with the main differences observed been the slightly distorted conformation of the phenyl moiety. A similar difference in binding pose is shown in Figure 5.5 D between analogues **92d** and **82d** as well as in Figure 5.5 F between compounds **93a** and **83a**. As for the poses shown in Figure 5.5 B, G and H, the amide and corresponding aniline ligands were ill-aligned.
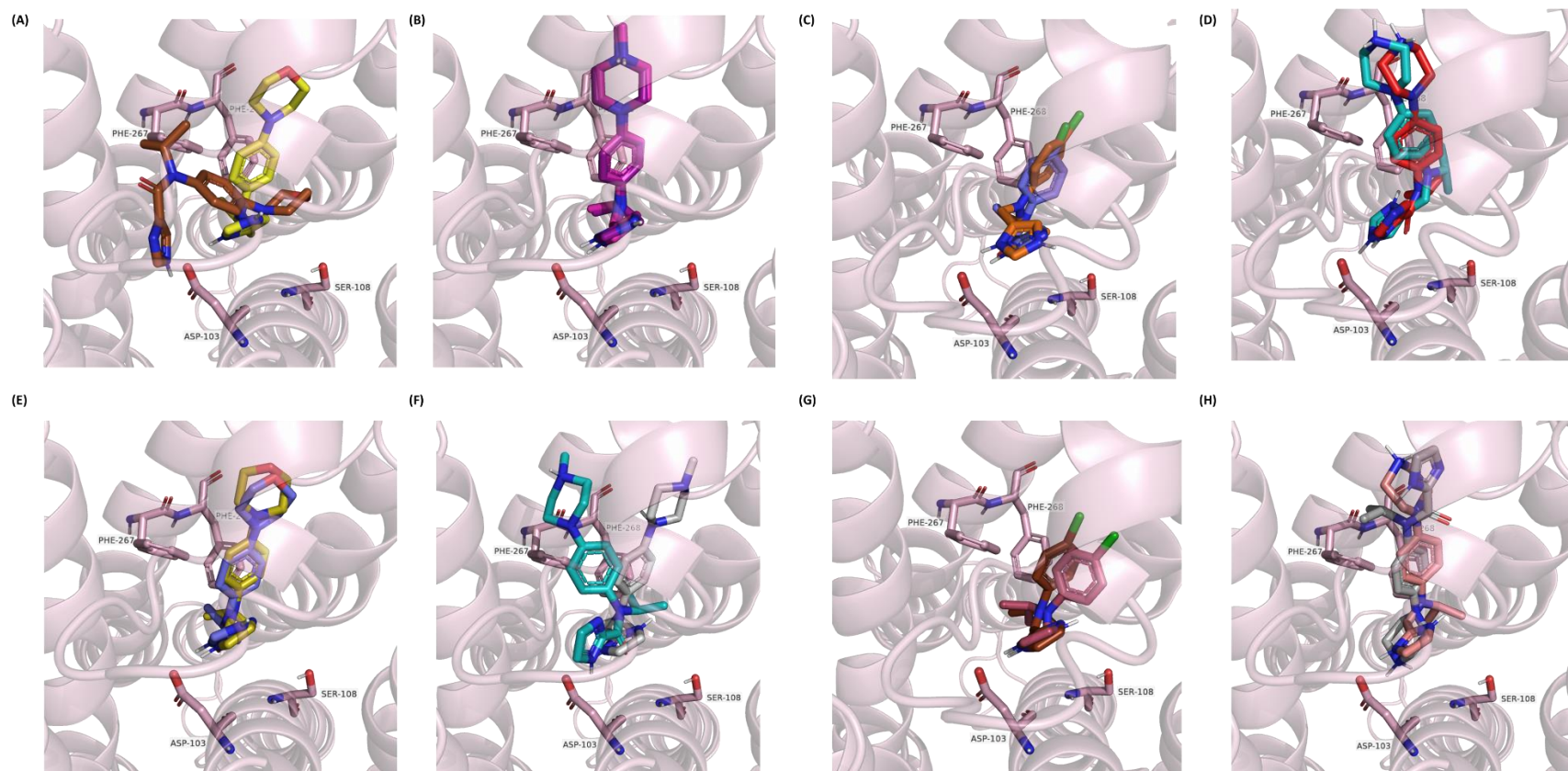
Figure 5.5 *Overlay of ligands containing an amide bond (**92a-d** and **93a-d**) with their corresponding aniline analogue. Docking performed using Schrödinger's Maestro and Glide 12.6 packages and images created using PyMOL 4.6.0. From left to right: **(A)** yellow; **82a**, chocolate; **92a**. **(B)** deep purple; **82b**, magenta; **92b**. **(C)** orange; **59**, skyblue; **92c**. **(D)** cyan; **82d**, red; **92d**. **(E)** slate; **83a**, lemon; **93a**. **(F)** grey; **83b**, cyan; **93b**. **(G)** raspberry; **76c**, brown; **93c**. **(H)** salmon; **83d**, grey; **93d**.*

5.1.2. Comparison between molecular docking into hTAAR1 homology modelling and hTAAR1 cryo-EM (PDB: 8W88)

Using the validated docking protocol, compounds **92a-d** and **93a-d** were docked into the cryo-EM structure (PDB: 8W88) to determine the accuracy of the binding poses obtained within the homology model. On initial visualisation of Figure 5.2, compounds **92a-d** and **93a-d** occupy a much tighter space within the binding site; however, as in the homology model variation between ligand orientation was observed (Figure 5.6). The binding poses obtained for compounds **92b**, **92d** and **93d** facilitates the imidazole moiety to be directed towards the top of TM 6 (Figure 5.6 A); subsequently all three compounds are not predicted to form a hydrogen bond with Asp103$^{3.32}$ via the imidazole ring, instead forming the crucial residue interaction with the piperazine moiety (Figure 5.7). This further suggests the imidazole moiety may be replaced with other heteroaromatic and cyclic functional groups whilst still maintaining activity at hTAAR1. As for the docked pose obtained in the homology model, the substituents present in analogues **93a**-**c** are positioned towards the top of TM 6, with the imidazole moiety bound deep into the binding site. Differing from the homology model, the docked pose of **92a** into cryo-EM structure (PDB: 8W88) was like that of compounds **93a-c** (Figure 5.6 B).
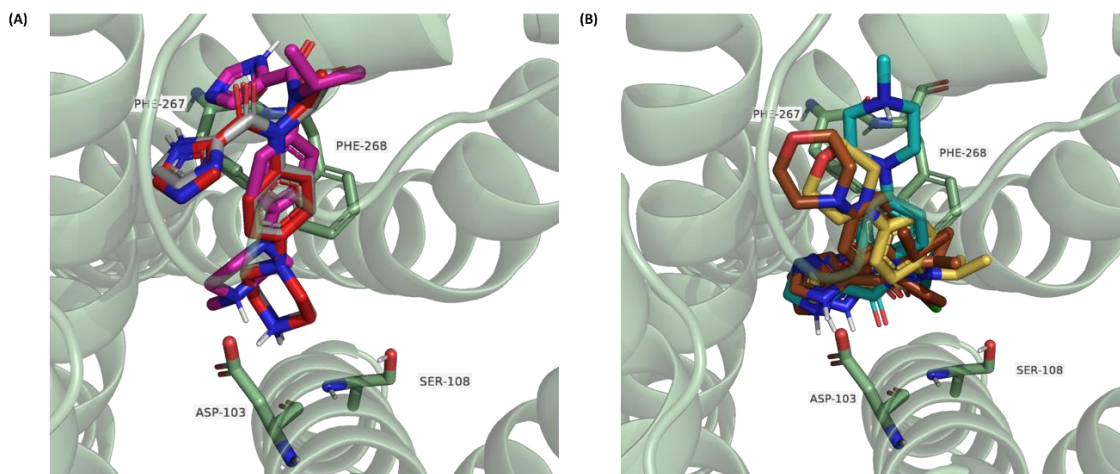
*Figure 5.6 Docked pose of compounds **92b** (magenta), **92d** (red) and **93d** (grey) into hTAAR1 cryo-EM structure (PDB: 8W88) showing imidazole orientation towards the top of TM 7 **(A)** and docked pose of compounds **92a** (brown), **93a** (yellow), **93b** (cyan) and **93c** (chocolate) into hTAAR1 cryo-EM structure (PDB: 8W88) showing the imidazole moiety positioned deep within the binding pocket **(B)**. Docking performed using Schrödinger's Maestro and Glide 12.6 packages and images created using PyMOL 4.6.0.*

Despite the differences between ligand interaction and hTAAR1 structure observed, the docking scores obtained within the cryo-EM structure (PDB: 8W88) are comparable to those obtained within the homology model for compounds **92a**, **92c-d**, **93a** and **93c-d**, Table 5.1**.** However, for both **92b** and **92b** much lower docking scores were obtained (-3.535 kcal/mol and -2.357 kcal/mol respectively) suggesting the methyl piperazine substituted compounds have opted a more favourable binding pose in the homology model. As both compounds underwent comparable further stabilisation via interactions with Phe185[ECL2] Phe267[6.51], Asp274[6.58] in both the homology model and cryo-EM structure (PDB: 8W88), it is difficult to determine why a more favourable binding pose was obtained in the validated homology model. As the main difference is that stabilisation between the ligands and homology model utilises π-π interactions with Phe185[ECL2], it is possible that this is responsible for generating the higher docking score obtained and more favourable binding pose (Figure 5.4).
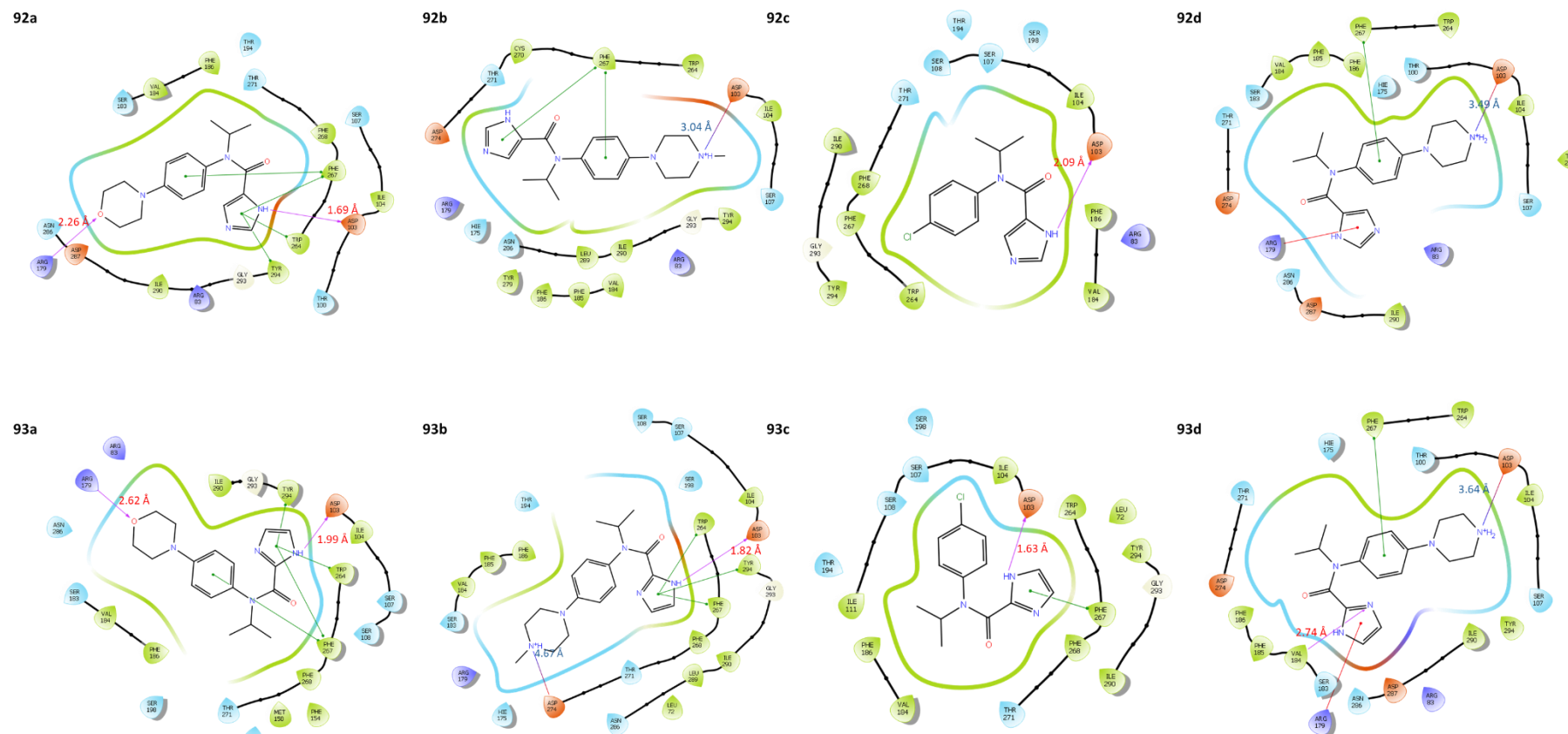
Figure 5.7 *Predicted interactions between hTAAR1 cryo-EM structure (PDD: 8W88) with compounds **92a-d** and **93a-d**. π-interactions and hydrogen bond length measurements shown in red. Expected length of salt bridges shown in blue. Amino acid description: Green; hydrophobic, blue; positively charged, cyan; polar.*

5.2. Attempted synthesis of 92a-d and 93a-d

The synthesis of amides can be broken down into two major synthetic pathways defined by the corresponding starting material, namely using a carbonyl group adjacent to a good leaving group or a coupling reagent as the reactant.

Scheme 5.1 *Amide coupling of **94** in the presence of HATU.*
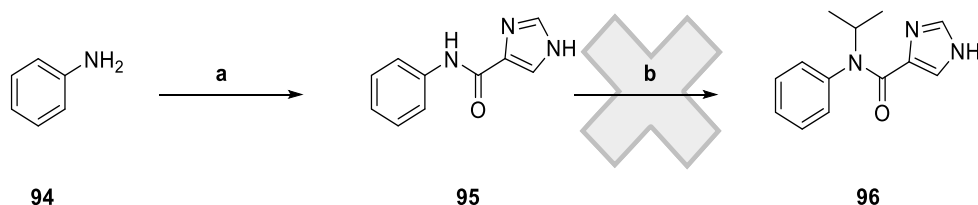
Reagents and conditions: (a) 1*H*-imidazole-4-carboxylic acid, HATU, DMF, DIPEA, 70°C, 18 hr (91%). **(b)** No suitable conditions attempted.

Synthesis of ligands **92a-d** and **93a-d** was attempted via several routes, with initial chemistry investigated via the reaction of aniline (**94**) with imidazole-4-carboxylic acid (**97**) in the presence of 1-[Bis(dimethylamino)methylene]-1*H*-1,2,3-triazolo[4,5-*b*]pyridinium 3-oxide hexafluorophosphate (HATU) to form **95** (Scheme 5.1). It was expected that further synthesis would allow for the attachment of the isopropyl moiety via alkylation to form **96**, although a thorough search of the literature delivered only a few potential experimental conditions due to the poor reactivity of compound **95**. One method, published by Chaturvedi *et al* [309] was identified whereby amides were reacted with iodomethane or bromoethane in dimethylformamide (DMF) at 0°C, before refluxing at 60°C for 12 hours to give the corresponding secondary amide in high yields (76-85%). It is expected the principles behind this method could be applied to the synthesis of **92a-d** and **93a-d**, by replacing iodomethane with 2-iodopropane, however this was not attempted.

To overcome the poor reactivity of the amide, various attempts were made to synthesise isopropyl-substituted secondary amines **98a-b**. Initially, *para*-substituted anilines (**80c**, **84b**) underwent reductive amination with 2-methoxypropene using NaBH(OAc)$_3$ as the reducing

agent, similar to the method described by Galley *et al* [173] (Scheme 5.2). Unfortunately, this reaction was not successful, and an undesired reaction occurred affording acetanilides **99b-c**, correlating with the findings reported by Pletz *et al*, Scheme 5.2 [310]. It is expected this by-product occurred due to the slow rate of imine formation, thus allowing nucleophilic substitution with NaBH(OAc)$_3$ to be more favourable (Scheme 5.3) [310]. Although not attempted, it is expected reductive amination between anilines (**80c** and **84b**) and acetone followed by hydrogenation of the imine would result in low yields, again due to the slow rate of imine formation. Furthermore, as compound **80c** contains a chlorophenyl group which introduces electron-withdrawing properties into the molecule, thus decreasing the nucleophilicity on the aniline and consequently further reducing the rate of imine formation [311].

*Scheme 5.2 Synthesis of **91** and **98a-c** and the undesired products **99b-c**.*

a	R = 4-morpholino
b	4-methylpiperazin-1-yl
c	Cl
90, 91	tert-butyl-4-piperazine-1-carboxylate
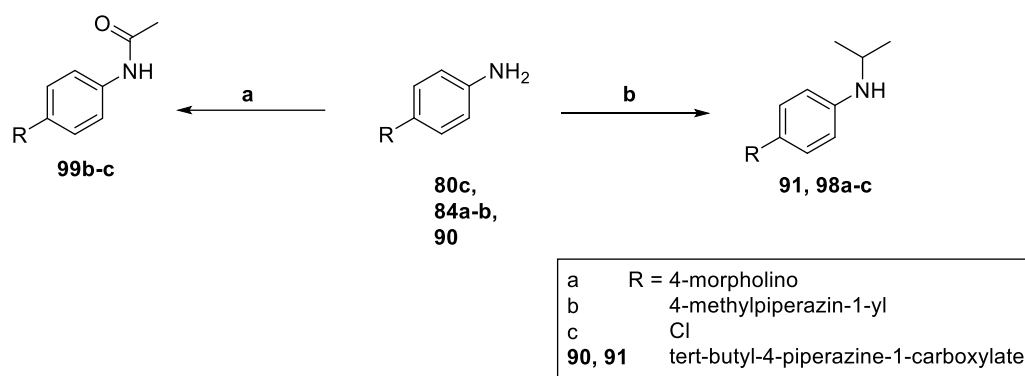
Reagents and conditions: (a) 2-methoxypropene, TFA, NaBH(OAc)$_3$, 1,2-DCE, 60°C, 5 hr (33-38%). **(b)** K$_2$CO$_3$, 2-iodopropane, 1,4-dioxane, microwave, 150°C, 1 hr (24-70%).

Scheme 5.3 *Proposed mechanism for formation of acetanilides* **99b-c**.

b	R = 4-methylpiperazin-1-yl
c	Cl
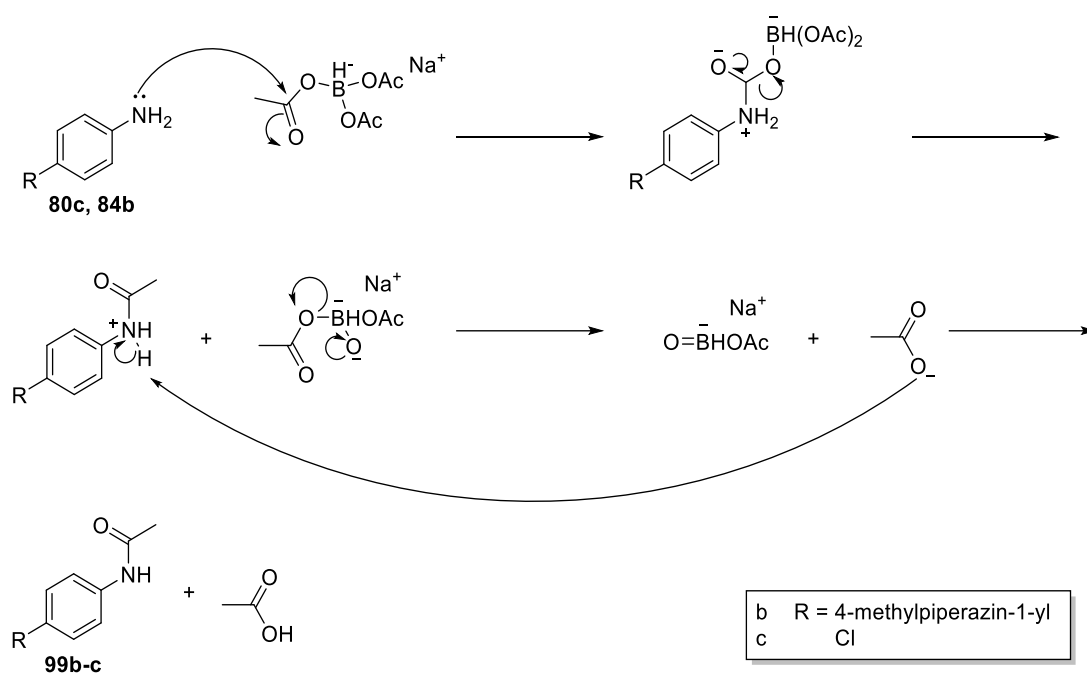
Alkylation of anilines has been shown to give secondary amines in high yields. When attempted following a method described by Guest *et al*, the reaction did not go to completion. ^{1}H-NMR confirmed the ratio of product: unreacted starting material to be 1: 0.8 or 1: 0.5 for compounds **98a-b** respectively. Due to the close R_f values, unreacted starting amine (**80c** and **84b**) co-eluted with products **98a** or **98b** during purification via automated flash column chromatography, thus further efforts were required to isolate the desired compounds [296]. Repeated purification did not result in separation of the two components; thus, it was prudent to optimise the reaction conditions, in turn allowing the alkylation to go to completion. During method optimisation, the acetonitrile solvent system was replaced with 1,4-dioxane and **91** and **98a-c** were successfully synthesised and isolated as their free base, evidenced by ^{1}H-NMR analysis (Scheme 5.2).

Several attempts were made to acylate isopropyl-substituted anilines **91**, **98a-c** with imidazole-4-carboxylic acid (**97**). Initial activation of **97** into the corresponding acid chloride was obtained via the addition of oxalyl chloride in the presence of a DMF catalyst, following the methods described by Jasim *et al* and Rippol *et al*, Scheme 5.4 [312, 313]. The resulting acyl chloride (**100**) was added dropwise to **98b-c** and reacted in the presence of *N,N*-Diisopropylethylamine (DIPEA)

overnight [314]. Reaction monitoring via thin layer chromatography (TLC) showed consumption of **98b-c**, suggesting the reaction had completed and thus was worked up.
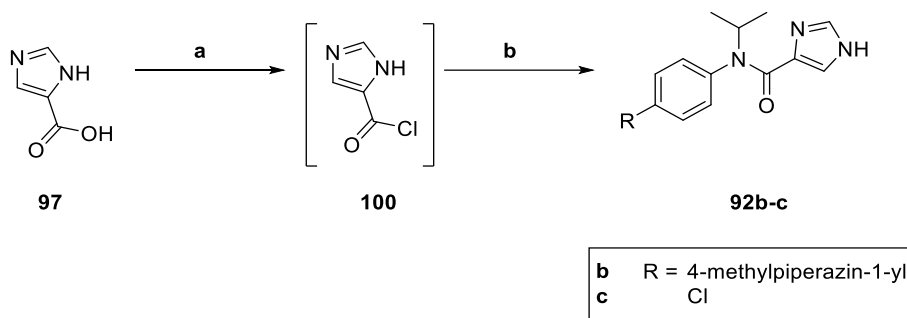
Reagents and conditions: (a) oxalyl chloride, anhydrous DMF, N$_2$, 60°C, 3 hr. **(b)** substituted amine (**98b/ 98c**), DIPEA, anhydrous DCM, rt, 18 hr.

^{1}H-NMR analysis of **92b** showed an absence of the expected CH$_3$ peak belonging to the methyl-piperazine moiety. Further investigation revealed the predicted pKa values of the piperazine nitrogen and imidazole ring being 8.15 and 9.13 respectively [315, 316], suggesting the compound was likely to be found in the aqueous layer. Therefore, all aqueous solvent was removed and the resulting solid re-extracted into acetonitrile. Although identified to be present via ^{1}H-NMR analysis, the yield was unfortunately too low to isolate the desired product purely. Compound **92c** was also re-extracted into acetonitrile but like **92b**, a low yield was obtained, and the product could not be isolated.

Formation of the amide bond using numerous coupling reagents was also attempted. As the reagents required for the synthesis of **98c** are cheap and readily available, all investigations were carried out using this compound. Firstly, **98c** and **97** were reacted with 1-((1-Cyano-2-ethyoxy-2-oxoethylideneaminooxy)dimethylaminomorpholino) uronium hexafluorophosphate (COMU) in DMF at room temperature and pressure [317]. After work up with EtOAc and aq. sodium bicarbonate, an orange oil was obtained and, unfortunately, only starting material was recovered from this reaction as confirmed by ^{1}H-NMR [318]. It is likely that conversion from **97** to

the activated ester complex with COMU did not proceed by this method. To assess whether temperature was a limiting factor, the reaction was repeated at 70°C. Evidence suggested the ester complex had formed due to the observation of a yellow colour change. This colour change was observed due to the charge transfer through π-π stacking between the aromatic compounds [319]; however like the reaction carried out at room temperature, the desired product was not obtained. Replacing COMU with HATU had little effect, and the formation of the amide was not evident by ^{1}H-NMR and LC-MS analysis.

Attempted formation of the amide bond was optimised utilising a variety of coupling reagents (Table 5.2). Initially **98c** was reacted at room temperature and pressure in the presence of a coupling reagent for 18 hours. Minimal changes were identified during monitoring via LC-MS for almost all conditions, however, formation of the activated ester complex was noted when using *N,N'*-dicyclohexylcarbodiimide (DCC) as the coupling reagent. After 24 hours, *N,N*-dimethylaminopyridine (DMAP) - a nucleophilic catalyst, was added to each reaction to increase the rate of product formation; however this had little effect.

Table 5.2 *Amide coupling of **98c** with imidazole-4-carboxylic acid using different coupling reagents for 18 hours. Representative active ester complex shown using DCC as an example. Ratio expressed as % relative to peak area of **99a** obtained via LC-MS analysis.*
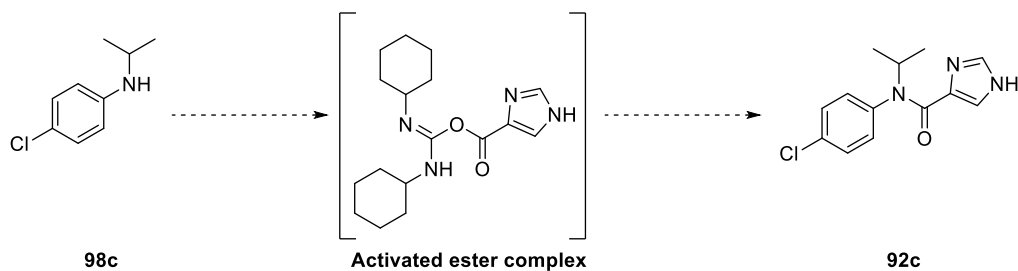
Coupling reagent	Ratio (%)		
	99a	Activated ester formation	Product (93a)
DCC	71.45	28.07	0.485
(3-Dimethylamino-propyl)-ethyl-carbodiimide hydrochloride (EDC HCl)	100	0	0
Benzotriazole-1-yloxytripyrrolidinophosphonium hexafluorophosphate (PyBOP)	100	0	0
Bromo(tri-1-pyrrolidinyl)phosphonium hexafluorophosphate (PyBrOP)	100	0	0
HATU	100	0	0
COMU	100	0	0
1,1'-carbonyldiimidazole (CDI)	100	0	0
EDC/Hydroxybenzotriazole (EDC/HOBt)	100	0	0

As the reaction involving DCC as the coupling reagent showed promise through the formation of the activated ester intermediate, further investigation was completed (Table 5.3). The reaction mixture was transferred to a sealed microwave vessel and heated in 30-minute increments over a range of temperatures. Although heating the reaction overcame some of the potential thermodynamic barrier and consumption of activated ester and starting amine was observed, an unknown impurity began to form. This is due to the observation of a new peak being detected (R_t: 3.02, $[M+H]^+$ found 301.2 and 449.4). It is expected the impurity observed is an acylated urea due to rearrangement of the activated ester complex occurring, however further characterisation is required to confirm this [320, 321]. To hinder the rate of impurity formation, and to favour the amide coupling, a high excess of starting amine (**98c**) was added. Unfortunately, this had little effect and minimal changes in activated ester, starting amine and impurity were observed (Table 5.3). The amide product (**92c**) could not be isolated due to the closeness of peaks shown on the LC-MS trace combined with the small scale the reaction was completed on.

As the desired product was unable to be isolated from using both an acid chloride or coupling reagent to form the amide bond, it was decided not to proceed with the synthesis of potential hTAAR1 agonists **92a-d** and **93a-d**. Therefore, amide formation using imidazole-2-carboxylic acid (**101**) and **91** and **98a-c** was not attempted and, consequently, the pharmacological properties of these compounds could not be evaluated.

Table 5.3 *Optimisation of amide coupling of **98c** with imidazole-4-carboxylic acid (**97**) using DCC as the coupling reagent. Predicted impurity is expected to have formed via rearrangement of the activated ester complex to form an acylated urea. Ratio expressed as % relative to peak area of **99a** obtained via LC-MS analysis.*
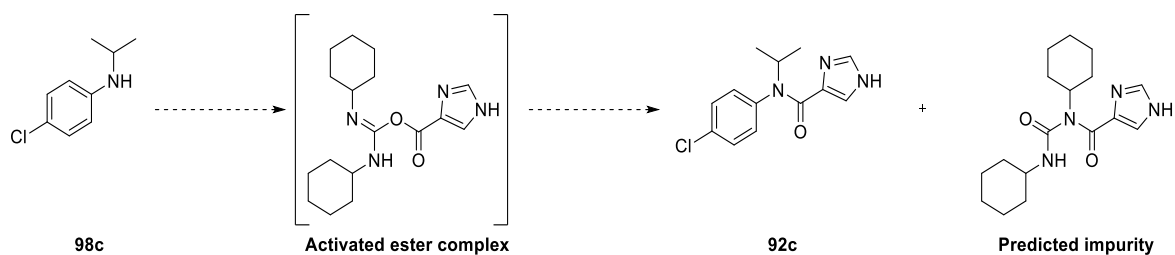
Coupling reagent	**Ratio**			
	98c	**Activated ester formation**	**Product (92c)**	**Impurity formation**
1 hr rt	71.44	28.07	0.486	n/a
24 hr rt	15.24	83.84	0.917	n/a
32 hr rt (DMAP added)	14.79	84.19	1.01	n/a
48 hr rt (DMAP added)	15.07	83.88	1.05	n/a
After 30 min @ 50°C	13.59	85.5	0.9	n/a
After 1.5 hr @ 50°C	13.47	79.7	1.56	5.26
After 30 min @ 80°C	12.62	76.95	1.85	8.57
After 30 min @ 100°C	13.08	68.44	2.05	16.42
After 1 hr @ 100°C	13.64	63.34	1.79	21.23
After 1.5 hr @ 100°C	13.00	63.58	1.76	21.66
Additional amine added, 30 min @ 100°C	63.87	25.10	1.75	9.27
After additional amine added, 1 hr @ 100°C	66.11	22.64	1.57	9.68

Table 5.3 Continued.

Coupling reagent	Ratio			
	98c	**Activated ester formation**	**Product (92c)**	**Impurity formation**
After additional amine added, 1.5 hr @ 100°C	68.20	20.31	1.59	9.88
After additional amine added, 2 hr @ 100°C	65.99	21.18	1.69	11.13

5.3. Conclusions

Docking studies of RO5073012 (**59**) and closely related compounds into a validated hTAAR1 homology model and cryo-EM structure (PDB: 8W88) show key interactions with hTAAR1 occur via the imidazole and phenyl moieties present. As the linker moiety was identified as a non-critical region for receptor binding during docking studies, it guided the design of eight amide analogues (**92a-d** and **93-d**) of RO5073012 (**59**). These analogues aimed to utilise the binding space through inducing additional interactions with hTAAR1, in turn increasing the compound's binding affinity for the therapeutic target.

Molecular docking of **92a-d** and **93a-d** into a validated hTAAR1 homology model resulted in variation in binding poses to be observed, with the pose generated for analogues **92a** and **93d** being ill-aligned with the previously reported pose for RO5073012 (**59**). Although the predicted binding pose of **93d** did not form the critical hydrogen bond with Asp103[3.32] via the pyrrolic NH of the imidazole ring, the desired interaction occurred via the piperazine moiety, suggesting further SAR exploration could occur through replacing the imidazole moiety with other heteroaromatic or cyclic structures. This hypothesis was further supported by the docking score obtained (-5.437 kcal/mol) being comparable to other analogues in this structure-activity relationship; however it was slightly lower than RO5073012 (**59**) (-6.045 kcal/mol). Docking into

a published hTAAR1 cryo-EM structure (PDB: 8W88) supported the poses observed in the validated homology model, with three compounds (**92b**, **92d** and **93d**) failing to form interactions with the conserved residue via the imidazole moiety, instead interaction occurred via the substitutions present on the aniline ring. In both structures, the predicted hydrogen-bond lengths are slightly shorter than the optimal range [221]; however further stabilisation via π-π interactions with Arg83[2.64], His99[3.28], Phe185[ECL2] and Asp274[6.58] is observed correlating with the literature [131]. Despite the rationale for the design of compounds **92a-d** and **93a-d** to allow for additional hydrogen bond interactions to occur between the drug-like molecule and hTAAR1 due to the incorporation of hydrogen bond donors and acceptors, only compound **92a** utilised interactions with the linker region, showing that changing the CH_2 linker to an amide moiety does not increase the binding affinity a ligand has for hTAAR1. Further exploration is required on linker modification to allow for additional ligand stabilisation in the hTAAR1 binding site.

Initial attempts at synthesising compounds **92b-c** involved using imidazole-4-carboxylic acid (**97**) as the starting material and activating it with oxalyl chloride to achieve the corresponding acid chloride (**100**), before reacting with substituted secondary anilines (**80c** and **84b**); however, challenges arose during multiple stages of this process. This included the formation of unwanted side products and difficulties in purification. To overcome these challenges, the reaction conditions were modified, and various coupling agents were screened attempting to form the amide. Of the 8 conditions tested, only one coupling reagent (DCC) showed promise due to the formation of the activated ester complex, however conversion to the amide progressed slowly. To increase the rate of reaction, the mixture was heated up to 100 °C for 6 hours and catalysed using DMAP. As for the use of an acyl chloride, this led to the formation of undesired side products. LC-MS analysis revealed the two products had very similar retention times thus the compounds were not able to be isolated from one another. Due to the time parameters of this project, attempted synthesis of compounds **92a-d** and **93a-d** was terminated and subsequently their pharmacological profile was not evaluated.

Further investigation is required to synthesise compounds **92a-d** and **93a-d**. This could include

increasing the nucleophilicity of the secondary aniline through deprotonating the nitrogen. An

online calculator predicted the pKa to be ~13.7 [316], thus it is expected potassium *tert*-butoxide

(pKa: 17) would be an appropriate base to complete this step. However, optimisation of the

deprotonation step may be required and a stronger base, such as sodium hydride (pKa: 35) could

be required. Alternatively, Sharma *et al* describe the two-step synthesis of *N*-(4-chlorophenyl)-

4,5-dihydro-1*H*-imidazole-2-carboxamide (**102**) by reacting **80c** with chloroacetylchloride in

glacial acetic acid to yield 2-chloro-*N*-(4-chlorophenyl)acetamide (**103**) (Scheme 5.5) [322]. This

acetamide product was further reacted with ethylenediamine and sulphur in toluene to yield

102. Scheme 5.6 shows a possible curly arrow mechanism for the proposed synthesis of **102**.

***Scheme 5.5** Synthesis of N-(4-chlorophenyl)-4,5-dihydro-1H-imidazole-2-carboxamide (**102**) described by Sharma et al*
[322].
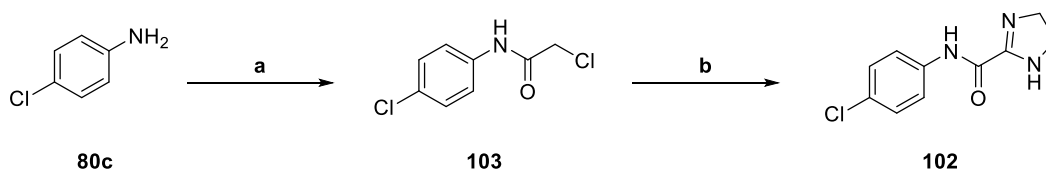
Reagents and conditions: (a) i. Chloroacetylchloride, glacial acetic acid, 10-30°C, 0.5 hr. **ii.** 60 % sodium

acetate solution, 30°C, 0.33 hr. **(b)** ethylenediamine, sulphur, toluene, 100°C, 6 hr.

Scheme 5.6 *Proposed mechanism for the synthesis of* **102**. *Modified from Yu et al* [323] *and Zhang et al* [324].
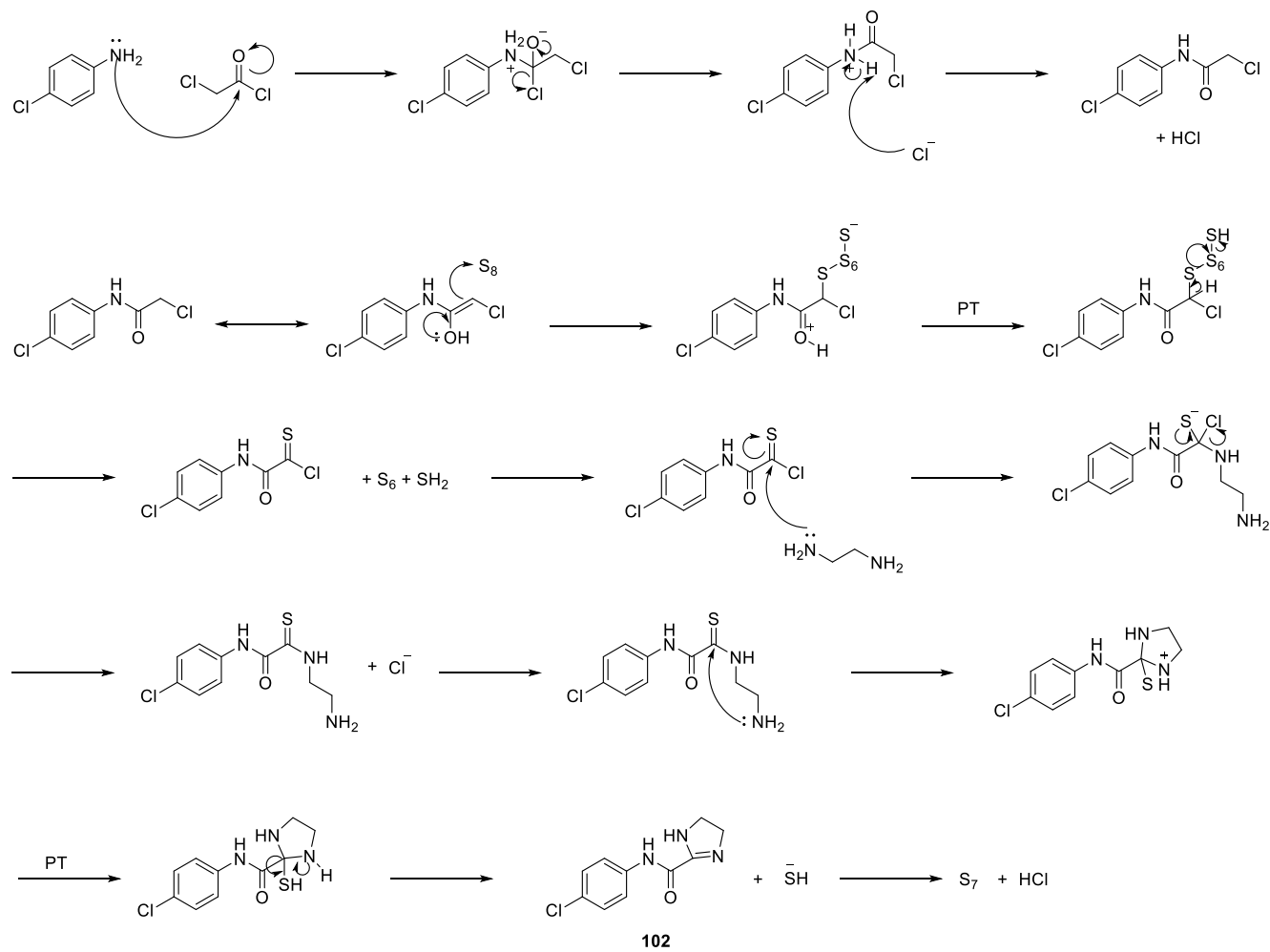
Modifying the method published by Sharma *et al* could yield compounds **93a-d** [322]. Shown in Scheme 5.7, dehydrogenation of the dihydro-imidazole moiety using barium permanganate should yield analogues **93a-d** [325].

Scheme 5.7 Proposed synthesis of analogues 93a-d using modified synthesis Sharma et al [322] and Hickman et al [325].
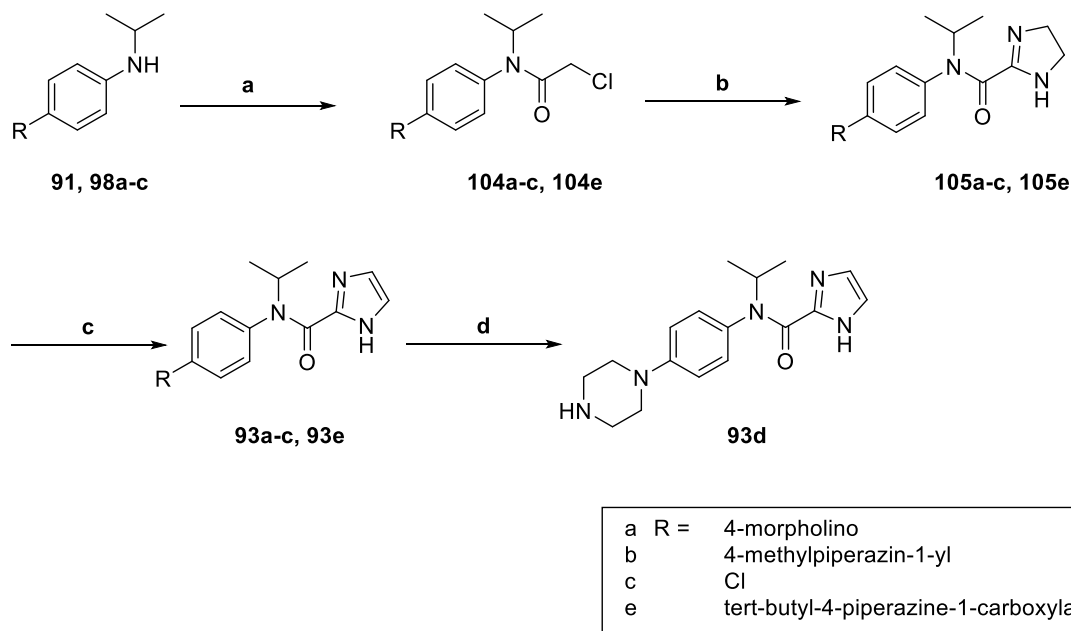
a	R =	4-morpholino
b		4-methylpiperazin-1-yl
c		Cl
e		tert-butyl-4-piperazine-1-carboxylate

Reagents and conditions: (a) i. chloroacetylchloride, glacial acetic acid, 10-30°C, 0.5 hr. **ii.** 60 % sodium acetate solution, 30°C, 0.33 hr. **(b)** ethylenediamine, sulphur, toluene, 100°C, 6 hr. **(c)** barium permanganate, DCM, reflux, 40 hr. **(d) 93e**, 4M HCl in dioxane, MeOH, rt, 30 min.

Due to the cyclisation of ethylenediamine, this method is unsuitable for the synthesis of the 4-imidazolyl substituted analogues **92a-d**. Although a retrosynthetic literature search has identified a potential approach for the synthesis of **92a-d** following the Debus-Radziszewski synthesis [326, 327], the use of 2,3-dioxopropanoic acid as a starting material is unfeasible, thus the scheme identified in Scheme 5.8 is inappropriate for the synthesis of the 4-imidazolyl derived analogues **92a-d**.

Scheme 5.8 *Proposed synthesis of analogues 92a-d.*

a	R =	4-morpholino
b		4-methylpiperazin-1-yl
c		4-Cl
e		tert-butyl-4-piperazine-1-carboxylate

Reagents and conditions: (a) 2,3-dioxopropanoic acid, triethylamine, acetonitrile, rt, 12 hr. **(b)** formaldehyde, ammonia, rt to reflux **(c) 92e,** 4M HCl in dioxane, MeOH, rt, 30 min.

Furthermore, the data obtained from the molecular docking studies of compounds **92a-d** and **93a-d** in two hTAAR1 structures suggest the imidazole moiety is not essential for interaction with the binding site when an amide linker and an alternative moiety capable of interacting with Asp103[3.32] (such as a 4-methyl-piperazin-1-yl substituent) is present, thus suggesting future SAR studies could explore replacing this moiety with an alternative heteroaromatic ring. Exchanging imidazole for an electro-deficient structure such as pyridine would result in a more electrophilic electrophile which could improve the success of synthesis when generating hTAAR1 agonists using an acyl chloride.

6. Conclusions and future directions

6.1. General conclusions

This thesis aimed to rationally design and synthesise a library of imidazole-based peripheral hTAAR1 agonists, thus it was essential to identify a lead compound (compound **59**) [173] which would be subjected to aromatic substitution and linker modifications. Additionally, it was vital to predict the binding pose of **59** in the hTAAR1 binding site to understand the functional groups essential for receptor interaction and activity to aid the design of novel TAAR1 agonists. Consequently, it was imperative to build and validate homology models of hTAAR1 due to the lack of structures available in the PDB at the time the project started. Extensive validation of hTAAR1 homology models is shown in Chapter 2 where homology model 17 was identified as a suitable representation of hTAAR1 as it could accurately differentiate between active and decoy compounds, the predicted interactions made and the compound positioning within the active site. As such this homology model was used for molecular docking. The chloro- and methoxy-substituents present in **59**, **75a-b** and **76a-c** were identified to not form any critical interactions with hTAAR1 and therefore could be modified to prevent BBB permeation. Additionally, no receptor-ligand interactions occurred via the CH_2 linker; thus this region could therefore be modified (Chapter 5) with hydrogen bond donor / acceptor moieties in an attempt to form more interactions between ligand and receptor. A cryo-EM structure of hTAAR1 with bound agonist **62** (PDB: 8W88) was published in 2023, allowing the comparison with the generated homology model [222]. The superimposition of the two hTAAR1 structures with docked compounds **18**, **24**, **59** and **60** showed differences in the binding poses of the two ligands - a twisted conformation was observed in the cryo-EM structure, likely due to variation observed between residues Phe267[6.51] and Phe268[6.52]. In Chapters 4 and 5 modified versions of **59** and **76c** were docked into the receptor and their binding poses corroborated with previous findings [131].

Chapter 3 reports the synthesis and pharmacological activity evaluation of Roche compounds **59**, **75a-b** and **76a-c** [173], whilst chapter 4 reports the synthesis and pharmacological activity for novel compounds **82a-d** and **83a-d**. The purpose of these initial studies was to evaluate the pharmacological profile of both known and novel compounds in our phenotypic pancreatic β-cells.

The molecular docking data presented in Chapters 2-4 allowed for the design of linker modified analogues **92a-d** and **93a-d** in which the attempted synthesis is shown in Chapter 5. 4-Chloroaniline and 4-(4-methylpiperidin-1-yl)aniline were initially reductively aminated with 2-methoxypropene; however an undesired reaction occurred affording acetanilides **99b-c** due to the slow rate of imine formation. As such, the desired products were synthesised via alkylation of para-substituted anilines [296]. Several unsuccessful attempts were made to acylate **91** and **98a-c** with the acid **97**. Imidazole-4-carboxylic acid (**97**) was activated into the corresponding acid chloride either via oxalyl chloride in DMF or the use of coupling reagents where amide formation was observed in the presence of DCC. To increase the rate of reaction, the reaction mixture was heated for 5.5 hours; however, an undesired product was detected. To outcompete the rate of impurity formation, an excess of 4-chloro-*N*-isopropylaniline was added; however, this had minimal successes, and the synthesis of **92a-d** and **93a-d** was terminated.

The data presented in Figure 3.8 and Figure 4.6 showed treating INS-1 cells with **59**, **76a**, **76c**, **82b** and **83a** enhanced insulin secretion in accompaniment to GSIS. Analysis of cAMP accumulation did not generate the expected response, with only compound **76c** shown to significantly enhance cAMP levels in INS-1 cells (Figure 4.7). Unfortunately, due to the cell-line used and functional response evaluated, the specific biological target remains unknown.

6.2. Future directions

Summarised in Figure 6.1 and described below is an overview of proposed experiments required to unambiguously confirm the biological target of these compounds.
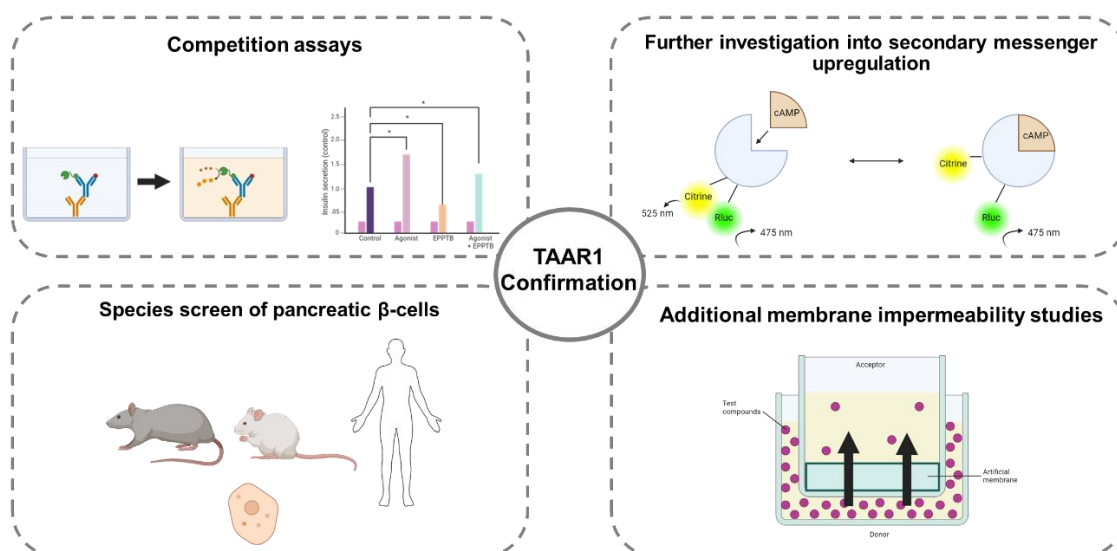
Figure 6.1 *Further investigation summary to unambiguously confirm the mechanism of action of analogues **59**, **75a-b**, **76a-c**, **82a-d** and **83a-d**.*

Competition assays

The effect of cAMP accumulation differed from the expected results for compounds **59**, **76a**, **82b**, **82a**, thus it is important to confirm enhancement of insulin secretion via TAAR1 interaction. The previously described insulin ELISA should be repeated for all compounds incubated in the presence of known inhibitors to identify cellular response variation.

Michael *et al* identified GSIS via TAAR1 activation through competition with known adenylyl cyclase dependant pathway inhibitors [9]; therefore, it is prudent to replicate these experiments. Application of methods validated within this project should evaluate the pharmacological response in the phenotypic β-cells. To achieve this, the EC_{50} should be calculated via concentration response curves for compounds **59**, **76a**, **76c**, **82b** and **83a** and the assay protocol repeated using the calculated EC_{50} concentration for **59**, **76a**, **76c**, **82b** and **83a** ± inhibitor. Table 6.1 contains the suggested inhibitors for use in this experiment, in which it is expected a significant rise in insulin secretion will be observed for any compound acting on TAAR1 albeit at a lower magnitude than the initial uncompetitive data.

Proposed inhibitors and their mode of action required to determine GSIS via TAAR1 activation.

Inhibitor	Mode of action
EPPTB (**70**) (CAS: 1110781-88-8)	TAAR1 antagonist
MDL-12,330A hydrochloride (CAS: 40297-09-4)	Inhibits adenylyl cyclase
H89 diihydrochloride (CAS: 130964-39-5)	Inhibits PKA
HJC-0350 (CAS: 885434-70-8)	Inhibits Epac2

Pharmacological screen of pancreatic cell lines

Species specificity is the main hinderance to advancing the development of TAAR1 agonists [328], thus it is imperative to establish any species and cell-type differences within TAAR1 signalling [329]. In this project all evaluation and pharmacological characterisation was determined using the rat INS-1 cell-line, therefore it is prudent to assess the effects of **59**, **75a-c**, **76a-c**, **82a-d** and **83a-d** across a range of pancreatic cell-lines including mouse and human models.

Replicating the cell function assays previously described in this thesis using the mouse pancreatic β-cell line, MIN6 and human pancreatic β-cell line, EndoC-βH1, would reduce variability, whilst increasing the reliability of the pharmacological effects observed by these compounds due to confirming that the effects observed in INS-1 cells are consistent across other species of pancreatic cells. Moreover, assessing the effects of **59, 75a-c, 76a-c, 82a-d** and **83a-d** in EndoC-βH1 would provide a greater insight into whether hTAAR1 is a potential therapeutic target in the treatment of T2DM, thus meeting the aims of this project. Once the initial pharmacological profile of analogues **59, 75a-c, 76a-c, 82a-d** and **83a-d** has been established in MIN6 and EndoC-βH1, any compounds which have been found to enhance insulin secretion should undergo further experimentation through the competition assays described in Section

6.1.1, to provide further evidence the pharmacological response observed is due to interaction with TAAR1.

Generation and screening of a transient cell line expressing hTAAR1 for secondary confirmation of cAMP activity

Barak *et al* states cAMP production is the only way to approach the pharmacological study of TAAR1 [162]; thus further experimentation is required to confirm the results shown in Chapter 4.3. Although replicating the assay completed in Chapter 4.3 with known inhibitors like that described in Chapter 6.1.1 would provide insight into the MoA of the compounds, there is a high associated cost, thus other methods to monitor cAMP production are required.

Developed via modification of the fluorescence resonance energy transfer (FRET)-based assay ICUE2 [330], a BRET-based cAMP biosensor is available, offering an efficient and cost effective method of measuring cAMP levels in real time [162]. Figure 6.2 shows the principles behind BRET-based assays and the sensor composition. Briefly, the *N*-terminus of Epac is tagged with *R. reniformis* luciferase (Rluc) and citrine – a yellow fluorescent protein. Upon cAMP binding, a decline in fluorescence is observed [162].
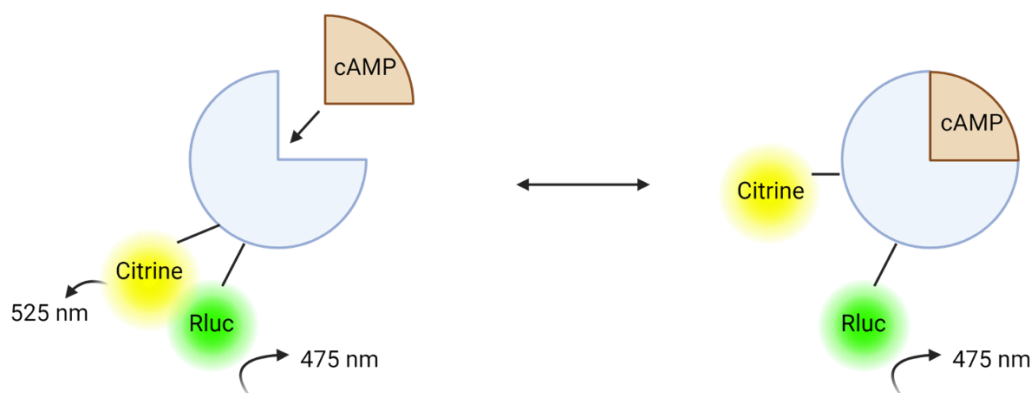
Figure 6.2 *Cartoon of molecular rearrangement of the full-length Epac protein in the absence and presence of cAMP. Adapted using Barak et al [162] and Salahpour et al [331]. Image created using Biorender.com.*

Several cell lines expressing hTAAR1 have been reported in the literature, most commonly exploiting the HEK-293 cell line [132, 162, 163, 173]. To further improve hTAAR1 expression, an *N*-glycosylated variant has been expressed in which the first nine residues of human β_2-adrenoceptors are inserted between the HA tag and *N*-terminus of hTAAR1. Using a similar method to those published by Barak *et al* [162], Guraiento *et al* [132] and Espinoza *et al* [163] HEK-293 cells should be transiently transfected with hTAAR1 and cAMP accumulation measured using the BRET-based cAMP biosensor. Although the *N*-glycosylated hTAAR1 variant is not a true representation of native hTAAR1, the modifications occur at a distinct site away from the binding pocket, thus should not affect the binding and interaction between hTAAR1 and prospective future TAAR1 agonist drugs such as **59**, **75a-c, 76a-c, 82a-d** and **83a-d**. As such the obtained data should be compared with that provided in Chapter 4.3, to indicate consistency between the two assays.

Investigation into the mechanism of action of compounds **76a** and **83a**

As compounds **76a** and **83a** significantly decreased cAMP accumulation (Figure 4.7), it suggests their MoA is not through the proposed adenylyl cyclase signalling pathway. Previous work within the Turner group (Nottingham Trent University, UK) has identified structurally similar compounds to those synthesised in this project, enhance insulin secretion in INS-1 cells via scavenging of reactive species [332], as such it is hypothesised compounds **76a** and **83a** might exert their therapeutic effects via this mechanism.

To prove this hypothesis, reactive oxygen species quantification should be determined using 2,7-dichlorofluorescin diacetate (H_2DCF-DA). H_2DCF-DA is a non-fluorescent cell-permeable probe which is deacetylated into 2,7-dichlorodihydrofluorescein (H_2DCF). H_2DCF is oxidised into the highly fluorescent 2,7-dichlorofluroescein (DCF) due to the presence of intracellular reactive oxygen species (Figure 6.3) [333, 334].
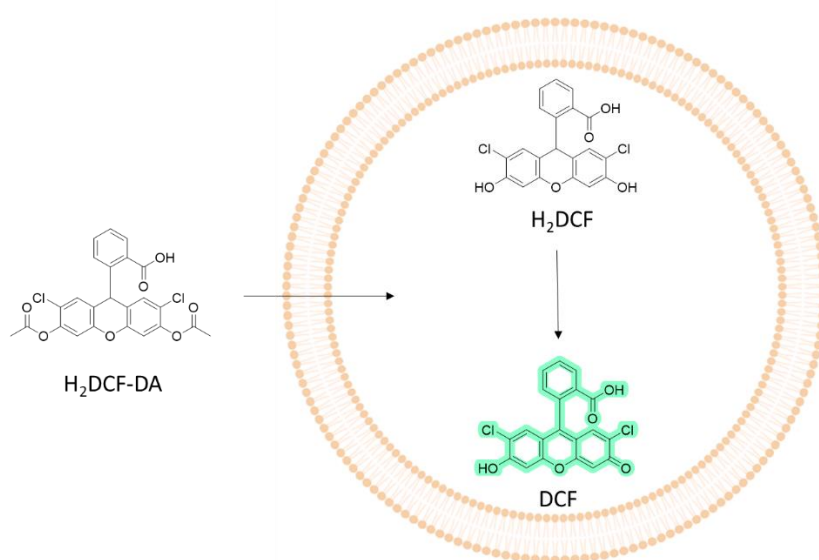
Figure 6.3 *Principle of scavenging assay using 2,7-dichlorofluorescin diacetate. H₂DCF-DA enters the cell and undergoes de-esterification to form H₂DCF. The presence of reactive species causes H₂DCF to be oxidised into DCF, a highly fluorescent compound. Image created using Biorender.com.*

The method published by Cripps *et al* could be used to determine whether **76a** and **83a** can scavenge reactive oxygen and nitrogen species, Figure 6.4[332].
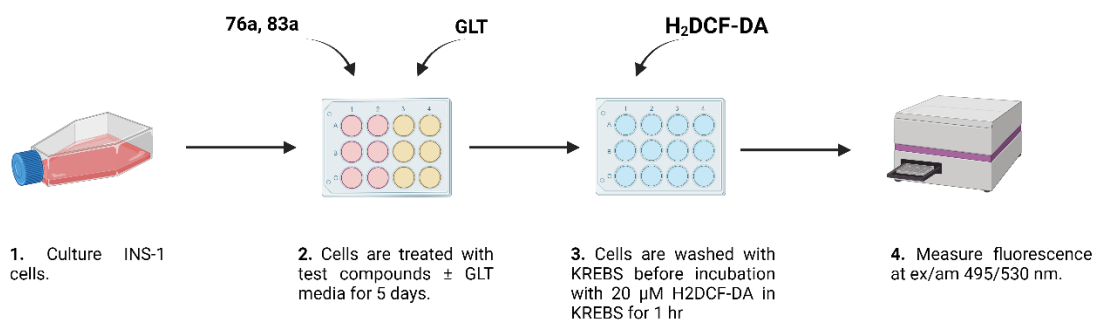
Figure 6.4 *Schematic representation of H₂DCF-DA scavenging assay. Image created using Biorender.com*

Alternatively, as shown in Figure 1.29, TAAR1 is observed to co-localise with dopamine D2 receptors. As D2 receptors are G_i-coupled GPCRs, they inhibit the adenylyl cyclase pathway thus preventing the formation of cAMP [335]. As the therapeutic effects observed for **76a** and **83a** are consistent with that of G_i-coupled GPCRs in response to cAMP upregulation, further

investigation is required to determine if these compounds act on heterodimers of TAAR1 and D2 receptors.

Further evidence to confirm lack of BBB permeation

Given that the development of previously reported hTAAR1 agonists were aimed at treating schizophrenia and thus have been shown to exert effects in the CNS, this project used predictive and experimental measures to estimate the likelihood of compounds **82a-d, 83a** and **83c** permeating the BBB, whereby contradictory results were obtained. The IAM chromatography data obtained suggests **82a-d**, **83a** and **83c** are likely to remain in the periphery whilst the computationally predicted log P, log $D_{7.4}$ and BBB score imply that they are likely to permeate the BBB. Further investigation using the BOILED-Egg model accessed via swissADME [264] indicated these compounds are likely to be P-glycoprotein substrates and thus would be actively effluxed back into the periphery should they cross the BBB. As the intracellular localisation of TAAR1 indicates agonists enter the cell via monoamine transporters (dopamine transporter, OCT2 and VMAT2), it is highly likely all TAAR1 agonists will cross the BBB. Therefore, it is vital all peripherally active TAAR1 agonists are substrates of P-glycoprotein like **82a-d**, **83a** and **83c** (Chapter 4).

PAMPA (Figure 6.5) was developed in 1998 in order to investigate passive absorption [336]. Utilising a non-biological artificial membrane, the assay predicts the passive diffusion of drug molecules in a high throughput manner [337], thus cannot simulate active transport [338, 339]. Recently a modified PAMPA assay, employing porcine brain lipids has been developed by Di *et al* to improve the prediction of BBB penetration which could be used to further determine the permeability potential of **82a-d, 83a** and **83c** [339, 340].
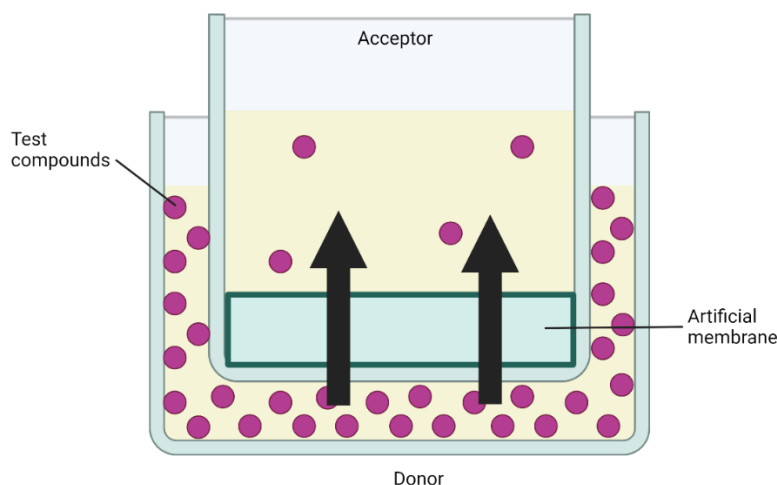
Figure 6.5 *Schematic of PAMPA model.*

The principal procedure of PAMPA is shown in Figure 6.5 - test compounds (**82a-d**, **83a** and **83c**) are added to the donor well and after an incubation period, the concentration of drug in the acceptor well is obtained. Quantification of compound permeability (P_{app}) is determined using Equation 4 where drug$_{equilibrium}$ is the total drug concentration in the total volume of the donor and acceptor compartments.

Equation 4 *Calculation to determine compound permeability (P_{app}) using PAMPA.*

$$P_{app} = C * \ln\left(1 - \frac{\lfloor drug_{acceptor}\rfloor}{\lfloor drug_{equilibrium}\rfloor}\right)$$

Where C is determined using the volume of the donor well (V_d), volume of acceptor well (V_a) and area is the membrane surface area multiplied by the porosity according to Equation 5.

Equation 5 *Calculation to determine the constant, C.*

$$C = \frac{(V_d * V_a)}{\left((V_d * V_a) * Area * Time\right)}$$

Literature analysis of reference compounds published by several PAMPA manufacturer's show drugs with low passive permeability had P_{app} values $< 10 \times 10^{-6}$ cm/s, whereas the drugs with high passive permeability had P_{app} values $> 10 \times 10^{-6}$ cm/s. Through comparing the P_{app} values obtained for ligands **82a-d**, **83a** and **83c** with their derived P_m values from IAM chromatography

experiments, it will solidify the results and allow us to say with more confidence whether **82a-d**, **83a** and **83c** are likely to permeate the BBB.

Overall, the work presented in this thesis has resulted in the design and development of a series of novel analogues modelled around RO5073012 (**59**) aimed to target TAAR1. Their application in insulin secretion ELISAs demonstrated enhanced secretion in both control conditions and our diabetic phenotype pancreatic β-cells using GLT media. Although the MoA of these compounds has yet to be confirmed, further development of compounds of this nature would provide the scientific community with a set of compounds that have the potential as new therapeutic agents for managing T2DM. This work also has the potential to lead to the thorough understanding of TAAR1 agonism, the intracellular trafficking and signalling pathways involved.

7. Experimental

7.1. Computational methods

7.1.1. Homology models using Modeller

All homology models built using Modeller software (https://salilab.org/modeller/) were provided by Prof. Charles Laughton, University of Nottingham, UK. Using high resolution x-ray or cryo-EM structures, several human β_2-adrenoceptors (PDB: 5JQH, 3PDS, 3P0G, 7DHR, 7DHI) [193-196] and one meleagris gallopavo structure (PDB: 4BVN) were used as the template for homology models 1-4 and 6-20 [197]. A human dopamine D4 receptor template was used to generate model 5 (PDB: 6ILQ)[198]. After initial research Prof. Laughton generated a further 1000 hTAAR1 models developed using model 4 as the core before screening against enantiomers of ((*R/S*)-4-(2,4-difluorophenyl-3-tritio)-4,5-dihydro-2-oxazolamine), to correlate with the radioligand binding assay conducted by Galley *et al* [173]. Models which preferred the *S* enantiomer were taken forward for analysis (models 6-20).

7.1.2. Homology models using I-TASSER

All models were obtained using the GPCR-HGmod for structural models of GPCRs in the Human Genome page of I-TASSER's website (https://zhanggroup.org/GPCR-HGmod/). Five models were downloaded by searching for UniProt ID: Q96RJ0.

7.1.3. Homology models using Robetta

All models built using the Robetta service required completion of a submission form (https://robetta.bakerlab.org/submit.php). hTAAR1 FASTA sequence was taken from UniProt and uploaded to the Robetta webservice. All parameters were set as standard with RoseTTAFold selected as an optional extra. Five homology models were provided via E-mail.

7.1.4. Building the ligand sets to be docked

Ligands were prepared using Schrödinger Maestro 2D sketcher and minimised to a low energy state using LigPrep with all parameters set to default settings.

7.1.5. Grid generation

Modeller, I-TASSER and Robetta models: For each hTAAR1 homology model, the grid box was generated using SiteMap with hydrogen bond constraints with Asp103$^{3.32}$ applied.

Dopamine D4 receptor homology model built using Modeller: The grid box was generated using the centroid of the workspace ligand ((*S*)-4-(2,4-difluorophenyl-3-tritio)-4,5-dihydro-2-oxazolamine) with hydrogen bond constraints at with Asp103$^{3.32}$ applied.

7.1.6. Model validation

Literature compounds where actively docked into each homology model with a hydrogen bond constraint at with Asp103$^{3.32}$ applied. For all models, docking was completed following standard precision. The docking was set to generate 5 poses per ligand (to ensure manageable data output) with all other parameters set at the default settings. Visualisation of the docked structure was observed in Schrödinger Maestro and PyMOL 4.6.0.

7.1.7. Docking of designed SAR compounds

SAR compounds where actively docked into each homology model with a hydrogen bond constraint at Asp103$^{3.32}$ applied. For all models, docking was completed following standard precision. The docking was set to generate 5 poses per ligand with all other parameters set at the default settings. Visualisation of the docked structure was observed in Schrödinger Maestro and PyMOL 4.6.0.

7.2. General Chemistry

Chemicals and solvents were purchased from standard suppliers and used without purification. Unless otherwise stated reactions were carried out at standard room temperature and pressure.

Reactions were monitored using TLC on precoated aluminium backed plates (Merck Kieselgel TLC Silica gel 60 Å F254) and were visualised under UV light (wavelengths: 254 and 366 nm). General staining was carried out using iodine, ninhydrin in ethanol, bromocresol green and $KMnO_4$.

After aqueous workups, all organic extracts were dried over $MgSO_4$ before gravity filtration with organic solvents evaporated *in vacuo* at 40°C. Flash chromatography was carried out using technical grade silica gel from Adrich, pore size 60 Å, 230-400 mesh and particle size 40-63 μm. Automated flash chromatography was performed using an Interchim Puriflash 4100 system (PF4100-250) equipped with a dual wavelength DAD UV detector (200-600 nm) using silica high performance cartridges. Preparative layer chromatography was carried out using precoated glass plates (Analtech uniplate silica gel GF, 20 x 20 cm, 2000 μm thickness).

Microwave reactions were carried out using a CEM discover 2.0 microwave reactor. All microwave vessels were sealed with a snap cap and reactions carried out with a maximum pressure and power of 250 psi and 200 W respectively. Reactions underwent 15 seconds of pre-stirring prior to the temperature increase.

^{1}H-NMR and ^{13}C-NMR spectra were recorded on a Bruker-AV 400. Chemical shifts (δ) are recorded as parts per million (ppm) and were referenced to the appropriate deuterated solvent peak. Multiplicities are described as singlets (s), doublets (d), doublet of doublets (dd), doublet of doublet of doublets (ddd), triplet (t), apparent triplets (app. t), doublet of triplets (dt), quartets (q), double of quartets (dq), pentets (p), heptets (h) and multiplets (m) with coupling constants (*J*) recorded in Hz. All spectra were recorded in $CDCl_3$, DMSO-d_6 or CD_3OD. All spectra were analysed using MestReNova x64 (14.3.0-30573) NMR software.

All final compounds were determined to be ≥ 96 % pure. General reaction monitoring or purity checks were performed via LC-MS or analytical RP-HPLC. LC-MS samples were run using a Shimadzu UFLCXR system combined with an Applied Biosystems API2000 electrospray ionization

mass spectrometer and visualized at 254 nm (channel 1) and 220 nm (channel 2). The buffers used were buffer A 0.1% formic acid in H_2O and buffer B 0.1% formic acid in MeCN. Analysis was completed using Phenomenex Gemini-NX C_{18} 110 Å column (50 mm × 2 mm x 3 μm) with a flow rate of 0.5 ml/min. All retention times (R_t) are quoted in minutes.

LC-MS reaction monitoring system 1: 1 min at 5 % buffer A, 5-98 % buffer B over 2 min, held at 98 % buffer B for 2 min, 98-5 % over 0.5 min and then 5 % buffer B for 1 min.

LC-MS reaction monitoring system 2: 0.5 min at 0 % buffer B, 0-30 % buffer B over 1.5 min, held at 30 % buffer B for 2 min, 30-0 % over 0.5 min and then 5 % buffer B for 1 min.

Analytical LC-MS system 1: 0.5 min at 5 % buffer B, 5-98 % buffer B over 7 min, held at 98 % buffer B for 3 min, 98-5 % buffer B over 0.5 min and then 5 % buffer B for 1 min.

Analytical LC-MS system 2: 0.5 min at 0 % buffer B, 0-30 % buffer B over 7 min, held at 30 % buffer B for 3 min, 30-0 % buffer B over 0.5 min and then 5 % buffer B for 1 min.

Analytical RP-HPLC was performed on a Shimadzu SCL-40 system controller, LC-40D XR solvent delivery module, SIL-40C XR autosampler, CTO40C column oven and SPD-M40 photodiode array detector equipped with a Phenomenex, Luna Omega polar C18 100 column (150 x 3 mm, 3 μm). The system was set at 40°C and a flow rate of 0.5 mL/min over a 22-minute period. The gradient protocol began by stabilising the column for 5 minutes at 100 % solvent A, followed by an increase to 95 % solvent B over 7 minutes. The system was held at 95 % solvent B for 5 minutes, before increasing to 100 % solvent A over 3 minutes, and finally held at 100 % solvent A for 2 minutes (solvent A = 0.001 % formic acid in H_2O, solvent B = 0.001% formic acid in MeCN). UV detection was carried out at 254 and 220 nm and spectra were analysed LabSolutions software version 5.111.

RP-HPLC using an immobilised artificial membrane column was performed on a Shimadzu SCL-40 system controller, LC-40D XR solvent delivery module, SIL-40C XR autosampler, CTO40C

column oven and SPD-M40 photodiode array detector equipped with a Regis IAM P.C DD2 column (30 x 4.6 mm, 10 μm (300 Å)). The system was set at 30°C and a flow rate of 1.5 ml/min over a 6-minute period. The gradient protocol began by increasing from 0 to 85 % solvent B over 4.75 minutes. The system was held at 85 % solvent B for 0.5 minutes before decreasing to 100 % solvent A over 0.5 minutes (solvent A = 50 mM ammonium acetate in H_2O, pH 7.4, solvent B = MeCN). All standard and sample solutions were injected at a volume of 10 μl at a final concentration of 1 mM. Experiments were performed in either duplicate or triplicate. A calibration curve using R_t and fixed CHI_{IAM} values was generated using Bio-Mimetic Chromatography Limited IAM Valko calibration mixture and used to determine unknown CHI_{IAM} values (Appendix 9.2). A suitability test was performed to assess column performance using both a propanol, indomethacin and colchicine solution and a solution composed of carbamazepine, warfarin and nicardipine. The data obtained from the suitability study was referenced to known CHI_{IAM} values ensuring they did not deviate more than 5 units (Appendix 9.2). Dead time was determined using a 50 mg/ml stock solution of citric acid in water and acetonitrile (Appendix 9.2). UV detection was carried out at 254 and 220 nm and spectra were analysed LabSolutions software.

High resolution mass spectra (HRMS) – time of flight, electrospray (TOF ES +/-) were recorded on Bruker MicroTOF.

7.2.2. General procedures

General procedure A: reductive amination with sodium borohydride in methanol

Substituted anilines (1 eq.) were added to imidazolecarboxaldehyde (1 eq.) and dissolved in MeOH (~15 ml). The reaction mixture was heated at 60°C and stirred overnight. The solution was cooled and stirred at room temperature with $NaBH_4$ (5 eq.) for 90 minutes, before being quenched with water. The reaction mixture was extracted into EtOAc and washed with water

three times (3 x 10 ml). The organic layer was dried over MgSO$_4$, and solvent removed *in vacuo*, with the resulting residue purified via flash chromatography.

General procedure B: optimised reductive amination with sodium borohydride in ethanol

Substituted anilines (1.2 eq.), imidazolecarboxaledhyde (1 eq.) and CeCl$_3$.7H$_2$O (0.02 – 0.1 eq.) were dissolved in EtOH (~5 ml) and stirred at room temperature until precipitate formed, before addition of NaBH$_4$ (2 eq.). The reaction was stirred at room temperature for 3 – 18 hours and dried under vacuum. The residue was extracted into EtOAc and washed with water three times (3 x 10 ml). The organic layer was dried over MgSO$_4$, and solvent removed *in vacuo*, with the resulting residue purified via flash chromatography.

General procedure C: reductive amination with sodium triacetoxyborohydride in 1,2-dichloroethane

To a solution of resulting products obtained from General procedures A, B and E (1 eq.) dissolved in 1,2-dichloroethane (~10 ml), 2-methoxypropene (1.5 eq.), TFA (1 eq.) and NaBH(OAc)$_3$ (1 eq.) were added. The reaction mixture was heated at 60°C and stirred for 5 - 18 hours. The solution was cooled and 1M aq. NaOH was added to achieve pH 8-14. The mixture was extracted into DCM and washed with water three times (3 x 10 ml). The organic layer was dried over MgSO$_4$, and solvent removed *in vacuo*. The crude residue was either purified via automated flash chromatography or dissolved in 1M HCl solution (~10 ml) and heated at 60°C and stirred for 1 hour. The mixture was cooled and 1M aq. NaOH added to achieve pH 8-14 and extracted into DCM and washed with water three times (3 x 10 ml). The organic layer was dried over MgSO$_4$, and solvent removed *in vacuo*, with the resulting residue purified via automated flash chromatography.

General procedure D: nucleophilic substitution of substituted anilines in acetonitrile

Substituted anilines (3 eq.), 2-iodopropane (1 eq.), K_2CO_3 (1.1 eq.) and acetonitrile (2 ml) were added to a microwave vessel containing a stir bar. The reaction mixture was microwaved at 150°C for 30 minutes and gravity filtered. The filtrate solvent was removed *in vacuo* and the resulting residue purified via automated flash chromatography.

General procedure E: nucleophilic substitution of substituted anilines in 1,4-dioxane

Substituted anilines (3 eq.), 2-iodopropane (1 eq.), K_2CO_3 (1.1 eq.) and 1,4-dioxane (7 ml) were added to a microwave vessel containing a stir bar. The reaction mixture was microwaved at 150°C for 30 minutes and gravity filtered. The filtrate solvent was removed *in vacuo* and the resulting residue purified via automated flash chromatography.

General procedure F: reductive amination with picoline borane in methanol

To a solution of resulting products obtained from General procedure E (1 eq.) dissolved in a methanol-acetic acid solution (10:1, 3 ml), imidazolecarboxaldehyde (1 eq.) and picoline borane (1 eq.) were added. The reaction mixture was stirred at room temperature for 18 hours and dried under vacuum. The residue was extracted into EtOAc and washed with aqueous sodium carbonate three times (3 x 10 ml). The organic layer was dried over $MgSO_4$ and solvent removed *in vacuo*, with the resulting residue purified via automated flash chromatography.

General procedure G: Boc-deprotection

The resulting product from General procedure F was dissolved in MeOH. 4M HCl in 1,4-dioxane (1.5 ml) was added and the reaction mixture was stirred at room temperature for 30 minutes and monitored via LC-MS. Once complete, the solvent was removed *in vacuo*, with the resulting residue purified via preparative layer chromatography.

General procedure H: amide coupling

Imidazolecarboxylic acid (1.1 eq.), *N,N*-diisopropylethylamine (2 eq.) and coupling reagent (1.2 eq.) were dissolved in DMF (1 ml). The reaction was stirred at room temperature for 20 minutes before the addition of substituted aniline obtained from General procedure F (1 eq.). The resulting solution was stirred at room temperature overnight and monitored via LC-MS. After 24 hours stirring, 4-dimethylaminopyridine (catalytic amount) was added. The resulting solution was stirred at room temperature overnight and monitored via LC-MS. The resulting solution was transferred to a microwave vial and heated in 30-minute increments at 50°C (1.5 hours total), 80°C (0.5 hours total) and 100°C (1.5 hours total) and monitored via LC-MS. A final addition of substituted aniline (2 eq.) was added, and the mixture heated in 30-minute increments at 100°C (2 hours total) once again before drying under vacuum. The residue was extracted into EtOAc and washed with water three times (3 x 10 ml). The organic layer was dried over MgSO$_4$ and solvent removed *in vacuo.*

7.2.3. Chemical characterisation

N-((1H-Imidazol-4-yl)methyl)-4-chloro-N-isopropylaniline (59)
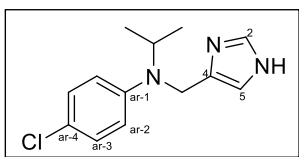
The reaction was performed according to General procedure C with N-((1H-Imidazol-4-yl)methyl)-4-chloroaniline (**77c**) (0.5 g, 2.4 mmol, 1 eq.), 2-methoxypropene (345 µl, 3.6 mmol, 1.5 eq.), TFA (180 µl, 2.4mmol, 1 eq.) NaBH(OAc)$_3$ (0.51 g, 2.4 mmol, 1 eq.), 1,2-DCE (10 ml) and 1M HCl (5 ml) and purified via manual flash chromatography (7.5 % MeOH in DCM), followed by recrystallization (DEE in cyC$_6$H$_{12}$) to give the title compound as an off-white powder (16 mg, 3 % yield). **^{1}H-NMR (400 MHz, DMSO)** δ 11.81 (s, 1H, imidazole-N**H**), 7.53 (s, 1H, imidazole-C**H**-2), 7.14 – 7.06 (m, 2H, ar-C**H**-3), 6.79 – 6.71 (m, 3H, imidazole-C**H**-4, imidazole-C**H**-5, ar-C**H**-2), 4.23 (s, 2H, C**H$_2$**), 4.10 (p, J = 6.6 Hz, 1H, C**H**), 1.16 (d, J = 6.5 Hz, 6H, C**H$_3$**). **^{13}C-NMR (101 MHz, DMSO)** δ 147.6 (ar-**C**-1), 134.6 (imidazole-**C**-2), 128.5 (ar-**C**-3), 128.4 (ar-**C**-4), 119.1 (imidazole-**C**-5), 114.4 (ar-**C**-2), 47.8 (**C**H), 42.0 (**C**H$_2$), 19.6 (**C**H$_3$). **HRMS (TOF ES$^+$)** C$_{13}$H$_{17}$ClN$_3$, [M+H]$^+$ calcd 250.1106; found 250.1109, R_t: 4.10.

N-((1H-Imidazol-4-yl)methyl)-N-isopropyl-3-methoxyaniline (75a)
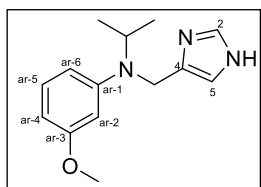
The reaction was performed according to General procedure C with N-((1H-Imidazol-4-yl)methyl)-3-methoxyaniline (**77a**) (0.57 g, 2.8 mmol, 1 eq.), 2-methoxypropene (401 µl, 4.2 mmol, 1.5 eq.), TFA (214 µl, 2.8 mmol, 1 eq.) NaBH(OAc)$_3$ (0.59 g, 2.8 mmol, 1 eq.), 1,2-DCE (20 ml), and 1M HCl (15 ml) and purified via manual flash chromatography (10% MeOH in DCM) to give the title compound as an orange oil (68 mg, 2 % yield). **^{1}H-NMR (400 MHz, DMSO)** δ 11.77 (s, 1H, imidazole-N**H**), 7.51 (s, 1H, imidazole-C**H**-2), 6.98 (app. t, J = 8.2 Hz, 1H, ar-C**H**-5), 6.74 (s, 1H, imidazole-C**H**-5), 6.36 (dd, J = 8.3, 2.5 Hz, 1H, ar-C**H**-6), 6.28 (app. t, J = 2.4 Hz, 1H, ar-C**H**-4), 6.16 (dd, J = 8.0, 2.3 Hz, 1H, ar-C**H**-2), 4.21 (s, 2H, C**H**$_2$), 4.11 (dt, J = 12.9, 6.2 Hz, 1H, C**H**), 3.63 (s, 3H, OC**H**$_3$), 1.16 (d, J = 6.5 Hz, 6H, CHC**H**$_3$). **^{13}C-NMR (101 MHz, DMSO)** δ 160.7 (ar-**C**-3), 150.2 (ar-**C**-1), 134.6 (imidazole-**C**-2), 130.1 (ar-**C**-5), 116.4 (imidazole-**C**-5), 107.18 (ar-**C**-4), 102.4 (ar-**C**-6), 100.7 (ar-**C**-2), 55.2 (O**C**H$_3$), 48.9 (**C**H$_2$), 20.0 (C**C**H$_3$). Missing: 132.4 (imidazole-**C**-4), 57.7 (**C**H). **HRMS (TOF ES$^+$)** C$_{14}$H$_{20}$ON$_3$, [M+H]$^+$ calcd 246.1601; found 246.1605, R_t: 3.09.

N-((*1H*-Imidazol-4-yl)methyl)-3-chloro-*N*-isopropylaniline (75b)
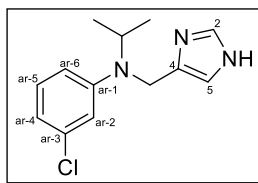
The reaction was performed according to General procedure C with *N*-((1*H*-Imidazol-4-yl)methyl)-3-chloroaniline (**77b**) (0.5 g, 2.4 mmol, 1 eq.), 2-methoxypropene (343 µl, 3.6 mmol, 1.5 eq.), TFA (184 µl, 2.4 mmol, 1 eq.), NaBH(OAc)$_3$ (0.5 g, 2.4 mmol, 1 eq.), 1,2-DCE (10 ml) and 1M HCl (5 ml) and purified via manual flash chromatography (gradient 5-10 % MeOH in DCM) to give the title compound as a white powder (220 mg, 37 % yield). **^{1}H-NMR (400 MHz, DMSO)** δ 11.84 (s, 1H, imidazole-N$\underline{H}$), 7.56 (d, *J* = 1.2 Hz, 1H, imidazole-C$\underline{H}$-5), 7.09 (app. t, *J* = 8.2 Hz, 1H, ar-C$\underline{H}$-5), 6.79 (d, *J* = 1.2 Hz, 1H, imidazole-C$\underline{H}$-2), 6.76 (app. t, *J* = 2.3 Hz, 1H, ar-C$\underline{H}$-4), 6.72 (dd, *J* = 8.3, 2.5 Hz, 1H ar-C$\underline{H}$-2), 6.60 – 6.53 (m, 1H, ar-C$\underline{H}$-6), 4.26 (s, 2H, C$\underline{H}_2$), 4.14 (h, 1H, C$\underline{H}$), 1.18 (d, *J* = 6.5 Hz, 6H, C$\underline{H}_3$). **^{13}C-NMR (101 MHz, DMSO)** δ 150.6 (ar-$\underline{C}$-1), 135.2 (imidazole-$\underline{C}$-2, 4), 134.1 (ar-$\underline{C}$-3), 130.6 (ar-$\underline{C}$-5), 115.4 (ar-$\underline{C}$-4), 112.6 (ar-$\underline{C}$-2), 111.8 (ar-$\underline{C}$-6), 48.2 ($\underline{C}$H), 42.4 ($\underline{C}$H$_2$), 20.1 ($\underline{C}$H$_3$). **HRMS (TOF ES$^+$)** C$_{13}$H$_{17}$ClN$_3$, [M+H]$^+$ calcd 250.1106; found 250.1104, *R*$_t$: 3.04.

N-((*1H*-Imidazol-2-yl)methyl)-*N*-isopropyl-3-methoxyaniline (76a)
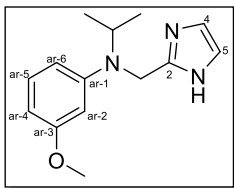
The reaction was performed according to General procedure C with *N*-((*1H*-Imidazol-2-yl)methyl)-3-methoxyaniline (**79a**) (0.6 g, 2.95 mmol, 1 eq.), 2-methoxypropene (425 µl, 4.43 mmol, 1.5 eq.), TFA (228 µl, 2.95 mmol, 1 eq.), NaBH(OAc)$_3$ (0.63 g, 2.95mmol, 1 eq.), 1,2-DCE (10 ml, and 1M HCl (7.5 ml) and purified via manual flash chromatography (5% MeOH in DCM) to give the title compound as an off-white powder (324 mg, 45 % yield). **^{1}H-NMR (400 MHz, DMSO)** δ 11.60 (s, 1H, imidazole-N**H**), 7.02 (t, *J* = 8.2 Hz, 1H, ar-C**H**-5), 6.88 (s, 2H, imidazole-C**H**-4,5), 6.36 (dd, *J* = 8.2, 2.4 Hz, 1H, ar-C**H**-6), 6.26 (app. t, *J* = 2.4 Hz, 1H, ar-C**H**-2), 6.22 (dd, *J* = 7.8, 2.3 Hz, 1H, ar-C**H**-4), 4.30 (s, 2H, C**H**$_2$), 4.16 (hept, *J* = 6.6 Hz, 1H, C**H**), 3.64 (s, 3H, OC**H**$_3$), 1.17 (d, *J* = 6.5 Hz, 6H, CHC**H**$_3$). **^{13}C-NMR (101 MHz, DMSO)** δ 160.0 (ar-**C**-3), 150.0 (ar-**C**-1), 146.4 (imidazole-**C**-2), 129.3 (ar-**C**-5), 106.1 (ar-**C**-4), 101.4 (ar-**C**-6), 99.6 (ar-**C**-2), 54.5 (O**C**H$_3$), 47.8 (**C**H), 42.4 (**C**H$_2$), 19.2 (CH**C**H$_3$). Missing: 121.4 (imidazole-**C**-4,5). **HRMS (TOF ES$^+$)** C$_{14}$H$_{20}$N$_3$O, [M+H]$^+$ calcd 246.1601; found 246.1594, *R*$_t$: 2.21.

N-((*1H*-Imidazol-2-yl)methyl)-3-chloro-*N*-isopropylaniline (76b)
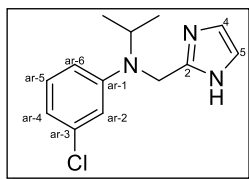
The reaction was performed according to General procedure C with *N*-((*1H*-Imidazol-2-yl)methyl)-3-chloroaniline (**79b**) (0.35 g, 1.69 mmol, 1 eq.) 2-methoxypropene (239 µl, 2.54 mmol, 1.5 eq.), TFA (128 µl, 1.69 mmol, 1 eq.) NaBH(OAc)$_3$ (0.36 g, 1.69 mmol, 1 eq.), 1,2-DCE (10 ml) and 1M HCl (5ml) and purified via manual flash chromatography (5% MeOH in DCM) to give the title compound as an off-white powder (190 mg, 45 % yield). **^{1}H-NMR (400 MHz, DMSO)** δ 11.66 (s, 1H, imidazole-N$\underline{H}$), 7.11 (app. t, *J* = 8.1 Hz, 1H, ar-C$\underline{H}$-5), 6.89 (s, 2H, imidazole-C$\underline{H}$-4,5), 6.74 (app. t, *J* = 2.3 Hz, 1H, ar-C$\underline{H}$-2), 6.69 (dd, *J* = 8.5, 2.5 Hz, 1H, ar-C$\underline{H}$-6), 6.61 (dd, *J* = 7.9, 1.9 Hz, 1H, ar-C$\underline{H}$-4), 4.34 (s, 2H, C$\underline{H}_2$), 4.17 (hept, *J* = 6.6 Hz, 1H, C$\underline{H}$), 1.17 (d, *J* = 6.5 Hz, 6H, C$\underline{H}_3$). **^{13}C-NMR (101 MHz, DMSO)** δ 150.6 (ar-$\underline{C}$-1), 146.4 (imidazole-$\underline{C}$-2), 134.1 (ar-$\underline{C}$-3), 130.7 (ar-$\underline{C}$-5), 116.1 (ar-$\underline{C}$-4, imidazole-$\underline{C}$-5), 113.0 (ar-$\underline{C}$-2), 112.0 (ar-$\underline{C}$-6), 48.5 ($\underline{C}$H), 42.7 ($\underline{C}$H$_2$), 19.8 ($\underline{C}$H$_3$). Missing 121.4 (imidazole-$\underline{C}$-4). **HRMS (TOF ES$^+$)** C$_{13}$H$_{17}$ClN$_3$, [M+H]$^+$ calcd 250.1106; found 250.1102, R_t: 2.66.

N-((*1H*-Imidazol-2-yl)methyl)-4-chloro-*N*-isopropylaniline (76c)
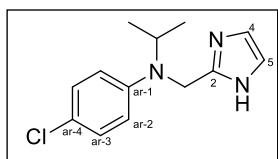
The reaction was performed according to General procedure C with *N*-((*1H*-Imidazol-2-yl)methyl)-4-chloroaniline (**79c**) (0.18 g, 1.29 mmol, 1 eq.), 2-methoxypropene (185 µl, 1.93 mmol, 1.5 eq.), TFA (98.7 µl, 1.29 mmol, 1 eq.), NaBH(OAc)$_3$ (0.27 g, 1.29 mmol, 1 eq.), 1,2-DCE (5 ml) and 1M HCl (5 ml) and purified via recrystallisation using DEE to give the title compound as off-white powder (80 mg, 25 % yield). **^{1}H-NMR (400 MHz, DMSO)** δ 11.64 (s, 1H, imidazole-N$\underline{H}$), 7.18 – 7.09 (m, 2H, ar-C$\underline{H}$-3), 6.89 (s, 2H, imidazole-C$\underline{H}$-4,5), 6.80 – 6.71 (m, 2H, ar-C$\underline{H}$-2), 4.32 (s, 2H, C$\underline{H}_2$), 4.14 (p, *J* = 6.6 Hz, 1H, C$\underline{H}$), 1.17 (d, *J* = 6.5 Hz, 6H, C$\underline{H}_3$). **^{13}C-NMR (101 MHz, DMSO)** δ 147.6 (ar-$\underline{C}$-1), 145.9 (imidazole-$\underline{C}$-2), 128.2 (ar-$\underline{C}$-3), 119.7 (imidazole-$\underline{C}$-4,5), 114.6 (ar-$\underline{C}$-2), 48.0 ($\underline{C}$H), 42.2 ($\underline{C}$H$_2$), 19.1 ($\underline{C}$H$_3$). Missing 127.2 (Ar-$\underline{C}$-4). **HRMS (TOF ES$^+$)** C$_{13}$H$_{17}$ClN$_3$, [M+H]$^+$ calcd 250.1106; found 250.1105, R_t: 2.67.

N-((*1H*-Imidazol-4-yl)methyl)-3-methoxyaniline (77a)
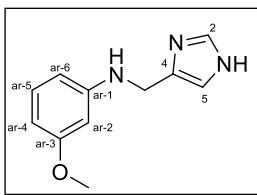
The reaction was performed according to General procedure B with 3-methoxyaniline (**80a**) (420 µl, 3.74 mmol, 1.2 eq.), 4-imidazolcarbaldehyde (300 mg, 3.12 mmol, 1 eq.), CeCl$_3$.7H$_2$O (22 mg, 0.06 mmol, 0.02 eq.) and NaBH$_4$ (238 mg, 6.24 mmol, 2 eq.) in EtOH (5 ml) purified via automated flash chromatography (gradient: 2-20% MeOH in DCM) to give the title compound as a white powder (358 mg, 57 % yield). **^{1}H-NMR (400 MHz, CDCl$_3$)** δ 7.59 (d, *J* = 1.3 Hz, 1H, imidazole-C**H**-2), 7.08 (t, *J* = 8.1 Hz, 1H, imidazole-C**H**-5), 6.96 (s, 1H, ar-C**H**-5), 6.29 (dt, *J* = 8.0, 2.0 Hz, 2H, ar-C**H**-2,4), 6.23 (app. t, *J* = 2.1 Hz, 1H, ar-C**H**-6), 4.30 (s, 2H, C**H**$_2$), 3.76 (d, *J* = 1.3 Hz, 3H, C**H**$_3$). Missing: 11.88 (imidazole-N**H**), 5.98 (N**H**). **^{13}C-NMR (101 MHz, CDCl$_3$)** δ 149.5 (ar-**C**-1), 135.0 (imidazole-**C**-2,4), 130.0 (ar-**C**-5), 106.3 (ar-**C**-6, imidazole-**C**-5), 103.0 (ar-**C**-4), 99.2 (ar-**C**-2), 55.1 (**C**H$_3$). Missing: 42.0 (**C**H$_2$). **LC-MS [M+H]$^+$** calc 204.1; found 204.1, *R*$_t$: 0.67.

N-((1*H*-Imidazol-4-yl)methyl)-3-chloroaniline (77b)
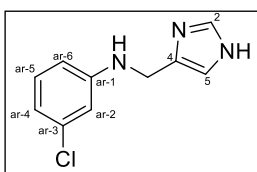
The reaction was performed according to General procedure B with 3-chloroaniline (**80b**) (1.28 ml, 12 mmol, 1.2 eq.), 4-imidazolcarbaldehyde (0.96 g, 10 mmol, 1 eq.), CeCl$_3$.7H$_2$O (0.075 g, 0.2 mmol, 0.02 eq.) and NaBH$_4$ (0.757 g, 20 mmol, 2 eq.) in EtOH (25 ml) and purified via manual flash chromatography (10% 1M MeOH NH$_3$ in EtOAc) to give the title compound as an off-white powder (1.36 g, 66 % yield). **^{1}H-NMR (400 MHz, CDCl$_3$)** δ 7.59 (d, *J* = 1.2 Hz, 1H, imidazole-C**H**-5), 7.05 (app. t, *J* = 8.0 Hz, 1H, ar-C**H**-5), 6.95 (d, *J* = 1.2 Hz, 1H, imidazole-C**H**-2), 6.67 (ddd, *J* = 7.9, 2.0, 0.9 Hz, 1H, ar-C**H**-2), 6.62 (app. t, *J* = 2.1 Hz, 1H, ar-C**H**-4), 6.51 (ddd, *J* = 8.2, 2.4, 0.9 Hz, 1H, ar-C**H**-6), 4.27 (d, *J* = 0.8 Hz, 2H, C**H**$_2$). Missing: 11.88 (imidazole-N**H**), 5.98 (N**H**). **^{13}C-NMR (101 MHz, DMSO)** δ 150.0 (ar-**C**-1), 134.7 (imidazole-**C**-2,4), 133.3 (ar-**C**-3), 130.0 (ar-**C**-5), 114.8 (ar-**C**-4, imidazole-**C**-5), 111.18 (ar-**C**-2), 110.7 (ar-**C**-6). Missing: 42.0 (**C**H$_2$). **LC-MS [M+H]$^+$** calcd 208.06; found 208.0, *R*$_t$: 1.71.

N-((1*H*-Imidazol-4-yl)methyl)-4-chloroaniline (77c)
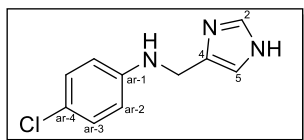
The reaction was performed according to General procedure B with 4-chloroaniline (**80c**) (1.5 g, 12 mmol, 1.2 eq.), 4-imidazolcarbaldehyde (0.96 g, 10 mmol, 1 eq.), CeCl$_3$.7H$_2$O (0.075 g, 0.2 mmol, 0.02 eq.) and NaBH$_4$ (0.76 g, 20 mmol, 2 eq.) in EtOH (25 ml) and purified via manual flash chromatography (10% 1M MeOH NH$_3$ in EtOAc) to give the title compound as a white powder (1.4 g, 70 % yield). **^{1}H-NMR (400 MHz, DMSO)** δ 11.88 (s, 1H, imidazole-N**H**), 7.56 (d, *J* = 1.2 Hz, 1H, imidazole-C**H**-5), 7.10 – 7.01 (m, 2H, ar-C**H**-3), 6.91 (s, 1H, imidazole-C**H**-2), 6.66 – 6.57 (m, 2H, ar-C**H**-2), 5.98 (t, *J* = 5.7 Hz, 1H, N**H**), 4.10 (d, *J* = 5.6 Hz, 2H, C**H**$_2$). **^{13}C-NMR (101 MHz, DMSO)** δ 148.1 (Ar-**C**-1), 135.3 (imidazole-**C**-2), 128.8 (Ar-**C**-3), 119.2 (Ar-**C**-4 and imidazole-**C**-4,5), 114.0 (Ar-**C**-2). Missing: 42.0 (**C**H$_2$). **LC-MS [M+H]$^+$** calcd 208.6; found 208.1, *R*$_t$: 1.77.

N-((*1H*-Imidazol-2-yl)methyl)-3-methoxyaniline (79a)
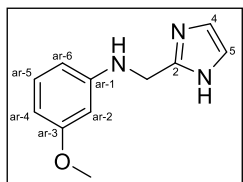
The reaction was performed according to General procedure A with 3-methoxyaniline (**80a**) (1.7 ml, 15.12 mmol, 1 eq.) and 2-imidazolcarbaldehyde (1.45 g, 15.12 mmol, 1 eq.) in methanol (40 ml) and sodium borohydride (2.86 g, 75.66 mmol, 5 eq.) and purified via automated flash chromatography (gradient: 0-5% MeOH in DCM) to give the title compound as a brown oil (859 mg, 41 % yield). **^{1}H-NMR (400 MHz, DMSO)** δ 11.85 (s, 1H, imidazole-N**H**), 6.95 (t, *J* = 8.1 Hz, 1H, imidazole-C**H**-5), 6.92 (s, 1H, imidazole-C**H**-4), 6.24 (ddd, *J* = 8.1, 2.2, 0.9 Hz, 1H, ar-C**H**-4), 6.20 (app. t, *J* = 2.3 Hz, 1H, ar-C**H**-2), 6.14 (dd, *J* = 8.1, 2.4, 0.9 Hz, 1H, ar-C**H**-6), 6.01 (app. t, *J* = 5.6 Hz, 1H, ar-C**H**-5), 5.76 (s, 1H, N**H**) 4.20 (d, *J* = 5.5 Hz, 2H, C**H**$_2$), 3.65 (s, 3H, C**H**$_3$). **^{13}C-NMR (101 MHz, DMSO)** δ 160.7 (ar-**C**-3), 150.3 (imidazole-**C**-2), 146.4 (ar-**C**-1), 129.9 (imidazole-**C**H-4,5), 106.0 (ar-**C**-6), 102.1 (ar-**C**-4), 98.7 (ar-**C**-2), 55.0 (**C**H$_3$), 41.6 (**C**H$_2$). **LC-MS [M+H]$^+$** calcd 204.1; found 204.1, *R*$_t$: 0.67.

N-((1H-Imidazol-2-yl)methyl)-3-chloroaniline (79b)
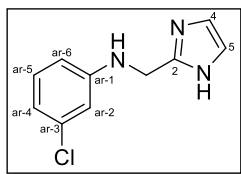
The reaction was performed according to General procedure B with 3-chloroaniline (**80b**) (397 µl, 3.74 mmol, 1.2 eq.), 2-imidazolcarbaldehyde (302 mg, 3.12 mmol, 1 eq.) CeCl$_3$.7H$_2$O (24 mg, 0.06 mmol, 0.02 eq.) and NaBH$_4$ (238 mg, 6.24 mmol, 2 eq.) in EtOH (3 ml) and purified via manual flash chromatography (5% MeOH in DCM) to give the title compound as a yellow oil (330 mg, 60 % yield). **^{1}H-NMR (400 MHz, DMSO)** δ 11.87 (s, 1H, imidazole-N**H**), 7.05 (app. t, *J* = 8.0 Hz, 1H, ar-C**H**-5), 6.92 (s, 2H, imidazole-C**H**-4, NH), 6.66 (q, *J* = 1.9 Hz, 1H, ar-C**H**-2), 6.61 – 6.51 (m, 2H, ar-C**H**-4,6), 6.38 (t, *J* = 5.6 Hz, 1H, imidazole-C**H**-5), 4.22 (d, *J* = 5.6 Hz, 2H, C**H**$_2$). **^{13}C-NMR (101 MHz, DMSO)** δ 150.5 (imidazole-**C**-2), 145.9 (ar-**C**-1), 134.0 (ar-**C**-3), 130.7 (ar-**C**-5, imidazole-**C**H-4), 115.9 (ar-**C**-4), 112.0 (ar-**C**-5, imidazole-**C**H-5), 111.6 (ar-**C**-2), 41.3 (**C**H$_2$). **LC-MS [M+H]$^+$** calc 208.06; found 207.9, *R*$_t$: 1.17.

N-((1H-Imidazol-2-yl)methyl)-4-chloroaniline (79c)
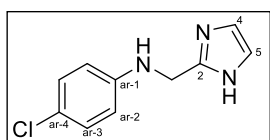
The reaction was performed according to General procedure B with 4-chloroaniline (**80c**) (0.55 g, 4.2 mmol, 1.2 eq), 2-imidazolcarbaldehyde (0.39 g, 4 mmol, 1 eq.), CeCl$_3$.7H$_2$O (0.035 g, 0.08 mmol, 0.02 eq.) and NaBH$_4$ (0.302 g, 8 mmol, 2 eq.) in EtOH (3 ml) and purified via manual flash chromatography (5% MeOH in DCM) to give the title compound as an off-white solid (266 mg, 32 % yield). **^{1}H-NMR (400 MHz, DMSO)** δ 11.86 (s, 1H, imidazole-N**H**), 7.12 – 7.03 (m, 2H, ar-C**H**-2), 6.91 (s, 2H, imidazole-C**H**-4), 6.68 – 6.58 (m, 2H, ar-C**H**-2), 6.23 (t, *J* = 5.6 Hz, 1H, imidazole-C**H**-5), 4.20 (d, *J* = 5.6 Hz, 2H-C**H**$_2$). Missing: 11.88 (imidazole-N**H**), 5.98 (N**H**). **^{13}C-NMR (101 MHz, DMSO)** δ 147.5 (imidazole-**C**-2), 145.6 (ar-**C**-1), 128.4 (ar-**C**-3), 119.4 (ar-**C**-4), 113.8 (ar-**C**-2), 41.14 (**C**H$_2$). Missing: 126.1 (imidazole-**C**-4,5). **LC-MS [M+H]$^+$** calc 208.06; found 208.0, *R*$_t$: 1.24.

### N-((1H-Imidazol-4-yl)methyl)-N-isopropyl-4-morpholinoaniline (82a)
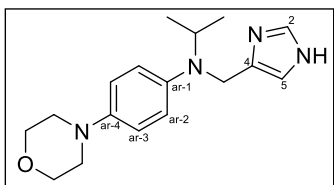
The reaction was performed according to General procedure C with *N*-((*1H*-Imidazol-4-yl)methyl)-4-morpholinoaniline (**85a**) (252 mg, 0.96 mmol, 1 eq.), 2-methoxypropene (138 µl, 1.45 mmol, 1.5 eq.), TFA (73 µl, 0.96 mmol, 1 eq.), NaBH(OAc)$_3$ (203 mg, 0.96 mmol, 1 eq.), 1,2-DCE (10 ml) and 1M HCl (7 ml) and purified via automated flash chromatography (gradient: 0-20 % MeOH in DCM) to give the title compound as a brown powder (90 mg, 31 % yield). **^{1}H-NMR (400 MHz, DMSO)** δ 11.74 (s, 1H, imidazole-N$\underline{H}$), 7.49 (s, 1H, imidazole-C$\underline{H}$-2), 6.76 (d, *J* = 9.2 Hz, 2H, ar-C$\underline{H}$-2), 6.72 (d, *J* = 9.2 Hz, 2H, ar-C$\underline{H}$-3), 6.69 (s, 1H, imidazole-C$\underline{H}$-5), 4.14 (s, 2H, C$\underline{H}_2$), 3.95 (p, *J* = 6.5 Hz, 1H, C$\underline{H}$), 3.69 (t, *J* = 4.7 Hz, 4H, NCH$_2$C$\underline{H}_2$O), 2.91 (t, *J* = 4.7 Hz, 4H, NC$\underline{H}_2$CH$_2$O), 1.11 (d, *J* = 6.5 Hz, 6H, C$\underline{H}_3$). **^{13}C-NMR (101 MHz, DMSO)** δ 143.4 (ar-$\underline{C}$-1,4), 134.8 (imidazole-$\underline{C}$-2), 117.4 (imidazole-$\underline{C}$-5), 116.2 (ar-$\underline{C}$-2), 66.7 (O-$\underline{C}$H$_2$), 50.5 ($\underline{C}$H), 49.3 ($\underline{C}$H$_2$), 20.0 ($\underline{C}$H$_3$). Missing: 132.4 (imidazole-$\underline{C}$-4), 53.3 (N-$\underline{C}$H$_2$CH$_2$). **HRMS (TOF ES$^+$)** C$_{17}$H$_{24}$N$_4$O [M+H]$^+$ calcd 301.2023; found 301.2034, *R*$_t$: 3.04.

N-((*1H*-Imidazol-4-yl)methyl)-*N*-isopropyl-4-(4-methylpiperazin-1-yl)aniline (82b)
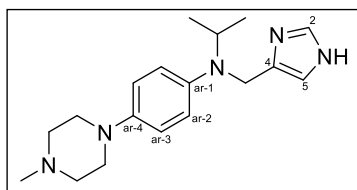
The reaction was performed according to General procedure C with *N*-((*1H*-Imidazol-4-yl)methyl)-4-(4-methylpiperazin-1-yl)aniline (**85b**) (155 mg, 0.57 mmol, 1 eq.), 2-methoxypropene (82 μl, 0.857 mmol, 1.5 eq.), TFA (43.5 μl, 0.57 mmol, 1 eq.), NaBH(OAc)$_3$ (120 mg, 0.57 mmol, 1 eq.), 1,2-DCE (7 ml), 1M HCl (1ml) and purified via automated flash chromatography (gradient 5-30 % MeOH in DCM) and preparative TLC (10 % 1M MeOH NH$_3$ in CHCl$_3$) to give the title compound as a white powder (3 mg, 2 % yield). **^{1}H-NMR (400 MHz, DMSO)** δ 11.74 (s, 1H, imidazole-N**H**), 7.50 (s, 1H, imidazole-C**H**-2), 6.72 (q, *J* = 8.1 Hz, 5H, ar-C**H**-2,3, imidazole-C**H**-5), 4.14 (d, *J* = 16.0 Hz, 2H, C**H**$_2$), 4.00 – 3.92 (m, 1H, C**H**), 2.98 – 2.88 (m, 4H, NC**H**$_2$CH$_2$NCH$_3$), 2.41 (t, *J* = 4.9 Hz, 4H, NCH$_2$C**H**$_2$NCH$_3$), 2.19 (s, 3H, NC**H**$_3$), 1.11 (d, *J* = 6.7 Hz, 6H, CHC**H**$_3$). **^{13}C-NMR (101 MHz, DMSO)** δ 142.4 (ar-**C**-1,4), 134.3 (imidazole-**C**-2), 116.9 (ar-**C**-2,3), 54.6 (N**C**H$_2$CH$_3$), 49.4 (**C**H), 48.4 (N**C**H$_2$CH$_2$), 45.6 (N-**C**H$_3$), 19.3 (**C**H$_3$). Missing: 132.4 (imidazole-**C**-4), 119.2 (imidazole-**C**-5), 39.3 (**C**H$_2$). **HRMS (TOF ES$^+$)** C$_{18}$H$_{27}$N$_5$, [M+H]$^+$ calcd 314.2339; found 314.2330, *R*$_t$: 0.30.

tert-Butyl 4-(4-(((1_H_-imidazol-4-yl)methyl)(isopropyl)amino)phenyl)piperazine-1-carboxylate (82c)
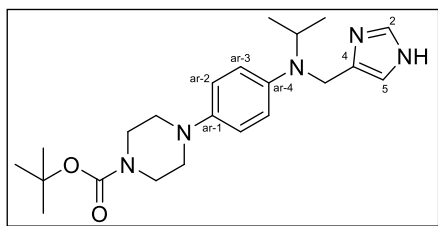
The reaction was performed according to General procedure F with _tert_-Butyl 4-(4-(isopropylamino)phenyl)piperazine-1-carboxylate (**91**) (50 mg, 0.16 mmol, 1 eq.), 4-imidazolecarboxaldehyde (15.5 mg, 0.16 mmol, 1 eq.), picoline borane (16.8 mg, 0.16 mmol, 1 eq.), 10:1 MeOH-AcOH (3 ml) and purified via automated flash chromatography (10 % MeOH in DCM) to give the title compound as a clear oil (20 mg, 31 % yield). **^{1}H-NMR (400 MHz, DMSO)** δ 11.79 (s, 1H, imidazole-N**H**), 7.50 (d, _J_ = 1.4 Hz, 1H, imidazole-C**H**-5), 6.78 (d, _J_ = 8.7 Hz, 2H, ar-C**H**-2), 6.72 (d, _J_ = 8.4 Hz, 3H, ar-C**H**-3, imidazole-C**H**-2), 4.15 (s, 2H, C**H**$_2$), 3.96 (p, _J_ = 6.6 Hz, 1H, C**H**), 3.40 (s, 4H, NCH$_2$C**H**$_2$N), 2.87 (t, _J_ = 5.1 Hz, 4H, NC**H**$_2$CH$_2$N), 1.41 (d, _J_ = 1.2 Hz, 9H, CC**H**$_3$), 1.15 – 1.08 (m, 6H, CHC**H**$_3$). **^{13}C-NMR (101 MHz, DMSO)** δ 154.3 (**C**=O), 143.0 (ar-**C**-1,4), 134.8 (imidazole-**C**-2), 118.5 (ar-**C**-2), 115.9 (ar-**C**-3), 79.3 (**C**CH$_3$), 50.6 (N**C**H$_2$**C**H$_2$N), 49.1 (**C**H$_2$), 28.5 (COO**C**H$_3$), 20.0 (CH**C**H$_3$). Missing 132.4 (imidazole-**C**-4). **HRMS (TOF ES$^+$)** C$_{22}$H$_{33}$N$_5$O$_2$, [M+H]$^+$ calcd 400.2707; found 400.2709, _R_$_t$: 2.01.

N-((1*H*-Imidazol-4-yl)methyl)-*N*-isopropyl-4-(piperazin-1-yl)aniline (82d)
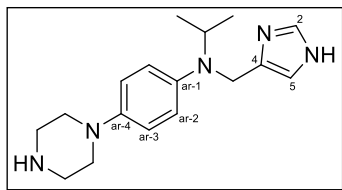
The reaction was performed according to General procedure G with *tert*-Butyl 4-(4-(((1*H*-imidazol-4-yl)methyl)(isopropyl)amino)phenyl)piperazine-1-carboxylate (**82c**) (20 mg), MeOH (0.5 ml) and 4M HCl in dioxane (1.5 ml) to give the title compound as a yellow oil. No further purification was required (12 mg, 80 %). **^{1}H-NMR (400 MHz, MeOD)** δ 8.88 (s, 1H, imidazole-C$\underline{H}$-2), 7.58 (t, *J* = 4.5 Hz, 3H, ar-C$\underline{H}$-3, imidazole-C$\underline{H}$-5), 7.17 (d, *J* = 8.6 Hz, 2H, ar-C$\underline{H}$-2), 5.09 (s, 2H, C$\underline{H}_2$), 4.20 (h, *J* = 6.6 Hz, 1H, C$\underline{H}$), 3.61 – 3.52 (m, 4H, NCH$_2$C$\underline{H}_2$NH), 3.40 (q, *J* = 4.9 Hz, 4H, NC$\underline{H}_2$CH$_2$NH), 1.47 (s, 6H, C$\underline{H}_3$). **^{13}C-NMR (101 MHz, MeOD)** δ 136.3 (imidazole-$\underline{C}$-2), 125.4 (imidazole-$\underline{C}$-5), 123.3 (ar-$\underline{C}$-3), 118.0 (ar-$\underline{C}$-2), 49.2 ($\underline{C}$H), 49.0 (N$\underline{C}$H$_2$CH$_2$NH), 46.5 (NCH$_2$$\underline{C}H_2$N), 44.5 ($\underline{C}H_2$), 18.8 ($\underline{C}H_3$). Missing: 139.1 (ar-$\underline{C}$-1,4, imidazole-$\underline{C}$-4). **HRMS (TOF ES$^+$)** C$_{17}H_{25}N_5$, [M+H]$^+$ calc 300.2183; found 300.2183, R_t: 3.09.

N-((*1H*-Imidazol-2-yl)methyl)-*N*-isopropyl-4-morpholinoaniline (83a)
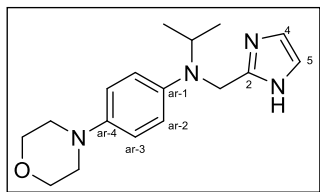
The reaction was performed according to General procedure C with *N*-((*1H*-Imidazol-2-yl)methyl)-4-morpholinoaniline (**86a**) (251 mg, 0.96 mmol, 1 eq.), 2-methoxypropene (139 µl, 1.45 mmol, 1.5 eq.), TFA (73 µl, 0.96 mmol, 1 eq.), NaBH(OAc)$_3$ (206 mg, 0.96 mmol, 1 eq.), 1,2-DCE (5 ml) and 1M HCl (4 ml) and purified via automated flash chromatography (5:95 MeOH: DCM) and preparative TLC (7 % 1M MeOH NH$_3$ in CHCl$_3$) to give the title compound as a white powder (27 mg, 8 % yield). **^{1}H-NMR (400 MHz, DMSO)** δ 11.52 (s, 1H, imidazole-N**H**), 6.93 – 6.87 (m, 1H, imidazole-C**H**-4), 6.82 – 6.67 (m, 5H, ar-C**H**-2,3, imidazole-C**H**-5), 4.21 (s, 2H, C**H**$_2$), 3.97 (p, *J* = 6.6 Hz, 1H, C**H**), 3.69 (dd, *J* = 5.7, 3.7 Hz, 4H, NCH$_2$C**H**$_2$O), 2.91 (t, *J* = 4.7 Hz, 4H, NC**H**$_2$CH$_2$O), 1.12 (d, *J* = 6.4 Hz, 6H, C**H**$_3$). **^{13}C-NMR (101 MHz, DMSO)** δ 146.7 (ar-**C**-1), 143.2 (ar-**C**-4), 142.6 (imidazole-**C**-2), 127.1 (imidazole-**C**-4), 116.6 (imidazole-**C**-5), 116.0 (ar-**C**-3), 115.5 (ar-**C**-2), 66.0 (O-**C**H$_2$), 49.7 (**C**H), 49.0 (N-**C**H$_2$CH$_2$O), 43.1 (**C**H$_2$), 19.0 (**C**H$_3$). **HRMS (TOF ES$^+$)** C$_{17}$H$_{24}$N$_4$O, [M+H]$^+$ calcd 301.2023; found 301.2021, *R*$_t$: 2.56.

N-((1H-Imidazol-2-yl)methyl)-N-isopropyl-4-(4-methylpiperazin-1-yl)aniline (83b)
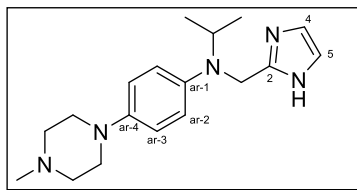
The reaction was performed according to General procedure C with N-((1H-Imidazol-2-yl)methyl)-4-(4-methylpiperazin-1-yl)aniline (**86b**) (250 mg, 0.92 mmol, 1 eq.), 2-methoxypropene (132 µl, 1.38 mmol, 1.5 eq.), TFA (70 µl, 0.92 mmol, 1 eq.), NaBH(OAc)$_3$ (194 mg, 0.92 mmol, 1 eq.), 1,2-DCE (5 ml), 1M HCl (4 ml) and purified via automated flash chromatography (gradient: 5-30 % MeOH in DCM) and preparative TLC (7 % 1M MeOH NH$_3$ in CHCl$_3$) to give the title compound as a white powder (42 mg, 14 % yield). **^{1}H-NMR (400 MHz, DMSO)** δ 11.52 (s, 1H, imidazole-N**H**), 6.90 (s, 1H, imidazole-C**H**-4), 6.83 – 6.63 (m, 5H, ar-C**H**-2,3), 6.48 (d, J = 8.4 Hz, 1H, imidazole-C**H**-5), 4.20 (s, 2H, C**H**$_2$), 3.96 (p, J = 6.5 Hz, 1H, C**H**), 2.93 (t, J = 4.9 Hz, 4H, NC**H**$_2$CH$_2$NCH$_3$), 2.41 (t, J = 4.9 Hz, 4H, NCH$_2$C**H**$_2$NCH$_3$), 2.19 (s, 3H, N-C**H**$_3$), 1.11 (d, J = 6.5 Hz, 6H, CHC**H**$_3$). **^{13}C-NMR (101 MHz, DMSO)** δ 147.1 (imidazole-**C**-2), 143.7 (ar-**C**-4), 142.7 (ar-**C**-1), 127.5 (imidazole-**C**-4), 117.2 (ar-**C**-2), 116.5 (ar-**C**-3), 116.0 (imidazole-**C**-5), 55.0 (NCH$_2$**C**H$_2$NCH$_3$), 50.4 (**C**H), 49.7 (**C**H$_2$), 49.6 (N**C**H$_2$CH$_2$NCH$_3$), 46.00 (N-**C**H$_3$), 19.4 (CH**C**H$_3$). **HRMS (TOF ES$^+$)** C$_{18}$H$_{27}$N$_5$, [M+H]$^+$ calcd 314.2339; found 314.2336, R_t: 0.37.

tert-Butyl 4-(4-(((1*H*-imidazol-2-yl)methyl)(isopropyl)amino)phenyl)piperazine-1-carboxylate (83c)
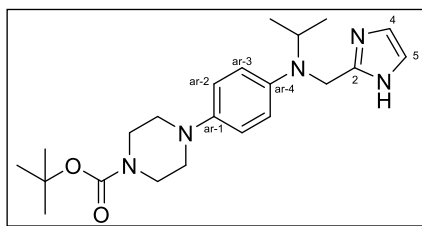
The reaction was performed according to General procedure F with *tert*-Butyl 4-(4-(isopropylamino)phenyl)piperazine-1-carboxylate (**91**) (50 mg, 0.16 mmol, 1 eq.), 2-imidazolecarboxaldehyde (15.5 mg, 0.16 mmol, 1 eq.), picoline borane (16.8 mg, 0.16 mmol, 1 eq.), 10:1 MeOH-AcOH (3 ml) and purified via automated flash chromatography (10 % MeOH in DCM) to give the title compound as a clear oil (11 mg, 17 % yield). **^{1}H-NMR (400 MHz, DMSO)** δ 11.52 (s, 1H, imidazole-N**H**), 6.90 (d, *J* = 1.8 Hz, 1H, imidazole-C**H**-4), 6.82 – 6.75 (m, 3H, ar-C**H**-3, imidazole-CH-5), 6.71 (d, *J* = 8.3 Hz, 2H, ar-C**H**-2), 4.21 (s, 2H, C**H**$_2$), 3.99 (p, *J* = 6.6 Hz, 1H, C**H**), 3.41 (t, *J* = 4.9 Hz, 4H, NCH$_2$C**H**$_2$N), 2.87 (t, *J* = 5.0 Hz, 4H, NC**H**$_2$CH$_2$N), 1.40 (d, *J* = 1.5 Hz, 9H, CC**H**$_3$), 1.12 (d, *J* = 6.4 Hz, 6H, CHC**H**$_3$). **^{13}C-NMR (101 MHz, DMSO)** δ 147.4 (ar-**C**-1,4), 143.6 (imidazole-**C**-2), 127.8 (imidazole-**C**-4), 118.4 (imidazole-**C**-5), 116.4 (ar-**C**-3), 116.3 (ar-**C**-2), 79.4 (**C**CH$_3$), 50.5 (N**C**H$_2$CH$_2$N), 49.6 (NCH$_2$**C**H$_2$N), 43.7 (**C**H$_2$), 28.5 (C**C**H$_3$), 19.7 (CH**C**H$_3$). **HRMS (TOF ES$^+$)** C$_{22}$H$_{33}$N$_5$O$_2$, [M+H]$^+$ calcd 400.2707; found 400.2707, R_t: 3.14.

N-((1*H*-Imidazol-2-yl)methyl)-*N*-isopropyl-4-(piperazin-1-yl)aniline (83d)
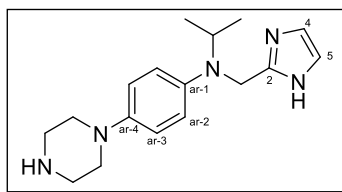
The reaction was performed according to General procedure G with *tert*-Butyl 4-(4-(((1*H*-imidazol-2-yl)methyl)(isopropyl)amino)phenyl)piperazine-1-carboxylate (**83c**) (11 mg) in MeOH (0.5 ml) and 4M HCl in dioxane (1.5 ml) and purified via preparative TLC (10 % 1M MeOH NH$_3$ in DCM) to give the title compound as a brown oil. No further purification was required (6 mg, 73 % yield). **^{1}H-NMR (400 MHz, MeOD)** δ 6.92 – 6.84 (m, 4H, ar-C**H**-3, imidazole-C**H**-4,5), 6.84 – 6.76 (m, 2H, ar-C**H**-2), 4.32 (s, 2H, C**H**$_2$), 4.04 (h, *J* = 6.6 Hz, 1H, C**H**), 3.08 (s, 8H, NC**H**$_2$C**H**$_2$N), 1.18 (d, *J* = 6.6 Hz, 6H, C**H**$_3$). **^{13}C-NMR (101 MHz, MeOD)** δ 118.2 (imidazole-**C**H-4,5), 117.4 (ar-**C**-2,3), 50.0 (**C**H), 44.6 (**C**H$_2$), 18.2 (**C**H$_3$). Missing 139.1 (ar-**C**-1,4), 138.9 (imidazole-**C**-2). **HRMS (TOF ES$^+$)** C$_{17}$H$_{25}$N$_5$, [M+H]$^+$ calc 300.2183; found 300.2191, *R*$_t$: 0.31.

N-((1*H*-Imidazol-4-yl)methyl)-4-morpholinoaniline (85a)
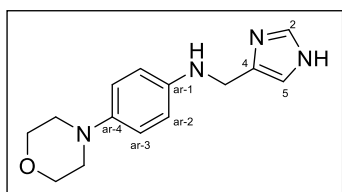
The reaction was performed according to General procedure B with 4-morpholinoaniline (**84a**) (0.55 g, 3.12 mmol, 1.2 eq.) and 4-imidazolcarbaldehyde (0.25 g, 2.6 mmol, 1 eq.), CeCl$_3$.7H$_2$O (19 mg, 0.052 mmol, 0.05 eq.) and NaBH$_4$ (196 mg, 5.2 mmol, 2 eq.) in ethanol (10 ml) and purified via automated flash chromatography (gradient: 5-20% MeOH in DCM) to give the title compound as an off-white powder (360 mg, 27 % yield). **^{1}H-NMR (400 MHz, DMSO)** δ 11.85 (s, 1H, imidazole-N**H**), 7.54 (s, 1H, imidazole-C**H**-2), 6.89 (s, 1H, imidazole-C**H**-5), 6.73 (d, *J* = 8.6 Hz, 2H, ar-C**H**-3), 6.58 (d, *J* = 8.5 Hz, 2H, ar-C**H**-2), 5.30 (s, 1H, N**H**), 4.06 (s, 2H, C**H**$_2$), 3.69 (t, *J* = 4.7 Hz, 4H, NCH$_2$C**H**$_2$O), 2.92 – 2.85 (m, 4H, NC**H**$_2$CH$_2$O). **^{13}C-NMR (101 MHz, DMSO)** δ 142.8 (ar-**C**-4), 142.2 (ar-**C**-1), 134.5 (imidazole-**C**-2,4), 117.2 (ar-**C**-2, imidazole-**C**-5), 113.0 (ar-**C**-3), 66.1 (O-**C**H$_2$), 50.3 (N-**C**H$_2$). Missing 42.0 (**C**H$_2$). **LC-MS [M+H]$^+$** calcd 259.3; found 259.1, *R*$_t$: 0.40.

_N_-((_1H_-Imidazol-4-yl)methyl)-4-(4-methylpiperazin-1-yl)aniline (85b)
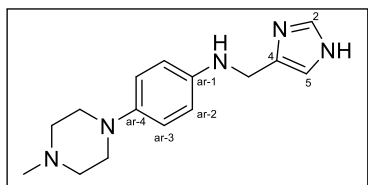
The reaction was performed according to General procedure B with 4-(4-methylpiperidin-1-yl)aniline (**84b**) (0.98 g, 5.22 mmol, 1.2 eq.), 4-imidazolcarbaldehyde (0.42 g, 4.33 mmol, 1 eq.), CeCl$_3$.7H$_2$O (89 mg, 0.22 mmol, 0.2 eq.) and NaBH$_4$ (329 mg, 8.66 mmol, 2 eq.) in EtOH (10 ml) and purified via automated flash chromatography (gradient:15-50 % MeOH in DCM) to give the title compound as a brown powder (495 mg, 42 % yield). **^{1}H-NMR (400 MHz, DMSO)** δ 11.84 (s, 1H, imidazole-N**H**), 7.54 (s, 1H, imidazole-C**H**-2), 6.88 (s, 1H, imidazole-C**H**-5), 6.77 – 6.66 (m, 2H, ar-C**H**-3), 6.63 – 6.48 (m, 2H, ar-C**H**-2), 5.26 (s, 1H, N**H**), 4.06 (s, 2H, C**H**$_2$), 2.90 (t, _J_ = 4.9 Hz, 4H, NC**H**$_2$CH$_2$NCH$_3$), 2.41 (t, _J_ = 4.9 Hz, 4H, NCH$_2$C**H**$_2$NCH$_3$), 2.19 (d, _J_ = 1.2 Hz, 3H, C**H**$_3$). **^{13}C-NMR (101 MHz, DMSO)** δ 134.5 (imidazole-**C**-2), 117.5 (ar-**C**-2,3), 113.0 (imidazole-**C**-5), 54.7 (N-**C**H$_2$CH$_3$), 49.9 (**C**H$_3$), 45.6 (N-**C**H$_2$). Missing: 138.8 (ar-**C**-1), 138.0 (ar-**C**-4), 132.4 (imidazole-**C**-4), 42.0 (**C**H$_2$). **LC-MS [M+H]$^+$** calcd 272.18; found 271.0, _R_$_t$: 0.36.

N-((*1H*-Imidazol-2-yl)methyl)-4-morpholinoaniline (86a)
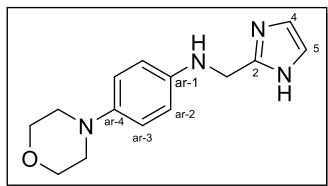
The reaction was performed according to General procedure B with 4-morpholinoaniline (**84a**) (504 mg, 2.82 mmol, 1.2 eq.) and 2-imidazolcarbaldehyde (227 mg, 2.35 mmol 1 eq.), CeCl$_3$.7H$_2$O (41 mg, 0.11 mmol, 0.1 eq.) and NaBH$_4$ (182 mg, 4.7 mmol, 2 eq.) in ethanol (10 ml) and purified via automated flash chromatography (gradient: 5-20% MeOH in DCM) to give the title compound as an off-white powder (308 mg, 51 % yield). **^{1}H-NMR (400 MHz, DMSO)** δ 11.78 (s, 1H, imidazole-N**H**), 6.89 (s, 2H, imidazole-C**H**-4,5), 6.73 (d, *J* = 8.5 Hz, 2H, ar-C**H**-3), 6.57 (d, *J* = 8.5 Hz, 2H, ar-C**H**-2), 5.55 (t, *J* = 5.7 Hz, 1H, N**H**), 4.16 (d, *J* = 5.4 Hz, 2H, C**H**$_2$), 3.69 (dd, *J* = 5.7, 3.7 Hz, 4H, NCH$_2$C**H**$_2$O), 2.88 (dd, *J* = 5.6, 3.6 Hz, 4H NC**H**$_2$CH$_2$O). **^{13}C-NMR (101 MHz, DMSO)** δ 146.6 (imidazole-**C**-2), 143.0 (ar-**C**-4), 142.9 (ar-**C**-1), 117.6 (ar-**C**-2), 113.6 (ar-**C**-3), 66.5 (O-**C**H$_2$), 50.7 (N-**C**H$_2$), 42.1 (**C**H$_2$). Missing: 121.4 (imidazole-**C**-4,5). **LC-MS [M+H]$^+$** calcd 259.3; found 259.1, *R*$_t$: 0.47.

N-((1H-Imidazol-2-yl)methyl)-4-(4-methylpiperazin-1-yl)aniline (86b)
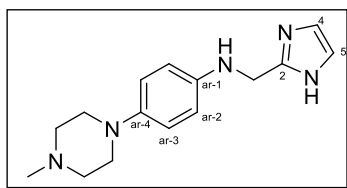
The reaction was performed according to General procedure B with 4-(4-methylpiperidin-1-yl)aniline (**84b**) (0.99 g, 5.22 mmol, 1.2 eq.), 2-imidazolcarbaldehyde (410 mg, 4.33 mmol, 1 eq.), CeCl$_3$.7H$_2$O (90 mg, 0.217 mmol, 0.2 eq.) and NaBH$_4$ (326 mg, 8.66 mmol, 2 eq.) in EtOH (10 ml) and purified via automated flash chromatography (15-50 % MeOH in DCM) to give the title compound as a pink powder (370 mg, 32 % yield). **^{1}H-NMR (400 MHz, DMSO)** δ 11.80 (s, 1H, imidazole-N**H**), 6.90 (s, 2H, imidazole-C**H**-4,5), 6.73 (d, J = 8.5 Hz, 2H, ar-C**H**-3), 6.56 (d, J = 8.5 Hz, 2H, ar-C**H**-2), 5.52 (t, J = 5.7 Hz, 1H, N**H**), 4.16 (d, J = 4.8 Hz, 2H, C**H**$_2$), 2.90 (t, J = 4.9 Hz, 4H, NC**H**$_2$CH$_2$NCH$_3$), 2.41 (t, J = 4.9 Hz, 4H, NCH$_2$C**H**$_2$NCH$_3$), 2.19 (d, J = 1.1 Hz, 3H, C**H**$_3$). **^{13}C-NMR (101 MHz, DMSO)** δ 146.6 (ar-**C**-1), 143.1 (ar-**C**-4), 142.6 (imidazole-**C**-2), 117.9 (imidazole-**C**-4,5), 113.6 (ar-**C**-2), 55.1 (N-**C**H$_2$CH$_3$), 50.2 (N-**C**H$_2$CH$_2$), 46.0 (**C**H$_3$), 42.2(**C**H$_2$). Missing: 129.0 (ar-**C**-3). **LC-MS [M+H]$^+$** calcd 272.2; found 272.0, R_t: 0.40.

N-((1H-Imidazol-4-yl)methyl)-4-bromoaniline (88a)
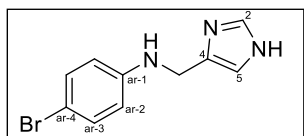
The reaction was performed according to General procedure B with of 4-bromoaniline (**87**) (2.19 g, 12.48 mmol, 1.2 eq.), 4-imidazolcarbaldehyde (1 g, 10.4 mmol, 1 eq.), CeCl$_3$.7H$_2$O (0.195 g, 0.52mmol, 0.5 eq.) and NaBH$_4$ (0.785g, 20.8 mmol, 2 eq.) in EtOH (20 ml) and purified via automated flash chromatography (5 % MeOH in DCM) to give the title compound as an off-white powder (770 mg, 29 % yield). **^{1}H-NMR (400 MHz, DMSO)** δ 11.87 (s, 1H, imidazole-N**H**), 7.56 (s, 1H,imidazole-C**H**-2), 7.17 (d, J = 8.4 Hz, 2H, ar-C**H**-3), 6.93 (s, 1H, NH), 6.62 – 6.55 (m, 2H, ar-C**H**-2), 6.05 (t, J = 5.6 Hz, 1H, imidazole-C**H**-5), 4.21 – 3.95 (m, 2H, C**H**$_2$). **^{13}C-NMR (101 MHz, DMSO)** δ 148.5 (ar-C-1), 135.4 (imidazole-**C**-2), 131.7 (ar-**C**-3), 114.7 (ar-**C**-2). Missing 132.4 (imidazole-**C**-4), 119.2 (imidazole-**C**-5), 42.0 (**C**H$_2$). **LC-MS [M+H]$^+$** calcd 252.1; found 252.0, R_t: 1.23.

N-((1H-Imidazol-2-yl)methyl)-4-bromoaniline (88b)
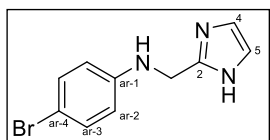
The reaction was performed according to General procedure B with of 4-bromoaniline (**87**) (2.14 g, 12.48 mmol, 1.2 eq.), 4-imidazolcarbaldehyde (1 g, 10.4 mmol, 1 eq.), CeCl₃.7H₂O (0.198 g, 0.52 mmol, 0.5 eq.) and NaBH₄ (0.788 g, 20.8 mmol, 2 eq.) in EtOH (20 ml) and purified via automated flash chromatography (5 % MeOH in DCM) to give the title compound as an off-white powder (1.05 g, 39 % yield). **¹H-NMR (400 MHz, DMSO)** δ 11.86 (s, 1H, imidazole-N**H**), 7.19 (d, *J* = 8.5 Hz, 2H, imidazole-C**H**-4,5), 6.91 (s, 2H, ar-C**H**-3), 6.64 – 6.55 (m, 2H, ar-C**H**-2), 6.26 (t, *J* = 5.6 Hz, 1H, N**H**), 4.20 (d, *J* = 5.5 Hz, 2H, C**H₂**). **¹³C-NMR (101 MHz, DMSO)** δ 148.3 (imidazole-**C**-2), 146.0 (ar-**C**-1), 131.7 (ar-**C**-3), 114.8 (ar-**C**-2), 41.5 (**C**H₂). Missing: 121.4 (imidazole-**C**-4,5), 115.1 (ar-**C**-4). **LC-MS [M+H]⁺** calcd 252.1; found 252.0, *R*ₜ: 1.24.

### N-((1H-Imidazol-4-yl)methyl)-4-bromo-N-isopropylaniline (89a)
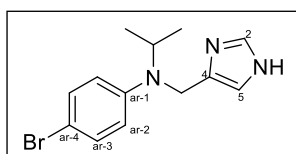
The reaction was performed according to General procedure C with N-((1H-Imidazol-4-yl)methyl)-4-bromoaniline (**88a**) (0.66 g, 2.2 mmol, 1 eq.), 2-methoxypropene (317 µl, 3.3 mmol, 1.5 eq.), TFA (168 µl, 2.2 mmol, 1 eq.), NaBH(OAc)₃ (0.47 g, 2.2 mmol, 1 eq.), 1,2-DCE (5 ml) and 1M HCl (2 ml) and purified via automated flash chromatography (10% MeOH in DCM) to give the title compound as an off-white powder (273 mg, 42 % yield). **¹H-NMR (400 MHz, DMSO)** δ 11.84 (s, 1H, imidazole-N**H**), 7.53 (d, *J* = 1.3 Hz, 1H, imidazole-C**H**-2), 7.21 (d, *J* = 8.7 Hz, 2H, ar-C**H**-3), 6.78 – 6.68 (m, 3H, ar-C**H**-2, imidazole-C**H**-5), 4.21 (d, *J* = 11.7 Hz, 2H, C**H₂**), 4.10 (q, *J* = 6.6 Hz, 1H, C**H**), 1.16 (dd, *J* = 6.5, 1.3 Hz, 6H, C**H₃**). **¹³C-NMR (101 MHz, DMSO)** δ 148.4 (ar-**C**-1), 135.3 (imidazole-**C**-2), 131.7 (imidazole-**C**-4), 131.6 (ar-**C**-3), 115.4 (ar-**C**-4), 115.3 (imidazole-**C**-5), 114.5 (ar-**C**-2), 49.6 (**C**H), 20.1 (**C**H₃). Missing: 39.3 (**C**H₂). **LC-MS [M+H]⁺** calcd 295.2; found 295.3, *R*ₜ: 1.34.

N-((*1H*-Imidazol-2-yl)methyl)-4-bromo-*N*-isopropylaniline (89b)
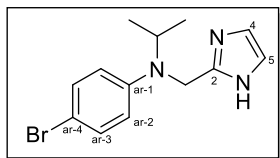
The reaction was performed according to General procedure C with *N*-((*1H*-Imidazol-2-yl)methyl)-4-bromoaniline (**88b**) (0.79 g, 2.7 mmol, 1 eq.), 2-methoxypropene (390 µl, 4.0 mmol, 1.5 eq.), TFA (208 µl, 2.7 mmol, 1 eq.), NaBH(OAc)$_3$ (0.57 g, 2.7 mmol, 1 eq.), 1,2-DCE (7 ml) and 1M HCl (4 ml) and purified via automated flash chromatography (10 % MeOH in DCM) to give the title compound as an orange powder (470 mg, 58.8 % yield). **^{1}H-NMR (400 MHz, DMSO)** δ 11.63 (s, 1H, imidazole-N**H**), 7.29 – 7.21 (m, 2H, ar-C**H**-3), 6.88 (s, 2H, imidazole-C**H**-4,5), 6.75 – 6.66 (m, 2H, ar-C**H**-2), 4.31 (s, 2H, C**H**$_2$), 4.15 (pt, *J* = 11.3, 6.1 Hz, 1H, C**H**), 1.16 (d, *J* = 6.5 Hz, 6H, C**H**$_3$). **^{13}C-NMR (101 MHz, DMSO)** δ 148.5 (imidazole-**C**-2), 146.5 (ar-**C**-1), 131.7 (ar-**C**-3), 115.7 (ar-**C**-2, imidazole-**C**-5), 107.8 (ar-**C**-4), 48.6 (**C**H), 42.8 (**C**H$_2$), 19.7 (**C**H$_3$). Missing: 121.4 (imidazole-**C**-4). **LC-MS [M+H]$^+$** calcd 294.2; found 294.1, *R*$_t$: 2.11.

tert-Butyl 4-(4-(isopropylamino)phenyl)piperazine-1-carboxylate (91)
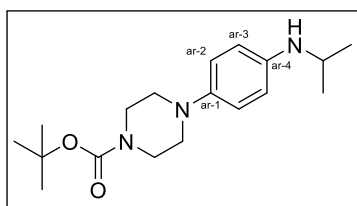
The reaction was performed according to General procedure E with *tert*-butyl 4-(4-aminophenyl)piperazine-1-carboxylate (**90**) (5.00 g, 18 mmol, 3 eq.), 2-iodopropane (600 µl, 6 mmol, 1 eq.) and potassium carbonate (913 mg, 6 mmol, 1.1 eq.) in 1,4-dioxane (7 ml) and purified via automated flash chromatography (30% EtOAc in cyC$_6$H$_{12}$) to give the title compound as an off-white powder (312 mg, 16 % yield). **^{1}H-NMR (400 MHz, DMSO)** δ 6.75 (d, *J* = 8.3 Hz, 2H, ar-C**H**-2), 6.48 (d, *J* = 8.3 Hz, 2H, ar-C**H**-3), 4.85 (s, 1H, N**H**), 3.53 – 3.36 (m, 5H, CHCH$_3$, NCH$_2$C**H**$_2$N), 2.84 (t, *J* = 5.0 Hz, 4H, NC**H**$_2$CH$_2$N), 1.41 (d, *J* = 1.3 Hz, 9H, CC**H**$_3$), 1.09 (dd, *J* = 6.3, 1.3 Hz, 6H, CHC**H**$_3$). **^{13}C-NMR (101 MHz, DMSO)** δ 143.2 (**C**=O), 142.3 (ar-**C**-1), 119.3 (ar-**C**-3), 113.8 (ar-**C**-2), 79.3 (O**C**CH$_3$), 51.2 (N-**C**H$_2$), 43.9 (**C**H), 28.6 (C**C**H$_3$), 23.1 (CH**C**H$_3$). Missing 137.1 (ar-**C**-4). **LC-MS [M+H]$^+$** calcd 319.4; found 319.9, *R*$_t$: 2.09.

N-Phenyl-1*H*-imidazole-4-carboxamide (96)
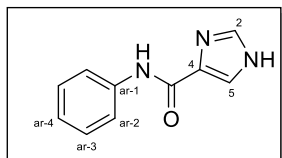
Aniline (**95**) (97.7 µl, 1.07 mmol, 1.2 eq.) was reacted with 4-imidazolecarboxylic acid (100mg, 0.89 mmol, 1 eq.), HATU (402 mg, 1.78 mmol, 2 eq.), DIPEA (310 µl, 1.78 mmol, 2 eq.) in DMF (3 ml) and purified via automated flash chromatography (5% MeOH in DCM) to give the title compound as a white solid (152 mg, 91 % yield). **^{1}H-NMR (400 MHz, DMSO)** δ 12.64 (s, 1H, imidazole-N**H**), 9.77 (s, 1H, N**H**), 7.82 (dd, *J* = 8.9, 4.1 Hz, 4H, ar-C**H**-2, imidazole-C**H**-2,5), 7.32 (t, *J* = 7.8 Hz, 2H, ar-C**H**-3), 7.05 (t, *J* = 7.4 Hz, 1H, ar-C**H**-4). **^{13}C-NMR** data was not obtained.

N-Isopropyl-4-morpholinoaniline (98a)
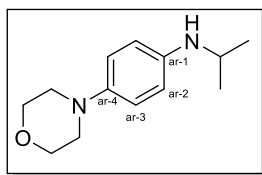
The reaction was performed according to General procedure E with 4-morpholinoaniline (**84a**) (2.00 g, 11.22 mmol, 3 eq.), 2-iodopropane (410 µl, 4.11 mmol, 1 eq.) and potassium carbonate (516.8 mg, 3.74 mmol, 1.1 eq.) in 1,4-dioxane (7 ml) and purified via automated flash chromatography (10% MeOH in DCM) to give the title compound as an orange solid (200 mg, 24 % yield). **^{1}H-NMR (400 MHz, DMSO)** δ 6.73 (d, *J* = 8.5 Hz, 2H, ar-C**H**-3), 6.49 (d, *J* = 8.6 Hz, 2H, ar-C**H**-2), 4.79 (d, *J* = 8.3 Hz, 1H, N**H**), 3.77 – 3.66 (m, 4H, NCH$_2$C**H**$_2$O), 3.44 (dq, *J* = 12.9, 6.2 Hz, 1H, CH), 2.91 – 2.85 (m, 4H, NC**H**$_2$CH$_2$O), 1.09 (dd, *J* = 6.3, 1.0 Hz, 6H, C**H**$_3$). **^{13}C-NMR (101 MHz, DMSO)** δ 142.9 (ar-**C**-4), 142.5 (ar-**C**-1), 118.1 (ar-**C**-3), 113.9 (ar-**C**-2), 66.8 (O-**C**H$_2$), 51.1 (N-**C**H$_2$), 44.0 (**C**H), 23.1 (**C**H$_3$). **LC-MS [M+H]$^+$** calcd 221.3; found 221.4, *R*$_t$: 0.57.

N-Isopropyl-4-(4-methylpiperazin-1-yl)aniline (98b)
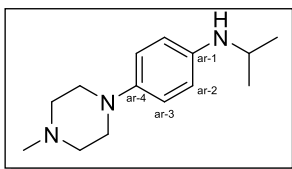
The reaction was performed according to General procedure E with 4-(4-methylpiperidin-1-yl)aniline (**84b**) (1.00 g, 5.2 mmol, 3 eq.), 2-iodopropane (174 µl, 1.74 mmol, 1 eq.) and potassium carbonate (270 mg, 1.92 mmol, 1.1 eq.) in 1,4-dioxane (5 ml) and purified via automated flash chromatography (10 % 1M MeOH NH$_3$ in DCM) to give the title compound as an orange oil (210 mg, 52 % yield). **^{1}H-NMR (400 MHz, DMSO)** δ 6.75 – 6.68 (m, 2H, ar-C**H**-3), 6.47 (d, *J* = 8.5 Hz, 2H, ar-C**H**-2), 4.75 (d, *J* = 7.4 Hz, 1H, N**H**), 3.43 (h, *J* = 6.4 Hz, 1H, C**H**), 2.90 (t, *J* = 4.9 Hz, 4H, NC**H**$_2$CH$_2$NCH$_3$), 2.42 (t, *J* = 4.9 Hz, 4H NCH$_2$C**H**$_2$NCH$_3$), 2.20 (s, 3H NC**H**$_3$), 1.09 (dd, *J* = 6.3, 1.0 Hz, 6H, CHC**H**$_3$). **^{13}C-NMR (101 MHz, DMSO)** δ 118.4 (ar-**C**-3), 113.9 (ar-**C**-2), 55.4 (NCH$_2$**C**H$_2$NCH$_3$), 50.6 (N**C**H$_2$CH$_2$NCH$_3$), 46.2 (**C**H), 44.0 (N-**C**H$_3$), 23.1 (**C**H$_3$). Missing 138.0 (ar-**C**-4), 137.1 (ar-**C**-1). **LC-MS [M+H]$^+$** calcd 234.3; found 234.3, *R*$_t$: 0.27.

4-Chloro-*N*-isopropylaniline (98c)
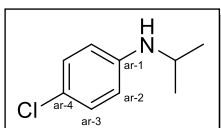
The reaction was performed according to General procedure E with 4-chloroaniline (**80c**) (899 mg, 6.6 mmol, 3 eq.), 2-iodopropane (221 µl, 2.2 mmol, 1 eq.) and potassium carbonate (335 mg, 2.4 mmol, 1.1 eq.) in 1,4-dioxane (5 ml) and purified via automated flash chromatography (5% EtOAc in cyC$_6$H$_{12}$) to give the title compound as a deep red oil (172 mg, 46 % yield). **^{1}H-NMR (400 MHz, DMSO)** δ 7.09 – 7.00 (m, 2H, ar-C**H**-3), 6.57 – 6.49 (m, 2H, ar-C**H**-2), 5.55 (d, *J* = 8.0 Hz, 1H, N**H**), 3.56 – 3.42 (m, 1H, C**H**), 1.10 (dd, *J* = 6.3, 1.3 Hz, 6H, C**H**$_3$). **^{13}C-NMR (101 MHz, DMSO)** δ 147.5 (ar-**C**-1), 129.3 (ar-**C**-3), 129.0 (ar-**C**-4), 114.1 (ar-**C**-2), 43.5 (**C**H), 22.8 (**C**H$_3$). **LC-MS [M+H]$^+$** calcd 169.6; found 170.1, *R*$_t$: 2.18.

N-(4-(4-Methylpiperazin-1-yl)phenyl)acetamide (99b)
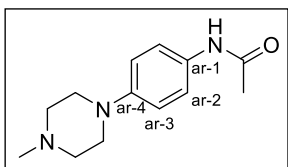
The reaction was performed according to General procedure C with 4-(4-methylpiperidin-1-yl)aniline (**84b**) (500 mg, 2.6 mmol, 1 eq.), 2-methoxypropene (375 µl, 3.92 mmol, 1.5 eq.), TFA (199.7 µl, 2.6 mmol, 1 eq.), sodium triacetoxyborohydride (553.2 mg, 2.61 mmol, 1 eq.) in 1,2-DCE (5 ml). The resulting residue was purified via automated flash chromatography (gradient: 7-10 % MeOH in DCM) to give the title compound as an orange powder (200 mg, 33 % yield). **¹H-NMR (400 MHz, DMSO)** δ 9.67 (s, 1H, N**H**), 7.40 (d, *J* = 8.6 Hz, 2H, ar-C**H**-2), 6.85 (d, *J* = 8.8 Hz, 2H, ar-C**H**-3), 3.04 (t, *J* = 5.0 Hz, 4H, NC**H**₂CH₂NCH₃), 2.43 (t, *J* = 5.0 Hz, 4H, NCH₂C**H**₂NCH₃), 2.21 (s, 3H, NC**H**₃), 1.98 (s, 3H, COC**H**₃). **¹³C-NMR (101 MHz, DMSO)** δ 142.4 (ar-**C**-4), 142.2 (ar-**C**-1), 118.1 (ar-**C**-2), 113.7 (ar-**C**-3), 55.1 (NCH₂**C**H₂NCH₃), 50.4 (N**C**H₂CH₂NCH₃), 46.0 (N-**C**H₃), 22.8 (CO**C**H₃). Missing: 168.9 (**C**=O). **LC-MS [M+H]⁺** calcd 234.3; found 234.1, R_t: 0.37.

N-(4-Chlorophenyl)acetamide (99c)
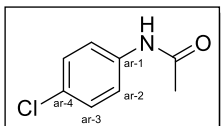
The reaction was performed according to General procedure C with 4-chloroaniline (**84c**) (1 g, 7.8 mmol, 1 eq.), 2-methoxypropene (1.2 ml, 11.76 mmol, 1.5 eq,), TFA (596 µl, 7.8 mmol, 1 eq.), sodium triacetoxyborohydride (1.65 g, 7.8 mmol, 1 eq.) in 1,2-DCE (7 ml). The resulting residue was purified via automated flash chromatography (100% DCM) to give the title compound as a brown powder (0.5 g, 38 % yield). **¹H-NMR (400 MHz, DMSO)** δ 10.05 (s, 1H, N**H**), 7.64 – 7.55 (m, 2H, ar-C**H**-2), 7.38 – 7.29 (m, 2H, ar-C**H**-3), 2.04 (d, *J* = 1.1 Hz, 3H, C**H**₃). **¹³C-NMR (101 MHz, DMSO)** δ 168.0 (**C**=O), 137.8 (ar-**C**-1), 128.1 (ar-**C**-3), 126.0 (ar-**C**-2), 120.0 (ar-**C**-2), 23.6 (**C**H₃). **LC-MS [M+H]⁺** calcd 170.6; found 170.1, R_t: 2.40.

7.3. General Pharmacology

All reagents and plasticware were purchased from standard suppliers. Calcein AM cell viability kits purchased from Abcam (UK), insulin secretion ELISA kits from Mercodia (Sweden) and Cayman Chemical cyclic AMP assay kit from Cambridge Bioscience (UK). All plates were read using the Tecan Mplex Plate Reader (Infinite M PLEX Monochromator for Absorbance (230-1000nm) and Top and Bottom Fluorescence (230-850nm) Luminescence.

7.3.1. Solutions and buffers

Solution	Composition
Krebs-Ringer Buffer (KREBS)	125 mM NaCl, 1.2 mM KH_2PO_4, 5 mM KCl, 2mM $MgSO_4$, 1 mM $CaCl_2$, 1.67 mM glucose, 25 mM HEPES, 0.1 % bovine serum albumin (BSA), pH 7.4
Phosphate buffered saline (PBS)	137 mM NaCl, 2.7 mM KCl, 10 mM Na_2HPO_4, 2 mM KH_2PO_4, pH 7.4
RIPA buffer	150 mM NaCl, 0.5 % sodium deoxycholate, 0.1 % SDS, 50 mM Tris base, 0.1 % triton X 100, pH 8
Cell lysis buffer	RIPA buffer supplemented with 1 protease inhibitor tablet (Sigma Aldrich, catalogue number: 4906837001) per 10 ml.

7.3.2. Cell culture

Medium preparation

INS-1 cells were cultured in complete Roswell Park Memorial Institute (RPMI)-1640 media. dH_2O was supplemented with pre-prepared 10.4 g RPMI-1640 powder, 26 mM sodium bicarbonate, 10 mM HEPES, 50 µM β-mercaptoethanol, 100 mM sodium pyruvate, 1 % penicillin / streptomycin solution (composition: 10,000 units/mL of penicillin and 10,000 µg/mL of streptomycin) and 10 % heat-inactivated foetal bovine serum with pH adjusted to 7.4. Cells were seeded in tissue culture-treated T75 flasks and incubated at 37°C with a 5 % CO_2 and 95 % air atmosphere.

Experimental media

Glucolipotoxicity medium was made by supplementing RPMI-1640 media with 17 mM glucose, 200 μM oleic acid, 200 μM palmitic acid, 2% BSA and stored at 4°C.

Cell passage and amplification

Cells were passaged at 85 % confluency. Spent medium was aspirated and cells washed with 5 ml PBS before incubation in 5 ml Trypsin-EDTA for 3 minutes at 37°C (5 % CO_2 and 95 % air atmosphere) until complete cell detachment. Detached cells were resuspended in 5 ml complete RPMI-1640 medium and centrifuged at 200 G for 5 minutes at room temperature. Cell pellets were washed with 5 ml PBS and resuspended in 5 ml complete RPMI-1640 medium before cell counting and seeding in new treated tissue culture plates or T75 flasks.

Cell counting and plate seeding

Cells were seeded in 6 well plates (~50,000 – 100,000 cells per well (exact number depended on number of viable cells available and quantity of 6 well plates required per experiment) in 2 ml medium) and incubated for 5 days with medium replaced day 1 and day 4. Cells growing in T75 tissue culture flasks were passaged using the method outlined above. Cells were manually counted using a haemocytometer. Upon pellet resuspension in complete RPMI-1640 medium, 10 μl cell solution was mixed with 10 μl trypan blue and loaded into a Neubauer chamber. Cell number was determined counting clockwise from the top-left square and cell concentration calculated.

7.3.3. Cell function assays

Cell viability

Calcein AM Assay Kit (Fluorometric) (Abcam) was used to calculate INS-1 cell viability. Cells were cultured in standard or experimental medium ± test compounds for 5 days before cell viability assay was performed. Spent medium was aspirated and cells washed with KREBS (3 x 1 ml).

Prepared Calcein AM solution (1:500, calcein AM: KREBS) was added and cells incubated for 1 hour at 37°C, before washing thrice with KREBS and lysing them with cell lysis buffer. Cell viability was measured via fluorescence with excitation and emission at 490 and 520 nm respectively. Data represented as % change compared to the control. Pictorial representation is shown in Figure 3.4.

Insulin secretion

INS-1 cells were grown in standard or experimental media ± test compounds for 5 days before washing with KREBS (3 x 1 ml) and incubated in KREBS ± insulin secretagogue cocktail (KREBS supplemented with 1 mM tolbutamide, 10 mM leucine, 10 mM glutamine, 1 µM phorbol 12-myristate 13-acetate, 1 mM isobutyl-methyxanthine and 10 mM glucose) for 2 hours. Supernatant was collected and centrifuged at 7700 G for 2 minutes at room temperature before insulin secretion was determined following the Mercodia High Range Rat Insulin ELISA standard protocol (Mercodia). The ELISA is based on the direct sandwich technique, with the principle procedure outlined in Figure 7.1.

1. Cells are treated with test compounds ± GLT media for 5 days.

2. Sample is added to wells that are pre-coated with mouse monoclonal anti-insulin antibodies.

3. Capture antibody binds to insulin present in the test sample with high specificity.

4. Primary antibody binds the immobilized insulin and peroxidase-conjugated labelled antibody binds to the detection antibody.

5. Substrate TMB binds to peroxidase and catalyses an enzymatic colour change.

6. Measure absorbance at 450 nm.

Figure 7.1 Schematic representation of high range rat insulin ELISA procedure. Image adapted and created using Biorender.com.

Data was normalised to cellular protein content determined using Pierce BCA protein assay kit protocol (ThermoFisher, Loughborough).

Pierce bicinchoninic acid (BCA) assay

The resulting cells from insulin secretion assays were lysed using an appropriate volume of cell lysis buffer. Cells were scraped, collected and centrifuged at 9000 RPM for 2 minutes at 4°C before protein concentration was determined following Pierce BCA protein assay kit standard protocol (ThermoFisher). The assay principles are shown in Scheme 7.1. Briefly, a cupric ion is reduced to the cuprous ion via the biuret reaction, which chelates with BCA to generate a purple complex. Absorbance of the BCA/copper complex is measured at 562 nm. Absorbance intensity increases with protein content [341].

BCA sodium salt   BCA-copper reaction
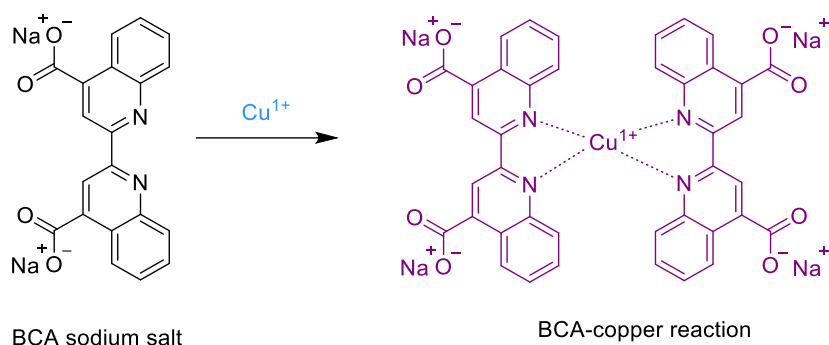
cAMP accumualtion

INS-1 cells were grown in standard or experimental media for 5 days before washing with KREBS (3 x 1 ml) and incubated in KREBS supplemented with 0.5 mM IBMX ± test compounds at stated concentrations for 30 minutes. The supernatant was removed, and cells were lysed following a 20-minute treatment with 0.1 M HCl (1ml/35cm^2 culture area) at room temperature. Cells were scraped, collected and centrifuged at 9000 RPM for 10 minutes at room temperature before cAMP accumulation was determined following Cayman Chemical cAMP select ELISA standard protocol (Cambridge Bioscience). A schematic of the cAMP ELISA procedure is shown in Figure 7.2.
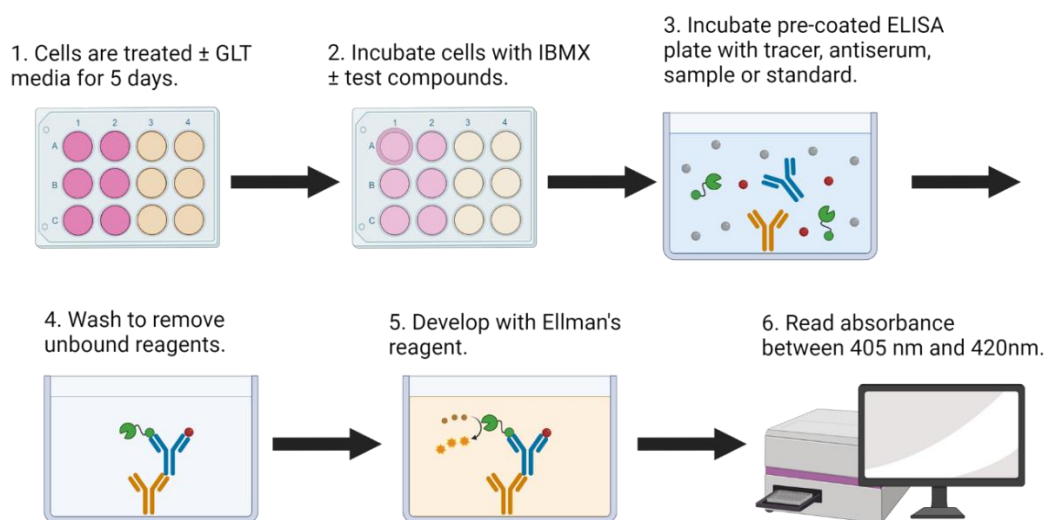
Figure 7.2 *Illustrative representation of cAMP select ELISA procedure. Image adapted from Enzo Life Sciences* [342] *and created using Biorender.com.*

8. References

1. Maji, H.S. and M. Ray, *Chapter 8 - Digestion and Inflammatory Responses*, in *Nutrition and Functional Foods in Boosting Digestion, Metabolism and Immune Health*, D. Bagchi and S.E. Ohia, Editors. 2022, Academic Press. p. 115-122.
2. Schertzer, J.D. and T.K.T. Lam, *Peripheral and Central Regulation of Insulin by the Intestine and Microbiome.* Am. J. Physiol. Endocrinol. Metab., 2021. **320**(2): p. E234-E239.
3. Zhao, X., X. An, C. Yang, W. Sun, H. Ji, and F. Lian, *The Crucial Role and Mechanism of Insulin Resistance in Metabolic Disease.* Front. Endocrinol., 2023. **14**: p. 1-24.
4. Freeman, A.M., L.A. Acevedo, and N. Pennings, *Insulin Resistance*, in *Statpearls*. 2024, StatPearls Publishing LLC.: Treasure Island (FL).
5. *International Diabetes Federation Diabetes Atlas*. 2021; Available from: https://www.diabetesatlas.org.
6. *World Health Organisation - Diabetes*. 2023; Available from: https://www.who.int/health-topics/diabetes#tab=tab_1.
7. *World Health Organisation - the Top 10 Causes of Death*. 2020; Available from: https://www.who.int/news-room/fact-sheets/detail/the-top-10-causes-of-death#:~:text=Diabetes%20has%20entered%20the%20top,an%2080%25%20increase%20since%202000.
8. Aynalem, S.B. and A.J. Zeleke, *Prevalence of Diabetes Mellitus and Its Risk Factors among Individuals Aged 15 Years and above in Mizan-Aman Town, Southwest Ethiopia, 2016: A Cross Sectional Study.* Int J Endocrinol, 2018. **2018**: p. 9317987.
9. Michael, E.S., L. Covic, and A. Kuliopulos, *Trace Amine-Associated Receptor 1 (TAAR1) Promotes Anti-Diabetic Signaling in Insulin-Secreting Cells.* J. Biol. Chem., 2019. **294**(12): p. 4401-4411.
10. Association, A.D., *Diagnosis and Classification of Diabetes Mellitus.* Diabetes Care, 2010. **33 Suppl 1**(Suppl 1): p. S62-S69.
11. *Diabetes Prevalence -Diabetes.Co.Uk*. 2019; Available from: https://www.diabetes.co.uk/diabetes-prevalence.html#:~:text=It%20is%20estimated%20that%20415,with%20diabetes%20worldwide%20by%202040.
12. Lee, Y.N. and M.S. Huda, *Uncommon Forms of Diabetes.* Clin. Med. (Lond), 2021. **21**(4): p. e337-e341.
13. Beltrand, J., K. Busiah, L. Vaivre-Douret, A.L. Fauret, M. Berdugo, H. Cavé, and M. Polak, *Neonatal Diabetes Mellitus.* Front. Pediatr., 2020. **8**: p. 540718-540727.
14. Khare, S., M. Desimone, N. Kasim, and C.L. Chan, *Cystic Fibrosis-Related Diabetes: Prevalence, Screening, and Diagnosis.* J. Clin. Transl. Endocrinol., 2022. **27**: p. 100290-100294.
15. *American Diabetes Association Diagnosis and Classification of Diabetes Mellitus.* Diabetes Care, 2010. **33**(Supplement_1): p. S62-S69.
16. Florkowski, C., *Hba1c as a Diagnostic Test for Diabetes Mellitus - Reviewing the Evidence.* Clin. Biochem. Rev., 2013. **34**(2): p. 75-83.
17. Eyth, E. and R. Naik, *Hemoglobin A1c*, in *Statpearls*. 2024, StatPearls Publishing LLC.: Treasure Island (FL).
18. Sherwani, S.I., H.A. Khan, A. Ekhzaimy, A. Masood, and M.K. Sakharkar, *Significance of Hba1c Test in Diagnosis and Prognosis of Diabetic Patients.* Biomark. Insights, 2016. **11**: p. 95-104.
19. Jerram, S.T. and R.D. Leslie *The Genetic Architecture of Type 1 Diabetes*. Genes, 2017. **8**, 1-22 DOI: 10.3390/genes8080209.

20. Streisand, R. and M. Monaghan, *Young Children with Type 1 Diabetes: Challenges, Research, and Future Directions.* Curr Diab Rep, 2014. **14**(9): p. 520.

21. Parkkola, A., T. Härkönen, S.J. Ryhänen, J. Ilonen, and M. Knip, *Extended Family History of Type 1 Diabetes and Phenotype and Genotype of Newly Diagnosed Children.* Diabetes Care, 2013. **36**(2): p. 348-354.

22. Antonelli, A., S.M. Ferrari, A. Di Domenicantonio, E. Ferrannini, and P. Fallahi, *Chapter 53 - Viral Infections and Type 1 Diabetes*, in *Infection and Autoimmunity (Second Edition)*, Y. Shoenfeld, N. Agmon-Levin, and N.R. Rose, Editors. 2015, Academic Press: Amsterdam. p. 877-889.

23. Simmons, K.M. and A.W. Michels, *Type 1 Diabetes: A Predictable Disease.* World J Diabetes, 2015. **6**(3): p. 380-390.

24. Kahanovitz, L., P.M. Sluss, and S.J. Russell, *Type 1 Diabetes - a Clinical Perspective.* Point Care, 2017. **16**(1): p. 37-40.

25. Thrower, S.L. and P.J. Bingley, *What Is Type 1 Diabetes?* Medicine, 2010. **38**(11): p. 592-596.

26. Pathak, V., N.M. Pathak, C.L. O'neill, J. Guduric-Fuchs, and R.J. Medina, *Therapies for Type 1 Diabetes: Current Scenario and Future Perspectives.* Clin. Med. Insights. Endocrinol., 2019. **12**: p. 1179551419844521-1179551419844521.

27. Olokoba, A.B., O.A. Obateru, and L.B. Olokoba, *Type 2 Diabetes Mellitus: A Review of Current Trends.* Oman. Med. J., 2012. **27**(4): p. 269-273.

28. Cichero, E. and M. Tonelli, *Targeting Species-Specific Trace Amine-Associated Receptor 1 Ligands: To Date Perspective of the Rational Drug Design Process.* Future Med. Chem., 2017. **9**(13): p. 1507-1527.

29. Bellou, V., L. Belbasis, I. Tzoulaki, and E. Evangelou, *Risk Factors for Type 2 Diabetes Mellitus: An Exposure-Wide Umbrella Review of Meta-Analyses.* PLoS One, 2018. **13**(3): p. e0194127-e0194127.

30. Aravinda, J., *Risk Factors in Patients with Type 2 Diabetes in Bengaluru: A Retrospective Study.* World J. Diabetes, 2019. **10**(4): p. 241-248.

31. Ley, S.H. and J.B. Meigs, *Epidemiology and Risk Factors of Type 2 Diabetes*, in *Diabetes Epidemiology, Genetics, Pathogenesis, Diagnosis, Prevention, and Treatment*, E. Bonora and R.A. Defronzo, Editors. 2018, Springer International Publishing: Cham. p. 55-80.

32. Buse, J.B., K.S. Polonsky, and C.F. Burant, *Chapter 31 - Type 2 Diabetes Mellitus*, in *Williams Textbook of Endocrinology (Twelfth Edition)*, S. Melmed, et al., Editors. 2011, W.B. Saunders: Philadelphia. p. 1371-1435.

33. Galicia-Garcia, U., A. Benito-Vicente, S. Jebari, A. Larrea-Sebal, H. Siddiqi, K.B. Uribe, H. Ostolaza, and C. Martín, *Pathophysiology of Type 2 Diabetes Mellitus.* Int. J. Mol. Sci., 2020. **21**(17): p. 1-34.

34. Wu, Y., Y. Ding, Y. Tanaka, and W. Zhang, *Risk Factors Contributing to Type 2 Diabetes and Recent Advances in the Treatment and Prevention.* Int. J. Med. Sci., 2014. **11**(11): p. 1185-1200.

35. Pratley, R.E., *The Early Treatment of Type 2 Diabetes.* Am. J. Med., 2013. **126**(9): p. S2-S9.

36. Mumtaz, M., *Gestational Diabetes Mellitus.* Malays J. Med. Sci., 2000. **7**(1): p. 4-9.

37. Piper, L.K., Z. Stewart, and H.R. Murphy, *Gestational Diabetes.* J. Reprod. Med. Gynaecol. Obstet., 2017. **27**(6): p. 171-176.

38. Kawamoto, K., C.S. Duvernoy, and M.B. Davis, *Chapter 12 - Sex Differences in Coronary Artery Disease*, in *Sex Differences in Cardiovascular Physiology and Pathophysiology*, B. Lamarca and B.T. Alexander, Editors. 2019, Academic Press. p. 185-201.

39. Plows, J.F., J.L. Stanley, P.N. Baker, C.M. Reynolds, and M.H. Vickers, *The Pathophysiology of Gestational Diabetes Mellitus.* Int. J. Mol. Sci., 2018. **19**(11): p. 1-21.

40.   Amed, S. and R. Oram, *Maturity-Onset Diabetes of the Young (Mody): Making the Right Diagnosis to Optimize Treatment.* Can. J. Diabetes, 2016. **40**(5): p. 449-454.

41.   Kreider, K.E., *The Diagnosis and Management of Atypical Types of Diabetes.* JNP, 2019. **15**(2): p. 171-176.

42.   Henley, K.D. and M. Gannon, *Normal Pancreatic Development*, in *Pathobiology of Human Disease*, L.M. Mcmanus and R.N. Mitchell, Editors. 2014, Academic Press: San Diego. p. 2216-2228.

43.   Liggitt, D. and S.M. Dintzis, *Chapter 14 - Pancreas*, in *Comparative Anatomy and Histology (Second Edition)*, P.M. Treuting, S.M. Dintzis, and K.S. Montine, Editors. 2018, Academic Press: San Diego. p. 241-250.

44.   Liehmann, L.M., *Chapter 33 - Pancreas*, in *Feline Soft Tissue and General Surgery*, S.J. Langley-Hobbs, J.L. Demetriou, and J.F. Ladlow, Editors. 2014, W.B. Saunders. p. 375-386.

45.   Gamble, A., A. Bruni, and A.M. James Shapiro, *Transplantation: Pancreatic and Islet Cells*, in *Encyclopedia of Endocrine Diseases (Second Edition)*, I. Huhtaniemi and L. Martini, Editors. 2019, Academic Press: Oxford. p. 259-269.

46.   Kim, J.W., J.Z.Q. Luo, and L. Luo, *Chapter 10 - Bone Marrow Mesenchymal Stem Cells as a New Therapeutic Approach for Diabetes Mellitus*, in *A Roadmap to Non-Hematopoietic Stem Cell-Based Therapeutics*, X.-D. Chen, Editor. 2019, Academic Press. p. 251-273.

47.   Bosco, D., M. Armanet, P. Morel, N. Niclauss, A. Sgroi, Y.D. Muller, L. Giovannoni, G. Parnaud, and T. Berney, *Unique Arrangement of Alpha- and Beta-Cells in Human Islets of Langerhans.* Diabetes, 2010. **59**(5): p. 1202-1210.

48.   Karpińska, M. and M. Czauderna, *Pancreas - Its Functions, Disorders, and Physiological Impact on the Mammals' Organism.* Front. Physiol., 2022. **13**: p. 807632-807643.

49.   Karamanou, M., A. Protogerou, G. Tsoucalas, G. Androutsos, and E. Poulakou-Rebelakou, *Milestones in the History of Diabetes Mellitus: The Main Contributors.* World J. Diabetes, 2016. **7**(1): p. 1-7.

50.   Quianzon, C.C. and I. Cheikh, *History of Insulin.* J Community Hosp. Intern. Med. Perspect, 2012. **2**(2): p. 1-3.

51.   Alarcon, C., B. Wicksteed, and C.J. Rhodes, *Insulin Processing*, in *Encyclopedia of Hormones*, H.L. Henry and A.W. Norman, Editors. 2003, Academic Press: New York. p. 359-368.

52.   Nishi, M. and K. Nanjo, *Insulin Gene Mutations and Diabetes.* J. Diabetes Investig., 2011. **2**(2): p. 92-100.

53.   Vakilian, M., Y. Tahamtani, and K. Ghaedi, *A Review on Insulin Trafficking and Exocytosis.* Gene, 2019. **706**: p. 52-61.

54.   Clark, J.L., A.H. Rubenstein, P.E. Oyer, J.J. Mackenzie, S. Cho, and D.F. Steiner, *Proinsulin and Insulin Biosynthesis**This Research Was Supported by Grant AM 04931 of the United States Public Health Service and in Part by a Grant-in-Aid from the Novo Company*, in *The Structure and Metabolism of the Pancreatic Islets*, S. Falkmer, B. Hellman, and I.B. Täljedal, Editors. 1970, Pergamon. p. 339-348.

55.   Steiner, D.F., C.J. Rhodes, L.H. Philipson, G.I. Bell, and S.J. Chan, *Chapter 31 - Biosynthesis, Processing, and Secretion of the Islet Hormones: Insulin, Islet Amyloid Polypeptide (Amylin), Glucagon, Somatostatin, and Pancreatic Polypeptide*, in *Endocrinology: Adult and Pediatric (Seventh Edition)*, J.L. Jameson, et al., Editors. 2016, W.B. Saunders: Philadelphia. p. 527-545.e526.

56.   Kemmler, W., J.D. Peterson, and D.F. Steiner, *Studies on the Conversion of Proinsulin to Insulin: I. Conversion in Vitro with Trypsin and Carboxypeptidase B.* Journal of Biological Chemistry, 1971. **246**(22): p. 6786-6791.

57.   Qaid, M.M. and M.M. Abdelrahman, *Role of Insulin and Other Related Hormones in Energy Metabolism - a Review.* Cogent food agric., 2016. **2**: p. 1267691-1267709.

58. Adams, M.J., T.L. Blundell, E.J. Dodson, G.G. Dodson, M. Vijayan, E.N. Baker, M.M. Harding, D.C. Hodgkin, B. Rimmer, and S. Sheat, *Structure of Rhombohedral 2 Zinc Insulin Crystals.* Nature, 1969. **224**(5218): p. 491-495.

59. Lawrence, M.C., *Understanding Insulin and Its Receptor from Their Three-Dimensional Structures.* Mol. Metab., 2021. **52**: p. 101255-101272.

60. Forbes, B.E., *Chapter 5 - the Three-Dimensional Structure of Insulin and Its Receptor*, in *Vitamins and Hormones*, G. Litwack, Editor. 2023, Academic Press. p. 151-185.

61. Pickup, J., *Human Insulin.* BMJ, 1989. **299**(6706): p. 991-993.

62. Ishihara, H., *Metabolism-Secretion Coupling in Glucose-Stimulated Insulin Secretion.* Diabetol. Int., 2022. **13**(3): p. 463-470.

63. Deepa Maheshvare, M., S. Raha, M. König, and D. Pal, *A Pathway Model of Glucose-Stimulated Insulin Secretion in the Pancreatic B-Cell.* Front Endocrinol. (Lausanne), 2023. **14**: p. 1185656-1185678.

64. Zhang, G.F., M.V. Jensen, S.M. Gray, K. El, Y. Wang, D. Lu, T.C. Becker, J.E. Campbell, and C.B. Newgard, *Reductive TCA Cycle Metabolism Fuels Glutamine- and Glucose-Stimulated Insulin Secretion.* Cell Metab., 2021. **33**(4): p. 804-817.e805.

65. Ojha, A., U. Ojha, R. Mohammed, A. Chandrashekar, and H. Ojha, *Current Perspective on the Role of Insulin and Glucagon in the Pathogenesis and Treatment of Type 2 Diabetes Mellitus.* Clin. Pharmacol., 2019. **11**: p. 57-65.

66. Komatsu, M., M. Takei, H. Ishii, and Y. Sato, *Glucose-Stimulated Insulin Secretion: A Newer Perspective.* J. Diabetes Investig., 2013. **4**(6): p. 511-516.

67. Nolan, C.J., M.S.R. Madiraju, V. Delghingaro-Augusto, M.-L. Peyot, and M. Prentki, *Fatty Acid Signaling in the B-Cell and Insulin Secretion.* Diabetes, 2006. **55**(Supplement_2): p. S16-S23.

68. Kim, J.-H., V. Delghingaro-Augusto, J.Y. Chan, D.R. Laybutt, J. Proietto, and C.J. Nolan, *The Role of Fatty Acid Signaling in Islet Beta-Cell Adaptation to Normal Pregnancy.* Front. Endocrinol., 2022. **12**: p. 1-15.

69. Newsholme, P. and M. Krause, *Nutritional Regulation of Insulin Secretion: Implications for Diabetes.* Clin. Biochem. Rev., 2012. **33**(2): p. 35-47.

70. Torres, N., L. Noriega, and A.R. Tovar, *Chapter 9 - Nutrient Modulation of Insulin Secretion*, in *Vitamins & Hormones*. 2009, Academic Press. p. 217-244.

71. Gao, Z., R.A. Young, M.M. Trucco, S.R. Greene, E.L. Hewlett, F.M. Matschinsky, and B.A. Wolf, *Protein Kinase a Translocation and Insulin Secretion in Pancreatic Beta-Cells: Studies with Adenylate Cyclase Toxin from Bordetella Pertussis.* Biochem. J., 2002. **368**(Pt 2): p. 397-404.

72. Tengholm, A., *Cyclic AMP Dynamics in the Pancreatic B-Cell.* Ups. J. Med. Sci., 2012. **117**(4): p. 355-369.

73. Althaher, A.R., *An Overview of Hormone-Sensitive Lipase (Hsl).* ScientificWorldJournal, 2022. **2022**: p. 1964684.

74. Wilcox, G., *Insulin and Insulin Resistance.* Clin. Biochem. Rev., 2005. **26**(2): p. 19-39.

75. Weber, F.L., Jr., G.L. Veach, and D.W. Friedman, *Effects of Insulin and Glucagon on the Uptake of Amino Acids from Arterial Blood by Canine Ileum.* Dig. Dis. Sci., 1981. **26**(2): p. 113-118.

76. Yee, L.D., J.E. Mortimer, R. Natarajan, E.C. Dietze, and V.L. Seewaldt, *Metabolic Health, Insulin, and Breast Cancer: Why Oncologists Should Care About Insulin.* Front. Endocrinol., 2020. **11**(58): p. 1-25.

77. Yunn, N.-O., J. Kim, S.H. Ryu, and Y. Cho, *A Stepwise Activation Model for the Insulin Receptor.* Exp. Mol. Med., 2023. **55**(10): p. 2147-2161.

78. Kahn, C.R., *The Molecular Mechanism of Insulin Action.* Annu. Rev. Med., 1985. **36**: p. 429-451.

79.   Petersen, M.C. and G.I. Shulman, *Mechanisms of Insulin Action and Insulin Resistance.* Physiol. Rev., 2018. **98**(4): p. 2133-2223.

80.   De Meyts, P., *The Insulin Receptor and Its Signal Transduction Network.* Endotext [Internet], 2016.

81.   Rahman, M.S., K.S. Hossain, S. Das, S. Kundu, E.O. Adegoke, M.A. Rahman, M.A. Hannan, M.J. Uddin, and M.G. Pang, *Role of Insulin in Health and Disease: An Update.* Int. J. Mol. Sci., 2021. **22**(12): p. 1-19.

82.   Arneth, B., R. Arneth, and M. Shams, *Metabolomics of Type 1 and Type 2 Diabetes.* Int. J. Mol. Sci., 2019. **20**(10): p. 2467-2481.

83.   Gabbouj, S., S. Ryhänen, M. Marttinen, R. Wittrahm, M. Takalo, S. Kemppainen, H. Martiskainen, H. Tanila, A. Haapasalo, M. Hiltunen, and T. Natunen, *Altered Insulin Signaling in Alzheimer's Disease Brain - Special Emphasis on Pi3k-Akt Pathway.* Front. Neurosci., 2019. **13**: p. 629-637.

84.   Wang, Y.W., S.J. He, X. Feng, J. Cheng, Y.T. Luo, L. Tian, and Q. Huang, *Metformin: A Review of Its Potential Indications.* Drug. Des. Devel. Ther., 2017. **11**: p. 2421-2429.

85.   Gustafson, D.R. and S.I. Mcfarlane, *Chapter 2 - Epidemiology of Type 2 Diabetes and Dementia*, in *Type 2 Diabetes and Dementia*, V. Srikanth and Z. Arvanitakis, Editors. 2018, Academic Press. p. 5-27.

86.   Foretz, M., B. Guigas, and B. Viollet, *Metformin: Update on Mechanisms of Action and Repurposing Potential.* Nat. Rev. Endocrinol., 2023. **19**(8): p. 460-476.

87.   Blackman, S.M. and D.W. Cooke, *Diabetes*, in *Encyclopedia of Biological Chemistry (Second Edition)*, W.J. Lennarz and M.D. Lane, Editors. 2013, Academic Press: Waltham. p. 649-658.

88.   Rao, C.V., *Biguanides*, in *Encyclopedia of Toxicology (Third Edition)*, P. Wexler, Editor. 2014, Academic Press: Oxford. p. 452-455.

89.   Nasri, H. and M. Rafieian-Kopaei, *Metformin: Current Knowledge.* J. Res. Med. Sci., 2014. **19**(7): p. 658-664.

90.   Gong, L., S. Goswami, K.M. Giacomini, R.B. Altman, and T.E. Klein, *Metformin Pathways: Pharmacokinetics and Pharmacodynamics.* Pharmacogenet Genomics, 2012. **22**(11): p. 820-827.

91.   Hossain, M.A. and R. Pervin, *Chapter 34 - Current Antidiabetic Drugs: Review of Their Efficacy and Safety*, in *Nutritional and Therapeutic Interventions for Diabetes and Metabolic Syndrome (Second Edition)*, D. Bagchi and S. Nair, Editors. 2018, Academic Press. p. 455-473.

92.   Aggarwal, A., A. Jain, S. Sachdeva, and Z.I. Kulairi, *Prolonged Glucosuria with Sodium-Glucose Cotransporter-2 (SGLT2) Inhibitors: A Case Report and Review of Literature.* Cureus, 2020. **12**(11): p. e11554.

93.   List, J.F. and J.M. Whaley, *Glucose Dynamics and Mechanistic Implications of SGLT2 Inhibitors in Animals and Humans.* Kidney Int Suppl, 2011(120): p. S20-27.

94.   Dardi, I., T. Kouvatsos, and S.A. Jabbour, *SGLT2 Inhibitors.* Biochem. Pharmacol., 2016. **101**: p. 27-39.

95.   Galasko, G., *Insulin, Oral Hypoglycemics, and Glucagon.* Pharmacology and Therapeutics for Dentistry, 7th ed.; Mosby: Omaha, NE, USA, 2017: p. 437-445.

96.   Kasina, S. and K.M. Baradhi, *Dipeptidyl Peptidase IV (DPP IV) Inhibitors*, in *Statpearls*. 2024, StatPearls Publishing LLC: Treasure Island (FL).

97.   *Glp-1 Agonists - Diabetes.Co.Uk.* 2024; Available from: https://www.diabetes.org.uk/guide-to-diabetes/managing-your-diabetes/treating-your-diabetes/tablets-and-medication/glp-1.

98.   Khoo, C.M., *Diabetes Mellitus Treatment*, in *International Encyclopedia of Public Health (Second Edition)*, S.R. Quah, Editor. 2017, Academic Press: Oxford. p. 288-293.

99.   Li, X. and Z.Q. Liu, *Chapter 7 - Pharmacogenetic Factors That Affect Drug Metabolism and Efficacy in Type 2 Diabetes Mellitus*, in *Drug Metabolism in Diseases*, W. Xie, Editor. 2017, Academic Press: Boston. p. 157-179.

100.   Sola, D., L. Rossi, G.P. Schianca, P. Maffioli, M. Bigliocca, R. Mella, F. Corlianò, G.P. Fra, E. Bartoli, and G. Derosa, *Sulfonylureas and Their Use in Clinical Practice.* Arch. Med. Sci., 2015. **11**(4): p. 840-848.

101.   Bardal, S.K., J.E. Waechter, and D.S. Martin, *Chapter 14 - Endocrinology*, in *Applied Pharmacology*, S.K. Bardal, J.E. Waechter, and D.S. Martin, Editors. 2011, W.B. Saunders: Philadelphia. p. 143-176.

102.   *Meglitinides*, in *Meyler's Side Effects of Drugs (Sixteenth Edition)*, J.K. Aronson, Editor. 2016, Elsevier: Oxford. p. 800-807.

103.   Ritz, E., M. Adamczak, and A. Wiecek, *Chapter 2 - Carbohydrate Metabolism in Kidney Disease and Kidney Failure*, in *Nutritional Management of Renal Disease (Third Edition)*, J.D. Kopple, S.G. Massry, and K. Kalantar-Zadeh, Editors. 2013, Academic Press. p. 17-30.

104.   Rosenbaum, D.M., S.G.F. Rasmussen, and B.K. Kobilka, *The Structure and Function of G-Protein-Coupled Receptors.* Nature, 2009. **459**(7245): p. 356-363.

105.   Randall, M.D., D. Kendall, and S.P. Alexander, *Fasttrack Pharmacology*. 2012: Pharmaceutical Press.

106.   Gurevich, V.V. and E.V. Gurevich, *GPCR Signaling Regulation: The Role of GRKs and Arrestins.* Front. Pharmacol., 2019. **10**: p. 1-11.

107.   Jean-Charles, P.Y., S. Kaur, and S.K. Shenoy, *G Protein-Coupled Receptor Signaling through B-Arrestin-Dependent Mechanisms.* J. Cardiovasc. Pharmacol., 2017. **70**(3): p. 142-158.

108.   Zhai, R., J. Snyder, S. Montgomery, and P.Y. Sato, *Double Life: How GRK2 and B-Arrestin Signaling Participate in Diseases.* Cell Signal, 2022. **94**: p. 110333-110362.

109.   Mccallum, L., S. Lip, and S. Padmanabhan, *Chapter 18 - Pharmacodynamic Pharmacogenomics*, in *Handbook of Pharmacogenomics and Stratified Medicine*, S. Padmanabhan, Editor. 2014, Academic Press: San Diego. p. 365-383.

110.   Sriram, K. and P.A. Insel, *G Protein-Coupled Receptors as Targets for Approved Drugs: How Many Targets and How Many Drugs?* Mol. Pharmacol., 2018. **93**(4): p. 251-258.

111.   Brogi, S., A. Tafi, L. Désaubry, and C.G. Nebigil, *Discovery of GPCR Ligands for Probing Signal Transduction Pathways.* Front. Pharmacol., 2014. **5**: p. 255-269.

112.   Negus, S.S., *Some Implications of Receptor Theory for in Vivo Assessment of Agonists, Antagonists and Inverse Agonists.* Biochem. Pharmacol., 2006. **71**(12): p. 1663-1670.

113.   Berg, K.A. and W.P. Clarke, *Making Sense of Pharmacology: Inverse Agonism and Functional Selectivity.* Int. J. Neuropsychopharmacol., 2018. **21**(10): p. 962-977.

114.   Schwache, D. and G. Müller-Newen, *Receptor Fusion Proteins for the Inhibition of Cytokines.* Eur. J. Cell Biol., 2012. **91**(6): p. 428-434.

115.   Kenakin, T., *Theoretical Aspects of GPCR–Ligand Complex Pharmacology.* Chemical Reviews, 2017. **117**(1): p. 4-20.

116.   Weiss, J.M., P.H. Morgan, M.W. Lutz, and T.P. Kenakin, *The Cubic Ternary Complex Receptor–Occupancy Model I. Model Description.* J. Theor. Biol., 1996. **178**(2): p. 151-167.

117.   Christian, S.L. and M.D. Berry, *Trace Amine-Associated Receptors as Novel Therapeutic Targets for Immunomodulatory Disorders.* Front. Pharmacol., 2018. **9**: p. 680-694.

118.   Berry, M.D., R.R. Gainetdinov, M.C. Hoener, and M. Shahid, *Pharmacology of Human Trace Amine-Associated Receptors: Therapeutic Opportunities and Challenges.* Pharmacol. Ther., 2017. **180**: p. 161-180.

119.   Xu, Z. and Q. Li, *TAAR Agonists.* Cell. Mol. Neurobiol., 2020. **40**(2): p. 257-272.

120. Halff, E.F., G. Rutigliano, A. Garcia-Hidalgo, and O.D. Howes, *Trace Amine-Associated Receptor 1 (TAAR1) Agonism as a New Treatment Strategy for Schizophrenia and Related Disorders.* Trends. Neurosci., 2023. **46**(1): p. 60-74.

121. Wainscott, D.B., S.P. Little, T. Yin, Y. Tu, V.P. Rocco, J.X. He, and D.L. Nelson, *Pharmacologic Characterization of the Cloned Human Trace Amine-Associated Receptor1 (TAAR1) and Evidence for Species Differences with the Rat TAAR1.* J. Pharmacol. Exp. Ther., 2007. **320**(1): p. 475-485.

122. Sherwani, S.I. and H.A. Khan, *Chapter 18 - Trace Amines in Neuropsychiatric Disorders*, in *Trace Amines and Neurological Disorders*, T. Farooqui and A.A. Farooqui, Editors. 2016, Academic Press: San Diego. p. 269-284.

123. Cichero, E., S. Espinoza, S. Franchini, S. Guariento, L. Brasili, R.R. Gainetdinov, and P. Fossa, *Further Insights into the Pharmacology of the Human Trace Amine-Associated Receptors: Discovery of Novel Ligands for TAAR1 by a Virtual Screening Approach.* Chem. Biol. Drug. Des., 2014. **84**(6): p. 712-720.

124. Lam, V.M., D. Rodríguez, T. Zhang, E.J. Koh, J. Carlsson, and A. Salahpour, *Discovery of Trace Amine-Associated Receptor 1 Ligands by Molecular Docking Screening against a Homology Model.* Med. Chem. Comm, 2015. **6**(12): p. 2216-2223.

125. Zilberg, G., A.K. Parpounas, A.L. Warren, S. Yang, and D. Wacker, *Molecular Basis of Human Trace Amine-Associated Receptor 1 Activation.* Nat. Commun., 2023. **15**(1): p. 1-14.

126. *Uniprot Align*. 2024; Available from: https://www.uniprot.org/align/clustalo-R20240731-125827-0415-37753819-p1m/overview.

127. Lindemann, L., C.A. Meyer, K. Jeanneau, A. Bradaia, L. Ozmen, H. Bluethmann, B. Bettler, J.G. Wettstein, E. Borroni, J.L. Moreau, and M.C. Hoener, *Trace Amine-Associated Receptor 1 Modulates Dopaminergic Activity.* J. Pharmacol. Exp. Ther., 2008. **324**(3): p. 948-956.

128. Eyun, S.I., H. Moriyama, F.G. Hoffmann, and E.N. Moriyama, *Molecular Evolution and Functional Divergence of Trace Amine-Associated Receptors.* PLoS One, 2016. **11**(3): p. e0151023.

129. Gainetdinov, R.R., M.C. Hoener, and M.D. Berry, *Trace Amines and Their Receptors.* Pharmacol. Rev., 2018. **70**(3): p. 549-620.

130. Cisneros, I.E. and A. Ghorpade, *Methamphetamine and Hiv-1-Induced Neurotoxicity: Role of Trace Amine Associated Receptor 1 cAMP Signaling in Astrocytes.* Neuropharmacology, 2014. **85**: p. 499-507.

131. Borowsky, B., N. Adham, K.A. Jones, R. Raddatz, R. Artymyshyn, K.L. Ogozalek, M.M. Durkin, P.P. Lakhlani, J.A. Bonini, S. Pathirana, N. Boyle, X. Pu, E. Kouranova, H. Lichtblau, F.Y. Ochoa, T.A. Branchek, and C. Gerald, *Trace Amines: Identification of a Family of Mammalian G Protein-Coupled Receptors.* Proc. Natl. Acas. Sci. USA, 2001. **98**(16): p. 8966-8971.

132. Guariento, S., M. Tonelli, S. Espinoza, A.S. Gerasimov, R.R. Gainetdinov, and E. Cichero, *Rational Design, Chemical Synthesis and Biological Evaluation of Novel Biguanides Exploring Species-Specificity Responsiveness of TAAR1 Agonists.* Eur. J. Med. Chem., 2018. **146**: p. 171-184.

133. Tonelli, M., S. Espinoza, R.R. Gainetdinov, and E. Cichero, *Novel Biguanide-Based Derivatives Scouted as TAAR1 Agonists: Synthesis, Biological Evaluation, ADME Prediction and Molecular Docking Studies.* Eur. J. Med. Chem., 2017. **127**: p. 781-792.

134. Babusyte, A., M. Kotthoff, J. Fiedler, and D. Krautwurst, *Biogenic Amines Activate Blood Leukocytes Via Trace Amine-Associated Receptors TAAR1 and TAAR2.* J. Leukoc. Biol., 2013. **93**(3): p. 387-394.

135. Duan, J., M. Martinez, A.R. Sanders, C. Hou, N. Saitou, T. Kitano, B.J. Mowry, R.R. Crowe, J.M. Silverman, D.F. Levinson, and P.V. Gejman, *Polymorphisms in the Trace Amine*

Receptor 4 (Taar4) Gene on Chromosome 6q23.2 Are Associated with Susceptibility to Schizophrenia. Am. J. Hum. Genet., 2004. **75**(4): p. 624-638.

136.   D'andrea, G., S. Terrazzino, D. Fortin, A. Farruggio, L. Rinaldi, and A. Leon, *HPLC Electrochemical Detection of Trace Amines in Human Plasma and Platelets and Expression of mRNA Transcripts of Trace Amine Receptors in Circulating Leukocytes.* Neurosci. Lett., 2003. **346**(1-2): p. 89-92.

137.   Regard, J.B., I.T. Sato, and S.R. Coughlin, *Anatomical Profiling of G Protein-Coupled Receptor Expression.* Cell, 2008. **135**(3): p. 561-571.

138.   Vanti, W.B., P. Muglia, T. Nguyen, R. Cheng, J.L. Kennedy, S.R. George, and B.F. O'dowd, *Discovery of a Null Mutation in a Human Trace Amine Receptor Gene.* Genomics, 2003. **82**(5): p. 531-536.

139.   Hussain, A., L.R. Saraiva, D.M. Ferrero, G. Ahuja, V.S. Krishna, S.D. Liberles, and S.I. Korsching, *High-Affinity Olfactory Receptor for the Death-Associated Odor Cadaverine.* Proc. Natl. Acad. Sci. USA, 2013. **110**(48): p. 19579-19584.

140.   Meyer, N. and J.H. Maccabe, *Schizophrenia.* Medicine, 2016. **44**(11): p. 649-653.

141.   Revel, F.G., J.L. Moreau, B. Pouzet, R. Mory, A. Bradaia, D. Buchy, V. Metzler, S. Chaboz, K. Groebke Zbinden, G. Galley, R.D. Norcross, D. Tuerck, A. Bruns, S.R. Morairty, T.S. Kilduff, T.L. Wallace, C. Risterucci, J.G. Wettstein, and M.C. Hoener, *A New Perspective for Schizophrenia: TAAR1 Agonists Reveal Antipsychotic- and Antidepressant-Like Activity, Improve Cognition and Control Body Weight.* Mol. Psychiatry, 2013. **18**(5): p. 543-556.

142.   Veljkovic, E., W. Xia, B. Phillips, E.T. Wong, J. Ho, A. Oviedo, J. Hoeng, and M. Peitsch, *Chapter 1 - Parkinson's Disease*, in *Nicotine and Other Tobacco Compounds in Neurodegenerative and Psychiatric Diseases*, E. Veljkovic, et al., Editors. 2018, Academic Press. p. 3-12.

143.   Bartel, W.P., V.S. Van Laar, and E.A. Burton, *Chapter 23 - Parkinson's Disease*, in *Behavioral and Neural Genetics of Zebrafish*, R.T. Gerlai, Editor. 2020, Academic Press. p. 377-412.

144.   Kenna, J. and R.S. Anderton, *Chapter 36 - the Role of the Gastrointestinal System and Gut Microbiota in Parkinson's Disease*, in *Genetics, Neurology, Behavior, and Diet in Parkinson's Disease*, C.R. Martin and V.R. Preedy, Editors. 2020, Academic Press. p. 569-582.

145.   Goldman, J.S. and S. Fahn, *Chapter 68 - Genetics of Parkinson Disease And related diseases*, in *Rosenberg's Molecular and Genetic Basis of Neurological and Psychiatric Disease (Fifth Edition)*, R.N. Rosenberg and J.M. Pascual, Editors. 2015, Academic Press: Boston. p. 769-778.

146.   Sotnikova, T.D., M.G. Caron, and R.R. Gainetdinov, *Trace Amine-Associated Receptors as Emerging Therapeutic Targets.* Mol. Pharmacol., 2009. **76**(2): p. 229-235.

147.   Jing, L. and J.X. Li, *Trace Amine-Associated Receptor 1: A Promising Target for the Treatment of Psychostimulant Addiction.* Eur. J. Pharmacol., 2015. **761**: p. 345-352.

148.   Rutigliano, G., A. Accorroni, and R. Zucchi, *The Case for TAAR1 as a Modulator of Central Nervous System Function.* Front. Pharmacol., 2017. **8**: p. 987-1005.

149.   Ferragud, A., A.D. Howell, C.F. Moore, T.L. Ta, M.C. Hoener, V. Sabino, and P. Cottone, *The Trace Amine-Associated Receptor 1 Agonist RO5256390 Blocks Compulsive, Binge-Like Eating in Rats.* Neuropsychopharmacology, 2017. **42**(7): p. 1458-1470.

150.   Mobbs, C.V., *Obesity*, in *Encyclopedia of the Neurological Sciences (Second Edition)*, M.J. Aminoff and R.B. Daroff, Editors. 2014, Academic Press: Oxford. p. 621-622.

151.   Klein, S. and J.A. Romijn, *Chapter 36 - Obesity*, in *Williams Textbook of Endocrinology (Thirteenth Edition)*, S. Melmed, et al., Editors. 2016, Elsevier: Philadelphia. p. 1633-1659.

152.   Rutigliano, G., L. Bandini, S. Sestito, and G. Chiellini, *3-Iodothyronamine and Derivatives: New Allies against Metabolic Syndrome?* Int. J. Mol. Sci., 2020. **21**(6): p. 1-19.

153.   Abbasnezhad, A. and R. Choghakhori, *Chapter 7 - Vitamin D and Quality of Life of Patients with Irritable Bowel Syndrome*, in *Dietary Interventions in Gastrointestinal Diseases*, R.R. Watson and V.R. Preedy, Editors. 2019, Academic Press. p. 81-88.

154.   Hennige, A.M., D.J. Burks, U. Ozcan, R.N. Kulkarni, J. Ye, S. Park, M. Schubert, T.L. Fisher, M.A. Dow, R. Leshan, M. Zakaria, M. Mossa-Basha, and M.F. White, *Upregulation of Insulin Receptor Substrate-2 in Pancreatic Beta Cells Prevents Diabetes.* J Clin Invest, 2003. **112**(10): p. 1521-1532.

155.   Zucchi, R., G. Chiellini, T.S. Scanlan, and D.K. Grandy, *Trace Amine-Associated Receptors and Their Ligands.* Br. J. Pharmacol., 2006. **149**(8): p. 967-978.

156.   Shi, X., T.L. Swanson, N.B. Miner, A.J. Eshleman, and A. Janowsky, *Activation of Trace Amine-Associated Receptor 1 Stimulates an Antiapoptotic Signal Cascade Via Extracellular Signal-Regulated Kinase 1/2.* Mol. pharmacol., 2019. **96**(4): p. 493-504.

157.   Lam, V.M., S. Espinoza, A.S. Gerasimov, R.R. Gainetdinov, and A. Salahpour, *In-Vivo Pharmacology of Trace-Amine Associated Receptor 1.* Eur. J. Pharmacol., 2015. **763**(Pt B): p. 136-142.

158.   Qatato, M., V. Venugopalan, A. Al-Hashimi, M. Rehders, A.D. Valentine, Z. Hein, U. Dallto, S. Springer, and K. Brix, *Trace Amine-Associated Receptor 1 Trafficking to Cilia of Thyroid Epithelial Cells.* Cells, 2021. **10**(6): p. 1-21.

159.   Miller, G.M., *The Emerging Role of Trace Amine-Associated Receptor 1 in the Functional Regulation of Monoamine Transporters and Dopaminergic Activity.* J Neurochem, 2011. **116**(2): p. 164-176.

160.   Saarinen, M., I. Mantas, I. Flais, R. Ågren, K. Sahlholm, M.J. Millan, and P. Svenningsson, *TAAR1 Dependent and Independent Actions of the Potential Antipsychotic and Dual TAAR1/5-Ht1a Receptor Agonist Sep-363856.* Neuropsychopharmacology, 2022. **47**(13): p. 2319-2329.

161.   Underhill, S.M., P.D. Hullihen, J. Chen, C. Fenollar-Ferrer, M.A. Rizzo, S.L. Ingram, and S.G. Amara, *Amphetamines Signal through Intracellular TAAR1 Receptors Coupled to Gα13 and Gαs in Discrete Subcellular Domains.* Molecular Psychiatry, 2021. **26**(4): p. 1208-1223.

162.   Barak, L.S., A. Salahpour, X. Zhang, B. Masri, T.D. Sotnikova, A.J. Ramsey, J.D. Violin, R.J. Lefkowitz, M.G. Caron, and R.R. Gainetdinov, *Pharmacological Characterization of Membrane-Expressed Human Trace Amine-Associated Receptor 1 (TAAR1) by a Bioluminescence Resonance Energy Transfer cAMP Biosensor.* Mol. Pharmacol., 2008. **74**(3): p. 585-594.

163.   Espinoza, S., A. Salahpour, B. Masri, T.D. Sotnikova, M. Messa, L.S. Barak, M.G. Caron, and R.R. Gainetdinov, *Functional Interaction between Trace Amine-Associated Receptor 1 and Dopamine D2 Receptor.* Mol. Pharmacol., 2011. **80**(3): p. 416-425.

164.   Francesconi, V., E. Cichero, E.V. Kanov, E. Laurini, S. Pricl, R.R. Gainetdinov, and M. Tonelli, *Novel 1-Amidino-4-Phenylpiperazines as Potent Agonists at Human TAAR1 Receptor: Rational Design, Synthesis, Biological Evaluation and Molecular Docking Studies.* Pharmaceuticals, 2020. **13**(11): p. 391-417.

165.   Bradaia, A., G. Trube, H. Stalder, R.D. Norcross, L. Ozmen, J.G. Wettstein, A. Pinard, D. Buchy, M. Gassmann, M.C. Hoener, and B. Bettler, *The Selective Antagonist EPPTB Reveals TAAR1-Mediated Regulatory Mechanisms in Dopaminergic Neurons of the Mesolimbic System.* PNAS, 2009. **106**(47): p. 20081-20087.

166.   Revel, F.G., J.L. Moreau, R.R. Gainetdinov, A. Bradaia, T.D. Sotnikova, R. Mory, S. Durkin, K.G. Zbinden, R. Norcross, C.A. Meyer, V. Metzler, S. Chaboz, L. Ozmen, G. Trube, B. Pouzet, B. Bettler, M.G. Caron, J.G. Wettstein, and M.C. Hoener, *TAAR1 Activation*

Modulates Monoaminergic Neurotransmission, Preventing Hyperdopaminergic and Hypoglutamatergic Activity. Proc. Natl. Acad. Sci. USA, 2011. **108**(20): p. 8485-8490.

167. Simmler, L.D., D. Buchy, S. Chaboz, M.C. Hoener, and M.E. Liechti, *In Vitro Characterization of Psychoactive Substances at Rat, Mouse, and Human Trace Amine-Associated Receptor 1.* J. Pharmacol. Exp. Ther., 2016. **357**(1): p. 134-144.

168. Farooqui, T. and A.A. Farooqui, *Chapter 25 - Perspective and Directions for Future Research on Trace Amines and Neurological Disorders*, in *Trace Amines and Neurological Disorders*, T. Farooqui and A.A. Farooqui, Editors. 2016, Academic Press: San Diego. p. 369-386.

169. Khan, M.Z. and W. Nawaz, *The Emerging Roles of Human Trace Amines and Human Trace Amine-Associated Receptors (hTAARs) in Central Nervous System.* Biomed. Pharmacother., 2016. **83**: p. 439-449.

170. Chiellini, G., G. Nesi, M. Digiacomo, R. Malvasi, S. Espinoza, M. Sabatini, S. Frascarelli, A. Laurino, E. Cichero, M. Macchia, R.R. Gainetdinov, P. Fossa, L. Raimondi, R. Zucchi, and S. Rapposelli, *Design, Synthesis, and Evaluation of Thyronamine Analogues as Novel Potent Mouse Trace Amine Associated Receptor 1 (mTAAR1) Agonists.* J. Med. Chem, 2015. **58**(12): p. 5096-5107.

171. Chiellini, G., G. Nesi, S. Sestito, S. Chiarugi, M. Runfola, S. Espinoza, M. Sabatini, L. Bellusci, A. Laurino, and E. Cichero, *Hit-to-Lead Optimization of Mouse Trace Amine Associated Receptor 1 (mTAAR1) Agonists with a Diphenylmethane-Scaffold: Design, Synthesis, and Biological Study.* J. Med. Chem., 2016. **59**(21): p. 9825-9836.

172. Galley, G., A. Beurier, G. Décoret, A. Goergler, R. Hutter, S. Mohr, A. Pähler, P. Schmid, D. Türck, R. Unger, K.G. Zbinden, M.C. Hoener, and R.D. Norcross, *Discovery and Characterization of 2-Aminooxazolines as Highly Potent, Selective, and Orally Active TAAR1 Agonists.* ACS Med. Chem. Lett., 2016. **7**(2): p. 192-197.

173. Galley, G., H. Stalder, A. Goergler, M.C. Hoener, and R.D. Norcross, *Optimisation of Imidazole Compounds as Selective TAAR1 Agonists: Discovery of RO5073012.* BMCL, 2012. **22**(16): p. 5244-5248.

174. Galley, G.H., M. Norcross, R. Pflieger, P. 5-Ethyl-4-Methyl-Pyrazole-3-Carboxamide Derivative Having Activity as Agonist of TAAR 2017 WO 2017/157873

175. Kuvarzin, S.R., I. Sukhanov, K. Onokhin, K. Zakharov, and R.R. Gainetdinov, *Unlocking the Therapeutic Potential of Ulotaront as a Trace Amine-Associated Receptor 1 Agonist for Neuropsychiatric Disorders.* Biomedicines, 2023. **11**(7): p. 1977-1997.

176. Heffernan, M.L.R., L.W. Herman, S. Brown, P.G. Jones, L. Shao, M.C. Hewitt, J.E. Campbell, N. Dedic, S.C. Hopkins, K.S. Koblan, and L. Xie, *Ulotaront: A TAAR1 Agonist for the Treatment of Schizophrenia.* ACS Med. Chem. Lett., 2022. **13**(1): p. 92-98.

177. Sadybekov, A.V. and V. Katritch, *Computational Approaches Streamlining Drug Discovery.* Nature, 2023. **616**(7958): p. 673-685.

178. Sliwoski, G., S. Kothiwale, J. Meiler, and E.W. Lowe, Jr., *Computational Methods in Drug Discovery.* Pharmacol. Rev., 2014. **66**(1): p. 334-395.

179. Pinzi, L. and G. Rastelli, *Molecular Docking: Shifting Paradigms in Drug Discovery.* Int. J. Mol. Sci., 2019. **20**(18): p. 4331-4354.

180. Meng, X.Y., H.X. Zhang, M. Mezei, and M. Cui, *Molecular Docking: A Powerful Approach for Structure-Based Drug Discovery.* Curr. Comput. Aided Drug. Des., 2011. **7**(2): p. 146-157.

181. Wang, G. and W. Zhu, *Molecular Docking for Drug Discovery and Development: A Widely Used Approach but Far from Perfect.* Future Med. Chem., 2016. **8**(14): p. 1707-17010.

182. Cavalla, D., E. Oerton, and A. Bender, *1.02 - Drug Repurposing Review*, in *Comprehensive Medicinal Chemistry Iii*, S. Chackalamannil, D. Rotella, and S.E. Ward, Editors. 2017, Elsevier: Oxford. p. 11-47.

183. Raval, K. and T. Ganatra, *Basics, Types and Applications of Molecular Docking: A Review.* IJCAP, 2022. **7**(1): p. 12-16.

184. Gschwend, D.A., A.C. Good, and I.D. Kuntz, *Molecular Docking Towards Drug Discovery.* J. Mol. Recognit., 1996. **9**(2): p. 175-186.

185. Muhammed, M.T. and E. Aki-Yalcin, *Homology Modeling in Drug Discovery: Overview, Current Applications, and Future Perspectives.* Chem. Biol. Drug. Des., 2019. **93**(1): p. 12-20.

186. Skariyachan, S. and S. Garka, *Chapter 1 - Exploring the Binding Potential of Carbon Nanotubes and Fullerene Towards Major Drug Targets of Multidrug Resistant Bacterial Pathogens and Their Utility as Novel Therapeutic Agents*, in *Fullerens, Graphenes and Nanotubes*, A.M. Grumezescu, Editor. 2018, William Andrew Publishing. p. 1-29.

187. Fiser, A., *Template-Based Protein Structure Modeling.* Methods Mol. Biol., 2010. **673**: p. 73-94.

188. Haddad, Y., V. Adam, and Z. Heger, *Ten Quick Tips for Homology Modeling of High-Resolution Protein 3d Structures.* PLoS Comput. Biol., 2020. **16**(4): p. e1007449.

189. Dalton, J.A. and R.M. Jackson, *An Evaluation of Automated Homology Modelling Methods at Low Target Template Sequence Similarity.* Bioinformatics, 2007. **23**(15): p. 1901-1908.

190. Kopp, J. and T. Schwede, *Automated Protein Structure Homology Modeling: A Progress Report.* Pharmacogenomics, 2004. **5**(4): p. 405-416.

191. Vyas, V.K., R.D. Ukawala, M. Ghate, and C. Chintha, *Homology Modeling a Fast Tool for Drug Discovery: Current Perspectives.* Indian J. Pharm. Sci., 2012. **74**(1): p. 1-17.

192. Gromiha, M.M., R. Nagarajan, and S. Selvaraj, *Protein Structural Bioinformatics: An Overview*, in *Encyclopedia of Bioinformatics and Computational Biology*, S. Ranganathan, et al., Editors. 2019, Academic Press: Oxford. p. 445-459.

193. Staus, D.P., R.T. Strachan, A. Manglik, B. Pani, A.W. Kahsai, T.H. Kim, L.M. Wingler, S. Ahn, A. Chatterjee, A. Masoudi, A.C. Kruse, E. Pardon, J. Steyaert, W.I. Weis, R.S. Prosser, B.K. Kobilka, T. Costa, and R.J. Lefkowitz, *Allosteric Nanobodies Reveal the Dynamic Range and Diverse Mechanisms of G-Protein-Coupled Receptor Activation.* Nature, 2016. **535**(7612): p. 448-452.

194. Rosenbaum, D.M., C. Zhang, J.A. Lyons, R. Holl, D. Aragao, D.H. Arlow, S.G.F. Rasmussen, H.-J. Choi, B.T. Devree, R.K. Sunahara, P.S. Chae, S.H. Gellman, R.O. Dror, D.E. Shaw, W.I. Weis, M. Caffrey, P. Gmeiner, and B.K. Kobilka, *Structure and Function of an Irreversible Agonist-Β2 Adrenoceptor Complex.* Nature, 2011. **469**(7329): p. 236-240.

195. Rasmussen, S.G.F., H.-J. Choi, J.J. Fung, E. Pardon, P. Casarosa, P.S. Chae, B.T. Devree, D.M. Rosenbaum, F.S. Thian, T.S. Kobilka, A. Schnapp, I. Konetzki, R.K. Sunahara, S.H. Gellman, A. Pautsch, J. Steyaert, W.I. Weis, and B.K. Kobilka, *Structure of a Nanobody-Stabilized Active State of the Β2 Adrenoceptor.* Nature, 2011. **469**(7329): p. 175-180.

196. Yang, F., S. Ling, Y. Zhou, Y. Zhang, P. Lv, S. Liu, W. Fang, W. Sun, L.A. Hu, L. Zhang, P. Shi, and C. Tian, *Different Conformational Responses of the Β2-Adrenergic Receptor-Gs Complex Upon Binding of the Partial Agonist Salbutamol or the Full Agonist Isoprenaline.* Natl. Sci. Rev., 2021. **8**(9): p. 1-10.

197. Miller-Gallacher, J.L., R. Nehmé, T. Warne, P.C. Edwards, G.F.X. Schertler, A.G.W. Leslie, and C.G. Tate, *The 2.1 Å Resolution Structure of Cyanopindolol-Bound Β1-Adrenoceptor Identifies an Intramembrane Na+ Ion That Stabilises the Ligand-Free Receptor.* PLoS One, 2014. **9**(3): p. e92727.

198. Zhou, Y., C. Cao, L. He, X. Wang, and X.C. Zhang, *Crystal Structure of Dopamine Receptor D4 Bound to the Subtype Selective Ligand, L745870.* eLife, 2019. **8**: p. e48822.

199. Rasmussen, S.G.F., B.T. Devree, Y. Zou, A.C. Kruse, K.Y. Chung, T.S. Kobilka, F.S. Thian, P.S. Chae, E. Pardon, D. Calinski, J.M. Mathiesen, S.T.A. Shah, J.A. Lyons, M. Caffrey, S.H. Gellman, J. Steyaert, G. Skiniotis, W.I. Weis, R.K. Sunahara, and B.K. Kobilka, *Crystal*

Structure of the B2 Adrenergic Receptor–Gs Protein Complex. Nature, 2011. **477**(7366): p. 549-555.

200. Krasavin, M., A. Lukin, I. Sukhanov, A.S. Gerasimov, S. Kuvarzin, E.V. Efimova, M. Dorofeikova, A. Nichugovskaya, A. Matveev, K. Onokhin, K. Zakharov, M. Gureev, and R.R. Gainetdinov, *Discovery of Trace Amine Associated Receptor 1 (TAAR1) Agonist 2-(5-(4'-Chloro-[1,1'-Biphenyl]-4-Yl)-4h-1,2,4-Triazol-3-Yl)Ethan-1-Amine (LK00764) for the Treatment of Psychotic Disorders.* Biomolecules, 2022. **12**(11): p. 1-28.

201. Šali, A. and T.L. Blundell, *Comparative Protein Modelling by Satisfaction of Spatial Restraints.* J. Mol. Bio, 1993. **234**(3): p. 779-815.

202. Zhang, J., J. Yang, R. Jang, and Y. Zhang, *GPCR-I-Tasser: A Hybrid Approach to G Protein-Coupled Receptor Structure Modeling and the Application to the Human Genome.* Structure, 2015. **23**(8): p. 1538-1549.

203. Baek, M., F. Dimaio, I. Anishchenko, J. Dauparas, S. Ovchinnikov, G.R. Lee, J. Wang, Q. Cong, L.N. Kinch, R.D. Schaeffer, C. Millán, H. Park, C. Adams, C.R. Glassman, A. Degiovanni, J.H. Pereira, A.V. Rodrigues, A.A. Van Dijk, A.C. Ebrecht, D.J. Opperman, T. Sagmeister, C. Buhlheller, T. Pavkov-Keller, M.K. Rathinaswamy, U. Dalwadi, C.K. Yip, J.E. Burke, K.C. Garcia, N.V. Grishin, P.D. Adams, R.J. Read, and D. Baker, *Accurate Prediction of Protein Structures and Interactions Using a Three-Track Neural Network.* Science, 2021. **373**(6557): p. 871-876.

204. Raman, S., R. Vernon, J. Thompson, M. Tyka, R. Sadreyev, J. Pei, D. Kim, E. Kellogg, F. Dimaio, O. Lange, L. Kinch, W. Sheffler, B.H. Kim, R. Das, N.V. Grishin, and D. Baker, *Structure Prediction for Casp8 with All-Atom Refinement Using Rosetta.* Proteins, 2009. **77 Suppl 9**(0 9): p. 89-99.

205. Song, Y., F. Dimaio, R.Y. Wang, D. Kim, C. Miles, T. Brunette, J. Thompson, and D. Baker, *High-Resolution Comparative Modeling with Rosettacm.* Structure, 2013. **21**(10): p. 1735-1742.

206. Torres, P.H.M., A.C.R. Sodero, P. Jofily, and F.P. Silva-Jr, *Key Topics in Molecular Docking for Drug Design.* Int. J. Mol. Sci., 2019. **20**(18): p. 4574-4603.

207. Friesner, R.A., J.L. Banks, R.B. Murphy, T.A. Halgren, J.J. Klicic, D.T. Mainz, M.P. Repasky, E.H. Knoll, M. Shelley, J.K. Perry, D.E. Shaw, P. Francis, and P.S. Shenkin, *Glide: A New Approach for Rapid, Accurate Docking and Scoring. 1. Method and Assessment of Docking Accuracy.* J. Med. Chem., 2004. **47**(7): p. 1739-1749.

208. *Schrodinger Support: What Is the Difference between the Docking Score and Glidescore from the Results of a Socking Run?* 2022 [cited 2024; Available from: https://support.schrodinger.com/s/article/348#:~:text=The%20docking%20score%20and%20the,the%20docking%20of%20your%20ligands.

209. *Knowledge Base, What Is Considered a Good Glidescore?* 2010 [cited 2021; Available from: https://www.schrodinger.com/kb/639#:~:text=For%20Glide%20SP%20or%20HTVS,9%20might%20be%20very%20good.

210. Halgren, T.A., *Identifying and Characterizing Binding Sites and Assessing Druggability.* J. Chem. Inf. Model., 2009. **49**(2): p. 377-389.

211. Halgren, T., *New Method for Fast and Accurate Binding-Site Identification and Analysis.* Chem. Biol. Drug Des., 2007. **69**(2): p. 146-148.

212. Reese, E.A., Y. Norimatsu, M.S. Grandy, K.L. Suchland, J.R. Bunzow, and D.K. Grandy, *Exploring the Determinants of Trace Amine-Associated Receptor 1's Functional Selectivity for the Stereoisomers of Amphetamine and Methamphetamine.* J. Med. Chem., 2014. **57**(2): p. 378-390.

213. Xu, Z., L. Guo, J. Yu, S. Shen, C. Wu, W. Zhang, C. Zhao, Y. Deng, X. Tian, Y. Feng, H. Hou, L. Su, H. Wang, S. Guo, H. Wang, K. Wang, P. Chen, J. Zhao, X. Zhang, X. Yong, L. Cheng, L. Liu, S. Yang, F. Yang, X. Wang, X. Yu, Y. Xu, J.-P. Sun, W. Yan, and Z. Shao, *Ligand*

Recognition and G-Protein Coupling of Trace Amine Receptor TAAR1. Nature, 2023. **624**(7992): p. 672-681.

214. Carugo, O. and S. Pongor, *A Normalized Root-Mean-Square Distance for Comparing Protein Three-Dimensional Structures.* Protein Sci, 2001. **10**(7): p. 1470-1473.

215. Kufareva, I. and R. Abagyan, *Methods of Protein Structure Comparison.* Methods Mol. Biol., 2012. **857**: p. 231-257.

216. Gore, P.A., *Chapter 11 - Cluster Analysis*, in *Handbook of Applied Multivariate Statistics and Mathematical Modeling*, H.E.A. Tinsley and S.D. Brown, Editors. 2000, Academic Press: San Diego. p. 297-321.

217. Wilks, D.S., *Chapter 15 - Cluster Analysis*, in *International Geophysics*, D.S. Wilks, Editor. 2011, Academic Press. p. 603-616.

218. Schrodinger. *What Should I Try If Glide Doesn't Give Me Reasonable Results?* [cited 2025; Available from: https://support.schrodinger.com/s/article/1033#:~:text=First%2C%20you%20should%20assess%20what,9%20might%20be%20very%20good.

219. Farooqui, T. and A.A. Farooqui, *Chapter 17 - Trace Amines and Their Relevance to Neurological Disorders: A Commentary*, in *Trace Amines and Neurological Disorders*, T. Farooqui and A.A. Farooqui, Editors. 2016, Academic Press: San Diego. p. 257-268.

220. Ledonne, A. and N.B. Mercuri, *Chapter 6 - Effects of Trace Amines on the Dopaminergic Mesencephalic System*, in *Trace Amines and Neurological Disorders*, T. Farooqui and A.A. Farooqui, Editors. 2016, Academic Press: San Diego. p. 83-95.

221. Mcree, D.E., *Chapter 3 - Computational Techniques*, in *Practical Protein Crystallography (Second Edition)*, D.E. Mcree, Editor. 1999, Academic Press: San Diego. p. 91-cp91.

222. Liu, H., Y. Zheng, Y. Wang, Y. Wang, X. He, P. Xu, S. Huang, Q. Yuan, X. Zhang, L. Wang, K. Jiang, H. Chen, Z. Li, W. Liu, S. Wang, H.E. Xu, and F. Xu, *Recognition of Methamphetamine and Other Amines by Trace Amine Receptor TAAR1.* Nature, 2023. **624**(7992): p. 663-671.

223. Stalder, H., M.C. Hoener, and R.D. Norcross, *Selective Antagonists of Mouse Trace Amine-Associated Receptor 1 (mTAAR1): Discovery of EPPTB (RO5212773).* BMCL, 2011. **21**(4): p. 1227-1231.

224. Liao, S., M.J. Pino, Jr., C. Deleon, M. Lindner-Jackson, and C. Wu, *Interaction Analyses of hTAAR1 and mTAAR1 with Antagonist EPPTB.* Life Sci., 2022. **300**: p. 120553-120564.

225. Stein, R.M., Y. Yang, T.E. Balius, M.J. O'meara, J. Lyu, J. Young, K. Tang, B.K. Shoichet, and J.J. Irwin, *Property-Unmatched Decoys in Docking Benchmarks.* J. Chem. Inf. Model., 2021. **61**(2): p. 699-714.

226. Rovnyak, G.C., S.Z. Ahmed, C.Z. Ding, S. Dzwonczyk, F.N. Ferrara, W.G. Humphreys, G.J. Grover, D. Santafianos, K.S. Atwal, A.J. Baird, L.G. Mclaughlin, D.E. Normandin, P.G. Sleph, and S.C. Traeger, *Cardioselective Antiischemic Atp-Sensitive Potassium Channel (KATP) Openers. 5. Identification of 4-(N-Aryl)-Substituted Benzopyran Derivatives with High Selectivity.* J. Med. Chem., 1997. **40**(1): p. 24-34.

227. Yang, Y.K.K., L.S; Sung-Eun, Y; Hee, S.J; Jeong, K.W; Kyung, H.S; Byung-Ho, L.; Won, S.O; Ock, L.C; Sang-Un, C. Benzopyran Derivatives Substituted with Secondary Amines Including Imidazole, Their Preparation and Pharmaceutical Compositions Containing Them 2004 WO2004014898A1 WO2004014898A1

228. Galli, U., R. Hysenlika, F. Meneghetti, E. Del Grosso, S. Pelliccia, E. Novellino, M. Giustiniano, and G.C. Tron *Exploiting the Nucleophilicity of the Nitrogen Atom of Imidazoles: One-Pot Three-Component Synthesis of Imidazo-Pyrazines*. Molecules, 2019. **24**, 1959-1976 DOI: 10.3390/molecules24101959.

229. Zhu, X., X. Zhou, and W. Zhang, *One-Pot Reductive Amination of Araldehydes by Aniline Using Borohydride with Cecl3·7h2o as Catalyst.* J. Chem. Res., 2015. **39**(7): p. 390-393.

230.   Raina, R. and M.L. Etter, *Liquid Chromatography with Post-Column Reagent Addition of Ammonia in Methanol Coupled to Negative Ion Electrospray Ionization Tandem Mass Spectrometry for Determination of Phenoxyacid Herbicides and Their Degradation Products in Surface Water.* Anal. Chem. Insights., 2010. **5**: p. 1-14.

231.   Vieira, A.J.S.C. and E.M.S.M. Gaspar, *Chapter 1.1 - Separation, Purification and Identification of the Components of a Mixture*, in *Comprehensive Organic Chemistry Experiments for the Laboratory Classroom*, C.a.M. Afonso, et al., Editors. 2016, The Royal Society of Chemistry. p. 0.

232.   Brocato, T.A., R.F. Hess, M. Moorman, and R.J. Simonson, *Investigations into the Chemical Structure Based Selectivity of the Microfabricated Nitrogen-Phosphorus Detector.* Sensors and Actuators B: Chemical, 2016. **224**: p. 618-623.

233.   Asfari, M., D. Janjic, P. Meda, G. Li, P.A. Halban, and C.B. Wollheim, *Establishment of 2-Mercaptoethanol-Dependent Differentiated Insulin-Secreting Cell Lines.* Endocrinology, 1992. **130**(1): p. 167-178.

234.   Giri, B., S. Dey, T. Das, M. Sarkar, J. Banerjee, and S.K. Dash, *Chronic Hyperglycemia Mediated Physiological Alteration and Metabolic Distortion Leads to Organ Dysfunction, Infection, Cancer Progression and Other Pathophysiological Consequences: An Update on Glucose Toxicity.* Biomed. Pharmacother., 2018. **107**: p. 306-328.

235.   Skelin, M., M. Rupnik, and A. Cencic, *Pancreatic Beta Cell Lines and Their Applications in Diabetes Mellitus Research.* Altex, 2010. **27**(2): p. 105-113.

236.   Maestre, I., J. Jordán, S. Calvo, J.A. Reig, V. Ceña, B. Soria, M. Prentki, and E. Roche, *Mitochondrial Dysfunction Is Involved in Apoptosis Induced by Serum Withdrawal and Fatty Acids in the Beta-Cell Line INS-1.* Endocrinology, 2003. **144**(1): p. 335-345.

237.   Poitout, V., *Glucolipotoxicity of the Pancreatic Beta-Cell: Myth or Reality?* Biochem. Soc. Trans., 2008. **36**(Pt 5): p. 901-904.

238.   Unger, R.H., *Lipotoxicity in the Pathogenesis of Obesity-Dependent Niddm. Genetic and Clinical Implications.* Diabetes, 1995. **44**(8): p. 863-870.

239.   Sako, Y. and V.E. Grill, *A 48-Hour Lipid Infusion in the Rat Time-Dependently Inhibits Glucose-Induced Insulin Secretion and B Cell Oxidation through a Process Likely Coupled to Fatty Acid Oxidation.* Endocrinology, 1990. **127**(4): p. 1580-1589.

240.   Elks, M.L., *Chronic Perifusion of Rat Islets with Palmitate Suppresses Glucose-Stimulated Insulin Release.* Endocrinology, 1993. **133**(1): p. 208-214.

241.   Roche, E., S. Farfari, L.A. Witters, F. Assimacopoulos-Jeannet, S. Thumelin, T. Brun, B.E. Corkey, A.K. Saha, and M. Prentki, *Long-Term Exposure of Beta-Ins Cells to High Glucose Concentrations Increases Anaplerosis, Lipogenesis, and Lipogenic Gene Expression.* Diabetes, 1998. **47**(7): p. 1086-1094.

242.   Lablanche, S., C. Cottet-Rousselle, F. Lamarche, P.Y. Benhamou, S. Halimi, X. Leverve, and E. Fontaine, *Protection of Pancreatic INS-1 B-Cells from Glucose- and Fructose-Induced Cell Death by Inhibiting Mitochondrial Permeability Transition with Cyclosporin a or Metformin.* Cell Death Dis., 2011. **2**(3): p. e134-e134.

243.   Tanaka, Y., P.O. Tran, J. Harmon, and R.P. Robertson, *A Role for Glutathione Peroxidase in Protecting Pancreatic Beta Cells against Oxidative Stress in a Model of Glucose Toxicity.* Proc. Natl. Acad. Sci. USA, 2002. **99**(19): p. 12363-12368.

244.   Laybutt, D.R., A. Sharma, D.C. Sgroi, J. Gaudet, S. Bonner-Weir, and G.C. Weir, *Genetic Regulation of Metabolic Pathways in B-Cells Disrupted by Hyperglycemia.* J. Biol. Chem., 2002. **277**(13): p. 10912-10921.

245.   Marshall, C., G.A. Hitman, P.G. Cassell, and M.D. Turner, *Effect of Glucolipotoxicity and Rosiglitazone Upon Insulin Secretion.* Biochem. Biophys. Res. Commun., 2007. **356**(3): p. 756-762.

246. Tremblay, P.G., C. Fortin, and M.-A. Sirard, *Gene Cascade Analysis in Human Granulosa Tumor Cells (Kgn) Following Exposure to High Levels of Free Fatty Acids and Insulin.* J. Ovarian Res., 2021. **14**(1): p. 178-193.

247. *Abcam - Calcein AM Assay Kit (Fluorometric) (Ab228556).* Available from: https://www.abcam.com/calcein-am-assay-kit-fluorometric-ab228556.html.

248. Miles, F.L., J.E. Lynch, and R.A. Sikes, *Cell-Based Assays Using Calcein Acetoxymethyl Ester Show Variation in Fluorescence with Treatment Conditions.* J. Biol. Methods, 2015. **2**(3): p. 1-12.

249. Cripps, M.J., M. Bagnati, T.A. Jones, B.W. Ogunkolade, S.R. Sayers, P.W. Caton, K. Hanna, M.P. Billacura, K. Fair, C. Nelson, R. Lowe, G.A. Hitman, M.D. Berry, and M.D. Turner, *Identification of a Subset of Trace Amine-Associated Receptors and Ligands as Potential Modulators of Insulin Secretion.* Biochem. Pharmacol., 2020. **171**: p. 113685-113694.

250. Guan, B., W. Li, F. Li, Y. Xie, Q. Ni, Y. Gu, X. Li, Q. Wang, H. Zhang, and G. Ning, *Sfrp5 Mediates Glucose-Induced Proliferation in Rat Pancreatic B-Cells.* J. Endocrinol., 2016. **229**(2): p. 73-83.

251. Brelje, T.C., N.V. Bhagroo, L.E. Stout, and R.L. Sorenson, *Prolactin and Oleic Acid Synergistically Stimulate B-Cell Proliferation and Growth in Rat Islets.* Islets, 2017. **9**(4): p. e1330234.

252. *Mercodia - High Range Rat Insulin ELISA.* 2023 [cited 2023; Available from: https://www.mercodia.com/products/high-range-rat-insulin-elisa/.

253. Bazwinsky-Wutschke, I., E. Mühlbauer, S. Wolgast, and E. Peschke, *Transcripts of Calcium/Calmodulin-Dependent Kinases Are Changed after Forskolin- or Ibmx-Induced Insulin Secretion Due to Melatonin Treatment of Rat Insulinoma B-Cells (INS-1).* Horm. Metab. Res., 2009. **41**(11): p. 805-813.

254. Hii, C.S., J. Stutchfield, and S.L. Howell, *Enhancement of Glucagon Secretion from Isolated Rat Islets of Langerhans by Phorbol 12-Myristate 13-Acetate.* Biochem. J., 1986. **233**(1): p. 287-289.

255. Zawalich, W.S., K.C. Zawalich, S. Ganesan, R. Calle, and H. Rasmussen, *Effects of the Phorbol Ester Phorbol 12-Myristate 13-Acetate (PMA) on Islet-Cell Responsiveness.* Biochem. J., 1991. **278**(1): p. 49-56.

256. Siegel, E.G., C.B. Wollheim, M. Kikuchi, A.E. Renold, and G.W. Sharp, *Dependency of Cyclic AMP-Induced Insulin Release on Intra- and Extracellular Calcium in Rat Islets of Langerhans.* J. Clin. Invest., 1980. **65**(2): p. 233-241.

257. Han, G., H. Takahashi, N. Murao, G. Gheni, N. Yokoi, Y. Hamamoto, S.I. Asahara, Y. Seino, Y. Kido, and S. Seino, *Glutamate Is an Essential Mediator in Glutamine-Amplified Insulin Secretion.* J. Diabetes Investig., 2021. **12**(6): p. 920-930.

258. Yang, J., Y. Chi, B.R. Burkhardt, Y. Guan, and B.A. Wolf, *Leucine Metabolism in Regulation of Insulin Secretion from Pancreatic Beta Cells.* Nutr. Rev., 2010. **68**(5): p. 270-279.

259. Li, C., C. Buettger, J. Kwagh, A. Matter, Y. Daikhin, I.B. Nissim, H.W. Collins, M. Yudkoff, C.A. Stanley, and F.M. Matschinsky, *A Signaling Role of Glutamine in Insulin Secretion.* J. Biol. Chem., 2004. **279**(14): p. 13393-13401.

260. Thoduvayil, S., J.S. Weerakkody, R.V.K. Sundaram, M. Topper, M. Bera, J. Coleman, X. Li, M. Mariappan, and S. Ramakrishnan, *Rapid Quantification of First and Second Phase Insulin Secretion Dynamics Using an in Vitro Platform for Improving Insulin Therapy.* Cell Calcium, 2023. **113**: p. 102766.

261. Dotiwala, A.K., C. Mccausland, and N.S. Samra, *Anatomy, Head and Neck: Blood Brain Barrier*, in *Statpearls*. 2024, StatPearls Publishing LLC.: Treasure Island (FL).

262. Kadry, H., B. Noorani, and L. Cucullo, *A Blood–Brain Barrier Overview on Structure, Function, Impairment, and Biomarkers of Integrity.* FBCNS, 2020. **17**(1): p. 69-93.

263. Gupta, M., H.J. Lee, C.J. Barden, and D.F. Weaver, *The Blood–Brain Barrier (BBB) Score.* J. Med. Chem, 2019. **62**(21): p. 9824-9836.

264.   Daina, A. and V. Zoete, *A Boiled-Egg to Predict Gastrointestinal Absorption and Brain Penetration of Small Molecules.* Chem. Med. Chem, 2016. **11**(11): p. 1117-11121.

265.   Pajouhesh, H. and G.R. Lenz, *Medicinal Chemical Properties of Successful Central Nervous System Drugs.* NeuroRx, 2005. **2**(4): p. 541-553.

266.   Li, X. and M.A. Cooper, *Measurement of Drug Lipophilicity and Pka Using Acoustics.* Analytical Chemistry, 2012. **84**(6): p. 2609-2613.

267.   Hermens, J.L.M., J.H.M. De Bruijn, and D.N. Brooke, *The Octanol–Water Partition Coefficient: Strengths and Limitations.* Environmental Toxicology and Chemistry, 2013. **32**(4): p. 732-733.

268.   Luco, J.M., A.P. Salinas, A.a.J. Torriero, R.N. Vázquez, J. Raba, and E. Marchevsky, *Immobilized Artificial Membrane Chromatography: Quantitative Structure-Retention Relationships of Structurally Diverse Drugs.* J. Chem. Inf. Model., 2003. **43**(6): p. 2129-2136.

269.   Ciura, K., S. Kovačević, M. Pastewska, H. Kapica, M. Kornela, and W. Sawicki, *Prediction of the Chromatographic Hydrophobicity Index with Immobilized Artificial Membrane Chromatography Using Simple Molecular Descriptors and Artificial Neural Networks.* J. Chromatogr. A, 2021. **1660**: p. 462666-462674.

270.   Janicka, M., M. Sztanke, and K. Sztanke, *Predicting the Blood-Brain Barrier Permeability of New Drug-Like Compounds Via HPLC with Various Stationary Phases.* Molecules, 2020. **25**(3): p. 1-23.

271.   Ong, S., H. Liu, and C. Pidgeon, *Immobilized-Artificial-Membrane Chromatography: Measurements of Membrane Partition Coefficient and Predicting Drug Membrane Permeability.* J. Chromatogr. A, 1996. **728**(1): p. 113-128.

272.   Valko, K., S. Rava, S. Bunally, and S. Anderson, *Revisiting the Application of Immobilized Artificial Membrane (IAM) Chromatography to Estimate in Vivo Distribution Properties of Drug Discovery Compounds Based on the Model of Marketed Drugs.* Admet dmpk, 2020. **8**(1): p. 78-97.

273.   Daina, A., O. Michielin, and V. Zoete, *Swissadme: A Free Web Tool to Evaluate Pharmacokinetics, Drug-Likeness and Medicinal Chemistry Friendliness of Small Molecules.* Scientific Reports, 2017. **7**(1): p. 42717.

274.   Valko, K.L., *Application of Biomimetic HPLC to Estimate in Vivo Behavior of Early Drug Discovery Compounds.* Future Drug Discovery, 2019. **1**(1): p. FDD11.

275.   Veber, D.F., S.R. Johnson, H.Y. Cheng, B.R. Smith, K.W. Ward, and K.D. Kopple, *Molecular Properties That Influence the Oral Bioavailability of Drug Candidates.* J. Med. Chem, 2002. **45**(12): p. 2615-2623.

276.   Lipinski, C.A., F. Lombardo, B.W. Dominy, and P.J. Feeney, *Experimental and Computational Approaches to Estimate Solubility and Permeability in Drug Discovery and Development Settings.* Adv. Drug Deliv. Rev., 1997. **23**(1): p. 3-25.

277.   Yoon, C.H., S.J. Kim, B.S. Shin, K.C. Lee, and S.D. Yoo, *Rapid Screening of Blood-Brain Barrier Penetration of Drugs Using the Immobilized Artificial Membrane Phosphatidylcholine Column Chromatography.* J. Biomol. Screen, 2006. **11**(1): p. 13-20.

278.   Karasova, J.Z., J. Korábečný, F. Zemek, V. Sepsova, and K. Kuča, *Acetylcholinesterase Inhibitors Used or Tested in Alzheimers Disease Therapy; Their Passive Diffusion through Blood Brain Barrier: In Vitro Study.* Afr. J. Pharmacy Pharmacol., 2013. **7**: p. 1471-1481.

279.   Proekt, A. and H.C. Hemmings, *Chapter 1 - Mechanisms of Drug Action*, in *Pharmacology and Physiology for Anesthesia (Second Edition)*, H.C. Hemmings and T.D. Egan, Editors. 2019, Elsevier: Philadelphia. p. 2-19.

280.   Joshi, T., P. Sharma, T. Joshi, S. Mathpal, S.C. Pandey, A. Pandey, and S. Chandra, *Chapter 4 - Recent Advances on Computational Approach Towards Potential Drug Discovery against Leishmaniasis*, in *Pathogenesis, Treatment and Prevention of*

Leishmaniasis, M. Samant and S. Chandra Pandey, Editors. 2021, Academic Press. p. 63-84.

281.   Galley, G.N., R. Pfleiger, P. *Pyrazole Carboxamide Derivatives as TAAR Modulators for Use in the Treatment of Several Disorders, Such as Depression, Diabetes and Parkinson's Disease.* 2014 WO 2014/041007 A1

282.   Galley, G.G., C. Norcross, R. Pflieger, P. *Triazole Carboxamide Derivatives* 2014 WO 2014/041106 A1

283.   Staveness, D., T.M. Sodano, K. Li, E.A. Burnham, K.D. Jackson, and C.R.J. Stephenson, *Providing a New Aniline Bioisostere through the Photochemical Production of 1-Aminonorbornanes.* Chem, 2019. **5**(1): p. 215-226.

284.   Zhang, Z. and W. Tang, *Drug Metabolism in Drug Discovery and Development.* Acta Pharmaceutica Sinica B, 2018. **8**(5): p. 721-732.

285.   Gusak, K.N., Z.V. Ignatovich, and E.V. Koroleva, *New Potential of the Reductive Alkylation of Amines.* Russ. Chem. Rev., 2015. **84**(3): p. 288-311.

286.   Selvaraj, S.P. and J.-Y. Chen, *Conjugation of Antimicrobial Peptides to Enhance Therapeutic Efficacy.* Eur. J. Med. Chem., 2023. **259**: p. 115680-115706.

287.   *Acs Green Chemistry Institute Pharmaceutical Roundtable - Reductive Amination*. 2024; Available from: https://reagents.acsgcipr.org/reagent-guides/reductive-amination/#:~:text=Reducing%20agents%20used%20are%20normally,acids%20are%20added%20as%20catalysts.

288.   Smith, M.B., *Chapter 7 - Functional Group Exchange Reactions: Reductions*, in *Organic Synthesis (Fourth Edition)*, M.B. Smith, Editor. 2017, Academic Press: Boston. p. 309-418.

289.   Ouellette, R.J. and J.D. Rawn, *Chapter 15 - Alcohols: Reactions and Synthesis*, in *Organic Chemistry*, R.J. Ouellette and J.D. Rawn, Editors. 2014, Elsevier: Boston. p. 491-534.

290.   Sato, S., T. Sakamoto, E. Miyazawa, and Y. Kikugawa, *One-Pot Reductive Amination of Aldehydes and Ketones with A-Picoline-Borane in Methanol, in Water, and in Neat Conditions.* Tetrahedron, 2004. **60**(36): p. 7899-7906.

291.   Abdel-Magid, A.F., K.G. Carson, B.D. Harris, C.A. Maryanoff, and R.D. Shah, *Reductive Amination of Aldehydes and Ketones with Sodium Triacetoxyborohydride. Studies on Direct and Indirect Reductive Amination Procedures1.* J. Org. Chem, 1996. **61**(11): p. 3849-3862.

292.   Cosenza, V.A., D.A. Navarro, and C.A. Stortz, *Usage of A-Picoline Borane for the Reductive Amination of Carbohydrates.* Arkivoc, 2011. **2011**(7): p. 182-194.

293.   Uchiyama, S., Y. Inaba, M. Matsumoto, and G. Suzuki, *Reductive Amination of Aldehyde 2,4-Dinitrophenylhydrazones Using 2-Picoline Borane and High-Performance Liquid Chromatographic Analysis.* Anal. Chem., 2009. **81**(1): p. 485-489.

294.   Pelter, A., R.M. Rosser, and S. Mills, *Reductive Aminations of Ketones and Aldehydes Using Borane–Pyridine.* J. Chem. Soc., 1984. **1**: p. 717-720.

295.   Dholkawala, F., C. Voshavar, and A.K. Dutta, *Synthesis and Characterization of Brain Penetrant Prodrug of Neuroprotective D-264: Potential Therapeutic Application in the Treatment of Parkinson's Disease.* Eur. J. Pharm. and Biopharm., 2016. **103**: p. 62-70.

296.   Guest, M., R. Mir, G. Foran, B. Hickson, A. Necakov, and T. Dudding, *Trisaminocyclopropenium Cations as Small-Molecule Organic Fluorophores: Design Guidelines and Bioimaging Applications.* J. Org. Chem., 2020. **85**(21): p. 13997-14011.

297.   Moser, H., Q. Lu, P.A. Patten, D. Wang, R. Kasar, S. Kaldor, and B.D. Patterson, *Antibacterial Agents*. 2008, Google Patents.

298.   Hachtel, S., O. Plettenburg, C. Schoenau, M. Loehn, S. Pfeiffer-Marek, M. Mendez-Perez, A. Kannt, J. Dedio, M. Kohlmann, and A. Schiffer, *6-(4-Hydroxy-Phenyl)-3-Alkyl-1h-Pyrazolo [3, 4-B] Pyridine-4-Carboxylic Acid Amide Derivatives as Kinase Inhibitors*. 2014, Google Patents.

299. Chen, J.A., H. Ma, Z. Liu, J. Tian, S. Lu, W. Fang, S. Ze, W. Lu, Q. Xie, J. Huang, and Y. Wang, *Discovery of Orally Available Retinoic Acid Receptor-Related Orphan Receptor Γ-T/Dihydroorotate Dehydrogenase Dual Inhibitors for the Treatment of Refractory Inflammatory Bowel Disease.* J. Med. Chem., 2022. **65**(1): p. 592-615.

300. Chemical, C. *Cayman Chemical - Cyclic AMP Select ELISA Kit.* [cited 2024; Available from: https://cdn.caymanchem.com/cdn/insert/501040.pdf.

301. Cherry, J.A. and V. Pho, *Characterization of cAMP Degradation by Phosphodiesterases in the Accessory Olfactory System.* Chem. Senses, 2002. **27**(7): p. 643-652.

302. Berg, K.A. and W.P. Clarke, *Making Sense of Pharmacology: Inverse Agonism and Functional Selectivity.* Int J Neuropsychopharmacol, 2018. **21**(10): p. 962-977.

303. Pardridge, W.M., *Drug Transport across the Blood–Brain Barrier.* Journal of cerebral blood flow & metabolism, 2012. **32**(11): p. 1959-1972.

304. Li, X., Y. Cai, Z. Zhang, and J. Zhou, *Glial and Vascular Cell Regulation of the Blood-Brain Barrier in Diabetes.* Diabetes & Metabolism Journal, 2022. **46**(2): p. 222-238.

305. Wątroba, M., A.D. Grabowska, and D. Szukiewicz, *Effects of Diabetes Mellitus-Related Dysglycemia on the Functions of Blood–Brain Barrier and the Risk of Dementia.* International Journal of Molecular Sciences, 2023. **24**(12): p. 10069.

306. Guo, Y., R.Y. Wang, J.X. Kang, Y.N. Ma, C.Q. Xu, J. Li, and X. Chen, *Efficient Synthesis of Primary and Secondary Amides Via Reacting Esters with Alkali Metal Amidoboranes.* Nat. Commun., 2021. **12**(1): p. 5964-5973.

307. Orsy, G., S. Shahmohammadi, and E. Forró, *A Sustainable Green Enzymatic Method for Amide Bond Formation.* Molecules, 2023. **28**(15): p. 1-11.

308. Kumari, S., A.V. Carmona, A.K. Tiwari, and P.C. Trippier, *Amide Bond Bioisosteres: Strategies, Synthesis, and Successes.* J. Med. Chem., 2020. **63**(21): p. 12290-12358.

309. Chaturvedi, J., C. Haldar, R. Bisht, G. Pandey, and B. Chattopadhyay, *Meta Selective C–H Borylation of Sterically Biased and Unbiased Substrates Directed by Electrostatic Interaction.* J. Am. Chem. Soc, 2021. **143**(20): p. 7604-7611.

310. Pletz, J., B. Berg, and R. Breinbauer, *A General and Direct Reductive Amination of Aldehydes and Ketones with Electron-Deficient Anilines.* Synthesis, 2016. **48**(09): p. 1301-1317.

311. Nuzhdin, A.L., M.V. Bukhtiyarova, and V.I. Bukhtiyarov, *Two-Step One-Pot Reductive Amination of Furanic Aldehydes Using Cualo(X) Catalyst in a Flow Reactor.* Molecules, 2020. **25**(20): p. 1-7.

312. Jasim, S.H., G.M. Abu Sheikha, H.M. Abuzaid, T.M. Al-Qirim, G.F. Shattat, D.A. Sabbah, S.A. Ata, S.A. Ala, M.S. Aboumair, K.A. Sweidan, and M.M. Bkhaitan, *Synthesis and in Vivo Lipid-Lowering Activity of Novel Imidazoles-5-Carboxamide Derivatives in Triton-Wr-1339-Induced Hyperlipidemic Wistar Rats.* Chem. Pharm. Bull., 2018. **66**(10): p. 953-958.

313. Ripoll, M., M.-C. Bernard, C. Vaure, E. Bazin, S. Commandeur, V. Perkov, K. Lemdani, M.-C. Nicolaï, P. Bonifassi, A. Kichler, B. Frisch, and J. Haensler, *An Imidazole Modified Lipid Confers Enhanced mRNA-Lnp Stability and Strong Immunization Properties in Mice and Non-Human Primates.* Biomaterials, 2022. **286**: p. 121570-121583.

314. Li, W., Z. Ma, J. Chen, G. Dong, L. Du, and M. Li, *Discovery of Environment-Sensitive Fluorescent Ligands of B-Adrenergic Receptors for Cell Imaging and Nanobret Assay.* Anal. Chem., 2022. **94**(19): p. 7021-7028.

315. *Chemaxon Marvinsketch* 2024; Available from: https://chemaxon.com/marvin.

316. *Xundrug - Pka Prediction by Graph-Convolutional Neural Network.* 2024; Available from: https://xundrug.cn/molgpka.

317. Fan, W., Y. Nakamura, and S. Yamago, *Synthesis of Multivalent Organotellurium Chain-Transfer Agents by Post-Modification and Their Applications in Living Radical Polymerization.* Chem. Eur. J., 2016. **22**(47): p. 17006-17010.

318. Yu, X., S. Li, X. Zhu, and Y. Kong, *Inhibitors of Protease-Activated Receptor 4 (PAR4): A Review of Recent Patents (2013–2021).* Expert Opin. Ther. Pat., 2022. **32**(2): p. 153-170.

319. Sharada, D., A. Saha, and B.K. Saha, *Charge Transfer Complexes as Colour Changing and Disappearing–Reappearing Colour Materials.* New J. Chem., 2019. **43**(20): p. 7562-7566.

320. Watté, J., W. Van Gompel, P. Lommens, K. Buysser, and I. Van Driessche, *Titania Nanocrystal Surface Functionalization through Silane Chemistry for Low Temperature Deposition on Polymers.* ACS Applied Materials & Interfaces, 2016. **8**.

321. Siengalewicz, P., J. Mulzer, and U. Rinner, *6.09 Synthesis of Esters and Lactones*, in *Comprehensive Organic Synthesis (Second Edition)*, P. Knochel, Editor. 2014, Elsevier: Amsterdam. p. 355-410.

322. Sharma, P., A. Kumar, and A. Mandloi, *Synthesis of 25,26,27-Tris(Ethoxycarbonylmethoxy)- 28-(Substituted Oxy-Carbonylmethoxy) Calix-4-Arene: First Example of Calix-Imidazole/Benzimidazole Analog.* Synth. Commun., 2002. **32**(17): p. 2619-2626.

323. Yu, P., Y. Wang, Z. Zeng, and Y. Chen, *Metal-Free C–N or C–C Bond Cleavages of A-Azido Ketones: An Oxidative-Amidation Strategy for the Synthesis of A-Ketothioamides and Amides.* The Journal of Organic Chemistry, 2019. **84**(22): p. 14883-14891.

324. Zhang, Q., L. Soulère, and Y. Queneau, *Towards More Practical Methods for the Chemical Synthesis of Thioamides Using Sulfuration Agents: A Decade Update.* Molecules, 2023. **28**(8): p. 3527.

325. Hickman, B.S., M. Mascal, J.J. Titman, and I.G. Wood, *Protonic Conduction in Imidazole: A Solid-State 15n Nmr Study.* J. Am. Chem. Soc, 1999. **121**(49): p. 11486-11490.

326. Yu, X.-L., Y.-H. Fan, X.-N. Zheng, J.-F. Gao, L.-G. Zhuang, Y.-L. Yu, J.-H. Xi, and D.-W. Zhang *Synthesis of Imidazole-Based Molecules under Ultrasonic Irradiation Approaches*. Molecules, 2023. **28**, 4845-4880 DOI: 10.3390/molecules28124845.

327. Klinger, K.M., F. Liebner, I. Fritz, A. Potthast, and T. Rosenau, *Formation and Ecotoxicity of N-Heterocyclic Compounds on Ammoxidation of Mono- and Polysaccharides.* J. Agric. Food Chem., 2013. **61**(38): p. 9004-9014.

328. Alnefeesi, Y., J.K. Tamura, L.M.W. Lui, M.Y. Jawad, F. Ceban, S. Ling, F. Nasri, J.D. Rosenblat, and R.S. Mcintyre, *Trace Amine-Associated Receptor 1 (TAAR1): Potential Application in Mood Disorders: A Systematic Review.* Neurosci. Biobehav. Rev., 2021. **131**: p. 192-210.

329. Nair, P.C., J.M. Chalker, R.A. Mckinnon, C.J. Langmead, K.J. Gregory, and T. Bastiampillai, *Trace Amine-Associated Receptor 1 (TAAR1): Molecular and Clinical Insights for the Treatment of Schizophrenia and Related Comorbidities.* ACS Pharmacol. Transl. Sci., 2022. **5**(3): p. 183-188.

330. Ponsioen, B., J. Zhao, J. Riedl, F. Zwartkruis, G. Van Der Krogt, M. Zaccolo, W.H. Moolenaar, J.L. Bos, and K. Jalink, *Detecting cAMP-Induced Epac Activation by Fluorescence Resonance Energy Transfer: Epac as a Novel cAMP Indicator.* EMBO Rep, 2004. **5**(12): p. 1176-1180.

331. Salahpour, A., S. Espinoza, B. Masri, V. Lam, L.S. Barak, and R.R. Gainetdinov, *BRET Biosensors to Study GPCR Biology, Pharmacology, and Signal Transduction.* Front Endocrinol., 2012. **3**: p. 105-114.

332. Cripps, M.J., K. Hanna, C. Lavilla, Jr., S.R. Sayers, P.W. Caton, C. Sims, L. De Girolamo, C. Sale, and M.D. Turner, *Carnosine Scavenging of Glucolipotoxic Free Radicals Enhances Insulin Secretion and Glucose Uptake.* Sci. Rep., 2017. **7**(1): p. 13313-13320.

333. López, E., C. Arce, M.J. Oset-Gasque, S. Cañadas, and M.P. González, *Cadmium Induces Reactive Oxygen Species Generation and Lipid Peroxidation in Cortical Neurons in Culture.* Free Radic. Biol. Med., 2006. **40**(6): p. 940-951.

334. Reiniers, M.J., R.F. Van Golen, S. Bonnet, M. Broekgaarden, T.M. Van Gulik, M.R. Egmond, and M. Heger, *Preparation and Practical Applications of 2',7'-Dichlorodihydrofluorescein in Redox Assays.* Anal. Chem., 2017. **89**(7): p. 3853-3857.

335. Opmeer, E.M., R. Kortekaas, and A. Aleman, *Depression and the Role of Genes Involved in Dopamine Metabolism and Signalling.* Prog. Neurobiol., 2010. **92**(2): p. 112-133.

336. Freeman, B.B., L. Yang, and Z. Rankovic, *Practical Approaches to Evaluating and Optimizing Brain Exposure in Early Drug Discovery.* Eur. J. Med. Chem., 2019. **182**: p. 111643-111657.

337. Stegemann, S., F. Leveiller, D. Franchi, H. De Jong, and H. Lindén, *When Poor Solubility Becomes an Issue: From Early Stage to Proof of Concept.* Eur. J. Pharm. Sci., 2007. **31**(5): p. 249-261.

338. Kato, R., W. Zeng, V.B. Siramshetty, J. Williams, M. Kabir, N. Hagen, E.C. Padilha, A.Q. Wang, E.A. Mathé, X. Xu, and P. Shah, *Development and Validation of PAMPA-BBB Qsar Model to Predict Brain Penetration Potential of Novel Drug Candidates.* Front. Pharm., 2023. **14**(1291246): p. 1-11.

339. Mensch, J., A. Melis, C. Mackie, G. Verreck, M.E. Brewster, and P. Augustijns, *Evaluation of Various Pampa Models to Identify the Most Discriminating Method for the Prediction of BBB Permeability.* Eur. J. Pharm. Biopharm., 2010. **74**(3): p. 495-502.

340. Di, L., E.H. Kerns, K. Fan, O.J. Mcconnell, and G.T. Carter, *High Throughput Artificial Membrane Permeability Assay for Blood–Brain Barrier.* Eur. J. Med. Chem., 2003. **38**(3): p. 223-232.

341. Scientific, T. *Chemistry of Protein Assays*. Available from: https://www.thermofisher.com/ca/en/home/life-science/protein-biology/protein-biology-learning-center/protein-biology-resource-library/pierce-protein-methods/chemistry-protein-assays.html.

342. *Enzo - Which Controls to Use in ELISA Assays?* . 2023; Available from: https://www.enzo.com/note/which-controls-to-use-in-elisa-assays/.

9. Appendix

9.1. Python Script

```
!pip3 install scikit-learn --user

!pip3 install matplotlib --user

!pip3 install pdb-tools

!pip3 install --upgrade pdb-tools

import mdtraj as mdt

import glob

import os.path as op

import numpy as np

from matplotlib import pyplot as plt

%matplotlib inline

from sklearn.manifold import MDS
```

```python
def long2short(res):
    '''
    Convert a 3-letter residue name to the 1-letter equivalent.
    '''
    l2s = {'ALA': 'A',
           'ASN': 'N',
           'ASP': 'D',
           'ARG': 'R',
           'CYS': 'C',
           'GLY': 'G',
           'GLN': 'Q',
           'GLU': 'E',
           'HIS': 'H',
           'ILE': 'I',
           'LEU': 'L',
           'LYS': 'K',
           'MET': 'M',
           'PHE': 'F',
           'PRO': 'P',
           'SER': 'S',
           'THR': 'T',
           'TYR': 'Y',
           'TRP': 'W',
           'VAL': 'V'}
    return l2s.get(res, ' ')
def sequence(model):
    '''
    Generate an amino acid sequence string for the model.
    '''
    rnames = [r.name for r in model.topology.residues]
```

```python
    rseqs = [r.resSeq for r in model.topology.residues]

    slist = [' ' for i in range(rseqs[-1] + 1)]

    for rseq, rname in zip(rseqs, rnames):

        slist[rseq - 1] = long2short(rname)

    return ''.join(slist)

def reduce_model(model, selection):

    '''

    Make a new model from a subset of the atoms in the input model.

    '''

    new_model = mdt.Trajectory(model.xyz, model.topology)

    sel = model.topology.select(selection)

    new_model.topology = model.topology.subset(sel)

    new_model.xyz = model.xyz[:, sel]

    return new_model

filenames = glob.glob('file_path_location/*.pdb')

filenames.sort()

model_names = [op.splitext(op.basename(f))[0] for f in filenames]

max_name_length = max([len(name) for name in model_names])

for i, model_name in enumerate(model_names):

    print(i, model_name)

models = [mdt.load(f) for f in filenames]

sequences = [sequence(model) for model in models]

max_sequence_length = max([len(s) for s in sequences])

row_length = 70

n_rows = 1 + max_sequence_length // row_length

row_start = 0

name_spacer = ' ' * max_name_length + '    '

markers = '         *' * 10

header_line = name_spacer + markers[:row_length+1]

row_format = '{{:{}s}}:{{:3d}}:{{}}'.format(max_name_length)
```

```python
for i in range(n_rows):

    print(header_line)

    row_end = row_start + row_length

    for i, seq in enumerate(sequences):

        print(row_format.format(model_names[i], row_start+1, seq[row_start:row_end]))

    print('')

    row_start = row_end

core_models = [reduce_model(model, 'name CA and (resSeq 1 to 13 or resSeq 22 to 37 or
resSeq 44 to 59 or resSeq 94 to 127) and mass > 2.0') for model in models] # change resSeq
values for appropriate amino acids in binding site

for model in core_models:

    print(model)

n_models = len(core_models)

rmsd_matrix = np.zeros((n_models, n_models))

for i in range(n_models):

    for j in range(n_models):

        rmsd_matrix[i, j] = mdt.rmsd(core_models[i], core_models[j])[0]

row_format = '{:5.2f' * n_models

for row in rmsd_matrix:

    print(row_format.format(*row))

plt.title('RMSD matrix for TAAR1 homology models')

plt.xlim((0, 21))

plt.ylim((0, 21))

plt.xticks(range(0,21,2))

plt.yticks(range(0,21,2))

plt.imshow(rmsd_matrix, origin='lower')

plt.colorbar()

plt.savefig (appropriate_filename.png', dpi=130)

rmsd_matrix = 0.5 * (rmsd_matrix + rmsd_matrix.T)

mds = MDS(dissimilarity='precomputed')
```

```
coordinates = mds.fit_transform(rmsd_matrix)

plt.figure(figsize=(7, 7))

plt.plot(coordinates[:,0], coordinates[:,1], 'x')

for i, xy in enumerate(coordinates):

    plt.annotate('{}'.format(i), xy)

plt.savefig ('appropriate_filename.png', dpi=65)
```

9.2. IAM Calibration

Table 9.1 *Data obtained from IAM RP-HPLC data to determine CHI$_{IAM}$ using Bio-Mimetic Chromatography Limited*

IAM Valko calibration mixture.

Calibration standard	Run 1 (min)	Run 2 (min)	Run 3 (min)	Average R$_t$	Fixed CHI$_{IAM}$
Octanophenone	3.471	3.474	3.473	3.473	49.4
Heptanophenone	3.268	3.269	3.27	3.269	45.7
Hexanophenone	3.028	3.031	3.032	3.030	41.8
Valerophenone	2.736	2.74	2.742	2.739	37.3
Butyrophenone	2.383	2.386	2.389	2.386	32
Propiophenone	1.962	1.964	1.966	1.964	25.9
Acetophenone	1.436	1.433	1.435	1.435	17.2
Acetanilide	1.169	1.162	1.163	1.165	11.5
Paracetamol	0.861	0.818	0.848	0.852	2.9

Figure 9.1 *IAM RP-HPLC calibration curve determined using Bio-Mimetic Chromatography Limited IAM Valko calibration mixture.*
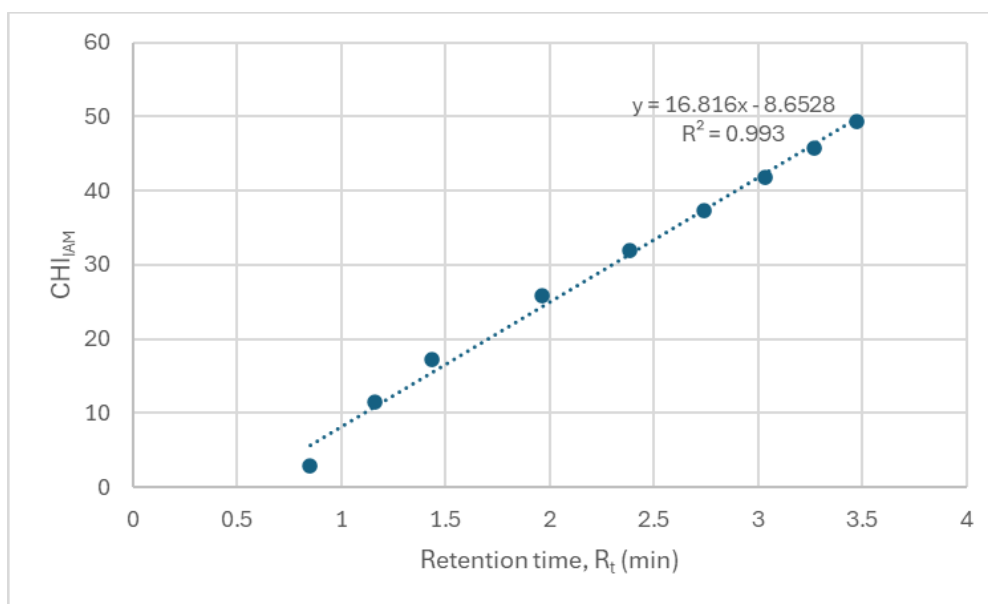

Table 9.2 *Suitability study to determine RP-HPLC IAM column performance showing the determined CHI_{IAM} is within ± 5 from the expected CHI_{IAM}.*

Calibration standard	Run 1 (min)	Run 2 (min)	Run 3 (min)	Average R_t	Determined CHI_{IAM}	Expected CHI_{IAM}
Carbamazepine	2.138	2.131	2.129	2.133	27.210	27
Colchicine	1.802	1.793	1.801	1.799	21.594	23
Warfarin	1.529	1.525	1.520	1.525	16.986	20
Indomethacin	2.114	2.106	2.112	2.11	26.840	30
Propranolol	3.339	3.332	3.340	3.337	47.462	42
Nicardipine	3.318	3.310	3.308	3.312	47.041	45

9.3. Reflection on professional internship for PhD students at Sygnature Discovery

Note to examiners:

This statement is included as an appendix to the thesis in order that the thesis accurately captures the PhD training experienced by the candidate as a BBSRC Doctoral Training Partnership student.

The professional Internship for PhD students is a compulsory 3-month placement which must by undertaken by DTP students. It is usually centred on a specific project and must not be related to the PhD project. This reflective statement is designed to capture the skills development which has taken place during the student's placement and the impact on their career plans it has had.

Statement:

As part of my PhD, I completed a 3-month internship at Sygnature Discovery (Nottingham, UK) under the supervision of Dr Diana Leite, where I researched lysosomal degradation and autophagy with respect to neurodegenerative disorders. During the internship, I was tasked with maintaining the cell culture of 4 different fibroblast conditions (1 x healthy, 1 x Alzheimer's disease and 2 x Parkinson's disease) and perform assays which measured differing pathological hallmarks of Parkinsons's disease and Alzheimer's disease.

By working primarily within the Bioscience department, it broadened my laboratory skillset. The project enabled me to learn new techniques including immunohistochemistry, cell mounting, confocal microscopy and data manipulation. As I was not familiar with immunohistology or the use of confocal microscopy, I was able to troubleshoot ideas, gain confidence working independently and develop new skills which will be beneficial when applying for future career opportunities. Additionally, the internship provided the opportunity to work with industry-

standard equipment, such as the use of electronic pipettes. Although I had used similar Gilson pipettes during my studies, the pipettes at Sygnature Discovery were automated and as such allowed for a pre-set volume of liquid to be aspirated or dispensed multiple times, thus making the assay setup more time effective.

During my internship at Sygnature Discovery my scientific network significantly increased. In addition to taking part in weekly social coffee and cake catch up meetings with other members of the department, I attended a charity away day held at Colwick Hall, Nottingham. The day began with a town hall meeting where I was able to learn and understand the process of running a successful contract research organisation across multiple national and international sites. Following lunch, an external charity, O3E, held a team building activity where within teams, we had to build and decorate skateboards for young people living in deprived areas. As each team consisted of staff members with differing job titles across all departments (Bioscience, Chemistry, Computational chemistry, DMPK and Human Resources), I was able to interact and build connections.

Due to my performance, I was invited to attend Sygnature Discovery's annual workshop for outstanding PhD and Postdoctoral students held at their Alderley Edge site, expanding my scientific knowledge and connections.

On reflection, my experience at Sygnature Discovery was beneficial. Completing a project unrelated to my PhD, I was able to gain confidence in an unfamiliar environment and subject area as well as learn new techniques. The internship has further developed my transferable skills and knowledge putting me in good stead for my scientific career.